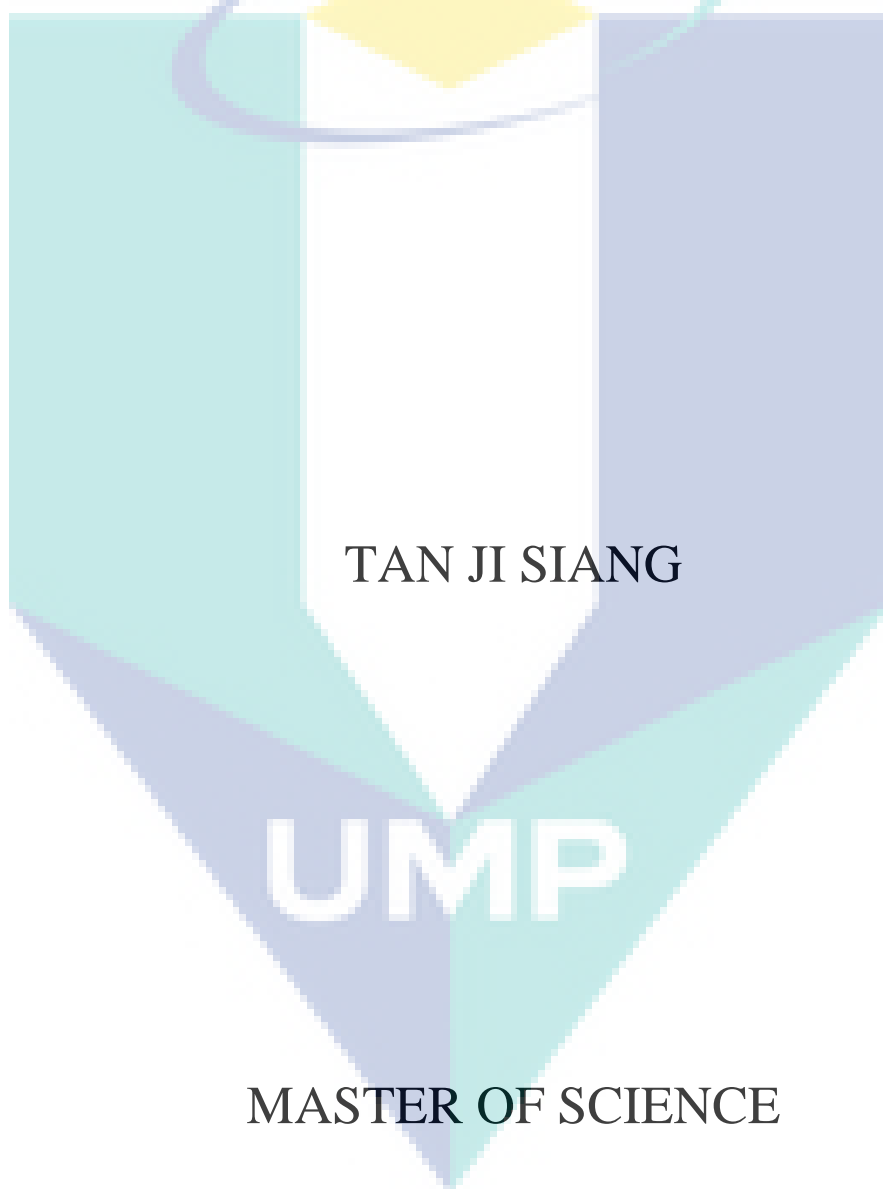


COMBINED STEAM AND CO<sub>2</sub> REFORMING  
OF METHANE OVER CARBON-RESISTANT  
BORON-PROMOTED Ni/SBA-15 CATALYSTS  
FOR SYNGAS PRODUCTION



MASTER OF SCIENCE

UNIVERSITI MALAYSIA PAHANG

## UNIVERSITI MALAYSIA PAHANG

### DECLARATION OF THESIS AND COPYRIGHT

Author's Full Name : \_\_\_\_\_

Date of Birth : \_\_\_\_\_

Title : \_\_\_\_\_

\_\_\_\_\_

Academic Session : \_\_\_\_\_

I declare that this thesis is classified as:

- CONFIDENTIAL (Contains confidential information under the Official Secret Act 1997)\*
- RESTRICTED (Contains restricted information as specified by the organization where research was done)\*
- OPEN ACCESS I agree that my thesis to be published as online open access (Full Text)

I acknowledge that Universiti Malaysia Pahang reserves the following rights:

1. The Thesis is the Property of Universiti Malaysia Pahang
2. The Library of Universiti Malaysia Pahang has the right to make copies of the thesis for the purpose of research only.
3. The Library has the right to make copies of the thesis for academic exchange.

Certified by:

\_\_\_\_\_  
(Student's Signature)

\_\_\_\_\_  
(Supervisor's Signature)

\_\_\_\_\_  
New IC/Passport Number

Date:

\_\_\_\_\_  
Name of Supervisor

Date:

NOTE : \* If the thesis is CONFIDENTIAL or RESTRICTED, please attach a thesis declaration letter.

### **SUPERVISOR'S DECLARATION**

We hereby declare that we have checked this thesis and in our opinion, this thesis is adequate in terms of scope and quality for the award of the degree of Master of Science.

---

(Supervisor's Signature)

Full Name : Dr. Dai-Viet N. Vo  
Position : Senior Lecturer  
Date :

---

(Co-supervisor's Signature)

Full Name : Dr. Herma Dina Binti Setiabudi  
Position : Senior Lecturer  
Date :

### **STUDENT'S DECLARATION**

I hereby declare that the work in this thesis is based on my original work except for quotations and citations which have been duly acknowledged. I also declare that it has not been previously or concurrently submitted for any other degree at Universiti Malaysia Pahang or any other institutions.

---

(Student's Signature)

Full Name : TAN JI SIANG

ID Number : MKC 15034

Date :



UMP

COMBINED STEAM AND CO<sub>2</sub> REFORMING OF METHANE OVER CARBON-  
RESISTANT BORON-PROMOTED Ni/SBA-15 CATALYSTS FOR SYNGAS  
PRODUCTION

The logo of the University of Malaysia Pahang (UMP) is a shield-shaped emblem. It features a central white vertical band. The left and right sides of the shield are colored light blue and light purple, respectively. At the top of the shield, there is a yellow diamond shape with a blue and green circular swoosh above it. The text 'TAN JI SIANG' is centered on the white band, and 'UMP' is written in large white letters across the bottom of the shield.

TAN JI SIANG

Thesis submitted in fulfillment of the requirements  
for the award of the degree of  
Master of Science

UMP

Faculty of Chemical & Natural Resources Engineering

UNIVERSITI MALAYSIA PAHANG

FEB 2018

## ACKNOWLEDGEMENTS

I would like to express my sincere gratitude to my supervisor, Dr. Dai-Viet N. Vo for his invaluable guidance, enthusiasm and continuous encouragement throughout the duration of this study. For these two years period, Dr. Dai-Viet N. Vo has imparted me with professional knowledge and unique insights as well as useful research skills in the reaction engineering and heterogeneous catalysis field for nurturing me as a qualified academician and researcher. I am truly grateful to his tolerance for my repeating mistakes and his commitment to my future career. I would also like to thank my co-supervisor, Dr. Herma Dina Binti Setiabudi for her advices and assistance in improving this work throughout the research.

I would like to appreciate all members of GTL research group, past and present, including Sharanjit Singh, Fahim Fayaz, Osaze Omeregbe, Mahadi Bahari, Attili Ramkiran for creating it a pleasant workplace. Special thanks to Sharanjit Singh for his help with laboratory equipment and reactor set-up. In addition, I would like to thank the assistance from lab mates and staffs of Faculty of Chemical and Natural Resources Engineering, Central lab and Centre of Excellence for Advanced Research in Fluid Flow, UMP in this study.

Additionally, I would like to acknowledge the financial support provided by the MyBrain15 from the Ministry of Higher Education and Universiti Malaysia Pahang (UMP Research Grant Scheme, RDU170326) to conduct this research.

My heartfelt thanks to Shi Yan for her patience and love throughout my grad school journey in this university. She has not only inspired me further as an academician but also has been my emotional anchor as well.

Lastly, I dedicate this thesis to my late-mother who was my main motivation in pursuing my studies. I appreciate my parents and brother's unconditional love and sacrifice in my life. I would have never come this far without their support and faith in me.

## ABSTRAK

Kebelakangan ini, gabungan stim dan CO<sub>2</sub> reformasi metana (CSCRM) muncul sebagai teknik yang menjanjikan kerana ia mampu menjana sumber tenaga hijau dan mampan daripada biogas. Sebenarnya, CSCRM dilaporkan sebagai proses pembaharuan yang menjanjikan kerana kestabilan pemangkin yang tinggi dalam kewujudan CO<sub>2</sub> dan H<sub>2</sub>O yang beroksidasi dan penyesuaian fleksibel nisbah H<sub>2</sub>/CO dengan memanipulasi komposisi bahan. Pemangkin yang berasaskan Ni menghadapi halangan yang mencabar, iaitu pembentukan kok dan pengukuhan Ni logam yang mengakibatkan penyahaktifan pemangkin yang cepat pada suhu yang tinggi. Oleh itu, tujuan penyelidikan ini adalah untuk mengkaji kesan B-promoter terhadap sifat fizikokimia pemangkin 10%Ni/SBA-15 dan mengkaji pengaruh suhu reaksi dan tekanan separa terhadap prestasi katalitik reaksi CSCRM. Pemangkin 10%Ni/SBA-15 yang tiada dan B-promoter menggunakan kaedah impregnasi basah yang baru dan diperiksa untuk pembaharuan bagi gabungan stim dan CO<sub>2</sub> reformasi metana (CSCRM) pada pelbagai suhu dari 973-1073 K dan stoikiometri komposisi bahan. Pengurangan yang tidak dapat dielakkan dalam permukaan permukaan BET dan saiz kristal NiO dengan kenaikan boron dari 1% hingga 5%B loading boleh disebabkan oleh pengumpulan zarah B<sub>2</sub>O<sub>3</sub> dan tindak balas pendedahan semasa penalaan dan dengan itu menghalangi mesopores sokongan SBA-15 pada komposisi B yang tinggi. Zarah NiO telah dikurangkan sepenuhnya kepada fasa Ni<sup>0</sup> logam semasa prapembakaran H<sub>2</sub> dan suhu pengurangan fasa NiO telah beralih ke suhu yang lebih tinggi dengan tambahan B disebabkan oleh peningkatan interaksi antara fasa asas NiO dan B<sub>2</sub>O<sub>3</sub> yang berasid. Untuk semua suhu yang digunakan, 3%B dianggap sebagai pemangkin promoter yang paling baik dari segi penukaran tindak balas dan 3%B-10%Ni/SBA-15 pemangkin menunjukkan hasil H<sub>2</sub> yang tertinggi sebanyak 69.4% pada 1073 K. Di samping itu, penukaran CH<sub>4</sub> dan CO<sub>2</sub> dipertingkatkan kira-kira 23.2% dan 32.4%, bersamaan dengan peningkatan suhu dari 973 hingga 1073 K disebabkan oleh sifat endotermik tindak balas CSCRM. Peningkatan tekanan separa CO<sub>2</sub> dari 15 hingga 25 kPa menghasilkan penurunan dalam penukaran CH<sub>4</sub> dan CO<sub>2</sub> mungkin disebabkan oleh penjerapan bersaing di antara reaktan. Selain itu, penurunan bagi penukaran CO<sub>2</sub> dan penambahan bagi penukaran CH<sub>4</sub> pada tekanan separa H<sub>2</sub>O yang melebihi daripada 20 kPa mencadangkan bahawa pembaharuan stim dengan metana lebih baik daripada reaksi pembaharuan CO<sub>2</sub> dengan metana. Pengurangan dalam penukaran reaktan dengan peningkatan tekanan separa CH<sub>4</sub> dapat mencadangkan kadar pembentukan karbon melalui pemendapan CH<sub>4</sub> adalah lebih tinggi daripada gasifikasi karbon oleh CO<sub>2</sub> dan agen pengoksida dalam CH<sub>4</sub> yang banyak. Pemangkin 3%B-10%Ni/SBA-15 dianggap stabil selama 24 jam pada komposisi stoikiometrik dan suhu 973 hingga 1073 K dari segi aktiviti pemangkin dan hasil produk. Pemangkin 3%B-10%Ni/SBA-15 mempamerkan tahap penyahaktif pemangkin yang paling rendah kerana kesan penambahan boron. Boron menindas pembentukan karbon grafit pada permukaan pemangkin dan jumlah pemendapan karbon dikurangkan kira-kira 4 kali.

## ABSTRACT

Combined steam and CO<sub>2</sub> reforming of methane (CSCRM) has recently appeared as a promising technique since it is capable of generating a green and sustainable energy source from biogas. In fact, CSCRM is reportedly a promising reforming process owing to its high catalytic stability in the coexistence of CO<sub>2</sub> and H<sub>2</sub>O oxidizing reactants and flexible adjustment of H<sub>2</sub>/CO ratios by the manipulation of feedstock composition. Ni-based catalysts are widely known encountering barriers of coke formation and Ni metal sintering lead to rapid catalyst deactivation at high reaction temperature. Hence, the aim of this research was to investigate the effect of B-promoter on the physicochemical properties of 10%Ni/SBA-15 catalyst and examine the influence of reaction temperature and reactant partial pressure on the catalytic performance of CSCRM reaction. The unpromoted and B-promoted 10%Ni/SBA-15 catalysts were prepared by sequential incipient wetness impregnation method and assessed for combined steam and CO<sub>2</sub> reforming of methane (CSCRM) at various reaction temperatures of 973-1073 K and stoichiometric feed composition. An inevitable decline in BET surface area and average NiO crystallite size with boron promotion from 1% to 5%B loading could be due to the agglomeration of B<sub>2</sub>O<sub>3</sub> particles and deboration reaction during calcination and hence blocking mesopores of SBA-15 support at elevated B composition. NiO particles were reduced completely to metallic Ni<sup>0</sup> phase during H<sub>2</sub> pretreatment and the reduction temperature of NiO phase was shifted towards higher temperature with B-addition due to enhancing interaction between the basic NiO and acidic B<sub>2</sub>O<sub>3</sub> phases. For all reaction temperature employed, 3%B appeared to be the best promoter loading in terms of reactant conversions and 3%B-10%Ni/SBA-15 catalyst exhibited the highest H<sub>2</sub> yield of 69.4% at 1073 K. The CH<sub>4</sub> and CO<sub>2</sub> conversions were enhanced about 23.2% and 32.4%, correspondingly with rising reaction temperature from 973 to 1073 K due to its endothermic nature. Additionally, the effect of various feed composition on CSCRM was also investigated in order to obtain the optimum feed ratio. The increase in CO<sub>2</sub> partial pressure from 15 to 25 kPa resulted in a decline in both CH<sub>4</sub> and CO<sub>2</sub> conversions probably due to the competing adsorption between reactants. In addition, the decline in CO<sub>2</sub> conversion and the increase in CH<sub>4</sub> conversion at H<sub>2</sub>O partial pressure greater than 20 kPa could suggest that steam reforming of methane was more preferable than CO<sub>2</sub> reforming of methane reaction. The reducing reactant conversions with rising CH<sub>4</sub> partial pressure could suggest that the rate of carbon formation via CH<sub>4</sub> deposition was superior to that of carbon gasification by CO<sub>2</sub> and oxidizing agents in CH<sub>4</sub>-rich feedstock. From the above results, the  $P_{CO_2}$  of 15 kPa,  $P_{H_2O}$  of 20 kPa and  $P_{CH_4}$  of 45 kPa appeared to be the best feed composition for the CSCRM reaction in terms of reactant conversions and product yields. Interestingly, irrespective of operating parameters, the H<sub>2</sub>/CO ratio was always varied within 1.1 to 2.6 appropriate for downstream Fischer-Tropsch synthesis. The 3%B-10%Ni/SBA-15 catalyst appeared to be stable for 24 h on-stream at stoichiometric feed composition and reaction temperature of 973 to 1073 K in terms of catalytic activity and product yield. The 3%B-10%Ni/SBA-15 catalyst exhibited the lowest degree of catalyst deactivation could be assigned to the promotional effect of boron addition. Boron promoter suppressed the formation of graphitic carbon on catalyst surface and the amount of carbonaceous deposition was reduced about 4 times.

## TABLE OF CONTENT

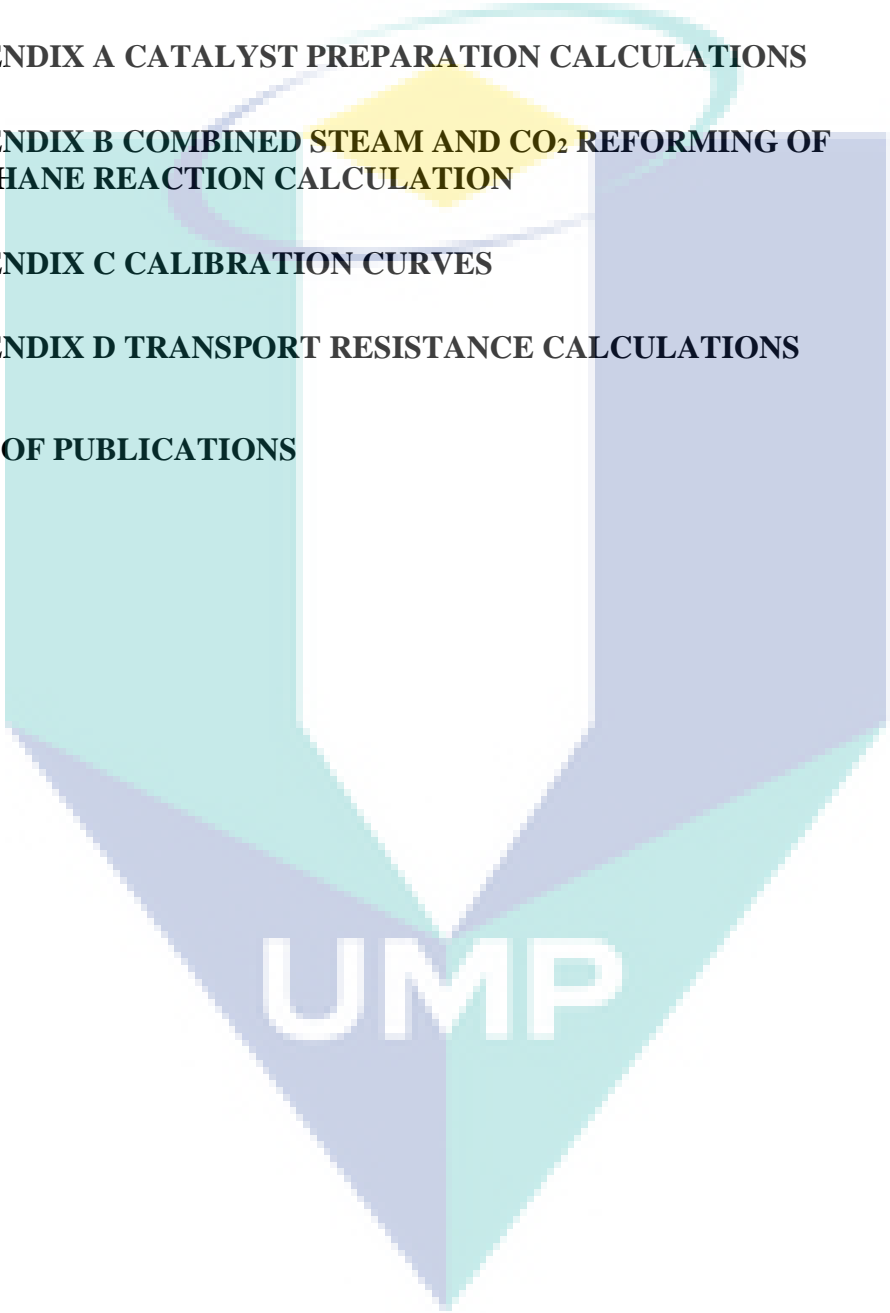
<b>DECLARATION</b>	
<b>TITLE PAGE</b>	
<b>ACKNOWLEDGEMENTS</b>	<b>ii</b>
<b>ABSTRAK</b>	<b>iii</b>
<b>ABSTRACT</b>	<b>iv</b>
<b>TABLE OF CONTENT</b>	<b>v</b>
<b>LIST OF TABLES</b>	<b>x</b>
<b>LIST OF FIGURES</b>	<b>xi</b>
<b>LIST OF SYMBOLS</b>	<b>xiv</b>
<b>LIST OF ABBREVIATIONS</b>	<b>xvi</b>
<b>CHAPTER 1 INTRODUCTION</b>	<b>1</b>
1.1 Introduction	1
1.2 Problem Statement	5
1.3 Research Objectives	6
1.4 Scopes of Study	6
1.5 Overview of Thesis	7
<b>CHAPTER 2 LITERATURE REVIEW</b>	<b>9</b>
2.1 Introduction	9
2.1.1 Gas Economy	9
2.2 Global Gas-To-Liquid (GTL) Plants	13
2.3 Methods to Syngas Production	14

2.3.1	Catalytic Steam Reforming of Methane (SRM)	16
2.3.2	Catalytic Dry Reforming of Methane (DRM)	17
2.3.3	Catalytic Combined Steam and CO <sub>2</sub> Reforming of Methane (CSCRM)	18
2.4	Reaction Mechanisms	19
2.5	Thermodynamic Equilibrium Analysis	23
2.6	Reforming Catalysts	26
2.6.1	Noble and Non-noble Metals	26
2.6.2	Catalyst Supports	28
2.6.3	Catalyst Promoters	31
2.7	Catalyst Preparation Methods	32
2.8	Catalyst Deactivation	34
2.8.1	Poisoning	35
2.8.2	Sintering (Aging)	37
2.8.3	Coking (Fouling)	38
2.9	Concluding Remarks	40
<b>CHAPTER 3 METHODOLOGY</b>		<b>41</b>
3.1	Introduction	41
3.2	Material	41
3.2.1	Chemicals	41
3.2.2	Gases	42
3.2.3	Equipment	43
3.3	Catalyst Preparation	43
3.3.1	SBA-15 Support	43
3.3.2	B-promoted 10%Ni/SBA-15 Catalysts	44
3.4	Catalyst Characterization	46

3.4.1	Textural Analyses	46
3.4.2	Fourier Transform Infrared Spectroscopy (FTIR) Analyses	47
3.4.3	X-ray Diffraction (XRD) Measurements	47
3.4.4	H <sub>2</sub> Temperature-programmed Reduction (H <sub>2</sub> -TPR) Analyses	49
3.4.5	Raman Spectroscopy Measurements	49
3.4.6	Scanning Electron Microscopy (SEM) Measurements	49
3.4.7	Transmission Electron Microscopy (TEM) Analyses	50
3.4.8	Temperature-programmed Oxidation (TPO) Measurements	50
3.5	Experimental Set-up	50
3.6	Syringe Pump and Mass Flow Controller (MFC) Calibration	53
3.7	Combined Steam and CO <sub>2</sub> Reforming of Methane Reaction Metrics	54
<b>CHAPTER 4 PRELIMINARY WORK</b>		<b>55</b>
4.1	Introduction	55
4.2	CSCRM Blank Test	55
4.3	Steps in Catalytic Reaction	56
4.3.1	External Mass Transfer Resistance	59
4.3.2	Internal Mass Transfer Resistance	60
4.3.3	External Heat Transfer Resistance	61
4.3.4	Internal Heat Transfer Resistance	62
4.3.5	Wall and Radial Heat Dispersion Effects	63
4.4	Concluding Remarks	64
<b>CHAPTER 5 CATALYST CHARACTERIZATION</b>		<b>65</b>
5.1	Introduction	65
5.2	Nitrogen Adsorption Studies	65

5.3	Fourier Transform Infrared Spectroscopy (FTIR) Analyses	67
5.4	X-ray Diffraction (XRD) Measurements	68
5.5	H <sub>2</sub> Temperature-programmed Reduction (H <sub>2</sub> -TPR) Analyses	70
5.6	Scanning Electron Microscopy (SEM) Measurements	72
5.7	Raman Spectroscopy Measurements	74
5.8	Concluding Remarks	75
<b>CHAPTER 6 COMBINED STEAM AND CO<sub>2</sub> REFORMING OF METHANE REACTION STUDY</b>		<b>76</b>
6.1	Introduction	76
6.2	Transient Profiles	76
6.3	Effect of Boron Loading with Various Reaction Temperature	78
6.4	Effect of Reactant Partial Pressure	83
6.4.1	Effect of CO <sub>2</sub> Partial Pressure	83
6.4.2	Effect of H <sub>2</sub> O Partial Pressure	85
6.4.3	Effect of CH <sub>4</sub> Partial Pressure	88
6.4.4	Summary	90
6.5	Longevity Test	91
6.6	Post-Reaction Characterization	97
6.6.1	Raman Spectroscopy Measurements	97
6.6.2	X-ray Diffraction (XRD) Measurements	98
6.6.3	Scanning Electron Microscopy (SEM) Measurements	101
6.6.4	Transmission Electron Microscopy (TEM) Measurements	102
6.6.5	Temperature-programmed Oxidation (TPO) Measurements	104
6.7	Concluding Remarks	106

<b>CHAPTER 7 CONCLUSIONS &amp; RECOMMENDATIONS</b>	<b>107</b>
7.1 Conclusions	107
7.2 Recommendations	109
<b>REFERENCES</b>	<b>110</b>
<b>APPENDIX A CATALYST PREPARATION CALCULATIONS</b>	<b>121</b>
<b>APPENDIX B COMBINED STEAM AND CO<sub>2</sub> REFORMING OF METHANE REACTION CALCULATION</b>	<b>126</b>
<b>APPENDIX C CALIBRATION CURVES</b>	<b>128</b>
<b>APPENDIX D TRANSPORT RESISTANCE CALCULATIONS</b>	<b>133</b>
<b>LIST OF PUBLICATIONS</b>	<b>145</b>

The logo for UIMP (Universiti Malaysia Perlis) is a large, downward-pointing arrow shape. It is composed of several overlapping geometric shapes in shades of teal, light blue, and yellow. The letters "UIMP" are written in a bold, white, sans-serif font across the bottom of the arrow.

**UIMP**

## LIST OF TABLES

Table 1.1	Variations of carbon dioxide emissions for about 1,000 years	1
Table 2.1	Worldwide capacity of current, under construction and planned gas-to-liquid (GTL) plants	14
Table 2.2	Surface reaction mechanism (thermodynamic-non-consistent version)	21
Table 2.3	Surface reaction mechanism (continued)	22
Table 2.4	List of main and side reactions possibly occurring during CSCR and probability of occurrence as assessed by	25
Table 2.5	List of supported metal catalysts which have been studied for reforming processes	27
Table 2.6	Bibliographic listing of catalytic performance of Ni-based catalysts with various supports in CSCR reaction	30
Table 2.7	Mechanisms of catalyst deactivation	34
Table 2.8	Catalyst poisons classifies based on chemical structure	36
Table 2.9	Catalyst poisons in various important reactions	37
Table 3.1	List of chemicals used for catalyst synthesis	42
Table 3.2	List of gases used	42
Table 3.3	List of equipment used	43
Table 3.4	Amount of material used for preparation of 5 g of 10%Ni/SBA-15 and 1-5%B-promoted 10%Ni/SBA-15 catalysts	44
Table 3.5	Information of standard gas from GC analysis	53
Table 4.1	Properties for CSCR and correspond calculated values	58
Table 5.1	Textural properties of SBA-15 support, unpromoted and B-promoted 10%Ni/SBA-15 catalysts	66
Table 6.1	Summary of degree of catalyst deactivation for CSCR reaction over various Ni-based catalysts recently reported in literature	96
Table 6.2	The weight loss of the spent promoted and unpromoted Ni-based catalysts	105

## LIST OF FIGURES

Figure 1.1	Energy-related CO <sub>2</sub> emissions from 1990 to 2016.	2
Figure 1.2	Energy consumption varies minimally across all annual energy outlook cases.	3
Figure 2.1	Role of petroleum in our daily lives.	10
Figure 2.2	Global energy system transition from 1850 to 2150.	12
Figure 2.3	The average global hydrogen supply and demand.	13
Figure 2.4	Equilibrium composition for combined steam and CO <sub>2</sub> reforming of methane reaction at different temperatures and atmospheric pressure calculated by HSC Chemistry.	23
Figure 2.5	Conceptual model of poisoning by sulphur atoms of a metal surface during ethylene hydrogenation.	35
Figure 2.6	Conceptual models for crystallite growth due to sintering: (A) atomic migration, and (B) crystallite migration.	38
Figure 2.7	Visual illustration for fouling, crystallite encapsulation and pore plugging of a supported metal catalyst due to carbon deposition.	39
Figure 2.8	Coke formation and transformation from hydrocarbons on metal surfaces.	39
Figure 3.1	Catalyst preparation flowchart.	45
Figure 3.2	The Bragg Law for XRD analysis.	48
Figure 3.3	Schematic diagram for CSCRM reaction.	52
Figure 3.4	CSCRM reaction flow chart.	52
Figure 5.1	FTIR spectra of (a) SBA-15 support, (b) 10%Ni/SBA-15, (c) 1%B-10%Ni/SBA-15, (d) 3%B-10%Ni/SBA-15 and (e) 5%B-10%Ni/SBA-15 catalysts.	68
Figure 5.2	XRD patterns of (a) SBA-15 support, (b) 10%Ni/SBA-15, (c) 1%B-10%Ni/SBA-15, (d) 3%B-10%Ni/SBA-15 and (e) 5%B-10%Ni/SBA-15 catalysts.	69
Figure 5.3	H <sub>2</sub> -TPR profiles of (a) 10%Ni/SBA-15, (b) 1%B-10%Ni/SBA-15, (c) 3%B-10%Ni/SBA-15 and (d) 5%B-10%Ni/SBA-15 catalysts.	71
Figure 5.4	Effect of B loading on reduction temperature during H <sub>2</sub> -TPR for X%B-10%Ni/SBA-15 catalysts.	71
Figure 5.5	SEM images of fresh (a) 10%Ni/SBA-15 and (b) 3%B-10%Ni/SBA-15 catalysts.	73
Figure 5.6	Raman spectra of fresh (a) SBA-15 support, (b) 10%Ni/SBA-15, (c) 1%B-10%Ni/SBA-15, (d) 3%B-10%Ni/SBA-15 and (e) 5%B-10%Ni/SBA-15 catalysts.	74

Figure 6.1	The CH <sub>4</sub> and CO <sub>2</sub> conversions for CSCRM reaction without catalyst at reaction temperature of 1073 K and stoichiometric feed composition ( $F_{CH_4} : F_{H_2O} : F_{CO_2} = 3 : 2 : 1$ ).	77
Figure 6.2	The CH <sub>4</sub> and CO <sub>2</sub> conversions for CSCRM reaction with 10%Ni/SBA-15 catalyst at reaction temperature of 1073 K and stoichiometric feed composition ( $F_{CH_4} : F_{H_2O} : F_{CO_2} = 3 : 2 : 1$ ).	78
Figure 6.3	Effect of reaction temperature and B loading on (a) CO <sub>2</sub> conversion and (b) CH <sub>4</sub> conversion of unpromoted and promoted 10%Ni/SBA-15 catalysts at stoichiometric feed composition ( $F_{CH_4} : F_{H_2O} : F_{CO_2} = 3 : 2 : 1$ ).	80
Figure 6.4	Effect of reaction temperature and B loading on (a) CO yield and (b) H <sub>2</sub> yield of unpromoted and promoted 10%Ni/SBA-15 catalysts at stoichiometric feed composition ( $F_{CH_4} : F_{H_2O} : F_{CO_2} = 3 : 2 : 1$ ).	81
Figure 6.5	Effect of reaction temperature and B loading on H <sub>2</sub> /CO ratio of unpromoted and promoted 10%Ni/SBA-15 catalysts at stoichiometric feed composition ( $F_{CH_4} : F_{H_2O} : F_{CO_2} = 3 : 2 : 1$ ).	82
Figure 6.6	Effect of CO <sub>2</sub> partial pressure on CH <sub>4</sub> and CO <sub>2</sub> conversions over 3%B-10%Ni/SBA-15 catalyst at $P_{CH_4} = 45$ kPa, $P_{H_2O} = 30$ kPa and 1073 K.	84
Figure 6.7	Effect of CO <sub>2</sub> partial pressure on H <sub>2</sub> /CO ratio, H <sub>2</sub> and CO yields over 3%B-10%Ni/SBA-15 catalyst at $P_{CH_4} = 45$ kPa, $P_{H_2O} = 30$ kPa and 1073 K.	85
Figure 6.8	Effect of H <sub>2</sub> O partial pressure on CH <sub>4</sub> and CO <sub>2</sub> conversions over 3%B-10%Ni/SBA-15 catalyst at $P_{CH_4} = 45$ kPa, $P_{CO_2} = 15$ kPa and 1073 K.	87
Figure 6.9	Effect of H <sub>2</sub> O partial pressure on H <sub>2</sub> /CO ratio, H <sub>2</sub> and CO yields over 3%B-10%Ni/SBA-15 catalyst at $P_{CH_4} = 45$ kPa, $P_{CO_2} = 15$ kPa and 1073 K.	88
Figure 6.10	Effect of CH <sub>4</sub> partial pressure on CH <sub>4</sub> and CO <sub>2</sub> conversions over 3%B-10%Ni/SBA-15 catalyst at $P_{H_2O} = 30$ kPa, $P_{CO_2} = 15$ kPa and 1073 K.	89
Figure 6.11	Effect of CH <sub>4</sub> partial pressure on CH <sub>4</sub> and CO <sub>2</sub> conversions over 3%B-10%Ni/SBA-15 catalyst at $P_{H_2O} = 30$ kPa, $P_{CO_2} = 15$ kPa and 1073 K.	90
Figure 6.12	Time-on-stream profile for (a) CO <sub>2</sub> and (b) CH <sub>4</sub> conversions over 3%B-10%Ni/SBA-15 catalyst at $P_{CH_4} = 45$ kPa, $P_{H_2O} = 30$ kPa, $P_{CO_2} = 15$ kPa and temperature of 973 to 1073 K.	92

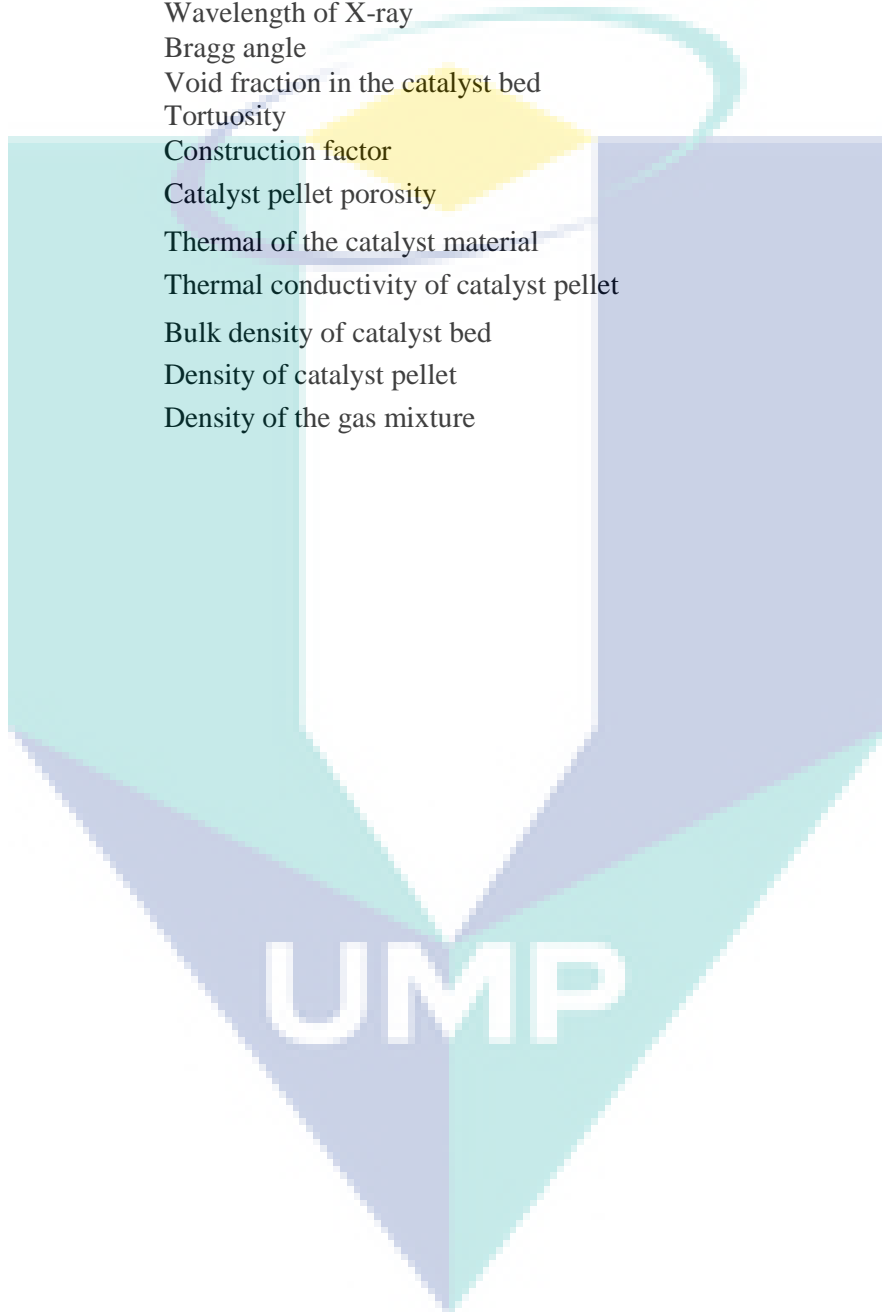
- Figure 6.13 Time-on-stream profile for (a) CO and (b) H<sub>2</sub> yields over 3%B-10%Ni/SBA-15 catalyst at  $P_{CH_4} = 45$  kPa,  $P_{H_2O} = 30$  kPa,  $P_{CO_2} = 15$  kPa and temperature of 973 to 1073 K. 93
- Figure 6.14 Time-on-stream profile for H<sub>2</sub>/CO ratio over 3%B-10%Ni/SBA-15 catalyst at  $P_{CH_4} = 45$  kPa,  $P_{H_2O} = 30$  kPa,  $P_{CO_2} = 15$  kPa and temperature of 973 to 1073 K. 94
- Figure 6.15 Raman spectra of (a) fresh 10%Ni/SBA-15, (b) spent 10%Ni/SBA-15 and (c) spent 3%B-10%Ni/SBA-15 catalysts after CSCRM at stoichiometric feed composition ( $F_{CH_4} : F_{H_2O} : F_{CO_2} = 3 : 2 : 1$ ) and 1073 K. 98
- Figure 6.16 XRD patterns of (a) fresh 10%Ni/SBA-15, (b) fresh 3%B-10%Ni/SBA-15, (c) spent 10%Ni/SBA-15 and (d) spent 3%B-10%Ni/SBA-15 catalysts after CSCRM at stoichiometric feed composition ( $F_{CH_4} : F_{H_2O} : F_{CO_2} = 3 : 2 : 1$ ) and 1073 K. 100
- Figure 6.17 SEM images of (a) fresh 10%Ni/SBA-15, (b) spent 10%Ni/SBA-15 fresh, (c) fresh 3%B-10%Ni/SBA-15 and (d) spent 3%B-10%Ni/SBA-15 catalysts after CSCRM at stoichiometric feed composition ( $F_{CH_4} : F_{H_2O} : F_{CO_2} = 3 : 2 : 1$ ) and 1073 K. 102
- Figure 6.18 TEM images of (a) fresh 10%Ni/SBA-15, (b) spent 10%Ni/SBA-15, (c) fresh 3%B-10%Ni/SBA-15 and (d) spent 3%B-10%Ni/SBA-15 catalysts after CSCRM at stoichiometric feed composition ( $F_{CH_4} : F_{H_2O} : F_{CO_2} = 3 : 2 : 1$ ) and 1073 K. 103
- Figure 6.19 TPO profiles of spent (a) 10%Ni/SBA-15 and (b) 3%B-10%Ni/SBA-15 catalysts after CSCRM at stoichiometric feed composition ( $F_{CH_4} : F_{H_2O} : F_{CO_2} = 3 : 2 : 1$ ) and 1073 K. 105

UMP

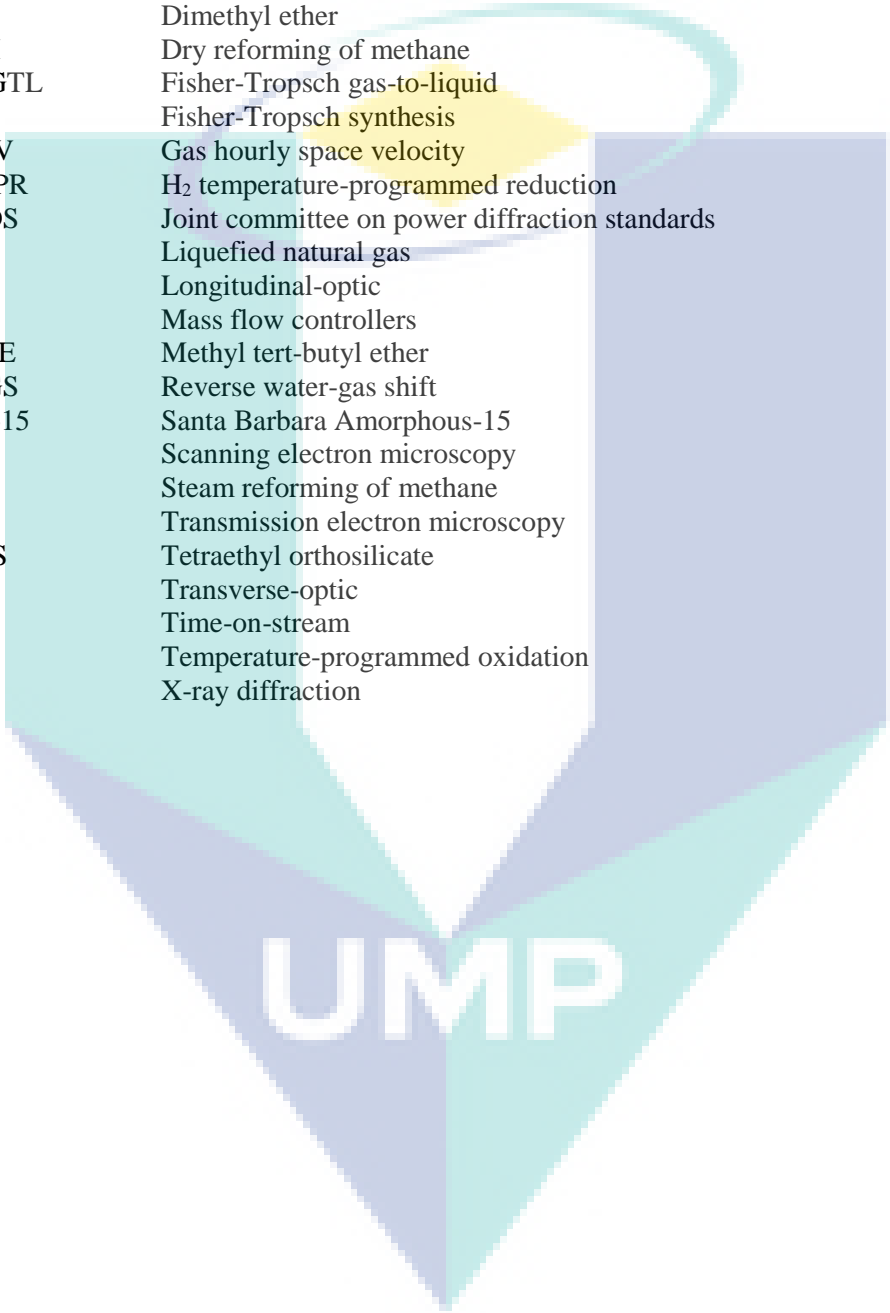
## LIST OF SYMBOLS

$B$	The line broadening at half the maximum intensity (FWHM)
$Bi_w$	Biot number
$b$	Inert solids fraction of the catalyst bed
$C_{Ab}$	Bulk gas-phase concentration
$C_{As}$	Concentration of CH <sub>4</sub> on the catalyst surface
$C_{pg}$	Specific heat capacity of feed gas mixture at constant pressure
$C_\alpha$	Carbon formed via hydrocarbon decomposition
$C_\beta$	Carbon formed via CO dissociation
$C_C$	Graphitic carbon
$C_\gamma$	Carbides
$C_v$	Whisker-like or vermicular carbon
$D_{eff}$	Effective diffusivity
$D_g$	Diffusivity
$D_p$	Average pore diameter
$d(\text{NiO})$	Average crystallite size of NiO phase
$d(\text{Ni}^0)$	Metallic Ni <sup>0</sup> particle size
$d_p$	Diameter of catalyst particle
$d_t$	Reactor tube diameter
$E_A$	Activation energy
$F$	Molar flow rates
$-\Delta H_r$	Heat of reaction
$h$	Heat transfer coefficient between gas mixture and catalyst
$h_w$	Heat transfer coefficient of reactor tube wall
$j_D$	Colburn's mass transfer factor
$j_H$	J-factor for heat transfer
$k_c$	Mass transfer coefficient
$L$	Length
$M$	Active site of the catalyst
$n$	Reaction order
O.D.	Outer diameter
$P$	Gaseous species partial pressure
$Pr$	Prandtl number
$R$	Ideal gas constant
$R_t$	Radius of reactor tube
$R_p$	Catalyst particle radius
$r$	Production of formation rates
$(-r_{exp})$	Rate of reaction
$S_c$	Schmidt number
$S_i$	Selectivity
$T_b$	Reactant gas bulk temperature
$T_s$	Reactant gas bulk temperature
$T_w$	Tube wall temperature
$T_{Hüttig}$	Hüttig temperature

$T_{Tamman}$	Tamman temperature
$T_{Melting}$	Melting temperature
$U$	Superficial gas velocity
$V_p$	Total pore volume
$W_{Cat.}$	Weight of catalyst
$X_i$	Reactant conversion
$Y_i$	Yield of products
$\lambda$	Wavelength of X-ray
$\theta$	Bragg angle
$\varepsilon$	Void fraction in the catalyst bed
$\theta$	Tortuosity
$\sigma_c$	Construction factor
$\omega_p$	Catalyst pellet porosity
$\lambda_m$	Thermal of the catalyst material
$\lambda_p$	Thermal conductivity of catalyst pellet
$\rho_b$	Bulk density of catalyst bed
$\rho_c$	Density of catalyst pellet
$\rho_g$	Density of the gas mixture



## LIST OF ABBREVIATIONS



AS	Asymmetric stretching
FTIR	Fourier-transform infrared
BET	Brunauer-Emmett-Teller
CSCRM	Combined steam and CO <sub>2</sub> reforming of methane
DFT	Density functional theory
DME	Dimethyl ether
DRM	Dry reforming of methane
F-T GTL	Fisher-Tropsch gas-to-liquid
FTS	Fisher-Tropsch synthesis
GHSV	Gas hourly space velocity
H <sub>2</sub> -TPR	H <sub>2</sub> temperature-programmed reduction
JCPDS	Joint committee on power diffraction standards
LNG	Liquefied natural gas
LO	Longitudinal-optic
MFC	Mass flow controllers
MTBE	Methyl tert-butyl ether
RWGS	Reverse water-gas shift
SBA-15	Santa Barbara Amorphous-15
SEM	Scanning electron microscopy
SRM	Steam reforming of methane
TEM	Transmission electron microscopy
TEOS	Tetraethyl orthosilicate
TO	Transverse-optic
TOS	Time-on-stream
TPO	Temperature-programmed oxidation
XRD	X-ray diffraction

## CHAPTER 1

### INTRODUCTION

#### 1.1 Introduction

Approximately 80% of the present global energy requirements is supplied by the hydrocarbon-based fossil fuels leading to a foreseeable and inevitable problem, depletion of limited fossil energy resources (Das, 2001). The utilization of fossil fuels is inevitably contributing to the global climate change due to the emission of CO<sub>2</sub> gases into atmosphere. According to Omae (2006), the amount of carbon dioxide emitted has increased by 90 ppm (480 billion tons) in about 200 years since 1800. Recently, it shows that the CO<sub>2</sub> released keeps increasing about 1.5 ppm per year as shown in Table 1.1 which reveals that the emission of CO<sub>2</sub> into the atmosphere is reaching 8 billion tons per year. In 2016, the U.S. Energy Information Administration (EIA) reported that carbon intensity of energy consumption was declined by 1.7%, particularly the average annual decline of 1.0% was achieved from 2005 to 2015 as shown in Figure 1.1. As a result, energy-related CO<sub>2</sub> emissions were 37 million metric tons lower than where they would have been had the prior trend continued during the middle of 19<sup>th</sup> century. This behavior indicated that emergence of green technologies gradually substitutes the former processes in energy production with less CO<sub>2</sub> emissions over this past 10 years.

Table 1.1 Variations of carbon dioxide emissions for about 1,000 years

Years	Period (year)	Concentration (ppm)	Increase (ppm)	Increase rate (ppm/year)
1000-1800	800	270-280	10	0.01
1800-1950	150	280-310	30	0.20
1958-1975	17	315-330	15	0.90
1975-2002	27	330-370	40	1.50

Source: Omae (2006).

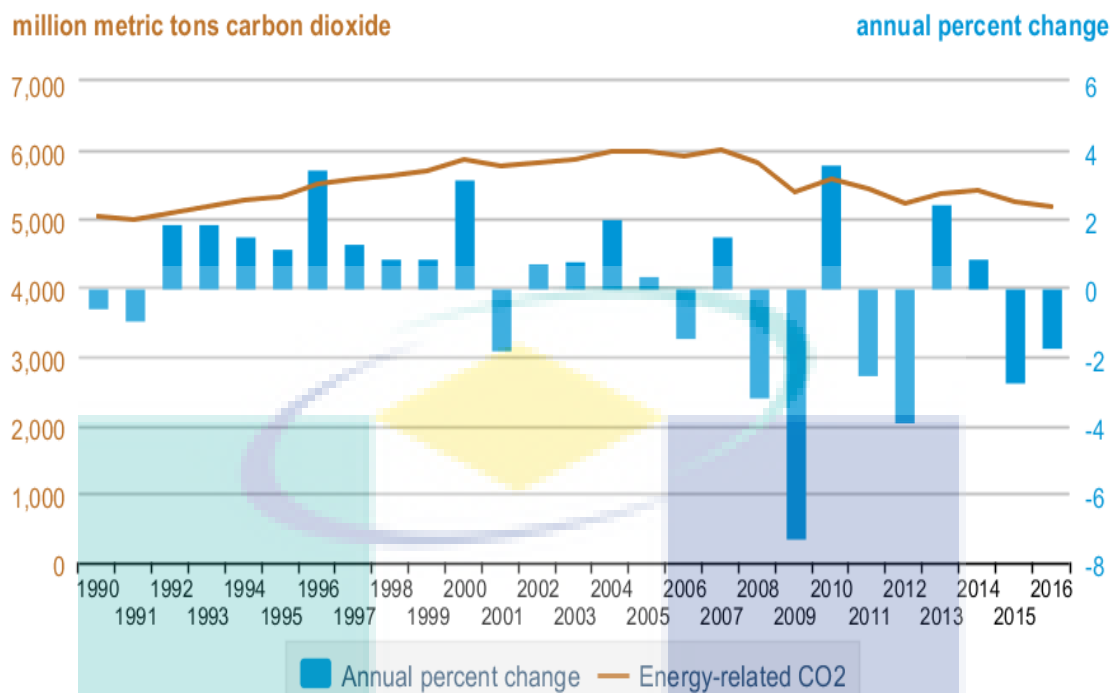


Figure 1.1 Energy-related CO<sub>2</sub> emissions from 1990 to 2016.

Source: Eia (2016).

The projection of global energy consumption up to year 2040 based on all energy outlook cases is shown in Figure 1.2. From 2016 to 2040, the total energy consumption is projected to be increased by 5% due to the economic assumptions, namely high and low economic growth cases which assumes compound annual growth rates for U.S. gross domestic product of 2.6% and 1.6%, respectively. With increasing concerns on the rise of anthropogenic greenhouse gas emission and security energy supply, various types of reforming reactions are proposed as promising methods for syngas production for downstream processes such as synthetic fuels generation from Fischer-Tropsch synthesis (Usman et al., 2015; Abdullah et al., 2017) and other essential chemicals, namely, methanol, dimethyl ether (DME) and methyl tert-butyl ether (MTBE) in petrochemical industries (Wang et al., 2011).

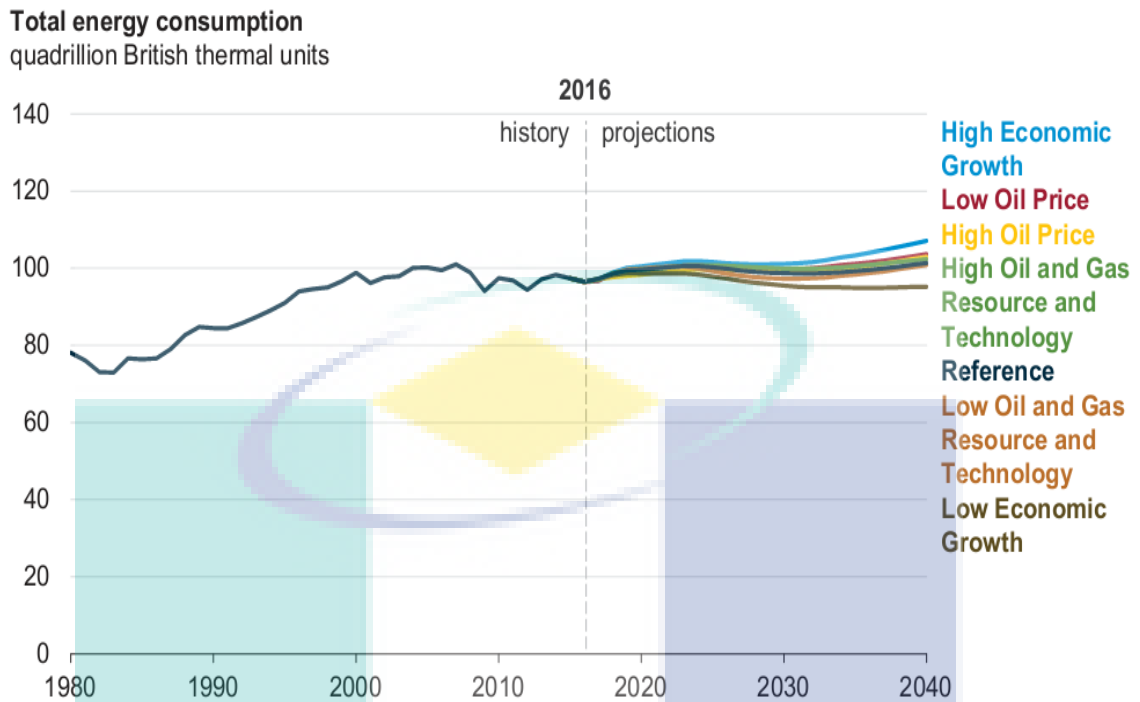


Figure 1.2 Energy consumption varies minimally across all annual energy outlook cases.

Source: Eia (2016).

In practice, the catalytic steam reforming of methane (SRM) reaction is the most prevalent and conventional route to produce syngas. However, the  $H_2/CO$  ratio of higher than 3 and large amount of undesired  $CO_2$  produced are always the main setbacks encountered with this approach (Ross, 2005). In addition, dry reforming of methane (DRM) could convert unwanted  $CO_2$  greenhouse gas into value-added syngas but the resulting  $H_2/CO$  ratio of less than unity is inappropriate for Fisher-Tropsch synthesis (FTS) and methanol production requiring a stoichiometric  $H_2/CO$  ratio of 2 (Inderwildi et al., 2008; Kapokova et al., 2011). Hence, by employing these two approaches, the implementation of auxiliary separation and purification steps for the downstream processes are imposed and thus increases the capital cost (Jabbour et al., 2017). From the above reasons, the combined steam and  $CO_2$  reforming of methane (CSCRM), also known as bi-reforming of methane, has recently appeared as a promising technique since it is capable of generating a green and sustainable energy source from biogas, a non-fossil fuel resource mainly consisting of methane, carbon dioxide and water (Olah et al., 2015). In fact, CSCRM is reportedly a prospective substitution of other common reforming processes owing to its high catalytic stability in

the coexistence of CO<sub>2</sub> and H<sub>2</sub>O oxidizing reactants and flexible adjustment of H<sub>2</sub>/CO ratios by the manipulation of feedstock composition (Roh et al., 2007; Holladay et al., 2009).

In general, from an industrial standpoint, Ni-based catalyst is recognized as one of the most attractive candidates for the large-scale industrial application of reforming processes since it is cost-effective, abundant availability and relatively high catalytic activity comparable to precious metals (Usman et al., 2015; Abdullah et al., 2017; Holladay et al., 2009). However, Ni-based catalysts could encounter challenging barriers of coke formation and Ni metal sintering resulting in rapid catalyst deactivation at high reaction temperature. In the research of CSCRM reaction over Ni-Ce/Al<sub>2</sub>O<sub>3</sub> catalyst, Koo et al. (2012) reported that high CH<sub>4</sub> and CO<sub>2</sub> conversions of about 90.9% and 69.2%, respectively were achieved at 1023 K with feed composition of CH<sub>4</sub>/H<sub>2</sub>O/CO<sub>2</sub>/N<sub>2</sub> = 1.0/0.8/0.4/1.0. However, the formation of graphitic carbon was still evident even with the utilization of redox CeO<sub>2</sub> promoter widely reported as carbon removal agent (Usman et al., 2015; Abdullah et al., 2017). The same behavior was also observed by Park et al. (2015) for spent La-Ni/MgAl<sub>2</sub>O<sub>4</sub> catalyst after CSCRM reaction at 1173 K and 5 atm with CH<sub>4</sub>/H<sub>2</sub>O/CO<sub>2</sub>/N<sub>2</sub> of 1/1.2/0.4/0.3. Thus, exploring a new catalyst system resistant to carbon deposition by the implementation of suitable combination of support and promoter is crucial in CSCRM.

In recent years, mesoporous siliceous Santa Barbara Amorphous-15 (SBA-15) support has drawn significant attention from both academics and industries for a wide range of heterogeneous catalytic reactions, namely, methane steam reforming (Wan et al., 2007; Arcotumapathy et al., 2015), methane dry reforming (Gálvez et al., 2015; Omoregbe et al., 2017) and methane cracking (Gómez et al., 2016) due to its substantially large specific surface area, thick framework walls with ordered mesoporous structure and high thermal stability (Yi et al., 2005). The confinement effect of highly ordered two-dimensional hexagonal SBA-15 support could anchor metal nanoparticles inside the mesoporous silica channels, inhibit metal sintering and hence resistance to carbon deposition (Jabbour et al., 2017; Liu et al., 2009). Apart from utilizing rare-earth metal oxides as redox promoters for elimination of carbonaceous species (Usman et al., 2015; Abdullah et al., 2017), by using first principles density functional theory (DFT) calculations, Saey's group found that boron promoter could

bind to the octahedral sites of the first subsurface layer of Ni (1 1 1) preferred for carbon adsorption and thus suppressing surface carbon diffusion for forming graphene islands (Xu and Saeys, 2006; Xu and Saeys, 2007; Xu et al., 2009). Therefore, the promotional effect of boron may also improve the carbon resistance and the catalytic performance for CSCRM reaction.

## 1.2 Problem Statement

The syngas production from combined steam and CO<sub>2</sub> reforming of methane (CSCRM) reaction recently gained significant interests from both academia and industry since it mitigates CO<sub>2</sub> emission by converting it into value-added syngas and providing flexible H<sub>2</sub>/CO ratios for downstream processes via manipulation of CH<sub>4</sub>/CO<sub>2</sub>/H<sub>2</sub>O feed composition. However, the CSCRM reaction encounters some unavoidable challenges that should be resolved in this research.

Firstly, the design of an appropriate reforming catalyst for CSCRM reaction is always the concern in catalysis field. Ni-based catalyst is considered as outstanding catalyst for reforming processes owing to its cost-effective, abundant availability and relatively high catalytic activity. However, coke formation leads to the rapid catalyst deactivation is inevitable at high reaction temperature (Sehested, 2006). Thus, studying a new carbon-resistant catalyst approach by introducing an effective combination of support and promoter is essential in CSCRM. However, to the best of our knowledge, there are no previous experimental studies about the synergetic effect of boron promoter and SBA-15 support for CSCRM reaction.

Secondly, the catalyst performance is highly reliant on the operating parameters of reaction. Hence, the screening process for reaction conditions is indispensable to attain the best operating conditions for CSCRM reaction. Nevertheless, the bibliographic knowledge about CSCRM reaction is still little-known as reported in literature due to the complexity of this reaction, particularly for boron-promoted Ni-based catalysts. Therefore, this thesis aims to design an excellent carbon-resistant catalyst for syngas production via CSCRM reaction and to study the effect of both reaction temperature and reactant partial pressure on CSCRM reaction in order to obtain the best operating conditions.

### 1.3 Research Objectives

The objectives of this research are:

- i. to synthesize the B-promoted Ni-based catalysts and examine their physicochemical properties by employing various characterization techniques.
- ii. to evaluate the catalytic performance of as-prepared catalysts for the CSCRM reaction at various operating conditions.

### 1.4 Scopes of Study

To meet the aforementioned objectives, the following scopes of research have been identified:

- i. to synthesize SBA-15 support, unpromoted 10%Ni/SBA-15 catalyst and 1%, 3% and 5%B-promoted 10%Ni/SBA-15 catalysts by using a sequential incipient wetness impregnation method.
- ii. to study the physicochemical attributes of the synthesized catalysts such as textural properties (BET surface area, total pore volume and average pore diameter) using Brunauer-Emmett-Teller (BET) method, Fourier-transform infrared (FTIR) spectroscopy analyses for surface chemistry, X-Ray Diffraction (XRD) and Raman spectroscopy measurements for crystallinity, H<sub>2</sub> Temperature-Programmed Reduction (H<sub>2</sub>-TPR) analyses for catalyst reducibility properties, Scanning Electron Microscopy (SEM) and Transmission Electron Microscopy (TEM) measurements for surface morphology. In addition, deposited carbon identification and quantification on spent catalyst surface will be determined using Temperature-Programmed Oxidation (TPO) measurements, XRD, SEM and TEM.
- iii. to investigate the effect of boron promoter loading (1%, 3% and 5%) on catalytic performance of 10%Ni/SBA-15 catalysts for CSCRM reaction at various reaction temperatures (973 K, 1023 K and 1073 K) and stoichiometric feedstock ratio (CH<sub>4</sub>:H<sub>2</sub>O:CO<sub>2</sub> = 3:2:1) for 10 h on-stream.

- iv. to study the influence of CSCRM operating conditions by employing various reactant partial pressures ( $\text{CH}_4$  partial pressure,  $P_{\text{CH}_4} = 35\text{--}50$  kPa;  $\text{H}_2\text{O}$  partial pressure,  $P_{\text{H}_2\text{O}} = 10\text{--}30$  kPa and  $\text{CO}_2$  partial pressure,  $P_{\text{CO}_2} = 10\text{--}25$  kPa) on the best catalyst at reaction temperature of 1073 K.
- v. to study the effect of 24 h on-stream on the catalytic performance and stability for CSCRM over the best catalyst at reaction temperature of 1073 K and stoichiometric feedstock ratio ( $\text{CH}_4\text{:H}_2\text{O}\text{:CO}_2 = 3\text{:}2\text{:}1$ ).

## 1.5 Overview of Thesis

This research study is consisting of 4 main sections including the information of research background, catalyst synthesis, catalyst characterization and catalytic evaluation for CSCRM. This thesis is divided into seven chapters and outlined as follows:

Chapter 1 presents the background information of CSCRM reaction and includes the problem statements, research objectives and scopes of the study. The complete outline of this thesis is also reported in this chapter.

Chapter 2 provides the literature review on the development of future energy system and future potential market of syngas. The overview of conventional reforming technologies for syngas production, relevant reaction mechanism and thermodynamic consideration for CSCRM are also provided in this chapter. The literature also includes review on reforming catalysts in terms of support, metal, promoter and degree of catalyst deactivation. At the end of this chapter, regarding to stability of CSCRM, a discussion about exploring a new catalyst system resistant to carbon deposition by the implementation of suitable combination of support and promoter has been provided.

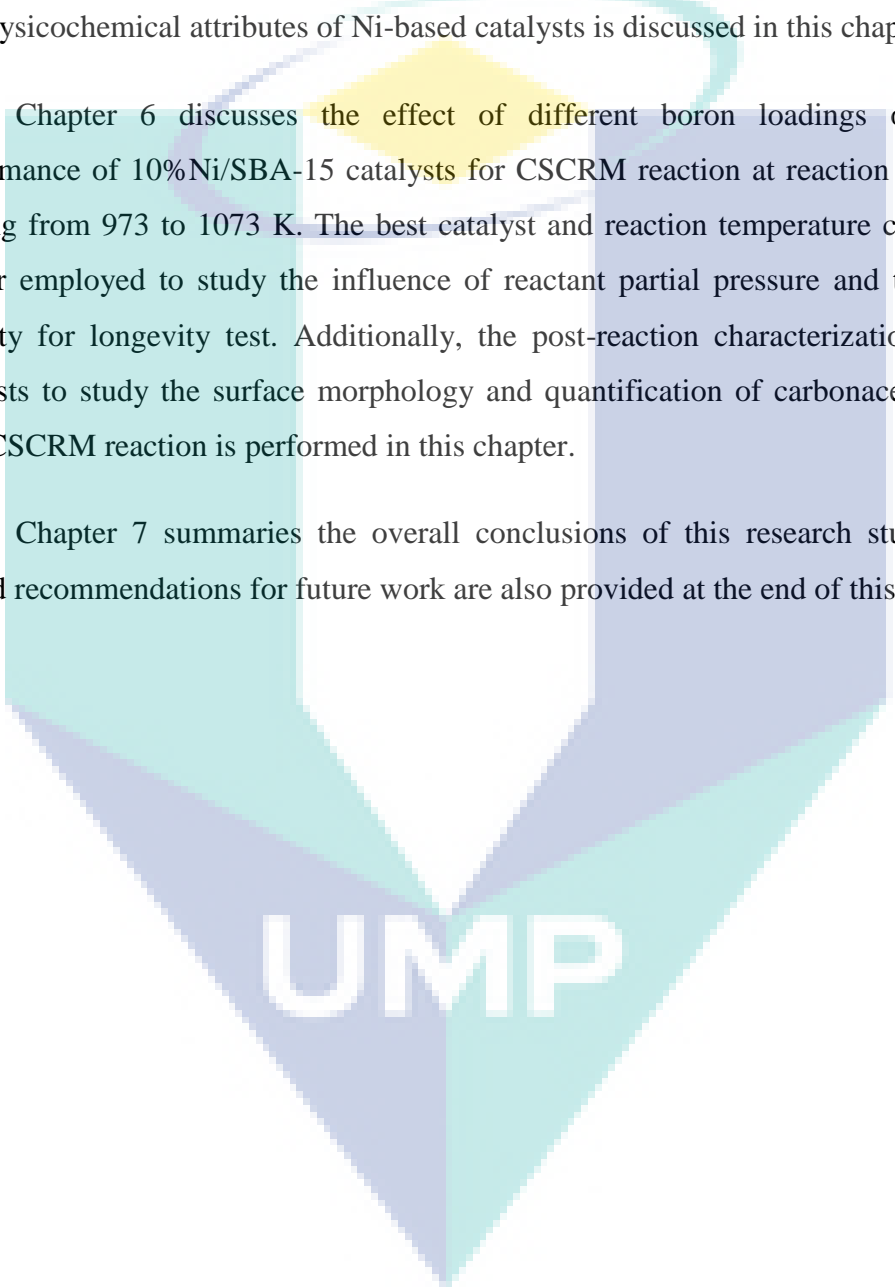
Chapter 3 describes the experimental methodology for synthesizing the SBA-15 support, unpromoted and B-promoted 10%Ni/SBA-15 catalysts. The techniques used for catalyst characterization and experimental set-up for CSCRM reaction at various operating conditions are also presented in this chapter.

Chapter 4 provides the comprehensive explanation of criteria employed for excluding the influence of the heat and mass transport resistances on CSCRM reaction, blank test measurement and reaction metrics during catalytic performance evaluation.

Chapter 5 presents the characterization results of SBA-15 support, unpromoted and B-promoted 10%Ni/SBA-15 catalysts. In addition, the effect of boron loading on the physicochemical attributes of Ni-based catalysts is discussed in this chapter.

Chapter 6 discusses the effect of different boron loadings on catalytic performance of 10%Ni/SBA-15 catalysts for CSCRM reaction at reaction temperature ranging from 973 to 1073 K. The best catalyst and reaction temperature condition are further employed to study the influence of reactant partial pressure and the catalytic stability for longevity test. Additionally, the post-reaction characterization for spent catalysts to study the surface morphology and quantification of carbonaceous species after CSCRM reaction is performed in this chapter.

Chapter 7 summaries the overall conclusions of this research study and the related recommendations for future work are also provided at the end of this chapter.



UMP

## CHAPTER 2

### LITERATURE REVIEW

#### 2.1 Introduction

This chapter provides the highlight of future energy market involving energy transition estimation, availability of gas-to liquid plants and CSCRM development including type of reforming technology, review on the existing catalyst literature and catalyst deactivation during reforming process.

##### 2.1.1 Gas Economy

The existing global energy requirements supplied by the hydrocarbon-based fossil fuels have led to a foreseeable and inevitable problems, depletion of limited fossil energy resources and irreversible environmental impact (Das, 2001). The increasing concerns on security of energy supply, global climate change and urban air pollution have driven the notion of a ‘gas economy’ moves beyond the understanding and realm of scientists and engineers as well as the lexicon of political and business leaders. Theoretically, the main concept and role of ‘gas economy’ are providing alternative options in order to create a truly new market in the future instead of only monetize gas for existing markets.

The hydrogen appears as a potential candidate to the future gas economy and to be the replacement of 20<sup>th</sup> century ‘hydrocarbon society’ since it can be easily found in many substances in nature such as fresh water, biomass and fossil fuels (Marbán and Valdés-Solís, 2007; Bakenne et al., 2016). In fact, the energy consumption in 20<sup>th</sup> century was 10 times higher than that of 1990 primarily due to the advanced utilization of fossil fuels in our daily lives as shown in Figure 2.1. The United Nations forecasts that the global population will be 9 to 10 billion in 2050 whilst the global annual energy

consumption will be reached at least 1000 EJ (EJ = exajoule =  $10^{18}$ ) fairly due to the developing countries with growth in economies and populations such as China and India (Bakenne et al., 2016). As a projection, global energy consumption over the next 20 years would be elevated up to 60% whilst the utilisation of coal and oil is estimated to increase by approximately 30% and 40%, respectively.

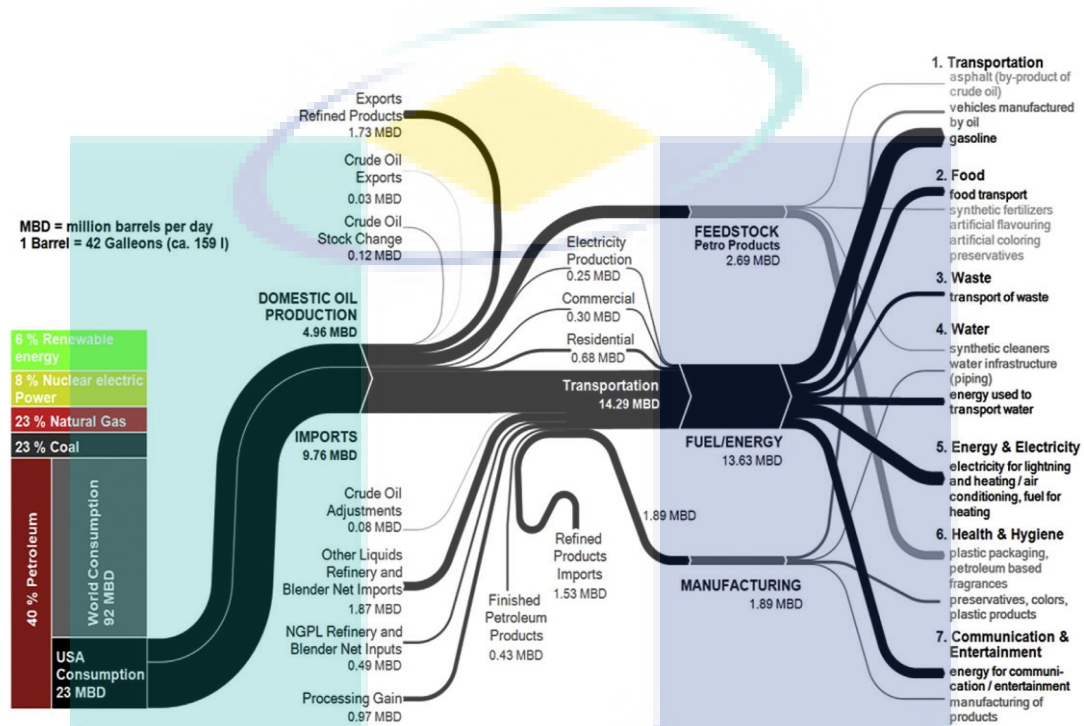


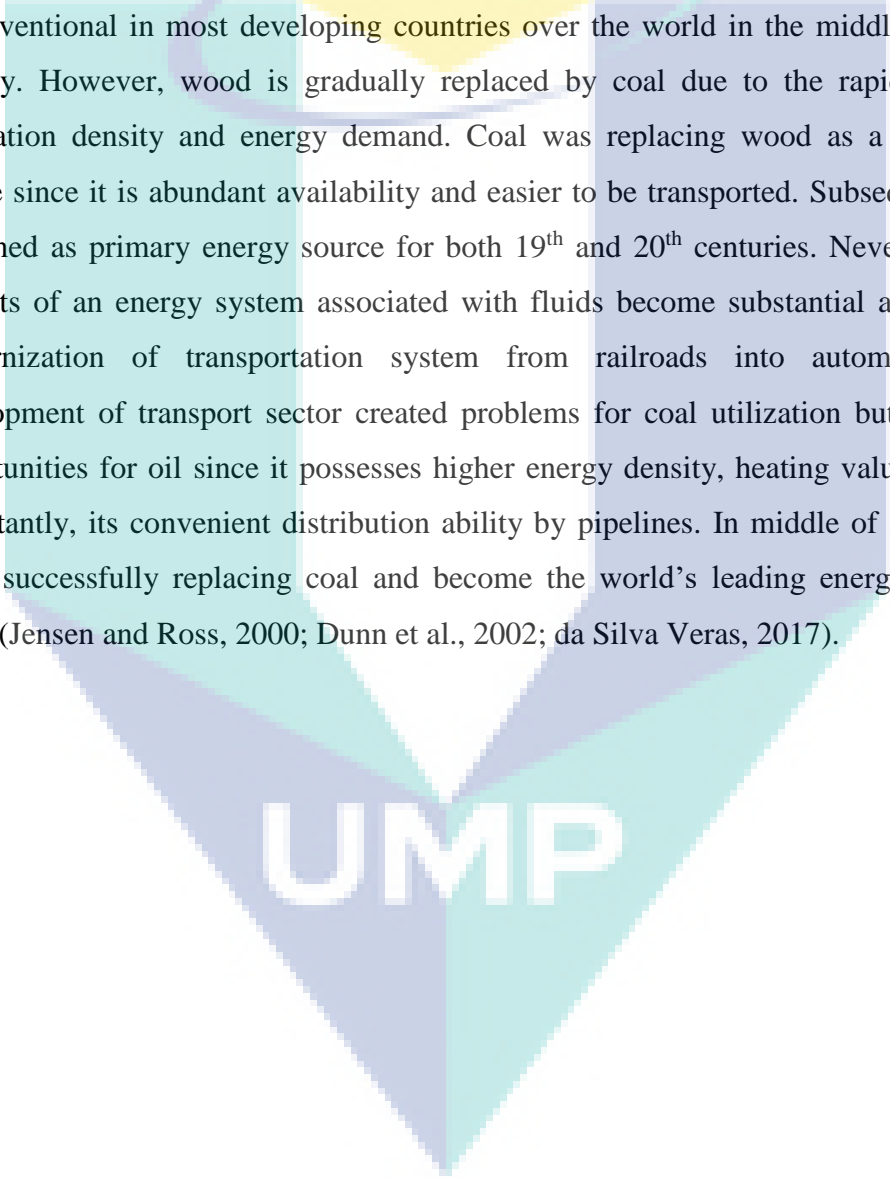
Figure 2.1 Role of petroleum in our daily lives.

Source: Bakenne et al. (2016).

Undeniably, the direction of energy growth in future is pointing to the development of transportation, in which motorization continues to rise and petroleum is still as primary fuel accounting for 95% from the total. In fact, development of alternatives for oil replacment would lighten the reliance on oil imports and thus, lowering the risk of military, political conflicts and economic disruption. In industrial nations, the share import of oil demand over the world increased from 56% to 72% in 2010. Meanwhile, coal was maintained as second largest demand in world's energy consumption holding more than half the world's power supply (Bakenne et al., 2016). The successive use in oil and coal exacerbates the level of urban air problem, particularly the industrialized cities surpassing air pollution health standards such as Beijing and Mexico City (Marbán and Valdés-Solís, 2007). Additionally, the annual

global carbon dioxide emissions from transportation and electricity associated with petroleum and coal are projected to be increased from 6.1 to 9.8 billion tons by 2020.

The reality of an eventual transition to hydrogen becomes more apparent and reliable when review the growth and evolution of energy history. The primary energy system in this world has been shifting from one form energy to another gradually since 19<sup>th</sup> century, in which transits from solids to liquids and eventually is projected to gases as shown in Figure 2.2 (da Silva Veras, 2017). Reliance on wood for energy production is conventional in most developing countries over the world in the middle of the 19<sup>th</sup> century. However, wood is gradually replaced by coal due to the rapid growth of population density and energy demand. Coal was replacing wood as a new energy source since it is abundant availability and easier to be transported. Subsequently, coal remained as primary energy source for both 19<sup>th</sup> and 20<sup>th</sup> centuries. Nevertheless, the benefits of an energy system associated with fluids become substantial and drive the modernization of transportation system from railroads into automobiles. The development of transport sector created problems for coal utilization but it provided opportunities for oil since it possesses higher energy density, heating values and most importantly, its convenient distribution ability by pipelines. In middle of 20<sup>th</sup> century, oil is successfully replacing coal and become the world's leading energy source till today (Jensen and Ross, 2000; Dunn et al., 2002; da Silva Veras, 2017).

The logo for UIMP (Universidade Metropolitana de Santos) is a large, stylized letter 'V' shape. The top part of the 'V' is a yellow circle. The two sides of the 'V' are composed of overlapping translucent shapes in shades of teal and light blue. The letters 'UIMP' are written in a bold, white, sans-serif font across the center of the 'V'.

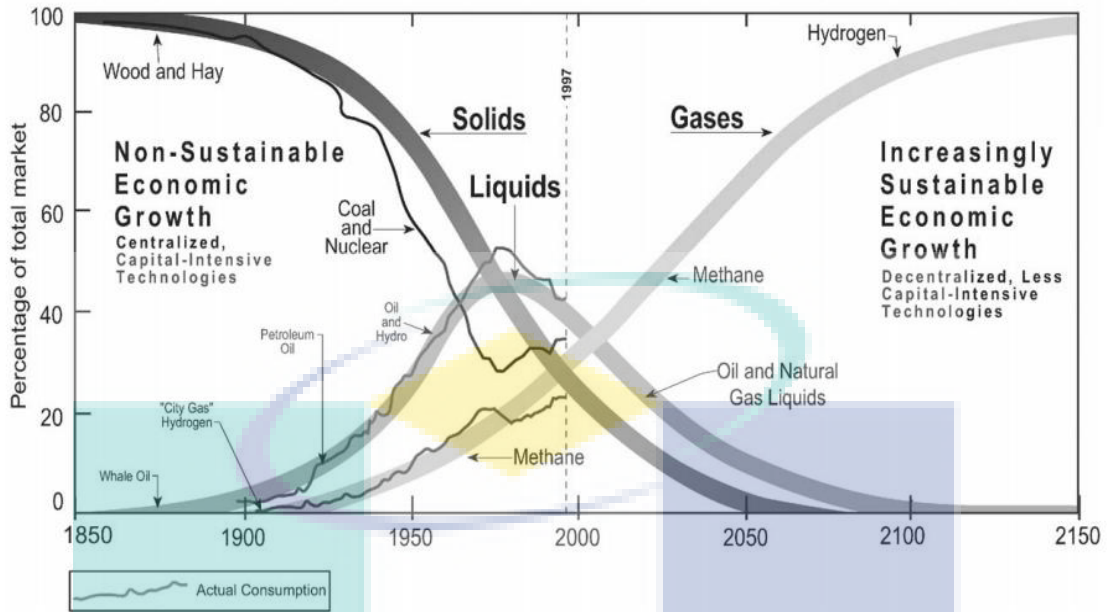


Figure 2.2 Global energy system transition from 1850 to 2150.

Source: da Silva Veras (2017).

The transition from petroleum to hydrogen is stagger and unavoidable as the world's major energy currency in future. In the paper of insights into hydrogen economy, Bakenne et al. (2016) reported that approximate 50 million metric tons of hydrogen is produced yearly for the uses of petroleum refining, fertilizer and methanol productions as well as food hydrogenation purposes (see Figure 2.3). In fact, 95% of the hydrogen production is employed to the applications associated with the petrochemical industries while only 5 to 10% of hydrogen produced is distributed to consumers. In addition, the consumption of hydrogen is estimated to be increased by 5 to 7% annually in 2018. In light of the above considerations, the emergence of hydrogen as a major energy carrier could initially constitutes a versatile building block on the existing natural gas network for its distribution. Eventually, hydrogen will likely has its own full-fledged network from various forms of renewable energy sources and producing a less carbon-intensive energy network in the distant future.

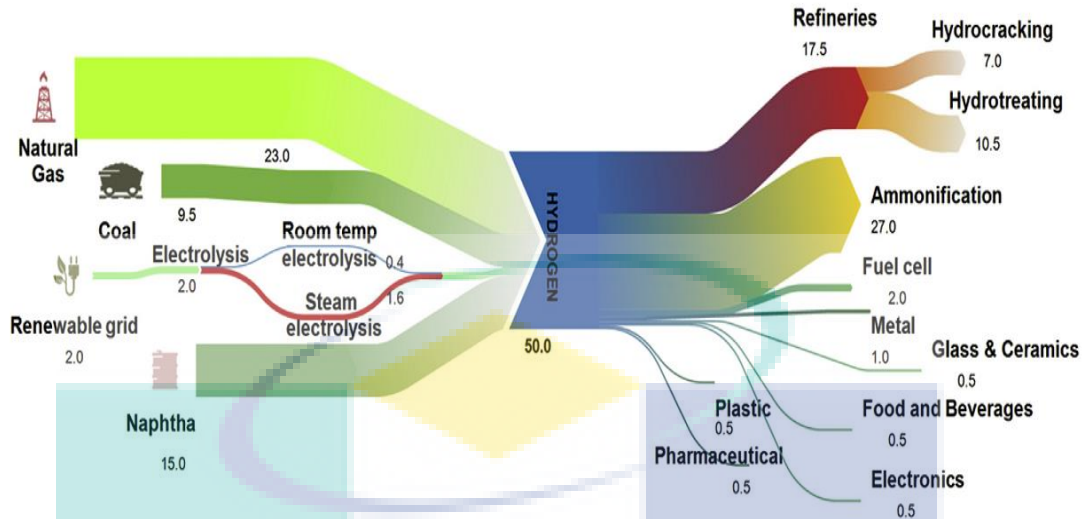


Figure 2.3 The average global hydrogen supply and demand.  
Source: Bakenne et al. (2016).

## 2.2 Global Gas-To-Liquid (GTL) Plants

The mixture of hydrogen and carbon monoxide, namely syngas is conventionally employed as a key feedstock for wide range of chemicals such as ammonia and dimethyl ether production, as well as for synthetic liquid fuels via Fischer-Tropsch gas-to-liquid (F-T GTL) synthesis. In fact, the increasing depletion of limited hydrocarbon-based energy has driven the development of renewable energy sources such as solar and wind power. However, in the medium term future for transition of energy system, the presence of liquid fuels are still essential, particularly for transportation purposes. Table 2.1 summarizes the growing GTL plants with the implementation of syngas production technologies.

Table 2.1 Worldwide capacity of current, under construction and planned gas-to-liquid (GTL) plants

Country	Company	Capacity (BPD)
<b>Current</b>		
Qatar	Qatar Petroleum/Sasol	34,000
South Africa	Sasol	15,600
	PetroSA	47,000
Malaysia	Shell	12,500
<b>Under Construction</b>		
Qatar	Qatar Petroleum/Shell	140,000
Nigeria	SasolChevron	34,000
<b>Probable</b>		
Qatar	Qatar Petroleum/SasolChevron	130,000
	Qatar Petroleum/ExxonMobil	154,000
	Qatar Petroleum/ConocoPhillips	80,000
	Syntroleum & Marathon	120,000
Iran	NPC/Sasol	116,000
	Statoil/PetroSA	60,000
Australia	SasolChevron	132,000
Egypt	Syntroleum	34,000
	Shell	75,000
Colombia	BP	84,000
Bolivia	Rentech/Bolivia GTL	10,000
Indonesia	Rentech/Pertamina	16,000
Russia	Syntroleum/Gazprom	13,000

Source: Eia (2016).

### 2.3 Methods to Syngas Production

Syngas is generally employed for production of various chemicals such as methanol, ammonia, oxo chemicals, and individual derivatives such as formaldehyde, urea, butanol, dimethyl ether (DME), and others (Wang et al., 2011; Abdullah et al., 2017). Simultaneously, synthetic hydrocarbon fuels such as diesel and gasoline are originated from syngas conversion through Fisher Tropsch synthesis (Usman et al., 2015). Hence, the requirement and changes in the domestic energy markets or global economic conditions are attributed as the driving force towards the development and improvement of technology for energy system such as catalytic reforming reaction.

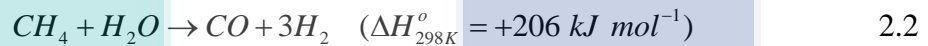
The conventional method for the production of syngas could be classified into two, steam reforming of methane (SRM) and the dry reforming of methane (DRM). However, this SRM yields undesirable  $H_2/CO$  ratio higher than 3 and substantially releases a large amount of unfavorable  $CO_2$  gaseous by-product (Usman et al., 2015; Abdullah et al., 2017). Although dry reforming of methane (DRM) could convert unwanted  $CO_2$  greenhouse gas to a value-added syngas, the resulting  $H_2/CO$  ratio of

less than unity makes this process inappropriate for FTS and methanol production requiring a stoichiometric H<sub>2</sub>/CO ratio of 2 (Olah et al., 2013; Kumar et al., 2015). Thus, the implementation of this approach could impose auxiliary separation and purification steps in the downstream process for adjusting H<sub>2</sub>/CO ratio to around 2 (Jabbour et al., 2017) and hence increasing capital cost. The reactions involved in combined steam and CO<sub>2</sub> reforming of methane (CSCRM) can be considered as a combination of the following net reactions:

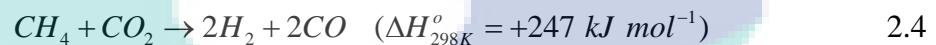
*Combined steam and CO<sub>2</sub> reforming of methane (CSCRM)*



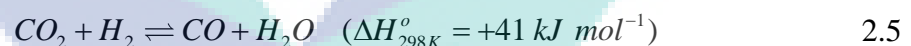
*Steam reforming of methane (SRM)*



*Dry reforming of methane (DRM)*



*Reverse water-gas shift (RWGS)*



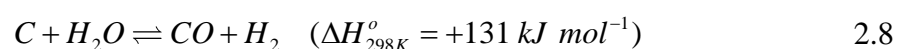
*Methane decomposition*



*Reverse Boudouard reaction*



*Steam gasification of carbon*



### 2.3.1 Catalytic Steam Reforming of Methane (SRM)

There are several reactions could be employed to produce syngas from methane. However, the only large-scale process exists for syngas production is the endothermic reaction, well known as steam reforming of methane (SRM) reaction. The scheme of the reaction of SRM is shown in Eqs. 2.2 and 2.3. The first description of a process relevant to the hydrocarbon conversion with steam was published in 1868 by Rostrup-Nielsen (2002) who used CaO as a medium resulting in the formation of H<sub>2</sub> and CaCO<sub>3</sub>. Subsequently, this process was further improved using Nickel-based catalyst and employed in combination with Fischer-Tropsch synthesis by Germany in World War II and South Africa during the Apartheid era for the synthesis of chemicals such as fuels and alcohols.

The SRM is well known as one of the conventional ways to produce syngas. However, it is necessary to supply a huge amount of heat to the reaction throughout the whole process. In a steam reforming plant, the energy required is supplied by combustion of a part of the fuel in a direct-fired or indirectly fired furnace. In fact, the high temperature and long residence time required for the SRM process to achieve a high conversion of the methane resulting in energy loss and a huge size for the methane reforming reactor (Usman et al., 2015) and hence, an advanced steam reforming technology has been explored and developed.

The advanced steam reforming technology has undeniably improved the overall efficiency of reactor and process flexibility (Ruckenstein et al., 1998; Usman et al., 201). However, the application of SRM presents several disadvantages such as the H<sub>2</sub>/CO ratio of 3 or above is inappropriate for downstream Fischer-Tropsch synthesis or methanol production and the occurrence of the water-gas shift reaction generating significant amount of CO<sub>2</sub> in the reformed product (Abdullah et al., 2017). Moreover, catalyst deactivation due to carbon deposition on catalyst surface at such a high reaction temperature is an unavoidable drawback although reaction temperature required for total conversion of the methane could be descended to below 1273 K with the presence of catalyst within considerable short residence time (Wang et al., 2011).

### 2.3.2 Catalytic Dry Reforming of Methane (DRM)

The Eq. 2.4 represents the syngas production from  $\text{CH}_4$  and  $\text{CO}_2$  gases. Particularly, the product equilibrium of DRM is influenced by the reverse water-gas shift (RWGS) reaction as shown in Eq. 2.5. Theoretically, as seen from the stoichiometric reaction equation, the presence of RWGS reaction is the factor for explaining the  $\text{H}_2/\text{CO}$  ratio always less than unity in DRM. Additionally, the catalyst deactivation is mainly ascribed to the deposited carbon originating from the  $\text{CH}_4$  decomposition and Boudouard reaction as shown in Eqs. 2.6 and 2.7, respectively (Bradford and Vannice, 1999). In fact, there is no drastic effect on the reaction mechanism by replacing steam with  $\text{CO}_2$  gas, as reported by Choudhary and Rajput (1996).

The interest in syngas production has mainly focus on the SRM after the first study by Fischer and Tropsch in 1928 (Foo et al., 2010). In the past decade, increasing concerns over global warming and anthropogenic greenhouse gas concentration has revived the interest in DRM. The  $\text{H}_2/\text{CO}$  ratio less than unity is considered as a preferable feedstock of Fischer-Tropsch synthesis for long chain hydrocarbon production in petrochemical industries without additional auxiliary separation process. However, the main difficulties encountered in DRM is the significant production of by-products, typically carbon which is severe than that of SRM. Carbon deposition is a phenomenon where carbon subsequently deposited on the surface of the catalyst impairing its activity in the reaction and eventually leads to catalyst deactivation. As a result, the carbon formation influences the lifespan of catalyst, especially to reforming process at high temperature while the presence of  $\text{CO}_2$  as a reagent accounts for the large formation of carbon. In addition, DRM is the unique reforming process that affected by two reagents that contain carbon from  $\text{CH}_4$  and  $\text{CO}_2$  and thus, the carbon deposition is severe than other reforming processes with this approach (Cheng et al., 2001).

The development of active catalytic materials is always appears to be main challenge for the industrial application of DRM in order to prolong the lifespan of catalyst via suppression of carbon formation. According to Foo et al. (2010), carbon formation could be controlled by using a support that favors the dissociation of  $\text{CO}_2$  into CO whilst the latter species is responsible for the cleaning purpose of the metallic

surface on support. Apart from that, combined reforming reactions (i.e. simultaneous CO<sub>2</sub> reforming coupled with steam reforming (Koo et al., 2012; Park et al., 2015) or oxidation (York et al., 2003)) have been studied to overcome the challenge. The combined reforming reactions offer a several advantages such as a desired product H<sub>2</sub>/CO ratios could be easily obtained by the adjustment of feedstock composition and the addition of H<sub>2</sub>O or CO<sub>2</sub> enhances the gasification of carbon on catalyst surface (Jabbour et al., 2017).

### **2.3.3 Catalytic Combined Steam and CO<sub>2</sub> Reforming of Methane (CSCRM)**

The DRM reaction is able to generate syngas with a stoichiometric ratio of H<sub>2</sub>/CO of unity and appears to be an effective way to utilize CO<sub>2</sub> directly but analogous to steam reforming, it is not well established for industrial applications due to the severe catalyst deactivation caused by carbon deposition. Thus, SRM is becoming the dominant process to produce syngas for industrial applications but its stoichiometric molar ratio of H<sub>2</sub>/CO around 3 is inappropriate for Fischer-Tropsch synthesis (Bae et al., 2011). Interestingly, by coupling the both steam and CO<sub>2</sub> reforming reactions, these problems can be solved.

The combined steam and CO<sub>2</sub> reforming of methane (CSCRM) (cf. Eq. 2.1) is beneficial to the gas to liquid (GTL) process. A desirable H<sub>2</sub>/CO ratio can be obtained easily and the severe carbon deposition can be reduced reasonably due to the oxidation of the deposited carbon (cf. Eq. 2.8) through the adjustment of the CH<sub>4</sub>/H<sub>2</sub>O/CO<sub>2</sub> ratio in the feed stream (Choudhary and Rajput, 2006; Soria et al., 2011). From an environmental perspective, the CSCRM converts harmful greenhouse gases (i.e. carbon dioxide and methane) into useful intermediate chemical products. Moreover, CSCRM reaction presents as a green and sustainable energy source whereby it attains its feedstock from biogas, a non-fossil fuel resource mainly consisting of methane, carbon dioxide and water (Olah et al., 2015). Therefore, from an economical and industrial standpoint, CSCRM reaction offers an alternative way to generate syngas from renewable energy sources without the implementation of auxiliary purification and separation process.

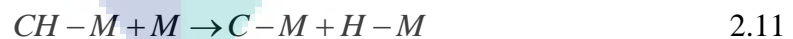
In the research of CSCRM reaction over Ni-Ce/Al<sub>2</sub>O<sub>3</sub> catalyst, Koo et al. (2012) reported that high CH<sub>4</sub> and CO<sub>2</sub> conversions of about 90.9% and 69.2%, respectively

were achieved at 1023 K with feed composition of  $\text{CH}_4/\text{H}_2\text{O}/\text{CO}_2/\text{N}_2 = 1.0/0.8/0.4/1.0$ . However, the formation of graphitic carbon was still evident even with the utilization of redox  $\text{CeO}_2$  promoter widely reported as carbon removal agent (Usman et al., 2015; Abdullah et al., 2017). The same behavior was also observed by Park et al. (2015) for spent  $\text{La-Ni/MgAl}_2\text{O}_4$  catalyst after CSCRM reaction at 1173 K and 5 atm with  $\text{CH}_4/\text{H}_2\text{O}/\text{CO}_2/\text{N}_2$  of 1/1.2/0.4/0.3. However, carbon deposition on the catalyst was an unavoidable issue although the rate of carbon deposition was mainly inhibited. In fact, the knowledge regarding CSCRM reaction is still little-known due to the complexity of this reaction involving steam and high temperature compared to SRM or DRM reaction alone. Thus, exploring a new catalyst system resistant to carbon deposition by the implementation of suitable combination of support and promoter is crucial in CSCRM.

## 2.4 Reaction Mechanisms

The reaction mechanism of the CSCRM is similar to that of SRM and CRM since it is a combination of these both reforming reactions. Kumar et al. (2015) suggested that the both SRM and DRM reactions are starting at the same time by dissociative  $\text{CH}_4$  adsorption on an active site to generate  $\text{CH}_2$  and  $\text{H}_2$  species. In addition, these two reactions share the same intermediate adsorbed O species produced from  $\text{H}_2\text{O}$  from  $\text{CO}_2$  dissociation and subsequently form the CO. The reaction mechanisms are predicted as Eqs. 2.9 to 2.16 with  $M$  being the active site of the catalyst).

*Activation of  $\text{CH}_4$*



*Decomposition of  $\text{H}_2\text{O}$  and  $\text{CO}_2$*



### Reaction of adsorbed species



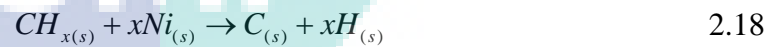
### Production of H<sub>2</sub> and CO



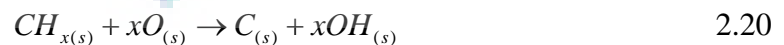
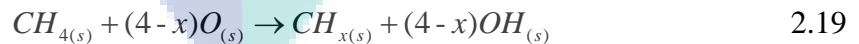
The aforementioned reaction mechanism explains the rapid rate of steam reforming compare to that of CO<sub>2</sub> reforming reasonably due to the involvement of excess H<sub>2</sub>O feeding besides the reverse water-gas shift (RWGS) reaction. In the study of the supported Ni catalysts in reforming process, Maier et al. (2011) proposed a model for detailed surface reaction mechanism associated with active sites of Ni as shown from Eqs. 2.17 to 2.23. The reaction mechanism consists of 42 reactions involving 14 surface species and 7 gas phase species. The reaction steps with their associated rate expressions are summarized in Table 2.2 and Table 2.3. The overall reforming process on Ni catalyst is described as follows.

### Adsorption-desorption of reactants and products (R1-R12).

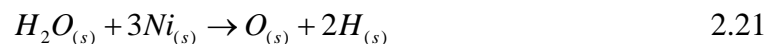
### Activation of CH<sub>4</sub> without oxygen (R13-R20).

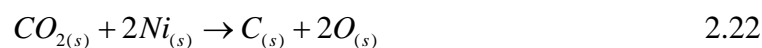


### Activation of CH<sub>4</sub> with absorbed oxygen (R21-R28).



### Decomposition of H<sub>2</sub>O (R29-R34) and CO<sub>2</sub> (R35-R38).





Reaction of adsorbed species and H<sub>2</sub> and CO production.

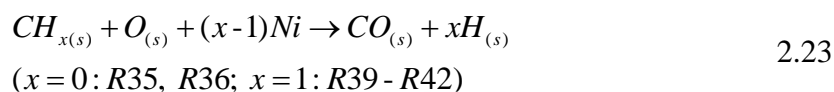


Table 2.2 Surface reaction mechanism (thermodynamic-non-consistent version)

Reaction	A <sup>a</sup> (cm mol <sup>-1</sup> s <sup>-1</sup> )	E <sub>a</sub> (kJ mol <sup>-1</sup> )
R1 $H_2 + 2Ni_{(s)} \rightarrow 2H_{(s)}$	$1.0 \times 10^{-2}$	0.0
R2 $O_2 + 2Ni_{(s)} \rightarrow 2O_{(s)}$	$1.0 \times 10^{-2d}$	0.0
R3 $CH_4 + Ni_{(s)} \rightarrow CH_{4(s)}$	$8.0 \times 10^{-3}$	0.0
R4 $H_2O + Ni_{(s)} \rightarrow H_2O_{(s)}$	$1.0 \times 10^{-1d}$	0.0
R5 $CO_2 + Ni_{(s)} \rightarrow CO_{2(s)}$	$1.0 \times 10^{-5}$	0.0
R6 $CO + Ni_{(s)} \rightarrow CO_{(s)}$	$5.0 \times 10^{-1b}$	0.0
R7 $2H_{(s)} \rightarrow 2Ni_{(s)} + H_2$	$3.0 \times 10^{21}$	98.0
R8 $2O_{(s)} \rightarrow 2Ni_{(s)} + O_2$	$1.3 \times 10^{22}$	464.0
R9 $H_2O_{(s)} \rightarrow H_2O + Ni_{(s)}$	$6.0 \times 10^{13}$	68.9
R10 $CO_{(s)} \rightarrow CO + Ni_{(s)}$	$1.0 \times 10^{13}$	$122.4 - 50\theta_{CO(s)}^c$
R11 $CO_{2(s)} \rightarrow CO_2 + Ni_{(s)}$	$1.0 \times 10^8$	27.3
R12 $CH_{4(s)} \rightarrow CH_4 + Ni_{(s)}$	$2.0 \times 10^{14}$	25.1
R13 $CH_{4(s)} + Ni_{(s)} \rightarrow CH_{3(s)} + H_{(s)}$	$3.7 \times 10^{21}$	57.7
R14 $CH_{3(s)} + H_{(s)} \rightarrow CH_{4(s)} + Ni_{(s)}$	$3.7 \times 10^{21}$	56.1
R15 $CH_{3(s)} + Ni_{(s)} \rightarrow CH_{2(s)} + H_{(s)}$	$3.7 \times 10^{24}$	100.0
R16 $CH_{2(s)} + H_{(s)} \rightarrow CH_{3(s)} + Ni_{(s)}$	$3.7 \times 10^{21}$	49.8
R17 $CH_{2(s)} + Ni_{(s)} \rightarrow CH_{(s)} + H_{(s)}$	$3.7 \times 10^{24}$	97.1
R18 $CH_{(s)} + H_{(s)} \rightarrow CH_{2(s)} + Ni_{(s)}$	$3.7 \times 10^{24}$	73.6
R19 $CH_{(s)} + Ni_{(s)} \rightarrow C_{(s)} + H_{(s)}$	$3.7 \times 10^{21}$	18.8
R20 $C_{(s)} + H_{(s)} \rightarrow CH_{(s)} + Ni_{(s)}$	$3.7 \times 10^{21}$	173.6

<sup>a</sup>The nominal value of the preexponential factor of an elementary reaction was assumed to be:  $10^{13} N_A/\Gamma$  (cm<sup>2</sup>/mol. s), where  $N_A$  is Avogadro's number;  $10^{13}$  (s<sup>-1</sup>) is the order of magnitude of  $\frac{k_B T}{h}$  ( $k_B$  = Boltzmann's constant,  $h$  = Planck's constant) and would be the value expected from

transition state theory;  $\Gamma = 1.5 \times 10^{15}$  (site/cm<sup>2</sup>) is the site density, that was calculated by assuming a site area of  $6.5 \times 10^{-2}$  nm<sup>2</sup> as observed for nickel.

<sup>b</sup>Literature value without temperature dependence of initial sticking coefficient.

<sup>c</sup>Coverage dependence applies due to thermodynamic constraints.

<sup>d</sup>Value for Rh(111).

<sup>e</sup>Estimated in this work based on the comparison of simulation and experiment.

Source: Maier et al. (2011).

Table 2.3 Surface reaction mechanism (continued)

Reaction	A <sup>a</sup> (cm mol <sup>-1</sup> s <sup>-1</sup> )	E <sub>a</sub> (kJ mol <sup>-1</sup> )
R21 $CH_{4(s)} + O_{(s)} \rightarrow CH_{3(s)} + OH_{(s)}$	$1.7 \times 10^{24}$	88.3
R22 $CH_{3(s)} + OH_{(s)} \rightarrow CH_{4(s)} + O_{(s)}$	$3.7 \times 10^{21}$	23.4
R23 $CH_{3(s)} + O_{(s)} \rightarrow CH_{2(s)} + OH_{(s)}$	$3.7 \times 10^{24}$	130.1
R24 $CH_{2(s)} + OH_{(s)} \rightarrow CH_{3(s)} + O_{(s)}$	$3.7 \times 10^{21}$	16.7
R25 $CH_{2(s)} + O_{(s)} \rightarrow CH_{(s)} + OH_{(s)}$	$3.7 \times 10^{24}$	126.8
R26 $CH_{(s)} + OH_{(s)} \rightarrow CH_{2(s)} + O_{(s)}$	$3.7 \times 10^{21}$	40.2
R27 $CH_{(s)} + O_{(s)} \rightarrow C_{(s)} + OH_{(s)}$	$3.7 \times 10^{21}$	48.1
R28 $C_{(s)} + OH_{(s)} \rightarrow CH_{(s)} + O_{(s)}$	$3.7 \times 10^{21}$	139.7
R29 $H_{(s)} + O_{(s)} \rightarrow OH_{(s)} + Ni_{(s)}$	$5.0 \times 10^{22}$	97.9
R30 $OH_{(s)} + Ni_{(s)} \rightarrow H_{(s)} + O_{(s)}$	$3.0 \times 10^{20}$	34.3
R31 $H_{(s)} + OH_{(s)} \rightarrow H_2O_{(s)} + Ni_{(s)}$	$3.0 \times 10^{20}$	42.7
R32 $H_2O_{(s)} + Ni_{(s)} \rightarrow H_{(s)} + OH_{(s)}$	$3.0 \times 10^{22}$	87.0
R33 $OH_{(s)} + OH_{(s)} \rightarrow H_2O_{(s)} + O_{(s)}$	$3.0 \times 10^{21}$	100.0 <sup>e</sup>
R34 $H_2O_{(s)} + O_{(s)} \rightarrow OH_{(s)} + OH_{(s)}$	$3.0 \times 10^{21}$	207.5 <sup>e</sup>
R35 $C_{(s)} + O_{(s)} \rightarrow CO_{(s)} + Ni_{(s)}$	$5.2 \times 10^{23}$	148.1
R36 $CO_{(s)} + Ni_{(s)} \rightarrow C_{(s)} + O_{(s)}$	$2.5 \times 10^{21}$	$139.7 - 50\theta_{CO(s)}^c$
R37 $CO_{(s)} + O_{(s)} \rightarrow CO_{2(s)} + Ni_{(s)}$	$3.0 \times 10^{19}$	$123.6 - 50\theta_{CO(s)}^{c, e}$
R38 $CO_{2(s)} + Ni_{(s)} \rightarrow CO_{(s)} + O_{(s)}$	$3.0 \times 10^{23}$	88.0 <sup>g</sup>
R39 $CO_{(s)} + H_{(s)} \rightarrow HCO_{(s)} + Ni_{(s)}$	$5.0 \times 10^{19}$	96.2
R40 $HCO_{(s)} + Ni_{(s)} \rightarrow CO_{(s)} + H_{(s)}$	$3.7 \times 10^{21}$	$0.0 + 50\theta_{CO(s)}^c$
R41 $HCO_{(s)} + Ni_{(s)} \rightarrow CH_{(s)} + O_{(s)}$	$3.7 \times 10^{24}$	95.8
R42 $CH_{(s)} + O_{(s)} \rightarrow HCO_{(s)} + Ni_{(s)}$	$3.7 \times 10^{21}$	146.0

<sup>a</sup>The nominal value of the preexponential factor of an elementary reaction was assumed to be:  $10^{13} N_A/\Gamma$  (cm<sup>2</sup>/mol. s), where  $N_A$  is Avogadro's number;  $10^{13}$  (s<sup>-1</sup>) is the order of magnitude of  $\frac{k_B T}{h}$  ( $k_B$  = Boltzmann's constant,  $h$  = Planck's constant) and would be the value expected from

transition state theory;  $\Gamma = 1.5 \times 10^{15}$  (site/cm<sup>2</sup>) is the site density, that was calculated by assuming a site area of  $6.5 \times 10^{-2}$  nm<sup>2</sup> as observed for nickel.

<sup>b</sup>Literature value without temperature dependence of initial sticking coefficient.

<sup>c</sup>Coverage dependence applies due to thermodynamic constraints.

<sup>d</sup>Value for Rh(111).

<sup>e</sup>Estimated in this work based on the comparison of simulation and experiment.

Source: Maier et al. (2011).

## 2.5 Thermodynamic Equilibrium Analysis

Thermodynamic analysis is a useful tool to be applied as a guide for experimental studies. Additionally, it is able to offer various ideas about the availability of reaction conditions in complex chemical reactions. In fact, the complexity of CSCRM reaction (cf. Eq. 2.1) involving multiple reactions, namely, SRM (see Eq. 2.2) and DRM (see Eq. 2.4) as well as several side reactions such as non-coke (*viz.* reverse water-gas shift reaction given in Eq. 2.5) and coke forming reactions (see Eqs. 2.6-2.8). Reactions of Eq. 2.5 and Eq. 2.7 are significant as they increase in  $\text{H}_2\text{O}$  and  $\text{CO}_2$  production and decrease  $\text{H}_2$  and  $\text{CO}$  in the product formation. Therefore, this section explains the thermodynamic feasibilities of these reactions under various reaction temperature.

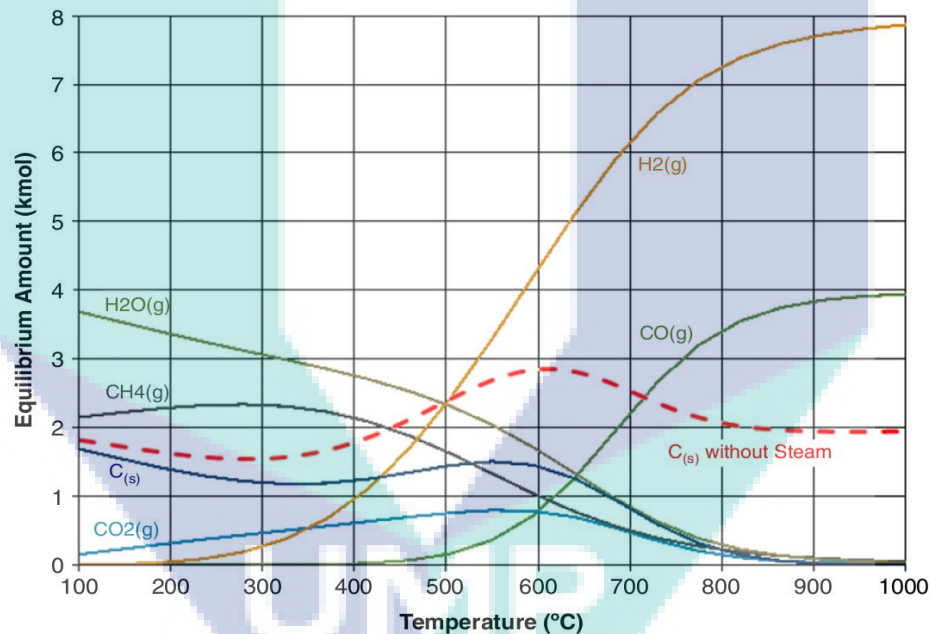
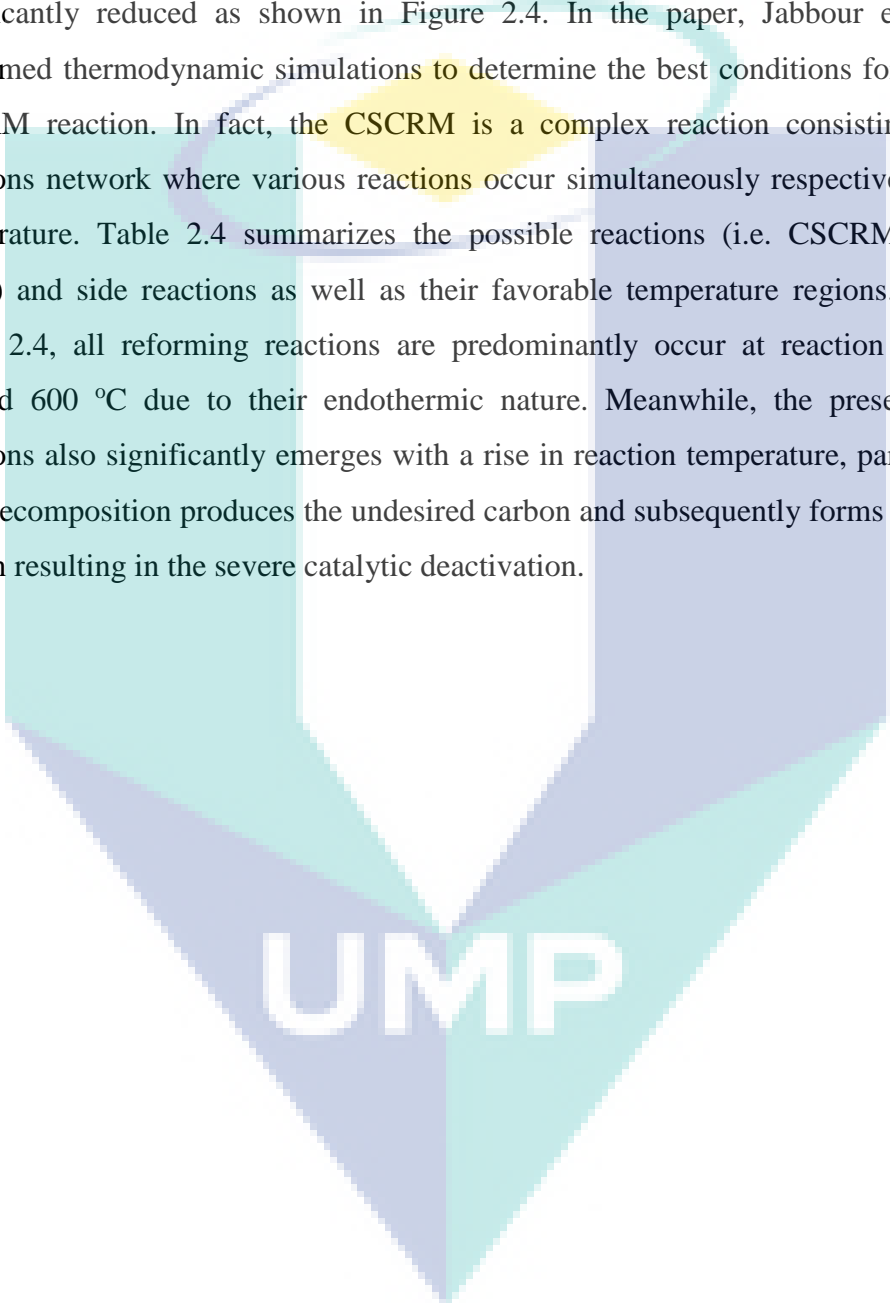


Figure 2.4 Equilibrium composition for combined steam and  $\text{CO}_2$  reforming of methane reaction at different temperatures and atmospheric pressure calculated by HSC Chemistry.

Source: Kumar et al. (2015).

In the thermodynamic equilibrium calculation of catalytic bi-reforming of methane using HSC Chemistry approach, Kumar et al. (2015) reported that the kinetics seems to constraint the reaction of carbon removal (i.e. reverse Boudouard reaction (see Eq. 2.7) and steam gasification of deposited carbon (see Eq. 2.8) at reaction temperature below 800 °C. In addition, the amount of carbon formed with the presence of steam is significantly reduced as shown in Figure 2.4. In the paper, Jabbour et al. (2017) performed thermodynamic simulations to determine the best conditions for conducting CSCRM reaction. In fact, the CSCRM is a complex reaction consisting of multi-reactions network where various reactions occur simultaneously respective of reaction temperature. Table 2.4 summarizes the possible reactions (i.e. CSCRM, SRM and DRM) and side reactions as well as their favorable temperature regions. As seen in Table 2.4, all reforming reactions are predominantly occur at reaction temperature beyond 600 °C due to their endothermic nature. Meanwhile, the presence of side reactions also significantly emerges with a rise in reaction temperature, particularly the CH<sub>4</sub> decomposition produces the undesired carbon and subsequently forms the graphitic carbon resulting in the severe catalytic deactivation.

The logo for UWP (University of Wollongong) is a large, stylized 'U' shape composed of several overlapping geometric shapes in shades of teal, light blue, and yellow. The letters 'UWP' are printed in white, bold, sans-serif font across the bottom of the 'U' shape.

UWP

Table 2.4 List of main and side reactions possibly occurring during CSCRM and probability of occurrence as assessed by thermodynamic calculations of the Gibbs free energy change

Reactions	Equations	Temperature range (°C)			
		100 - 400	400 - 600	600 - 800	800 - 1000
<b>Reforming reactions</b>					
Steam reforming of methane (SRM)	$CH_4 + H_2O \rightarrow 3H_2 + CO$	N.F. – F.	F.	F.	F.
CO <sub>2</sub> reforming of methane (CRM)	$CH_4 + CO_2 \rightarrow 2H_2 + 2CO$	N.F.	N.F. – F.	F.	F.
Combined steam and CO <sub>2</sub> reforming of methane (CSCRM)	$3CH_4 + 2H_2O + CO_2 \rightarrow 8H_2 + 4CO$	N.F.	N.F.	N.F. – F.	F.
<b>Side reactions (non-coke forming)</b>					
Water gas shift (WGS)	$CO + H_2O \rightarrow H_2 + CO_2$	F.	F.	F. – N.F.	N.F.
Reverse water gas shift (RWGS)	$H_2 + CO_2 \rightarrow CO + H_2O$	N.F.	N.F. – F.	F.	F. – N.F.
CO <sub>2</sub> methanation	$CO_2 + 4H_2 \rightarrow CH_4 + 2H_2O$	F.	F. – N.F.	N.F.	N.F.
<b>Side reactions (coke forming)</b>					
CO <sub>2</sub> hydrogenation	$CO_2 + 2H_2 \rightarrow C_{(s)} + 2H_2O$	F.	F. – N.F.	N.F.	N.F.
CH <sub>4</sub> decomposition	$CH_4 \rightarrow C_{(s)} + 2H_2$	N.F.	N.F. – F.	F.	F. – N.F.
Boudouard reaction	$2CO \rightarrow CO_2 + C_{(s)}$	F.	F.	F. – N.F.	N.F.
CO dehydrogenation	$CO + H_2 \rightarrow C_{(s)} + H_2O$	F.	F. – N.F.	N.F.	N.F.

where F. = favored reaction; N.F. = not favored reaction; N.F. – F. (or F. – N.F.) = from not favored to favored (or vice versa).

Source: Jabbour et al. (2017).

## 2.6 Reforming Catalysts

The growth of carbonaceous species on catalyst surface is considerably one of the frequent causes responsible for deactivation of catalyst restraining wide application of numerous heterogeneous catalytic systems such as CSCRM. This reforming process would be the most suitable for the utilization of biogas, a product mainly consists of methane, carbon dioxide and water. In addition, the CSCRM allows the conversion of greenhouse gases ( $\text{CH}_4$  and  $\text{CO}_2$ ) into value-added syngas product, which can be widely employed as feedstock for the synthetic fuels generation and chemical intermediates in petrochemical industries. Theoretically, carbon growth is originating from carbon formation happening on the metal such as methane decomposition, reverse water-gas shift (RWGS), CO disproportionation and carbon gasification. In the case of CSCRM, carbon is formed and consumed via side reactions occurring in parallel with the dominant CSCRM reaction. The poison chemicals in the reactants or products are the main factor causing the rapid decrease in reforming activity with time-on-stream, as suggested by Laosiripojana et al. (2005). Theoretically, the poisoning of catalyst could be mainly categorized into three groups (i) poisoning to the intrinsic activity, (ii) poisoning to the activity of single pellets and, (iii) poisoning of the complete reactor. Thus, in order to overcome the problem, several different transition metals are studied and employed as catalyst in the development of reforming reaction.

### 2.6.1 Noble and Non-noble Metals

Rostrup-Nielsen (2002) reported that the noble metals generally used as active metal in catalyst involving in reforming of methane process are Ni, Ru, Pd, Ir and Pt. From the economic perspective and consideration, Ni becomes the favor in industrial application from the set. Table 2.5 presents the supported metal catalysts which have been studied for reforming processes. The Ni-based reforming catalysts are active and cost-effective for the CSCRM but it is more pronounced to the formation of carbon. In fact, the dissociative adsorption of  $\text{CH}_4$  on nickel nanocluster surfaces, namely  $\text{CH}_4$  decomposition is reported as the main rate determining reaction steps forming S- $\text{CH}_x$  surface species and subsequent  $\text{H}_2$  formation (Verykios, 2003; Wei and Iglesia, 2004; Usman et al., 2015). The  $\text{CH}_4$  decomposition is considerably structure sensitive reliant on support nature and metal cluster size (Hu and Ruckenstein, 2004).

Table 2.5 List of supported metal catalysts which have been studied for reforming processes

Metal	Support	References
Ni	Al <sub>2</sub> O <sub>3</sub>	(Wang, 1999); (Castro Luna and Iriarte, 2008); (García-Diéguez et al., 2010); (Hou et al., 2006); (Zangouei et al., 2010); (Roh et al., 2004)
	SiO <sub>2</sub>	(Kroll et al., 1996); (Hou et al., 2006); (Bradford and Vannice, 1999); (Zangouei et al., 2010)
	TiO <sub>2</sub>	(Hou et al., 2006); (Bradford and Vannice, 1999)
	MgO	(Rostrup-Nielsen, 2002); (Jun et al., 2007)
	SBA-15	(Huang et al., 2011)
	La <sub>2</sub> O <sub>3</sub>	(Tsipouriari et al., 2001)
Co	Al <sub>2</sub> O <sub>3</sub>	(Hou et al., 2006); (Roh et al., 2004)
	TiO <sub>2</sub>	(Zangouei et al., 2010)
	MgO	(Rostrup-Nielsen, 2002)
Rh	Al <sub>2</sub> O <sub>3</sub>	(Hou et al., 2006); (Stevens et al., 2004)
	SiO <sub>2</sub>	(Zangouei et al., 2010); (Tsipouriari et al., 1994)
	TiO <sub>2</sub>	(Zangouei et al., 2010); (Tsipouriari et al., 1994)
	MgO	(Rostrup-Nielsen, 2002)
	CeO <sub>2</sub>	(Tsipouriari et al., 1994)
Ru	YSZ	(Tsipouriari et al., 1994)
	Al <sub>2</sub> O <sub>3</sub>	(Hou et al., 2006)
	SiO <sub>2</sub>	(Hou et al., 2006); (Zangouei et al., 2010)
	TiO <sub>2</sub>	(Zangouei et al., 2010)
Pt	MgO	(Rostrup-Nielsen, 2002)
	Al <sub>2</sub> O <sub>3</sub>	(García-Diéguez et al., 2010); (Hou et al., 2006)
	SiO <sub>2</sub>	(Zangouei et al., 2010)
	TiO <sub>2</sub>	(Zangouei et al., 2010)
Pd	MgO	(Rostrup-Nielsen, 2002)
	Al <sub>2</sub> O <sub>3</sub>	(Erdöhelyi et al., 1994); (Hou et al., 2006)
	SiO <sub>2</sub>	(Erdöhelyi et al., 1994); (Zangouei et al., 2010)
	TiO <sub>2</sub>	(Erdöhelyi et al., 1994); (Zangouei et al., 2010)
Ir	MgO	(Rostrup-Nielsen, 2002)
	Al <sub>2</sub> O <sub>3</sub>	(Hou et al., 2006)
	TiO <sub>2</sub>	(Zangouei et al., 2010)

The hydrogen-depleted S-CH<sub>x</sub> species is mainly having two different following reaction routes, (i) hydrogen-depleted S-CH<sub>x</sub> species reacts with hydroxyl and/or oxygen species to generate H<sub>2</sub> and CO or, (ii) further decomposes to produce carbon atoms. Carbon is purportedly having a higher solubility in the nickel's lattice compared to noble metals' lattices. Therefore, carbon can either remain on the catalyst surface as amorphous carbon or diffuse into subsurface octahedral sites towards carbon growth centers where graphene layer starts to accumulate (Abild-Pedersen et al., 2006). The carbon growth mechanism and the catalytic system are the dominant factors for the formation of various types of carbon species on catalyst surface. The graphene layer in subsurface may encapsulate the Ni particles or detach the Ni particles from the support and eventually become filamentous carbon, carbon nanofibers and/or carbon nanotubes (Abild-Pedersen et al., 2006).

### 2.6.2 Catalyst Supports

The general supports such as Al<sub>2</sub>O<sub>3</sub>, MgO, TiO<sub>2</sub> and La<sub>2</sub>O<sub>3</sub> are employed as reforming catalyst owing to their thermal stability and high surface area to increase the metal dispersion of active metals. However, sintering of the Ni particles on conventional supports is an inevitable obstacle during reforming reaction at high temperature. Therefore, a support having an ordered mesoporous structure is essential to confine the Ni particles in the channels of the mesoporous material from preventing the occurrence of Ni particles sintering and subsequently improve the stability of catalyst (Yi et al., 2005). In recent years, mesoporous SBA-15 has attracted significant attention and to be studied as a reforming catalyst support due to its large specific surface area, thick framework walls, complementary textural porosity, high thermal stability and most importantly, a highly ordered hexagonal structure with narrow pore size distribution. In comparison with straight pores in conventional supports such as Al<sub>2</sub>O<sub>3</sub>, the highly two-dimensional hexagonal structure of SBA-15 is capable to confine and anchors the metal nanoparticle and simultaneously inhibits the occurrence of metal sintering by mobility of species. Apart from that, the surface silanol groups over the mesostructure provide a unique platform for immobilizing metal precursors inside the channels of SBA-15 (Liu et al., 2009). Table 2.6 summarizes the catalytic performance of Ni-based catalysts with various supports for CSCRM reaction. In the study of MgO promoter effect on Ni-based SBA-15 catalysts for CSCRM, the Ni/MgO/SBA-15

catalyst (Huang et al., 2008) reportedly exhibited a higher catalytic activity by increased of 20.5% and 14.9% in CH<sub>4</sub> conversion compared to that of Ni/MgAl<sub>2</sub>O<sub>4</sub> catalyst by Koo et al. (2014) and Park et al. (2015), respectively.

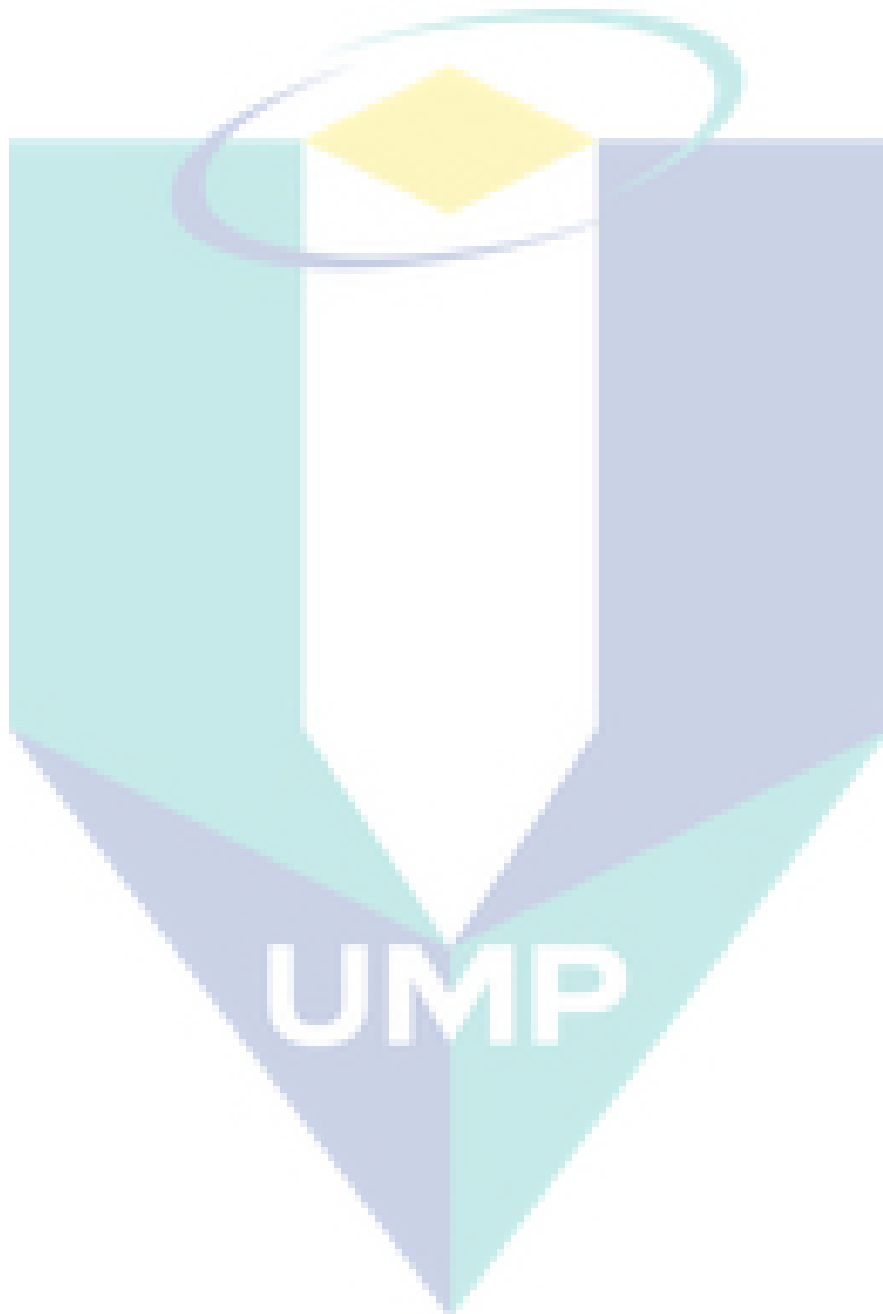


Table 2.6 Bibliographic listing of catalytic performance of Ni-based catalysts with various supports in CSCRM reaction

Catalysts	Fr <sup>a</sup>	T (K)	GHSV (L g <sub>cat</sub> <sup>-1</sup> h <sup>-1</sup> )	Initial performance			TOS <sup>b</sup> (h)	Final performance			Ref.
				CH <sub>4</sub> conversion (%)	CO <sub>2</sub> conversion (%)	H <sub>2</sub> /CO ratio		CH <sub>4</sub> conversion (%)	CO <sub>2</sub> conversion (%)	H <sub>2</sub> /CO ratio	
Ni/Al <sub>2</sub> O <sub>3</sub>	1.0/0.8/0.4	923	530	63.1	51.7	n.m.	20	18.1	10.7	n.m.	(Koo et al., 2012)
Ni/Ce/Al <sub>2</sub> O <sub>3</sub>	1.0/0.8/0.4	923	530	68.6	54.0	n.m.	20	36.9	16.9	n.m.	
Ni-Ce/Al <sub>2</sub> O <sub>3</sub>	1.0/0.8/0.4	923	530	72.9	56.8	n.m.	20	70.6	41.6	n.m.	
Ni/SBA-15	1.0/0.75/0.5	1123	27	98.0	86.0	1.7	660	85.0	50.0	2.2	(Huang et al., 2008)
Ni/MgO/SBA-15	1.0/0.75/0.5	1123	27	98.0	91.0	1.7	660	98.0	79.0	1.9	(Son et al., 2013)
Ni/Al <sub>2</sub> O <sub>3</sub>	1.0/0.8/0.4	1123	50.7	93.8	76.1	2.08	200	91.0	71.6	2.17	(Son et al., 2013)
Ni/MgAl <sub>2</sub> O <sub>4</sub>	1.0/0.8/0.4	973	530	77.5	62.5	2.2	20	n.m.	n.m.	n.m.	(Koo et al., 2014)
Ni-Ce/MgAl <sub>2</sub> O <sub>4</sub>	1.0/0.8/0.4	973	530	81.3	65.9	2.1	20	n.m.	n.m.	n.m.	
Ni-Ce/MgAl <sub>2</sub> O <sub>4</sub>	1.0/0.8/0.4	973	530	80.1	67.1	2.1	20	n.m.	n.m.	n.m.	
Ni-Ce/MgAl <sub>2</sub> O <sub>4</sub>	1.0/0.8/0.4	973	530	74.9	52.3	2.2	20	n.m.	n.m.	n.m.	
Ni/MgAl <sub>2</sub> O <sub>4</sub>	1.0/1.2/0.4	1173	4680	83.1	57.4	3.0	5	55.3	39.2	3.5	(Park et al., 2015)
Ni-La/MgAl <sub>2</sub> O <sub>4</sub>	1.0/1.2/0.4	1173	4680	83.9	59.0	3.3	5	62.6	40.6	3.2	
Ni-La/MgAl <sub>2</sub> O <sub>4</sub>	1.0/1.2/0.4	1173	4680	80.6	58.0	3.2	5	72.7	46.6	3.3	
Ni-La/MgAl <sub>2</sub> O <sub>4</sub>	1.0/1.2/0.4	1173	4680	77.7	54.8	3.1	5	68.1	44.7	3.1	

<sup>a</sup>Molar feedstock ratio (CH<sub>4</sub>/H<sub>2</sub>O/CO<sub>2</sub>).

<sup>b</sup>Time-on-stream defined as the duration of stability measurements at a fixed temperature. where n.m. = not mentioned.

### 2.6.3 Catalyst Promoters

There are numerous approaches developed in suppression of the catalyst deactivation from accumulation of carbonaceous residues. Generally, the modification methods of the reforming catalysts to overcome catalyst deactivation rely on the addition of second active metals such as  $\text{CeO}_2$  or adjustment of particle size of nickel by modification of the supports. The presence of  $\text{CeO}_2$  (Koo et al., 2012; Koo et al., 2014) and  $\text{La}_2\text{O}_3$  (Park et al., 2015) reportedly improves the strong metal to support interaction (SMSI) resulting in a great inhibition to the agglomeration of Ni particles. Additionally, the reduced  $\text{CeO}_{2-x}$  and  $\text{LaO}_x$  species accelerate the mobility of active oxygen from  $\text{H}_2\text{O}$  and  $\text{CO}_2$  to catalyst surface and hence, facilitating the carbon gasification process. In the research, Koo et al. (2012) reported that the addition of  $\text{CeO}_2$  via co-impregnation enhanced the Ni dispersion and reducibility causing a high catalytic activity with 20 h of reaction run. Similarly, as seen in Table 2.6, La promotion gave a great improvement in the catalytic activity after 40 h-on-stream longevity test rationally due to the enhanced SMSI and suppressed Ni particles sintering at high temperature (Park et al., 2015). Moreover, in terms of catalyst lifespan, both authors are good in an agreement that the addition of second active metal,  $\text{CeO}_2$  and  $\text{La}_2\text{O}_3$  substantially improves the coke resistance of catalyst.

Apart from the aforementioned approaches, the recent developments in reforming catalyst have shown boron appears to be a potential promoter with proven success as a coke resistant and achieves efficient catalytic activity. Based on the Density Functional Theory (DFT) calculation, boron reportedly possesses an analogous relative binding preference of carbon atom indicating boron atom is preferentially bind to octahedral site and to step site under the subsurface of catalyst (Xu et al., 2006). Hence, boron atom blocks the most stable binding sites before carbon atom might greatly inhibits the growth of graphite layer via carbon accumulation. Interestingly, subsurface boron become more stable with the rise in concentration due to the strong interaction between boron atoms in neighbouring octahedral sites. However, the strong interaction between boron atoms has a significant influence on the surface structure of Ni-based catalyst, namely surface reconstruction. Thus, the catalytic activity might be declined due to a rise in the  $\text{CH}_4$  activation barrier at concentrated boron loading since it exhibits a similar chemisorption preference as carbon atom. Fortunately, the DFT calculation

shows that the surface reconstruction caused by subsurface boron insignificantly increased the CH<sub>4</sub> activation energy required (Xu et al., 2007). Hence, boron promotion is suggested to improve the catalyst stability without sacrificing the catalytic activity.

Additionally, a study about effect of boron promotion on the catalytic stability and activity of Ni-based catalyst over methane steam reforming was conducted by Xu et al. (2009). They found that the carbon content on the boron-promoted catalyst was lesser than that of unpromoted catalyst after reaction but a decline in catalytic activity with time-on-stream was observed over boron-promoted catalyst. In the study of effect of boron-modified Ni-based catalyst on carbon deposition for DRM, Fouskas et al. (2014) reported that the small amount of boron addition not only enhanced the Ni dispersion and electronic environment of Ni ions but also significantly improved the carbon resistance by obtaining 74-86% less carbon on the B-promoted catalyst compared to that of unpromoted catalyst. In addition, in terms of graphitization and degree of catalyst deactivation, the absence of nanofibers and thin graphene layers formed on the B-promoted catalyst surface further corroborates the excellent catalytic stability exhibited by B-promoted catalyst.

## 2.7 Catalyst Preparation Methods

Apart from the effects of support and promoter, the catalyst preparation methods also play a crucial role and having a substantial influence over the physicochemical properties and catalytic performance of catalyst. In the paper of methane dry reforming evaluation over Ce-promoted Pt/ZrO<sub>2</sub> catalyst, Özkara-Aydinoğlu et al. (2009) synthesized the catalyst using two different approaches, namely co-impregnation and sequential impregnation. The study revealed that the co-impregnated catalyst exhibited a higher catalytic activity, in which CH<sub>4</sub> and CO<sub>2</sub> conversion were 88% and 87%, respectively compared to that of sequential impregnated catalyst. This behaviour was ascribed to the higher dispersion of Pt particles strengthened the interaction between Pt and Ce particles using co-impregnation approach and hence, suppressing the carbon formation. Additionally, in the comparison of catalyst prepared using various approaches (i.e., co-precipitation without surfactant, co-precipitation-surfactant and impregnation), Ni/Ce<sub>0.75</sub>Zr<sub>0.25</sub>O<sub>2</sub> catalyst with co-precipitation-surfactant method reportedly possessed a strong metal-support interaction and higher dispersion due to the

successful embedment of  $\text{Ni}^{2+}$  into solid solution of  $\text{Ce}_{0.75}\text{Zr}_{0.25}\text{O}_2$  support, resulting in the enhancement in catalytic activities (Chen et al., 2008; Usman et al., 2015).

The catalytic performance of  $\text{Co}/\gamma\text{-Al}_2\text{O}_3$  catalysts synthesized by various types of preparation methods, namely direct sol-gel method ( $\text{CoAl}_{\text{SG}}$ ), common wetness impregnation method ( $\text{CoAl}_{\text{CO-IM}}$ ) and impregnation method with support originated from sol-gel method ( $\text{CoAl}_{\text{SG-IM}}$ ) was assessed for methane dry reforming reaction (Budiman et al., 2012). Regardless of the preparation approaches, all catalysts exhibited similar catalytic activity at high temperature. However, in terms of carbonaceous deposition,  $\text{CoAl}_{\text{SG}}$  catalyst had a better carbon-resistance compared to that of  $\text{CoAl}_{\text{CO-IM}}$  and  $\text{CoAl}_{\text{SG-IM}}$  catalysts. This behaviour was probably due to the  $\text{CoAl}_{\text{SG}}$  catalyst possessed a richer oxidizing OH species on the catalyst surface, higher dispersion of small metallic cobalt particles and stronger metal-support interaction using direct sol-gel approach. Similarly, Li et al. (2014) also found that the  $\text{Ni}/\text{SiO}_2$  catalyst prepared by impregnation and sol-gel methods showed a higher catalytic performance, catalytic stability and lesser deposited carbon on the catalyst surface indicating the presence of strong interaction between Ni particles and  $\text{SiO}_2$  support in the interfacial layer leading to the lower formation of carbonaceous species during reaction.

Apart from the aforementioned approaches, incipient wetness impregnation method appears as a promising technique in the catalyst preparation. In the paper of evaluation of ethanol steam reforming over incipient wetness impregnated  $\text{Ni}/\text{SBA-15}$  catalyst, He et al. (2017) found that the use of incipient wetness impregnation significantly improved the interaction between  $\text{NiO}$  particles and  $\text{SBA-15}$  support and hence, enhancing the homogeneous distribution of nickel species to obtain the small nickel particles with high dispersion as evidenced by  $\text{H}_2\text{-TPR}$ , XRD and TEM results. In addition, the characterization results revealed that the high dispersion and strong interaction resulted in much lower carbon deposition on the spent incipient wetness impregnated  $\text{Ni}/\text{SBA-15}$  catalyst surface without substantial deactivation during a longevity test for 25 h on-stream. In summary, these studies indicated that proper choice of preparation method would impart certain textural properties, support activity, and enhanced metal-support interaction that gave rise to higher catalytic activity and lower carbon deposition.

## 2.8 Catalyst Deactivation

Catalyst deactivation is defined as the loss of catalytic activity over time-on-stream, particularly in chemical processes with various operating parameters. In practice, the cost for catalyst replacement and procedure shutdown of industrial catalytic processes could be up to tens of billions of dollars annually (Argyle and Bartholomew, 2015). This decline in catalytic activity due to catalyst deactivation is inevitable and thus, exploring a new catalytic system is essential. The major challenges for reforming reactions is the high thermodynamic potential to coke formation inducing catalyst deactivation, especially formation of carbon filaments from amorphous carbon (Rostrup-Nielsen, 2002). Table 2.7 summarizes the inherent mechanisms of catalyst deactivation involving sintering, fouling and poisoning (Bartholomew, 2001; Argyle and Bartholomew, 2015).

Table 2.7 Mechanisms of catalyst deactivation

Mechanism	Type	Description
Poisoning	Chemical	Strong chemisorption of species on catalytic sites resulting in blocked sites.
Fouling	Mechanical	Physical deposition of species from fluid phase onto catalytic surface and pores.
Thermal degradation	Thermal	Thermally-induced loss of catalytic surface area, support area and active phase-support reactions.
Vapour formation	Chemical	Reaction of gas with catalyst phase to produce volatile compound.
Vapour-solid and solid-solid reactions	Chemical	Reaction of fluid, support or promoter with catalytic phase to produce inactive phase.
Attrition/crushing	Mechanical	Loss of catalytic material from abrasion. Loss of internal surface area from mechanical-induced crushing of catalyst.

### 2.8.1 Poisoning

Poisoning refers to the loss of activity due to impurities from the feed depositing on the active portion and eventually, leading to a decline in the existing active sites for the reaction. In fact, the poisoning has its operational meaning where a species plays as a poison depends on its adsorption strength relative to the other species competing for catalyst sites. Additionally, the physical blockage on adsorption sites by adsorbed poisons may induce changes in the geometric and electronic structure of the surface (Bartholomew, 2001). The conceptual two-dimensional model of sulphur poisoning of ethylene hydrogenation on metal surface as shown in Figure 2.5. At the beginning, a strongly adsorbed atom of sulphur substantially blocks the fourfold adsorption site and three or four topside sites on the metal surface. The neighbouring metal atoms are electronically modified due to the strong chemical bond between the adsorbed sulphur atom and metal surface, thereby influencing the abilities to adsorb and dissociate reactant molecules (i.e.  $H_2$  and ethylene). As a result, the adsorbed poison possibly restructures the surface and thus, resulting in the dramatic alteration in catalytic attributes (Argyle and Bartholomew, 2015).

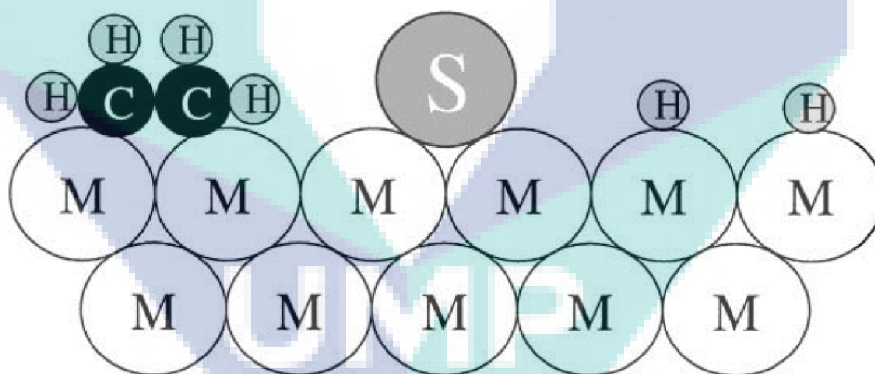


Figure 2.5 Conceptual model of poisoning by sulphur atoms of a metal surface during ethylene hydrogenation.

Source: Argyle and Bartholomew (2015).

Generally, poison adsorption is a fast process and the effect on the nature of the poison is mainly depends on amount of feed. Bartholomew (2001) proposed that pre-treatment for the feed is a feasible option to decrease the concentration of the poison to an acceptable level and thus, resulting in the adsorption strength between catalyst surface and poison molecule requires a higher temperature for the interaction cracking.

Additionally, the resistance of the metallic active sites for poisoning effect should be taken into consideration under the exploration for active catalyst (Argyle and Bartholomew, 2015; Usman et al., 2015; Abdullah et al., 2017). Table 2.8 summarizes catalyst poison groups classified based on their chemical origin and type of interactions of group VA – VIIIA elements with catalytic metal phases relative to oxidation state of former.

Table 2.8 Catalyst poisons classifies based on chemical structure

Chemical type	Examples	Type of interaction with metals
Groups VA and VIA	N, P, As, Sb, O, S, Se, Te	Through s- and p-orbitals; shielded structures are less toxic.
Group VIIA	F, Cl, Br, I	Through s- and p-orbitals; formation of volatile halides.
Toxic heavy metals and ions	As, Pb, hg, Bi, Sn, Zn, Cd, Cu, Fe	Occupy d-orbitals; may form alloys.
Molecules which adsorb with multiple bonds	CO, NO, HCN, benzene, acetylene, other unsaturated hydrocarbons	Chemisorption through multiple bonds and back bonding.

Table 2.9 lists a number of common poisons for chosen catalysts in various reactions. The organic bases and ammonia are general poisons for acidic solids, such as silica-aluminas and zeolites in cracking and hydrocracking reactions, respectively. In addition, arsenic-containing and sulfur-containing compounds are characteristic poisons for metals in dehydrogenation, hydrogenation and reactions of steam reforming. Metal compounds (i.e. Ni, Pb, V, and Zn) are generally known as poisons in hydrotreating and catalytic cracking processes while acetylene is a poison for oxidation of ethene and asphaltenes are ordinary poisons in hydrotreating of petroleum residuum (Argyle and Bartholomew, 2015).

Table 2.9 Catalyst poisons in various important reactions

Catalyst	Reaction	Poisons
Silica-alumina, zeolites	Cracking	Organic bases, hydrocarbons heavy metals
Nickel, platinum, palladium	Hydrogenation, dehydrogenation	Compounds of S, P, As, Zn, Hg, halides, Pb, NH <sub>3</sub> , C <sub>2</sub> H <sub>2</sub>
Nickel	SRM, naphtha	H <sub>2</sub> S, As
Iron, ruthenium	Ammonia synthesis	O <sub>2</sub> , H <sub>2</sub> O, CO, S, C <sub>2</sub> H <sub>2</sub>
Cobalt, Iron	Fischer-Tropsch synthesis	H <sub>2</sub> S, COS, As, NH <sub>3</sub> , metal carbonyls
Noble metals on zeolites	Hydrocracking	NH <sub>3</sub> , S, Se, Te, P
Silver	Ethylene oxidation to ethylene oxide	C <sub>2</sub> H <sub>2</sub>
Vanadium oxide	Oxidation selective catalytic reduction	As, Fe, K, Na from fly ash
Platinum, palladium	Oxidation of CO and hydrocarbons	Pb, P, Zn, SO <sub>2</sub> , Fe
Cobalt and molybdenum sulfides	Hydrotreating of residue	Asphaltenes, N compounds, Ni, V

### 2.8.2 Sintering (Aging)

Sintering also known as aging, the loss of catalyst activity due to structural changes in the crystals on the catalyst surface and stemming from prolonged high temperature exposure. It is generally triggered by excessive temperatures and is an irreversible process leads to the formation of crystal structures with lower surface area (Di Marcoberardino et al., 2015). However, the concentration of main reactant stream gas is possibly one of the factors for the catalyst deactivation via sintering. In the case of supported metal catalysts, sintering process is occurred due to the loss of active surface area via crystal agglomeration and growth of the metals deposited on the support narrowing the pore inside the catalyst pellet. There are two model descriptions for sintering mechanism, crystallites migration and atomic migration models as seen in Figure 2.6. The atomic migration (see 'A' in Figure 2.6) involves detachment of metal atoms or molecular metal clusters from crystallites, migration of these atoms over the support surface, and ultimately, capture by larger crystallites. Crystallite

migration (see 'B' in Figure 2.6) involves the migration of entire crystallites over the support surface, followed by collision and coalescence (Argyle and Bartholomew, 2015).

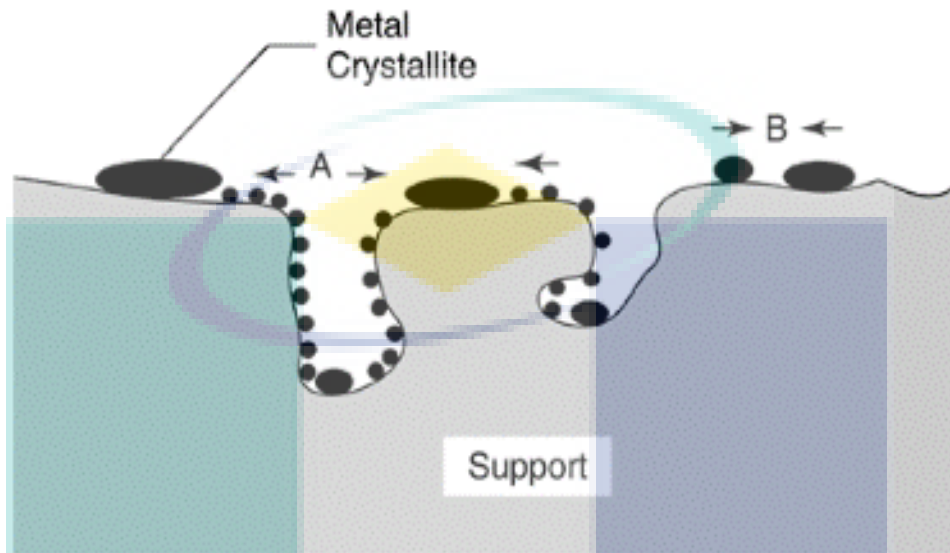


Figure 2.6 Conceptual models for crystallite growth due to sintering: (A) atomic migration, and (B) crystallite migration.

Source: Argyle and Bartholomew (2015).

### 2.8.3 Coking (Fouling)

Coking also known as fouling is a physical type of deactivation and reflects the loss of the catalyst active surface area due to deposition of species resulting in the blockage of sites and pores (Argyle and Bartholomew, 2015). Coke deposition is a major problem for the reforming reactions due to methane cracking and the Boudouard reaction, leading to loss of adsorption sites for the reactants on catalyst surface. Therefore, carbon lay-down is the main complexity problem hinders the reforming reaction from commercial application. As illustrated in Figure 2.7, carbon chemisorbed or physisorbed leads to encapsulation on the metallic active sites with subsequent plugging for micro and mesopores of the support. As a result, production loss and pressure build-up in the plugged reactor and eventually, a costly shutdown is only the solution to resolve the crisis.

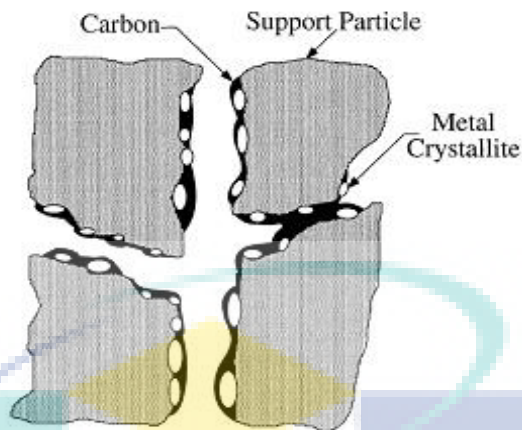


Figure 2.7 Visual illustration for fouling, crystallite encapsulation and pore plugging of a supported metal catalyst due to carbon deposition.

Source: Argyle and Bartholomew (2015).

The mechanism of coke formation from CO and hydrocarbons is presented in Figure 2.8. The  $C_\alpha$  is formed via hydrocarbon decomposition and CO dissociation before transforms into polymeric  $C_\beta$ . This amorphous carbon is more reactive and favored at low temperature and further converts into less reactive graphitic  $C_C$  after a prolonged exposure at high temperature (Kaczmarczyk and Gurgul, 2014). Additionally, other carbon forms from dissolution of carbon into the bulk metal include the carbide,  $C_\gamma$ , or the whisker-like or vermicular carbon,  $C_v$ .

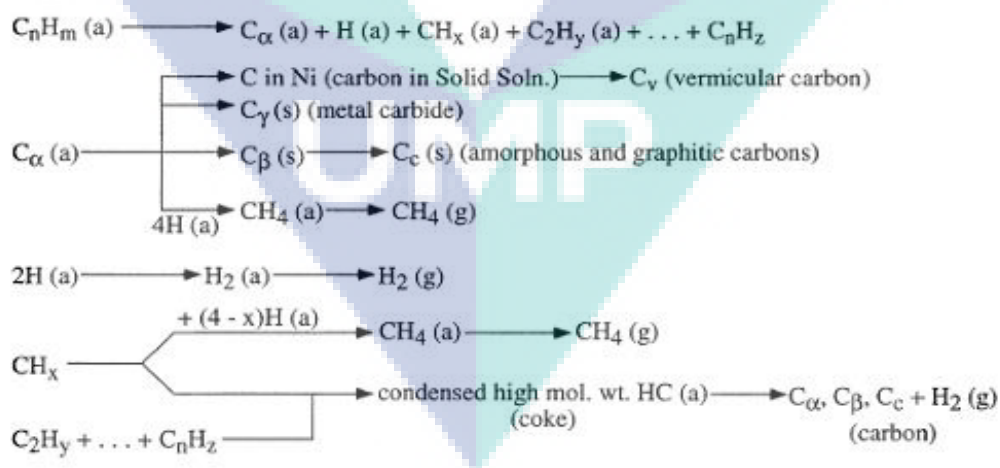


Figure 2.8 Coke formation and transformation from hydrocarbons on metal surfaces.

Source: Kaczmarczyk and Gurgul (2014).

Regarding to the coke characterization, numerous studies about catalyst deactivation due to coking have been investigated but challenge for the complex nature of coke is always inevitable (Sahoo et al., 2004). Undeniably, the carbon formation has brought disruptive effects and hence, minimizing carbon deposition especially in industrial reactors is crucial. Zhang et al. (2009) suggested increasing basicity of the catalyst suppressed the carbon deposition rationally due to the enhancement of CO<sub>2</sub> chemisorption of catalyst and shifts to the reverse Boudouard (or CO disproportionation) reaction. In fact, the ensemble size required for carbon formation is larger than that of reforming reactions and thus, controlling the metal particle size could be considered as alternative way for suppressing carbon deposition (Rostrup-Nielsen, 2002).

## 2.9 Concluding Remarks

As a summary in this chapter, CSCRM reaction is utilizing the renewable biogas as feedstock and has the potential to be developed as a simultaneously catalytic system to the main synthesis gas production route, in which the steam and CO<sub>2</sub> reforming are carried out at the same spot under same operating condition to generate syngas. In order to study the CSCRM reaction, common catalysts used and catalyst deactivation processes were provided and discussed. Carbon deposition leads to catalyst deactivation is often a mutual problem for the reforming reactions. Various researches have documented mechanisms about the Boudouard reaction and CH<sub>4</sub> decomposition are commonly occurring in reforming processes and responsible for carbon deposition. Among the catalyst studies, compared to noble metals, Ni-based catalysts have attracted attention owing to their high activity and stability and cost effectively. Despite the Ni-based SBA-15 supported catalysts is preferable, latter it was found that incorporation of boron into SBA-15 framework as promoter can significantly enhance the catalysts' carbon resilience and hence, B-promoted Ni/SBA-15 catalysts will be extensively investigated in this study.

## CHAPTER 3

### METHODOLOGY

#### 3.1 Introduction

This chapter provides the detailed description of the materials, equipment used and the experimental procedures for catalyst preparation, catalyst characterization and reaction runs. This chapter also includes the grade of chemicals and gases, equipment information and supplier. Additionally, the theoretical outlines and operational aspects of the various catalyst characterization instruments are presented in this chapter.

#### 3.2 Material

##### 3.2.1 Chemicals

A list of chemicals used in this work is provided in Table 3.1. Tetraethyl orthosilicate (TEOS) and Pluronic P123:  $\text{EO}_{20}\text{PO}_{70}\text{EO}_{20}$  were used in the support synthesis, metal nitrates used as catalysts precursors were purchased from Sigma-Aldrich (Kuala Lumpur, Malaysia). All solutions in this study were prepared using water purified by a water distillation unit (Hamilton, England).

Table 3.1 List of chemicals used for catalyst synthesis

Chemical	Formula	Purity/Concentration	Application
Tetraethyl orthosilicate (TEOS)	Si(OC <sub>2</sub> H <sub>5</sub> ) <sub>4</sub>	≥ 99%	Support preparation
Poly(ethylene glycol)-block-poly(propylene glycol)-block-poly(ethylene glycol)/Pluronic P123	EO <sub>20</sub> PO <sub>70</sub> EO <sub>20</sub>	PEG, 30 wt. %	Support preparation
Hydrochloric acid	HCL	37 wt. %	Support preparation
Nickel (II) nitrate hexahydrate	Ni(NO <sub>3</sub> ) <sub>2</sub> ·6H <sub>2</sub> O	≥ 99%	Catalyst Preparation
Boric acid	H <sub>3</sub> BO <sub>3</sub>	99%	Catalyst Preparation
Drierite, indicating 8 mesh	CaSO <sub>4</sub>	99%	Catalyst Preparation

### 3.2.2 Gases

Table 3.2 shows the list of gases used in this work together with their purities, grades and the applications. All cylinder gases were supplied by Air Products (Singapore). Compressed air was used as the drying and calcination gas for catalyst preparation as well as for gas-solid reaction characterization such as temperature-programmed oxidation measurement.

Table 3.2 List of gases used

Gases	Purity/Concentration	Application
CH <sub>4</sub>	99.5%	Reactant
CO <sub>2</sub>	99.5%	Reactant
H <sub>2</sub> O	99.9%	Reactant
H <sub>2</sub>	99.9%	Catalyst reduction, H <sub>2</sub> -TPR
N <sub>2</sub>	99.9%	Diluent, adsorbate for BET analysis, carrier gas for H <sub>2</sub> -chemisorption
Compressed Air	99.9%	GC carrier gas, TPO

### 3.2.3 Equipment

Table 3.3 shows the list of equipment employed in support synthesis, catalyst preparation and combined steam and CO<sub>2</sub> reforming of methane reaction runs. The Table 3.3 summarizes the brands, models and the applications of equipment.

Table 3.3 List of equipment used

Equipment	Model	Application
Hotplate	JlabTech LMS-3003	Mixture was stirred at desired temperature.
Oven	Memmert Germany UFB-500	The catalysts were dried at desired temperature.
Furnace	Carbolite AAF 11/3	The catalysts were calcined at desired temperature.
Rotatory evaporator	BÜCHI Rotavapor R-200	The mixture was stirred at desired temperature.
Syringe pump	KellyMed KL-602	Water was fed to mixer.

## 3.3 Catalyst Preparation

This section presents the details of catalyst preparation procedure. Sequential incipient wetness impregnation technique was employed for preparing both unpromoted and promoted catalysts. The entire SBA-15 support synthesis and catalyst preparation procedures were presented below while the detailed calculations were provided in Appendix A.

### 3.3.1 SBA-15 Support

The hydrothermal synthesis method and ratio of P123:TEOS:H<sub>2</sub>O = 1:2.1:36 were applied in the preparation of siliceous SBA-15 support. A 8.256 g of triblock-poly(ethylene glycol)-block-poly(propylene glycol)-block-poly(ethylene glycol), also known as P-123 (EO<sub>20</sub>PO<sub>70</sub>EO<sub>20</sub>) was initially dissolved into 297.216 mL of 1.6 M hydrochloric acid (HCl) solution with a controlled pH value of about 1 at 313 K. This mixture was continuously stirred for 2 h at 313 K to allow P-123 triblock copolymer completely dissolved into diluted HCl solution, followed by addition of 17.338 g of tetraethyl orthosilicate (TEOS) and vigorously stirring at 313 K for 24 h. The mixture

was subjected to hydrothermal treatment in a Teflon-lined autoclave at 373 K for 24 h and the resulting white slurry was filtered and washed by distilled water until a pH value of around 4 was obtained. The air-calcination at 823 K was carried out with a heating rate of 2 K min<sup>-1</sup> for 5 h after the white slurry was dried in an oven at 323 K overnight. The flow process for mesoporous SBA-15 support synthesis is presented in Figure 3.1.

### 3.3.2 B-promoted 10%Ni/SBA-15 Catalysts

The B-promoted 10%Ni/SBA-15 catalysts were prepared by sequential incipient wetness impregnation approach between the SBA-15 support and corresponding Ni(NO<sub>3</sub>)<sub>2</sub>·6H<sub>2</sub>O and H<sub>3</sub>BO<sub>3</sub> as metallic precursor. The Ni content for the catalyst was fixed at 10% while the boron content was set at 1%, 3% and 5%. A precise amount of Ni(NO<sub>3</sub>)<sub>2</sub>·6H<sub>2</sub>O aqueous solution was impregnated with as-prepared SBA-15 support and thoroughly stirred at 333 K for 3 h in a rotary evaporator, followed by drying in an oven at 373 K overnight and calcination in flowing air at 1073 K with a heating rate of 2 K min<sup>-1</sup> for 5 h. The similar impregnation procedures were repeated with promotion of different calculated quantity of H<sub>3</sub>BO<sub>3</sub> precursor solution into the as-synthesized 10%Ni/SBA-15 catalyst in order to synthesize 1%, 3% and 5%B-promoted 10%Ni/SBA-15 catalysts (see Table 3.4). The entire unpromoted and B-promoted 10%Ni/SBA-15 catalyst preparations are presented in Figure 3.1.

Table 3.4 Amount of material used for preparation of 5 g of 10%Ni/SBA-15 and 1-5%B-promoted 10%Ni/SBA-15 catalysts

Catalyst	SBA-15 (g)	Ni(NO <sub>3</sub> ) <sub>2</sub> ·6H <sub>2</sub> O (g)	Water needed for Ni(NO <sub>3</sub> ) <sub>2</sub> ·6H <sub>2</sub> O (mL)	H <sub>3</sub> BO <sub>3</sub> (g)	Water needed for H <sub>3</sub> BO <sub>3</sub> (mL)
10%Ni/SBA-15	4.500	2.477	3.0	-	-
1%B-10%Ni/SBA-15	4.450	2.477	3.0	0.286	5.018
3%B-10%Ni/SBA-15	4.350	2.477	3.0	0.858	15.053
5%B-10%Ni/SBA-15	4.250	2.477	3.0	1.430	25.088

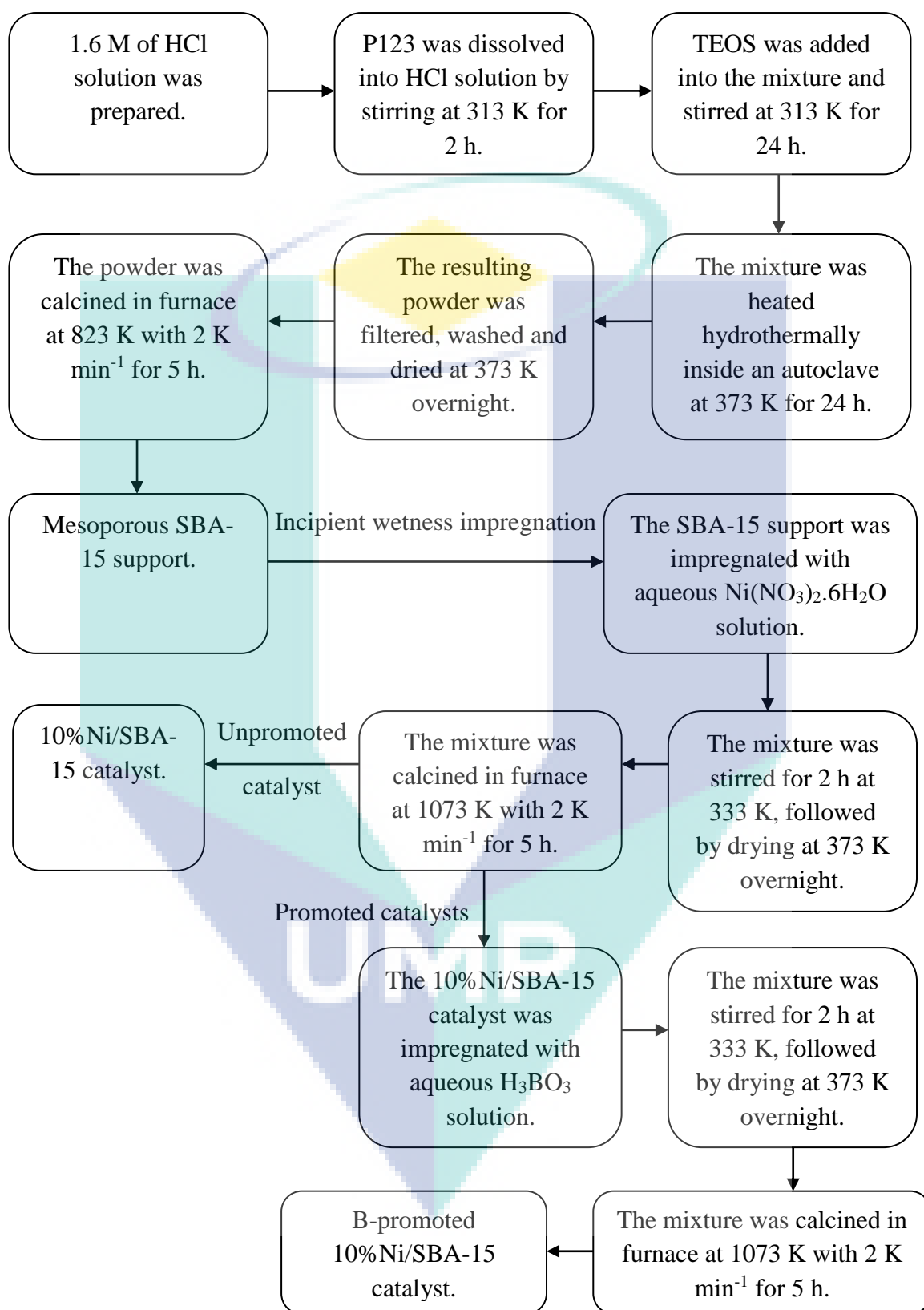


Figure 3.1 Catalyst preparation flowchart.

### 3.4 Catalyst Characterization

#### 3.4.1 Textural Analyses

The textural properties of SBA-15 support, unpromoted and B-promoted Ni-based catalysts including Brunauer-Emmett-Teller (BET) surface area, total pore volume and average pore diameter were conducted in a Micromeritics ASAP-2010 apparatus using N<sub>2</sub> physisorption isotherms data obtained at 77 K. Prior to adsorption step, the specimen was pretreated at 573 K for 1 h in N<sub>2</sub> flow to eliminate traced moisture and volatile contamination on sample surface for each measurement. After the pretreatment, the specimen was subjected into analyser unit from degasser unit for physisorption assessment purpose. A Dewar filled with N<sub>2</sub> liquid was positioned onto a holder below the sample tube and the movement of the flask towards the sample tube was accurately regulated by the Surfer Acquisition software aided by thermistors detecting the existing level of N<sub>2</sub> liquid.

With the assumption of full coverage of adsorbate on catalyst pores, the pore volume of catalyst can be estimated based on the amount of gas adsorbed at the relative pressure,  $p/p^0 \approx 1$ . Thus, the volume of N<sub>2</sub> ( $V_{N_2}$ ) can be calculated by Eq. 3.1.

$$V_{N_2} = \frac{P_a V_{ads} v_m}{RT_a} \quad 3.1$$

with  $P_a$ ,  $T_a$ ,  $R$  and  $v_m$  are being ambient pressure, ambient temperature, universal gas constant and molar volume of the adsorbate (34.7 cm<sup>3</sup> mol<sup>-1</sup> for N<sub>2</sub>), respectively.

By assuming the pore geometry of catalyst to be cylindrical, the pore size of catalyst,  $r_K$  can be computed by Kelvin equation as given in Eq. 3.2 (Gregg and Sing, 1982).

$$r_K = \frac{-2\gamma_s v_m}{RT_b \ln \frac{P}{P_s}} \quad 3.2$$

where  $r_K$ ,  $\gamma_s$ ,  $v_m$ ,  $R$ ,  $T_b$ ,  $\frac{P}{P_s}$  represent the corresponding Kelvin radius of the pore, N<sub>2</sub> surface tension at boiling point, molar volume of liquid N<sub>2</sub>, universal gas constant, boiling point of N<sub>2</sub> and relative pressure of N<sub>2</sub>.

Nevertheless, the Kelvin radius does not represent the real radius since partial adsorption on wall pores probably happen before condensation. Hence, the real radius,  $r_p$  can be estimated by Eq. 3.3.

$$r_p = r_K + t_{ads} \quad 3.3$$

where  $t_{ads}$  represents the thickness of the adsorbed layer which can be calculated employing Eq. 3.4 suggested by de Boer (Singh, 2008).

$$t_{ads} = \left( \frac{13.99}{\log \frac{P_s}{P} + 0.034} \right)^{\frac{1}{2}} \quad 3.4$$

### 3.4.2 Fourier Transform Infrared Spectroscopy (FTIR) Analyses

The presence of functional groups on the SBA-15 support, unpromoted and promoted catalysts was identified by Fourier-Transform Infrared (FTIR) spectroscopy measurement. The FTIR spectra of support and catalysts was recorded in the range of 400-4000 cm<sup>-1</sup> and spectral resolution of 4 cm<sup>-1</sup>. The number of scans of 100 was employed on a Thermo Fisher Scientific Nicolet iS5 FTIR spectrometer equipped with an iD7 ATR attachment. Prior to measurement, a background check was conducted for each run on the ATR sample holder and the crystal plate was cleaned with acetone and dried for 15 min to completely remove contamination. The spectra for support and catalysts were interpreted using OMNIC software version 8.

### 3.4.3 X-ray Diffraction (XRD) Measurements

X-ray diffraction (XRD) measurements were commonly employed to determine the crystalline phase over catalysts and average crystallite size. The Rigaku Miniflex II system using a Cu monochromatic X-ray radiation with a wavelength,  $\lambda$  of 1.5418 Å was utilized for X-ray diffraction (XRD) measurements. This system was operated at 15

mA and 30 kV. During scanning within the  $2\theta$  range of  $3^\circ$  to  $80^\circ$ , a relatively small scan speed and a step size of corresponding  $1^\circ \text{ min}^{-1}$  and  $0.02^\circ$  were implemented to obtain high-resolution patterns. In XRD measurement, the specimen was irradiated with X-rays and hence, occurrence of diffraction as presented in Figure 3.2. The obtained angles are matched with Joint Committee on Powder Diffraction Standards (JCPDS) database for phase identification. According to Bragg, the lattice spacing could be estimated from X-ray diffraction of crystal planes via Eq. 3.5 (Cooper et al., 2008).

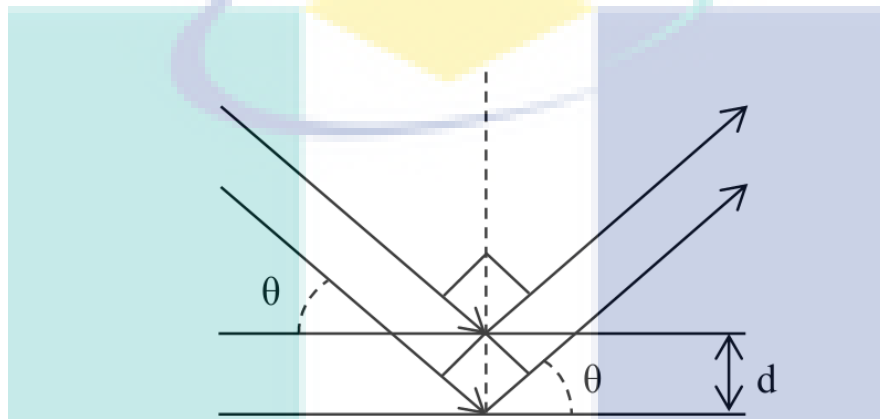


Figure 3.2 The Bragg Law for XRD analysis.

$$n\lambda = 2d \sin \theta \quad 3.5$$

where  $n$ ,  $\lambda$ ,  $d$  and  $\theta$  represent the corresponding the order of reflection, wavelength of the X-rays, distance between two planes and angle between the incident X-rays and the scattering plane.

In addition, the Scherrer equation (cf. Eq. 3.6) was also employed for computing the average crystallite size of NiO phase,  $d(\text{NiO})$  (Patterson, 1939).

$$d(\text{NiO}) = \frac{0.94\lambda}{B \times \cos \theta} \quad 3.6$$

where  $\lambda$ ,  $B$  and  $\theta$  represent the wavelength of X-ray, the line broadening at half the maximum intensity (FWHM) and Bragg angle, respectively. Based on the relative molar volumes of metallic  $\text{Ni}^0$  and NiO phases, the metallic  $\text{Ni}^0$  particle size,  $d(\text{Ni}^0)$  after the

H<sub>2</sub> reduction of NiO particles could be approximately estimated from Eq. 3.7 (Xu et al., 2009; Baum, 1998).

$$d(Ni^0) = 0.84d(NiO) \quad 3.7$$

#### 3.4.4 H<sub>2</sub> Temperature-programmed Reduction (H<sub>2</sub>-TPR) Analyses

H<sub>2</sub> temperature-programmed reduction (H<sub>2</sub>-TPR) is generally used to assess the reducibility of catalyst depending on temperature. In this study, H<sub>2</sub>-TPR was conducted using an AutoChem II-2920 system. About 0.1 g of catalyst was loaded by quartz wool in the middle of a quartz U-tube. The pre-treatment was carried out at 373 K for 30 min in 50 mL min<sup>-1</sup> of flowing He inert gas for the elimination of moisture prior to H<sub>2</sub> reduction. The specimen underwent reduction step with a temperature range from 373 to 1173 K with a heating rate of 10 K min<sup>-1</sup> in flowing 50 mL min<sup>-1</sup> of 10% H<sub>2</sub>/Ar mixture.

#### 3.4.5 Raman Spectroscopy Measurements

Raman scattering is a spectroscopic technique provides information about molecular vibrations that can be used for sample identification. Raman spectroscopy analysis of fresh and spent catalysts as well as SBA-15 support was performed on a JASCO NRS-3100 Raman spectrometer unit with a green laser of 532 nm and laser power of below 5 mW during measurement in ambient air.

#### 3.4.6 Scanning Electron Microscopy (SEM) Measurements

Scanning Electron Microscopy (SEM) technique uses a focused beam of highly energetic electrons to obtain surface topography image with high resolution. SEM image is attained when an area of sample surface is scanned by concentrated incident electron beam via electromagnetic lenses. The emitted electrons are detected for each position in the scanned area of sample using electron detector and the intensity of the emitted electron signal is showed in different brightness levels on screen monitor as digital image file.

SEM measurements of fresh and spent catalysts were carried out on a Carl Zeiss AG - EVO<sup>®</sup> 50 Series instrument using a SmartSEM software. The specimens were coated on platinum plate using a BAL-TEC SCD 005 Sputter Coater to enhance the sharpness of SEM images.

### 3.4.7 Transmission Electron Microscopy (TEM) Analyses

Transmission Electron Microscopy (TEM) technique can provide morphological, topographical, compositional and crystalline information about a sample. In TEM measurement, electron beam generated from electromagnetic lenses was focused and thoroughly penetrate the specimen. Unlike SEM, TEM technique can provide the internal structure and texture of sample such as morphology and crystallization.

TEM analyses were conducted for selective spent catalysts using a FEI Tecnai G<sup>2</sup> F20 TEM unit. Prior to TEM test, the solid sample was suspended in ethanol solution for 1 h to minimize particle agglomeration and one drop of this slurry was placed on a copper grid coated with porous carbon film.

### 3.4.8 Temperature-programmed Oxidation (TPO) Measurements

Temperature-programmed oxidation (TPO) measurements were employed to identify and quantify deposited carbon on spent catalyst surface. The TPO tests were conducted for unpromoted and selective promoted catalysts after CSCRM reaction on a TGA Q500 unit from TA Instruments. The specimen was heated from ambient temperature to 373 K with a heating rate of 10 K min<sup>-1</sup> and held isothermally for 30 min in order to remove moisture and volatile compounds. The temperature was then increased to 1023 K with a ramping rate of 10 K min<sup>-1</sup> in purging 20% O<sub>2</sub>/N<sub>2</sub> mixture (100 mL min<sup>-1</sup>). Sample was further kept at the same temperature for 30 min in the previous purging gas mixture to ensure the complete oxidation of carbonaceous deposition followed by cooling down to room temperature.

## 3.5 Experimental Set-up

The detailed schematic diagram for CSCRM is shown as Figure 3.3. The CSCRM reaction was conducted at 973-1073 K at stoichiometric feed composition ( $F_{CH_4} : F_{H_2O} : F_{CO_2} = 3:2:1$  with  $F$  represents molar flow rates (mol s<sup>-1</sup>)) under atmospheric pressure in a quartz tube fixed-bed continuous flow reactor (length,  $L = 17$  inch and outer diameter, O.D. = 3/8 inch). Approximately 0.1 g of catalyst was mounted by quartz wool in the middle of reactor placed vertically in a temperature-controlled furnace and the reaction temperature was systematically and continuously monitored

with time-on-stream (TOS). The purified water precisely fed by KellyMed KL-602 syringe pump to the top of reactor was vaporized and mixed with other gaseous reactants (viz., CH<sub>4</sub> and CO<sub>2</sub>) previously diluted with N<sub>2</sub> inert gas. The Alicat mass flow controllers were used for accurately regulating the flow rates of all gases. The N<sub>2</sub> diluent gas plays as a tie component for material balance purpose and guaranteeing that the total flow rate of 60 mL min<sup>-1</sup> for each run was obtained whilst high gas hourly space velocity, GHSV of 36 L g<sub>cat</sub><sup>-1</sup> h<sup>-1</sup> and small average particle size ranging of 100-140 μm were employed for all runs to neglect the presence of internal and external transport resistances for obtaining the intrinsic catalytic activity.

The loaded catalyst was initially reduced in-situ with 60 mL min<sup>-1</sup> of 50% H<sub>2</sub>/N<sub>2</sub> mixture at 1073 K for 2 h followed by N<sub>2</sub> purging (60 mL min<sup>-1</sup>) for 30 min before switching to the mixture of gaseous reactants for CSCRM reaction. In order to investigate the effect of feed composition on CSCRM performance, one reactant (CH<sub>4</sub> or H<sub>2</sub>O or CO<sub>2</sub>) was kept constant at partial pressure ( $P_{CH_4} = 45$  kPa,  $P_{H_2O} = 30$  kPa,  $P_{CO_2} = 15$  kPa) whilst  $P$  of other reactant was varied from 10 to 50 kPa. The Agilent 6890 Series GC system installed with TCD detector and HP-PLOT Q capillary column (30 m × 0.53 mm × 40 μm) was used to analyze the composition of gaseous effluent from the outlet of fixed-bed reactor. The unreacted steam in effluent gases was condensed and completely adsorbed by a cold trap and a drierite adsorbent bed, respectively before GC analysis. The process flow chart of experiment set-up is presented in Figure 3.4.

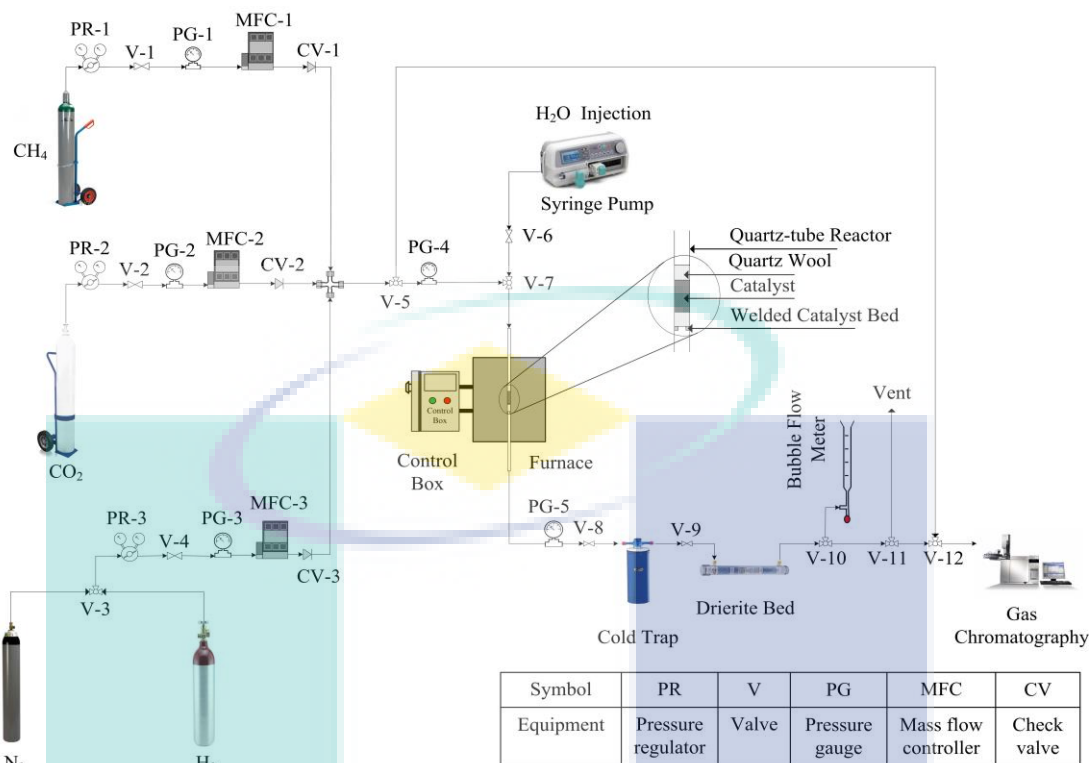


Figure 3.3 Schematic diagram for CSCRM reaction.

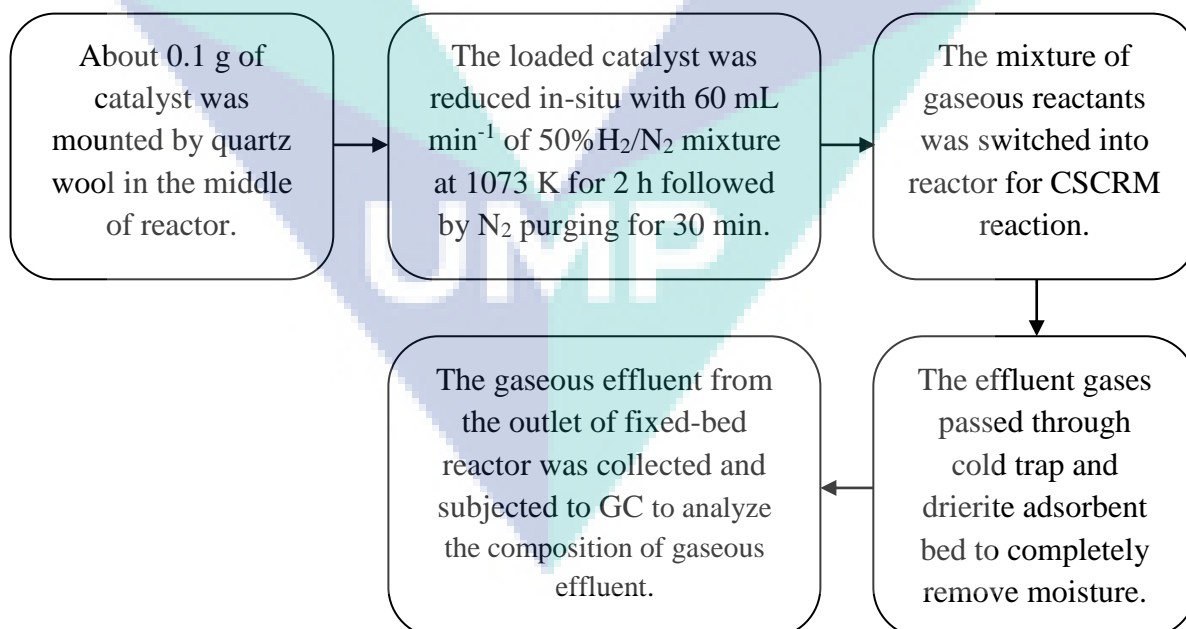


Figure 3.4 CSCRM reaction flow chart.

The gaseous product analysis was performed by using Agilent 6890 Series gas chromatograph equipped with thermal conductivity detector and capillary column, HP-MOLSIV (30.0 m × 530 μm × 40.0 μm). The temperature of oven was kept constant at 393 K whilst the column was conducted at 353 K with Helium as carrier gas. The standard gas with known composition was injected for five times to obtain the gas chromatography calibration. Furthermore, the experimental data obtained from CSCRM reaction was compared to the results of calibration curves and standard gas analysis while the Table 3.5 summarizes the standard gas information including compound composition and retention time from GC analysis. Regarding to the GC calibration, a five times separate injection of standard gas into the GC was conducted in order to obtain the average calibration value for each component (cf. Table 3.5).

Table 3.5 Information of standard gas from GC analysis

Compound	Composition (%)	Retention time (min)
CO <sub>2</sub>	19.98	10.07
H <sub>2</sub>	25.06	5.39
CH <sub>4</sub>	5.07	7.24
CO	24.89	13.73

### 3.6 Syringe Pump and Mass Flow Controller (MFC) Calibration

The syringe pump is calibrated with water while mass flow controllers (MFC) are calibrated with the relevant gases supplied to the CSCRM system (CH<sub>4</sub>, CO<sub>2</sub> and N<sub>2</sub>). For each calibration, measurements are conducted for at least 5 points and the calibration procedure yielded a linear plots of signal versus actual flow rate. The detailed calibration graphs for each reactant are plotted in Appendix C.

### 3.7 Combined Steam and CO<sub>2</sub> Reforming of Methane Reaction Metrics

The reactant conversion,  $X_i$  (with  $i$  being CH<sub>4</sub> or CO<sub>2</sub>) to gaseous products during CSCRM reaction is determined by using equations as seen in Eq. 3.8. A detailed example for calculation of catalytic performance is computed in Appendix B.

$$X_i(\%) = \frac{F_i^{in} - F_i^{out}}{F_i^{in}} \times 100\% \quad 3.8$$

where  $F^{In}$  and  $F^{Out}$  are the corresponding inlet and outlet molar flow rates (mol s<sup>-1</sup>).

Yield of individual products ( $Y_i$ ) and gaseous product ratio (H<sub>2</sub>/CO) are defined as:

$$Y_{H_2}(\%) = \frac{2F_{H_2}^{Out}}{4F_{CH_4}^{In} + 2F_{H_2O}^{In}} \times 100\% \quad 3.9$$

$$Y_{CO}(\%) = \frac{F_{CO}^{Out}}{F_{CH_4}^{In} + F_{CO_2}^{In}} \times 100\% \quad 3.10$$

$$\frac{H_2}{CO} = \frac{r_{H_2}}{r_{CO}} \quad 3.11$$

where  $r$  = production or formation rates (mol g<sub>cat</sub><sup>-1</sup> s<sup>-1</sup>).

UMP

## CHAPTER 4

### PRELIMINARY WORK

#### 4.1 Introduction

This chapter describes the detailed discussions of preliminary works including the availability of CSCRM blank test (without the presence of catalyst) and transport resistance considerations such as of mass and heat transport limitations for CSCRM evaluation in order to confirm that the rate data collected were free from undesired incursions such as mass and heat transport resistances. Additionally, the end of this chapter suggests the appropriate operating conditions (i.e., reaction temperature range, reactant feed composition and reaction time-on-stream) for CSCRM based on the evaluation of mass and heat transport limitations.

#### 4.2 CSCRM Blank Test

The CSCRM blank test was conducted without the presence of catalyst in a vertical fixed-bed continuous flow reactor at temperature of 973 K under atmospheric pressure and stoichiometric feed composition ( $F_{CH_4} : F_{H_2O} : F_{CO_2} = 3 : 2 : 1$ ) for 10 h. A total flow rate of  $60 \text{ ml min}^{-1}$  was employed with the feed of  $N_2$  flow simultaneously. The insignificant  $H_2$  and  $CO$  peaks were detected in GC spectrum could suggest the presence of methane decomposition at the operating condition. The  $CH_4$  and  $CO_2$  conversions obtained from blank test had relatively low values of 13.10% and 25.09% (see the discussions in Chapter 6.2), respectively. In addition, these values were substantially enhanced with the existence of catalyst (see the discussions in Chapter 6.3). Therefore, the enhancement in catalytic activity during CSCRM reaction over Ni-

based catalysts in this research was reliant on the physicochemical properties and efficient participation of employed catalysts.

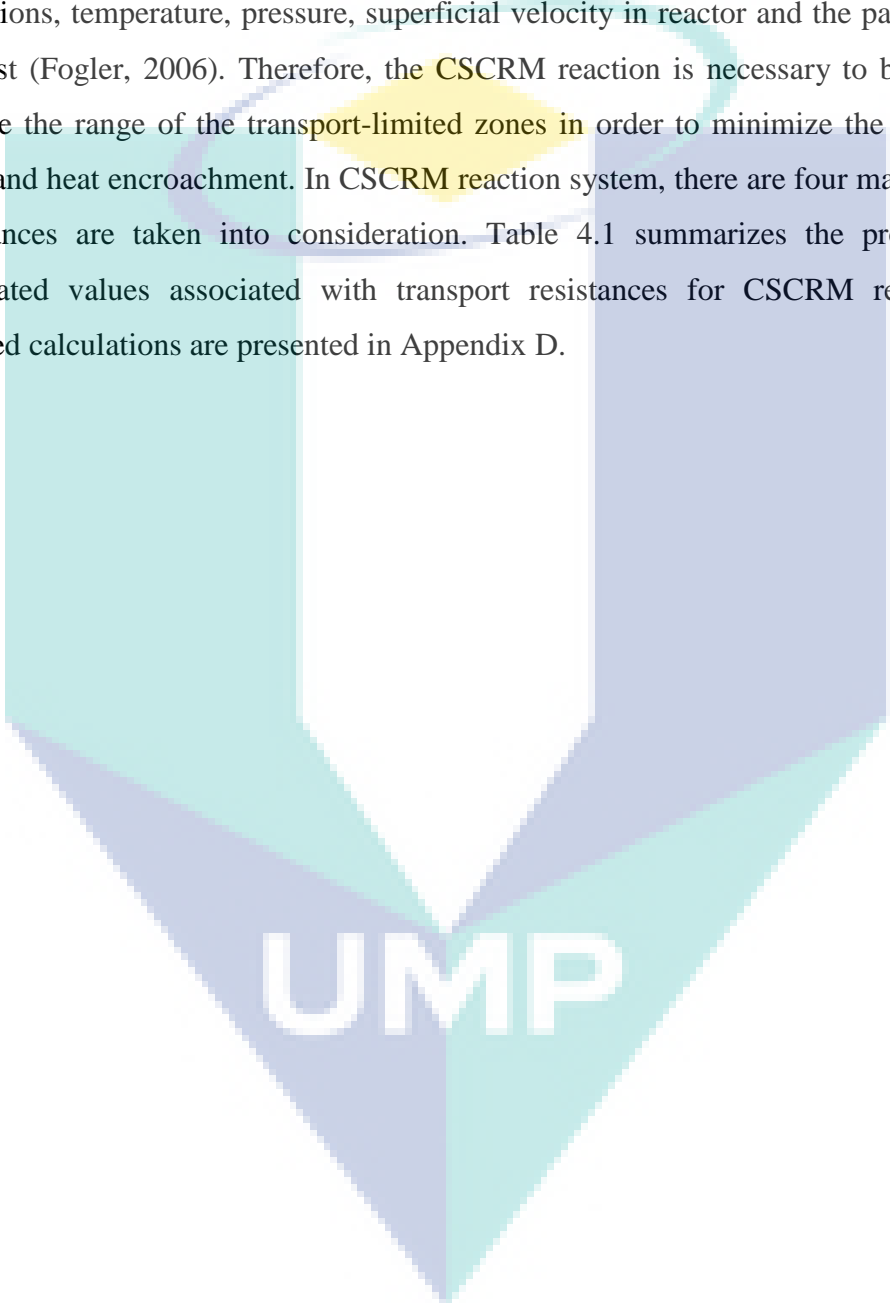
### 4.3 Steps in Catalytic Reaction

In the book of Klaewkla et al. (2011), there are classical inherent seven steps for a heterogeneous catalytic system involving the interaction between reactants and catalyst surface. The seven steps are described as follow:

1. Diffusion of reactants from the bulk fluid (boundary layer) to the external surface of the catalyst (film diffusion or interphase diffusion).
2. Diffusion of the reactant from the pore mouth through the catalyst pores to the immediate vicinity of the internal catalytic surface where the chemical transformation take places (pore diffusion or intraparticle diffusion).
3. Adsorption of reactants onto the interior of catalyst surface.
4. Reaction at specific active sites on the interior of catalyst surface.
5. Desorption of the products from the inner catalyst surface.
6. Diffusion of the products from the inner catalyst surface to the pore mouth at the external surface.
7. Diffusion of the products from the external catalyst surface to the bulk fluid (interphase diffusion).

The adsorption, surface reaction and desorption are the sequential steps for a catalytic reaction. Nevertheless, the steady state of mass transfer rate to the reactive surface (intraparticle diffusion) is as crucial as reaction rate during occurrence of a chemical reaction on catalyst surface. The chemical kinetics are represented in steps of 3, 4 and 5. The steps of 1 and 7 are representing the external mass transfer processes whilst steps 2 and 6 are associated with the internal mass transfer processes. In fact, the mass transfer steps of 1, 2, 6 and 7 are negligible and occurring rapidly if no resistance is present for the diffusion from bulk to the particle surface and from particle surface to the active sites on the inner pore.

Theoretically, there is no drastic influence on the reaction rate by mass transferring steps if the concentration around the catalyst sites and bulk is equivalent. If mass transfer from bulk to catalyst surface is slow, the external mass transfer resistance is significant and to be an essential factor in consideration respect to reaction rate. However, the relevant factors for external mass transfer resistance includes flow conditions, temperature, pressure, superficial velocity in reactor and the particle size of catalyst (Fogler, 2006). Therefore, the CSCRM reaction is necessary to be conducted outside the range of the transport-limited zones in order to minimize the influence of mass and heat encroachment. In CSCRM reaction system, there are four major transport resistances are taken into consideration. Table 4.1 summarizes the properties and calculated values associated with transport resistances for CSCRM reaction. The detailed calculations are presented in Appendix D.

The logo for UIMP (Universiti Malaysia Perlis) is a large, downward-pointing arrow shape. It is composed of four triangular sections meeting at a central point. The top-left and bottom-right sections are light blue, while the top-right and bottom-left sections are a slightly darker shade of blue. The letters 'UIMP' are printed in white, bold, sans-serif font across the center of the arrow.

UIMP

Table 4.1 Properties for CSCRM and correspond calculated values

Parameter	Value	Source
$A$	$4.90 \times 10^{-5} \text{ m}^2$	Reactor tube property
$C_{Ab}$	$4.09 \times 10^{-5} \text{ mol cm}^{-3}$	Experimental condition
$C_{p-CH_4}$	$4.72 \times 10^3 \text{ J kg}^{-1} \text{ K}^{-1}$	(Green and Perry, 2008)
$C_{p-H_2O}$	$2.34 \times 10^3 \text{ J kg}^{-1} \text{ K}^{-1}$	(Green and Perry, 2008)
$C_{p-CO_2}$	$1.26 \times 10^3 \text{ J kg}^{-1} \text{ K}^{-1}$	(Green and Perry, 2008)
$C_{p-N_2}$	$1.18 \times 10^3 \text{ J kg}^{-1} \text{ K}^{-1}$	(Green and Perry, 2008)
$h_w$	$30 \text{ J m}^{-1} \text{ s}^{-1} \text{ K}^{-1}$	(Green and Perry, 2008)
$R$	$8.314 \text{ J mol}^{-1} \text{ K}^{-1}$	(Green and Perry, 2008)
$\lambda_{CH_4}$	$0.186 \text{ J m}^{-1} \text{ s}^{-1} \text{ K}^{-1}$	(Green and Perry, 2008)
$\lambda_{H_2O}$	$0.106 \text{ J m}^{-1} \text{ s}^{-1} \text{ K}^{-1}$	(Green and Perry, 2008)
$\lambda_{CO_2}$	$0.07 \text{ J m}^{-1} \text{ s}^{-1} \text{ K}^{-1}$	(Green and Perry, 2008)
$\lambda_{N_2}$	$0.07 \text{ J m}^{-1} \text{ s}^{-1} \text{ K}^{-1}$	(Green and Perry, 2008)
$\lambda_m$	$2.60 \text{ J m}^{-1} \text{ s}^{-1} \text{ K}^{-1}$	(Green and Perry, 2008)
$\lambda_p$	$6.42 \times 10^3 \text{ J m}^{-1} \text{ s}^{-1} \text{ K}^{-1}$	Calculation
$\mu_{CH_4}$	$2.94 \times 10^{-5} \text{ kg m}^{-1} \text{ s}^{-1}$	(Green and Perry, 2008)
$\mu_{H_2O}$	$4.08 \times 10^{-5} \text{ kg m}^{-1} \text{ s}^{-1}$	(Green and Perry, 2008)
$\mu_{CO_2}$	$4.19 \times 10^{-5} \text{ kg m}^{-1} \text{ s}^{-1}$	(Green and Perry, 2008)
$\mu_{N_2}$	$4.35 \times 10^{-5} \text{ kg m}^{-1} \text{ s}^{-1}$	(Green and Perry, 2008)
$D_{eff}$	$2.38 \times 10^{-5} \text{ m}^2 \text{ s}^{-1}$	Calculation
$D_g$	$2.23 \times 10^{-4} \text{ m}^2 \text{ s}^{-1}$	Calculation
$d_p$	$1.95 \times 10^{-4} \text{ m}$	Experimental condition
$d_t$	$7.90 \times 10^{-3} \text{ m}$	Reactor tube property
$E_A$	$87.37 \text{ kJ mol}^{-1}$	Experimental condition
$-\Delta H_r$	$245.45 \text{ kJ mol}^{-1}$	Experimental condition
$-r_{exp}$	$6.32 \times 10^{-5} \text{ mol g}_{cat}^{-1} \text{ s}^{-1}$	Experimental condition
$R_p$	$9.75 \times 10^{-5} \text{ m}$	Experimental condition
$T$	1073 K	Experimental condition
$V$	$60 \text{ mL min}^{-1}$	Experimental condition
$\varepsilon$	0.8	(Adhikari et al., 2007)
$\rho_c$	$3.35 \text{ g cm}^{-3}$	Experimental condition
$\rho_b$	$0.67 \text{ g cm}^{-3}$	$(1 - \varepsilon)\rho_c$
$\rho_g$	$0.251 \text{ kg m}^{-3}$	Calculation
$\sigma_c$	0.8	(Fogler, 2006)
$\theta$	3.0	(Fogler, 2006)
$\omega_p$	0.4	(Fogler, 2006)
$n$	1.4	(Park et al., 2015)

### 4.3.1 External Mass Transfer Resistance

The external mass transfer resistance may exist between the bulk fluid and the external catalyst surface and thus, the Mears criterion (Mears, 1971) as shown in Eq. 4.1 must be satisfied to neglect the effect of external mass transfer resistance.

$$\frac{(-r_{\text{exp}})\rho_b R_p n}{k_c C_{Ab}} < 0.15 \quad 4.1$$

where

$(-r_{\text{exp}})$  = rate of reaction ( $\text{mol g}_{\text{cat}}^{-1} \text{s}^{-1}$ ) (the highest reaction rate obtained from experimental data was employed for calculation)

$\rho_b$  = bulk density of catalyst bed ( $\text{g cm}^{-3}$ )

$R_p$  = catalyst particle radius (m)

$n$  = reaction order (Park et al., 2015)

$C_{Ab}$  = bulk gas-phase concentration of  $\text{CH}_4$  ( $\text{mol cm}^{-3}$ )

$k_c$  = mass transfer coefficient ( $\text{cm s}^{-1}$ )

The mass transfer coefficient,  $k_c$  can be calculated from Eq. 4.2, as indicated by (Dwivedi and Upadhyay, 1977).

$$k_c = \frac{j_D U}{S_c^{2/3}} \quad 4.2$$

where

$j_D$  = Colburn's mass transfer factor

$U$  = superficial gas velocity ( $\text{m s}^{-1}$ )

$S_c$  = Schmidt number

The value of Mears criterion in Eq. 4.1 is obtained about  $2.04 \times 10^{-4} < 0.15$  indicating the effect of external mass transfer resistance for CSCRM reaction is negligible. Hence, the total flow rate of  $60 \text{ mL min}^{-1}$  for each CSCRM reaction run is sufficient to be employed in CSCRM.

### 4.3.2 Internal Mass Transfer Resistance

The internal mass transfer resistance generally occurs during the diffusion of reactants and products through the pores of catalyst. The effect of internal mass transfer can be neglected if Weisz-Prater criterion (Fogler, 2006) in Eq. 4.3 is met.

$$\frac{(-r_{\text{exp}})\rho_c R_p^2}{D_{\text{eff}} C_{Ab}} < 1 \quad 4.3$$

where

$\rho_c$  = density of catalyst pellet ( $\text{g cm}^{-3}$ )

$C_{As}$  = concentration of  $\text{CH}_4$  on the catalyst surface ( $\text{mol cm}^{-3}$ )

$D_{\text{eff}}$  = effective diffusivity of  $\text{CH}_4$  in a mixture of  $\text{H}_2\text{O}$ ,  $\text{CO}_2$  and  $\text{N}_2$  ( $\text{m}^2 \text{s}^{-1}$ )

The concentration of  $\text{CH}_4$  on the catalyst surface ( $C_{Ab}$ ) is equivalent to the concentration of  $\text{CH}_4$  in the bulk gas-phase ( $C_{As}$ ) since the external mass transport resistance is negligible. Therefore, the effective diffusivity ( $D_{\text{eff}}$ ) can be estimated from Eq. 4.4.

$$D_{\text{eff}} = \frac{D_g \omega_p \sigma_c}{\tilde{\tau}} \quad 4.4$$

where

$D_g$  = diffusivity of  $\text{CH}_4$  into a mixture of  $\text{H}_2\text{O}$ ,  $\text{CO}_2$  and  $\text{N}_2$  ( $\text{m}^2 \text{s}^{-1}$ )

$\omega_p$  = catalyst pellet porosity

$\sigma_c$  = construction factor;  $\tilde{\tau}$  = tortuosity

The value for the left-hand side of Eq. 4.3 was about  $2.07 \times 10^{-3}$  extremely less than unity, suggesting that the internal mass transfer resistance can be neglected. Hence, the total flow rate of  $60 \text{ mL min}^{-1}$  for each CSCRM reaction run is sufficient to be employed in CSCRM.

### 4.3.3 External Heat Transfer Resistance

Fogler (2006) reported that the external heat transport resistance in a reactor may be insignificant if Mears criterion in Eq. 4.5 is fulfilled.

$$\frac{|(-\Delta H_r)|(-r_{\text{exp}})\rho_b R_p E_A}{hRT_b^2} < 0.15 \quad 4.5$$

Where  $-\Delta H_r$  = heat of reaction for CSCRM ( $\text{J mol}^{-1}$ )

$E_A$  = activation energy ( $\text{J mol}^{-1}$ )

$h$  = heat transfer coefficient between gas mixture and catalyst ( $\text{J m}^{-2} \text{ s}^{-1} \text{ K}^{-1}$ )

$R$  = ideal gas constant ( $\text{mol}^{-1} \text{ K}^{-1}$ )

$T_b$  = reactant gas bulk temperature (K)

The heat transfer coefficient ( $h$ ) may be achieved from the correlation between  $j$ -factor of heat and mass transfer given by Colburn-Chilton analogy (Green and Perry, 2008).

$$j_D = j_H = \frac{h \text{Pr}^{\frac{2}{3}}}{C_{pg} \rho_g U} \quad 4.6$$

where  $j_H$  =  $j$ -factor for heat transfer ( $j_H = j_D$ )

$C_{pg}$  = specific heat capacity of feed gas mixture at constant pressure ( $\text{J kg}^{-1} \text{ K}^{-1}$ )

$\text{Pr}$  = Prandtl number

$\rho_g$  = density of the gas mixture ( $\text{kg m}^{-3}$ );  $U$  = superficial gas velocity ( $\text{m s}^{-1}$ )

After substituting the suitable values in both equations, the left hand side of Eq. 4.5 obtained as  $3.01 \times 10^{-5} < 0.15$ . This indicates that the CSCRM reaction system was free from external heat transport resistance. Hence, the reaction temperature ranging of 973 K to 1073 K is sufficient to be employed in CSCRM.

#### 4.3.4 Internal Heat Transfer Resistance

The internal heat transfer resistance is considered to be negligible if the experimental conditions and reaction rate data for CSCRM reaction meets the Anderson criterion as provided in Eq. 4.7 (Anderson, 1963).

$$\frac{|(-\Delta H_r)|(-r_{\text{exp}})\rho_b R_p^2 E_A}{\lambda_p R T_s^2} < 0.75 \quad 4.7$$

where  $\lambda_p$  = thermal conductivity of catalyst pellet ( $\text{J m}^{-2} \text{s}^{-1} \text{K}^{-1}$ )

$T_s$  = reactant gas bulk temperature (K)

The gas phase bulk temperature ( $T_b$ ) is considered equivalent to the catalyst surface temperature ( $T_s$ ) since the external heat transfer is negligible from the previous calculation. The thermal conductivity of catalyst pellet ( $\lambda_p$ ) is determined from the thermal conductivity of the catalyst material ( $\lambda_m$ ) using the correlation provided in Eq. 4.8 (Wilhelm et al., 1948).

$$\log(\lambda_p \times 10^5) = 0.859 + 3.12 \left( \frac{\lambda_m}{\omega_p} \right) \quad 4.8$$

where  $\lambda_m$  = thermal of the catalyst material ( $\text{J m}^{-1} \text{s}^{-1} \text{K}^{-1}$ )

Therefore, the value for the left hand side of Eq. 4.7 is calculated as around  $1.51 \times 10^{-11} < 0.75$ , suggesting the negligibility of internal heat transfer resistance. Hence, the reaction temperature ranging of 973 K to 1073 K is sufficient to be employed in CSCRM.

### 4.3.5 Wall and Radial Heat Dispersion Effects

According to Dixon (1997), the wall heat transfer effects can be neglected if the ratio of reactor tube diameter ( $d_t$ ) to the catalyst particle diameter ( $d_p$ ) is greater than 4. For this CSCRM system, the  $d_t/d_p$  is about 40.5, satisfying the criteria for neglecting wall effects. However, a high ratio of  $d_t/d_p$  may contribute to radial heat transfer effects. Thus, Mears' criterion (Mears, 1971) as shown in Eq. 4.9 is applied to determine the insignificant effects of the radial heat transfer.

$$\left( \frac{E_A}{RT_w} \right) \left( \frac{(-\Delta H_r)(-r_{\text{exp}})\rho_b R_p^2 [(1-\varepsilon)/(1-b)]}{4\lambda_p T_w} \right) \left( \frac{1}{8} + \frac{B_p}{Bi_w R_t} \right) < 0.05 \quad 4.9$$

where

$T_w = T_b$  = tube wall temperature (K)

$\varepsilon$  = void fraction in the catalyst bed

$b$  = inert solids fraction of the catalyst bed

$R_t$  = radius of reactor tube (m)

Wall Biot number ( $Bi_w$ ) can be determined by Eq. 4.10.

$$Bi_w = \frac{h_w d_p}{\lambda_p} \quad 4.10$$

where

$h_w$  = heat transfer coefficient of reactor tube wall ( $\text{J m}^{-2} \text{ s}^{-2} \text{ K}^{-1}$ )

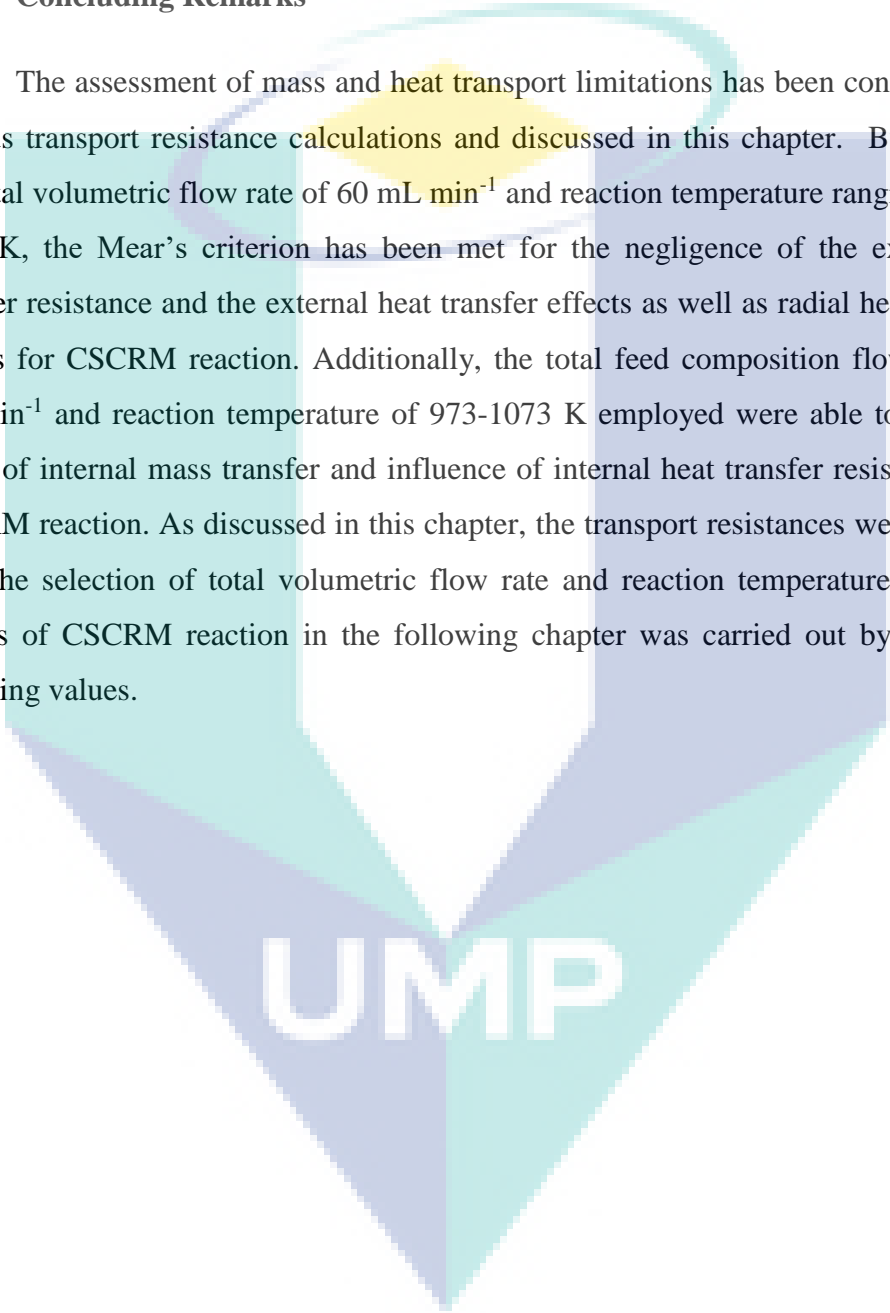
$d_p$  = diameter of catalyst particle (m)

$\lambda_p$  = thermal conductivity of catalyst pellet ( $\text{J m}^{-2} \text{ s}^{-1} \text{ K}^{-1}$ )

The left hand side of Eq. 4.9 is calculated to be  $2.05 \times 10^{-9}$ . Therefore, the reactor system is able to meet Mears' criterion for neglecting the radial heat dispersion effects. Hence, the reaction temperature ranging of 973 K to 1073 K is sufficient to be employed in CSCRM.

#### 4.4 Concluding Remarks

The assessment of mass and heat transport limitations has been conducted using various transport resistance calculations and discussed in this chapter. By employing the total volumetric flow rate of  $60 \text{ mL min}^{-1}$  and reaction temperature ranging of 973 to 1073 K, the Mear's criterion has been met for the negligence of the external mass transfer resistance and the external heat transfer effects as well as radial heat dispersion effects for CSCRM reaction. Additionally, the total feed composition flow rate of  $60 \text{ mL min}^{-1}$  and reaction temperature of 973-1073 K employed were able to neglect the effect of internal mass transfer and influence of internal heat transfer resistance during CSCRM reaction. As discussed in this chapter, the transport resistances were negligible with the selection of total volumetric flow rate and reaction temperature. Hence, the studies of CSCRM reaction in the following chapter was carried out by using these operating values.



UMP

## CHAPTER 5

### CATALYST CHARACTERIZATION

#### 5.1 Introduction

Catalyst characterization is crucial in the study of heterogeneous catalytic reaction since the physicochemical characteristics of catalyst control the catalytic activity, selectivity and stability. In this chapter, catalyst characterization is divided into several sections in view of investigating textural properties, transient weight responses under temperature-programmed methods, acid character, morphology and carbon deposition. The physicochemical properties of unpromoted and B-promoted 10%Ni/SBA-15 catalysts were investigated in this chapter for comparison purposes. In addition, B-promoted catalysts with different B loadings of 1-5wt% were examined since it exhibited the greater catalytic performance in terms of CH<sub>4</sub> conversions and the H<sub>2</sub>/CO ratio approximate of 2 at stoichiometric feed composition for all employed reaction temperatures (see Chapter 6). In addition, B-promoted catalysts resulted in the greatest H<sub>2</sub> yield regardless of operation conditions as seen in Chapter 6.

#### 5.2 Nitrogen Adsorption Studies

Table 5.1 summarizes the textural properties of SBA-15 support, unpromoted and boron-promoted Ni-based catalysts with different B loadings. SBA-15 support possessed a high BET surface area of 780.1 m<sup>2</sup> g<sup>-1</sup> comparable with other studies (Yang et al., 2003; Song et al., 2005). However, a noticeable and inevitable decrease in textural properties including BET surface area, total pore volume and average pore diameter with the addition of NiO during impregnation would suggest the successful embedment of nano-sized NiO particles into the mesoporous structure of SBA-15 support.

As seen in Table 5.1, the BET surface area of 10%Ni/SBA-15 catalyst (493.7 m<sup>2</sup> g<sup>-1</sup>) dropped significantly with increasing boron loading to 5.4 m<sup>2</sup> g<sup>-1</sup> (5%B loading). This observation could be due to the agglomeration of B<sub>2</sub>O<sub>3</sub> particles plugging the mesoporous structure of SBA-15 support at high B loading. Eswaramoorthi and Dalai (2006) also observed the reduction in BET surface area with B-addition and attributed it to the deboration reaction during calcination (cf. Eq. 5.1) and hence blockage of mesopores.



In addition, the considerably low BET surface area of 5%B-10%Ni/SBA-15 catalyst (5.4 m<sup>2</sup> g<sup>-1</sup>) was most likely owing to the collapse of thin pore walls of SBA-15 support in extremely acidic environment with high boric acid concentration (Fouskas et al., 2014). In fact, the total pore volume and average pore diameter also experienced a pronounced decline with rising B loading (cf. Table 5.1) further confirming the loss in BET surface area.

Table 5.1 Textural properties of SBA-15 support, unpromoted and B-promoted 10%Ni/SBA-15 catalysts

Sample	Average BET surface area (m <sup>2</sup> g <sup>-1</sup> )	Total pore volume, $V_p$ (cm <sup>3</sup> g <sup>-1</sup> ) <sup>a</sup>	Average pore diameter, $D_p$ (nm) <sup>b</sup>	Average crystallite size of NiO, $d(NiO)^c$ (nm)	Average crystallite size of Ni <sup>0</sup> , $d(Ni^0)^d$ (nm)
SBA-15 support	780.1	1.35	6.94	-	-
10%Ni/SBA-15	493.7	0.97	6.69	15.6	13.1
1%B-10%Ni/SBA-15	408.1	0.68	6.68	20.4	17.1
3%B-10%Ni/SBA-15	213.2	0.35	6.52	20.5	17.2
5%B-10%Ni/SBA-15	5.4	0.01	5.84	21.4	18.0

<sup>a</sup>Total pore volume was obtained at  $p/p^0 = 0.99$ .

<sup>b</sup>Average pore diameter was calculated using Barret-Joyner-Halenda (BJH) desorption method.

<sup>c</sup>Average NiO crystal size was estimated using Scherrer equation for the most intense NiO peak at  $2\theta$  of 43.54°.

<sup>d</sup>Average crystallite size of Ni<sup>0</sup> was estimated from Eq. 3.7.

### 5.3 Fourier Transform Infrared Spectroscopy (FTIR) Analyses

The FTIR spectra of bare SBA-15 support, unpromoted and B-promoted 10%Ni/SBA-15 catalysts are shown in Figure 5.1. As seen in the spectrum of SBA-15 support (cf. Figure 5.1 (a)), the significant and broad absorption band ranging from 1000 to 1300  $\text{cm}^{-1}$  with a shoulder at about 1225  $\text{cm}^{-1}$  was assigned to the asymmetric stretching (AS) modes of Si-O-Si vibrational moiety (Azizi et al., 2013). In fact, the AS motion of Si-O-Si bond was composed of two main vibrational modes, namely, AS<sub>1</sub> and AS<sub>2</sub> modes. In the first AS<sub>1</sub> mode, two adjacent oxygen atoms reportedly perform the AS motion in phase with the central silicon atom while the out-of-phase motion of two adjacent oxygen atoms with the central silicon atom is reported for AS<sub>2</sub> mode (Azizi et al., 2013). Particularly, the absorbance bands at 1059 and 1225  $\text{cm}^{-1}$  were due to the corresponding transverse-optic (TO) and longitudinal-optic (LO) vibrational modes of AS<sub>1</sub> stretching of Si-O-Si bond (Azizi et al., 2013; Wang et al., 1999). In addition, the detected bands at around 450  $\text{cm}^{-1}$  and 814  $\text{cm}^{-1}$  could be ascribed to the asymmetric and symmetric stretching vibrations of Si-O bond in this order (Pudukudy et al., 2015). Additionally, the small peak detected at 965  $\text{cm}^{-1}$  for the bare SBA-15 support was probably due to the vibration of Si-OH group (Rath and Parida, 2011). The appearance of these typical bonds, *viz.*, Si-O-Si, Si-O and Si-OH could be indicative of the presence of mesoporous SBA-15 support in agreement with other studies (Pudukudy et al., 2015). These aforementioned characteristic bands were also observed for both unpromoted and B-promoted Ni/SBA-15 catalysts regardless of B loadings (see Figure 5.1 (b)-(e)).

As seen in Figure 5.1 (c)-(e), for B-promoted catalysts, the main band detected in the high wavenumber of 1280-1530  $\text{cm}^{-1}$  was possibly due to the asymmetric stretching relaxation of B-O bonds from the trigonal borate anions ( $\text{BO}_3^{3-}$ ) in various borate groups (Rada et al., 2008; Chen et al., 2017). A low intensity peak located at around 670  $\text{cm}^{-1}$  was also attributed to B-O-B bending vibrations (Chen et al., 2017; Neumair et al., 2012). The detection of above-mentioned B-O and B-O-B vibrations could suggest the formation of vitreous  $\text{B}_2\text{O}_3$  phase on the surface of B-promoted catalysts. Rada et al. (2008) also reported that the glassy  $\text{B}_2\text{O}_3$  form is normally present in the boroxol rings,  $\text{B}_3\text{O}_6$  interconnected by individual  $[\text{BO}_3]$  groups. Moreover, the intensity of both B-O and B-O-B bands gradually strengthens with an increase in B content (see Figure 5.1 (c)-(e)) rationally owing to the rising amount of  $\text{B}_2\text{O}_3$  formation.

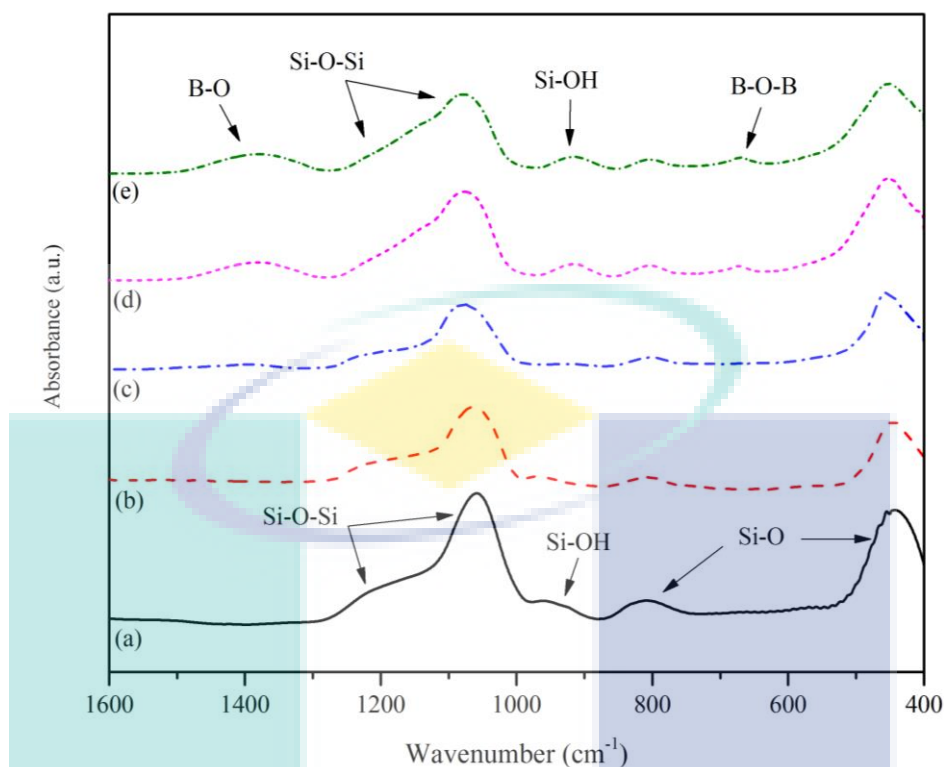


Figure 5.1 FTIR spectra of (a) SBA-15 support, (b) 10%Ni/SBA-15, (c) 1%B-10%Ni/SBA-15, (d) 3%B-10%Ni/SBA-15 and (e) 5%B-10%Ni/SBA-15 catalysts.

#### 5.4 X-ray Diffraction (XRD) Measurements

Figure 5.2 shows the X-ray diffractograms of SBA-15 support and fresh X%B-10%Ni/SBA-15 catalysts. All XRD patterns were interpreted based on the Joint Committee on Power Diffraction Standards (JCPDS) database (2000) and the XRD pattern of SBA-15 support was used for comparison and facilitation of XRD analysis. A similar broad diffraction peak was clearly observed for all samples at  $2\theta$  of around  $22.16^\circ$  assigned to the presence of amorphous  $\text{SiO}_2$  framework of SBA-15 support (JCPDS card No. 29-0085) (Landau et al., 2005). In addition, the five sharp peaks with high intensity identified at  $2\theta$  of  $37.46^\circ$ ,  $43.54^\circ$ ,  $63.03^\circ$ ,  $75.14^\circ$  and  $79.52^\circ$  were attributed to the corresponding (1 1 1), (2 0 0), (2 2 0), (3 1 1) and (2 2 2) crystal planes of NiO phase (JCPDS card No. 47-1049) for X%B-10%Ni/SBA-15 catalysts (see Figure 5.2 (b)-(e)) (Mironova-Ulmane et al., 2011). Additionally, there are no typical peaks corresponding to any boron oxide phases detected. This could be due to the fine dispersion of boron oxide particles with a considerably small crystallite size below the detection limit of XRD measurement. In fact, Fouskas et al. (2014) also observed the

same behavior for boron-modified Ni/Al<sub>2</sub>O<sub>3</sub> catalysts during XRD measurements and suggested the formation of amorphous glassy boron oxide phases since boron oxides were reportedly difficult to be crystallized. Moreover, as seen in Figs. 5.2(c)-(e), the intensity of peaks located at  $2\theta$  of 37.46°, 43.54° and 63.03° was substantially increased with B-addition compared to that of unpromoted 10%Ni/SBA-15 catalyst. This observation could imply that the aggregation of NiO particles on the mesoporous SBA-15 framework due to the lessening amount of SBA-15 support employed during impregnation at high boron promotion.

The average crystallite size of NiO particles and metallic Ni<sup>0</sup> particles for all catalysts was estimated using Scherrer equation and summarized in Table 5.1. The NiO crystallite size somewhat increased from 15.6 to 21.4 nm with rising B-loadings from 0 to 5%, respectively and the same trend was evidenced for the average crystallite size of metallic Ni<sup>0</sup> phase. The increasing crystallite size with B-addition could be due to the reducing composition of SBA-15 support at high boron loading and hence growing metal agglomeration on support surface.

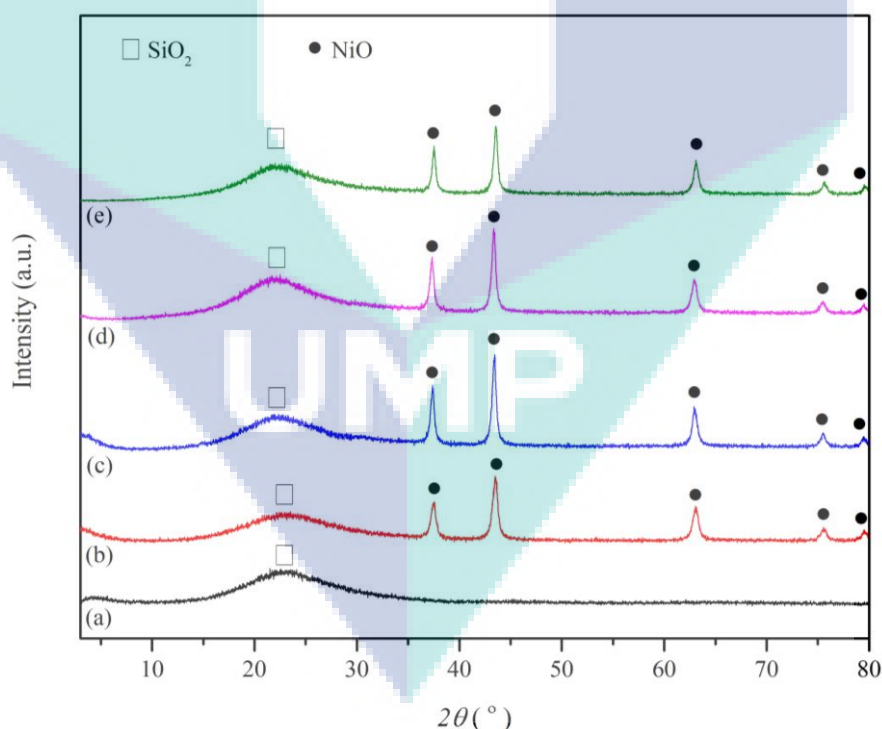


Figure 5.2 XRD patterns of (a) SBA-15 support, (b) 10%Ni/SBA-15, (c) 1%B-10%Ni/SBA-15, (d) 3%B-10%Ni/SBA-15 and (e) 5%B-10%Ni/SBA-15 catalysts.

## 5.5 H<sub>2</sub> Temperature-programmed Reduction (H<sub>2</sub>-TPR) Analyses

H<sub>2</sub>-TPR measurements of X%B-10%Ni/SBA-15 catalysts carried out to investigate the reducibility of active metal oxide are shown in Figure 5.3. The reduction of NiO phase to metallic Ni<sup>0</sup> phase was widely reported as a direct process without intermediate phase formation (Oemar et al., 2016). In addition, boric oxide was allegedly stable and resistant to H<sub>2</sub> reduction (Zheng et al., 2012). Thus, the two noteworthy peaks (T1 and T2) observed for all catalysts were ascribed to NiO reduction to metallic Ni<sup>0</sup> phase depending on the strength of metal-support interaction associated with the crystallite size and location of NiO particles on mesoporous SBA-15 support (Li et al., 2015). In fact, the low temperature peak T1 could belong to the reduction of large or surface NiO particles having a weak interaction with support whilst the second reduction peak (T2) located at high temperature was due to the reducibility of NiO nanoparticles (located inside the mesoporous channels of SBA-15 support) possessing a strong metal-support interaction (Oemar et al., 2016; Kim et al., 2015).

Notably, both peaks T1 and T2 were shifted towards higher temperature region with B-addition and the reduction temperature increased linearly with rising B loading (see Figure 5.4) most likely due to the strengthening interaction between the basic NiO and acidic B<sub>2</sub>O<sub>3</sub> phases (Chen et al., 2017; Zhu et al., 2013). In fact, Xu and Saeys (2006) also found that boron promoter favorably adsorbs in the octahedral sites of the first subsurface layer of the Ni (1 1 1) by using ab initio density functional theory calculations further confirming the strong interaction between B<sub>2</sub>O<sub>3</sub> and NiO phases. As seen in Figure 5.3, there are no detected H<sub>2</sub> consumption peaks for both promoted and unpromoted catalysts at beyond 1070 K indicating that all NiO particles were completely reduced in H<sub>2</sub> pretreatment. Thus, high reduction temperature of 1073 K and long holding time of 2 h were implemented in this study for activating all catalysts during H<sub>2</sub> reduction.

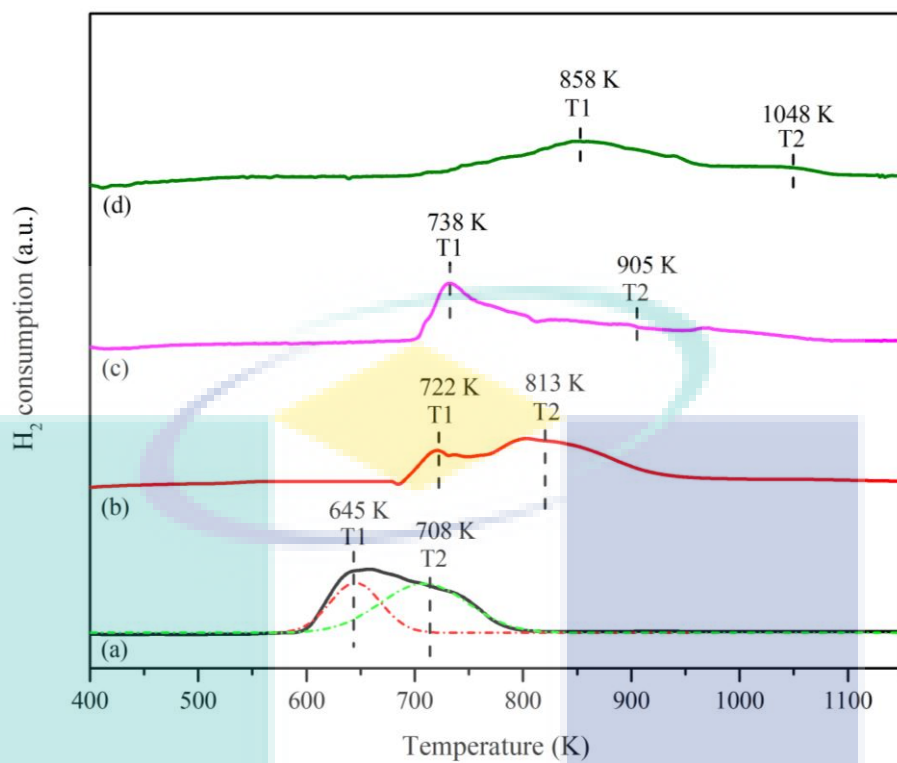


Figure 5.3 H<sub>2</sub>-TPR profiles of (a) 10%Ni/SBA-15, (b) 1%B-10%Ni/SBA-15, (c) 3%B-10%Ni/SBA-15 and (d) 5%B-10%Ni/SBA-15 catalysts.

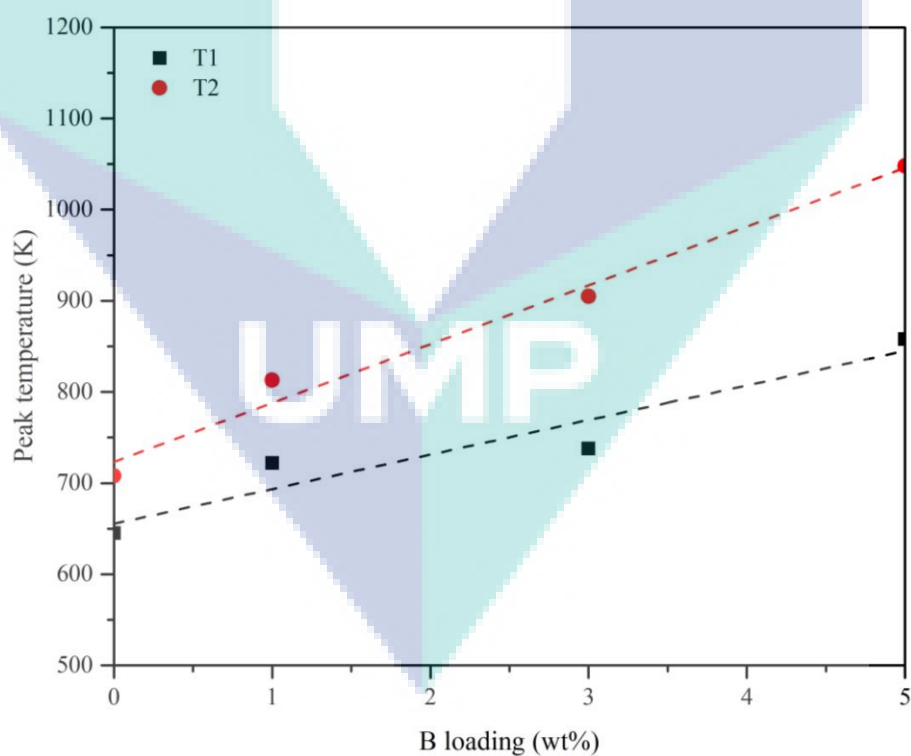
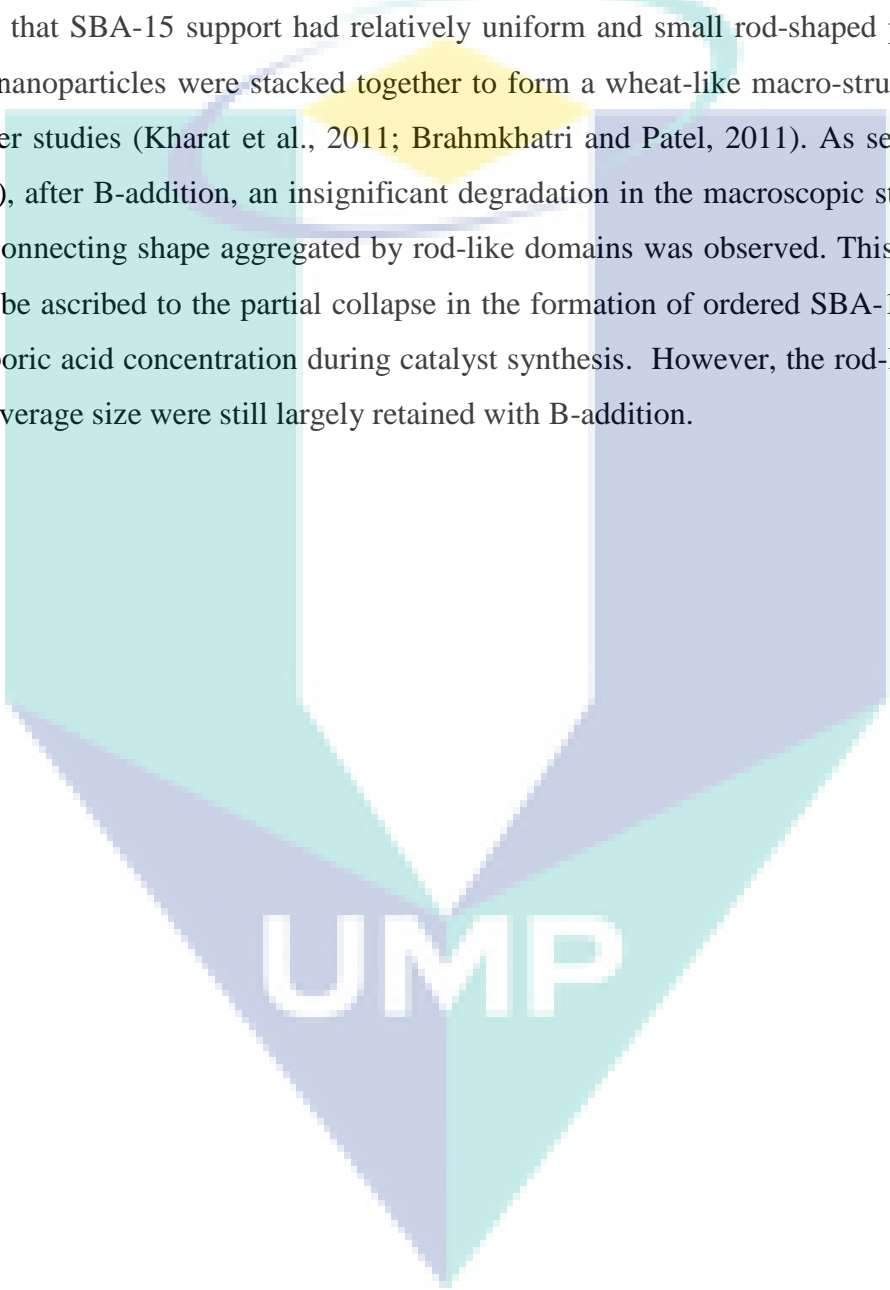


Figure 5.4 Effect of B loading on reduction temperature during H<sub>2</sub>-TPR for X%B-10%Ni/SBA-15 catalysts.

## 5.6 Scanning Electron Microscopy (SEM) Measurements

In order to investigate the morphology of catalysts, SEM measurements were also conducted for unpromoted catalyst and representative B-promoted catalyst. The SEM micrographs of fresh 10%Ni/SBA-15 and selected 3%B-10%Ni/SBA-15 catalysts are shown in Figure 5.5. The SEM image of unpromoted catalyst (see Figure 5.5 (a)) shows that SBA-15 support had relatively uniform and small rod-shaped particles and these nanoparticles were stacked together to form a wheat-like macro-structure similar to other studies (Kharat et al., 2011; Brahmkhatri and Patel, 2011). As seen in Figure 5.5 (b), after B-addition, an insignificant degradation in the macroscopic structure with long-connecting shape aggregated by rod-like domains was observed. This observation could be ascribed to the partial collapse in the formation of ordered SBA-15 support at high boric acid concentration during catalyst synthesis. However, the rod-like domains with average size were still largely retained with B-addition.

The logo of UMPA (Universitas Mitra Bina Nusantara) is a large, stylized shield shape. It is divided into four quadrants by a white 'V' shape pointing downwards. The top-left and bottom-right quadrants are light blue, while the top-right and bottom-left quadrants are light purple. The letters 'UMPA' are written in white, bold, sans-serif font across the center of the shield.

UMPA

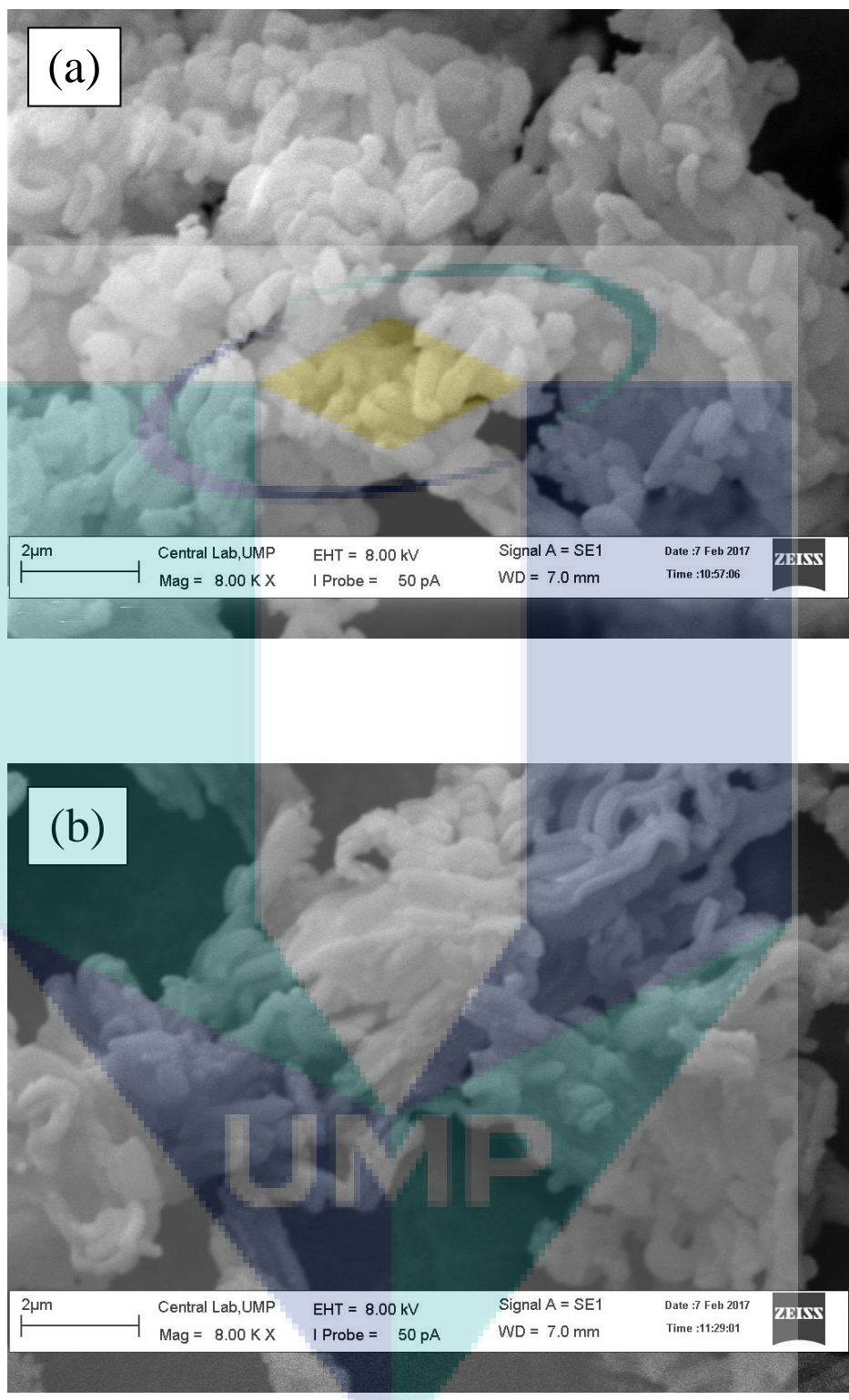


Figure 5.5 SEM images of fresh (a) 10%Ni/SBA-15 and (b) 3%B-10%Ni/SBA-15 catalysts.

## 5.7 Raman Spectroscopy Measurements

Raman spectroscopy measurements were conducted to investigate the type and structure of carbonaceous species present on the catalyst surface. Raman spectra of fresh SBA-15 support, unpromoted 10%Ni/SBA-15 and B-promoted 10%Ni/SBA-15 catalysts were performed. As seen in Figure 5.6, for fresh SBA-15 support and all SBA-15 supported catalysts exhibited two peaks at Raman shift of about  $487.3\text{ cm}^{-1}$  (P1) and  $1068.7\text{ cm}^{-1}$  (P2) were attributed to the corresponding cyclic tetrasiloxane rings and Si-OH stretching mode, typical for SBA-15 support (Lin et al., 2014; Thielemann et al., 2011) in agreement with FTIR results (cf. Figure 5.1).

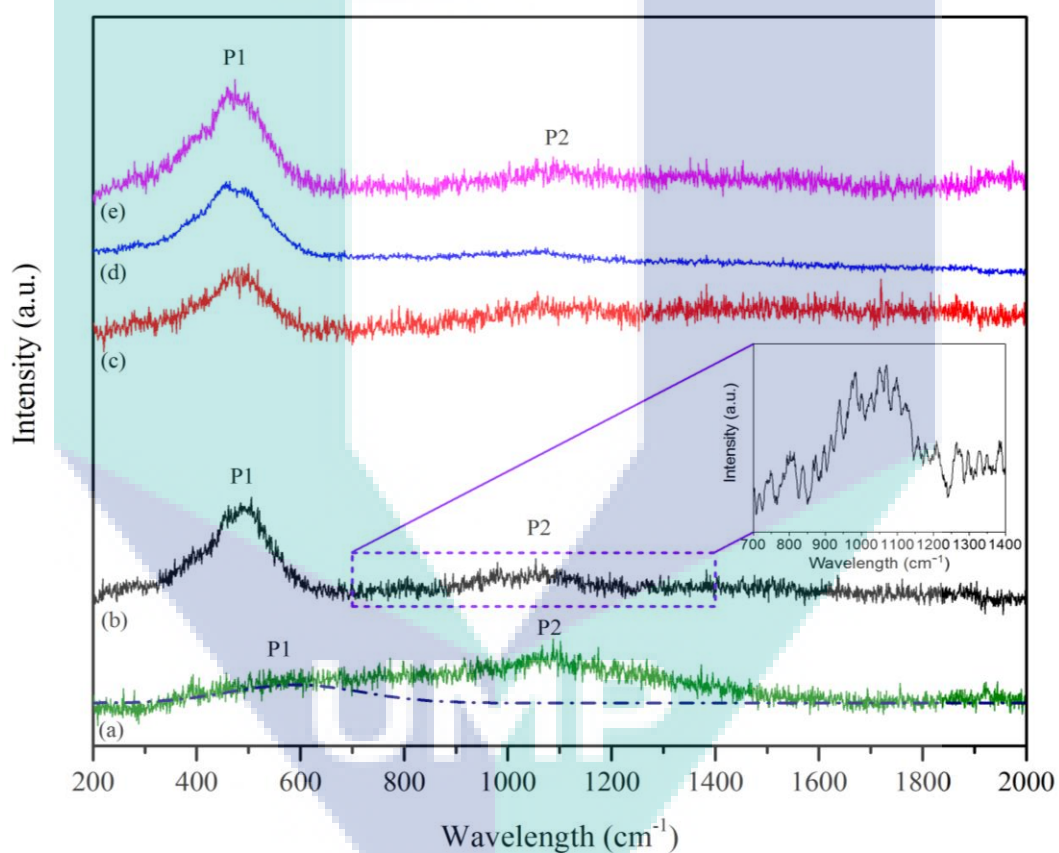


Figure 5.6 Raman spectra of fresh (a) SBA-15 support, (b) 10%Ni/SBA-15, (c) 1%B-10%Ni/SBA-15, (d) 3%B-10%Ni/SBA-15 and (e) 5%B-10%Ni/SBA-15 catalysts.

As seen in Figure 5.6, the intensity of peak P1 for promoted and unpromoted 10%Ni/SBA-15 catalysts was considerably greater than that of original SBA-15 support (see Figure 5.6 (a)). This could be ascribed to the presence of NiO phase exhibiting Ni-O bond oscillation at the similar Raman band (de Sousa et al., 2012; Bahari et al.,

2016). However, boric oxide phase was also not identified for all B-promoted 10%Ni/SBA-15 catalysts probably owing to the vitreous feature of  $B_2O_3$  form (Brik et al., 2002) consistent with the observation from XRD measurements (see Figure 5.2).

## 5.8 Concluding Remarks

The beneficial effect of B promoter on the physicochemical properties of 10%Ni/SBA-15 catalysts has been investigated extensively with various characterization techniques and discussed in this chapter. An unavoidable decrease in BET surface area and average NiO crystallite size with boron promotion from 1% to 5%B loading could be due to the agglomeration of  $B_2O_3$  particles and deboration reaction during calcination and hence blocking mesopores of SBA-15 support at elevated B composition. The FTIR analyses evidenced the presence of mesoporous SBA-15 support and indicative of B-O and B-O-B vibrations elucidated that the formation of vitreous  $B_2O_3$  phase on the surface of B-promoted catalysts.  $H_2$ -TPR profiles revealed that the interaction between basic NiO and acidic  $B_2O_3$  phases was strengthened with increasing boron loading, resulting in a linear shift of reduction temperatures to higher temperature regions. The XRD analysis evidenced the presence of  $SiO_2$  and NiO phases for all unpromoted and promoted catalysts. The increasing crystallite size with B-addition could be due to the reducing composition of SBA-15 support at high boron loading and hence growing metal agglomeration on support surface. The SEM micrographs displayed that both promoted and unpromoted catalysts possessed relatively uniform particles with small rope-like shape. However, long-connecting shape aggregated by rod-like domains was observed for B-promoted catalyst indicating partial failure in SBA-15 formation with B-addition. Boric oxide phase was not identified in Raman spectra for all B-promoted 10%Ni/SBA-15 catalysts probably owing to the vitreous feature of  $B_2O_3$  form consistent with the observation from XRD measurements. As discussed in this chapter, the physicochemical properties of 10%Ni/SBA-15 catalysts was slightly influenced with the addition of  $B_2O_3$  promoter. Hence, a detailed discussion for studies about the effect of promoter loadings on combined steam and  $CO_2$  reforming of methane reaction was presented in the next chapter.

## CHAPTER 6

### COMBINED STEAM AND CO<sub>2</sub> REFORMING OF METHANE REACTION STUDY

#### 6.1 Introduction

This chapter studies the influence of boron promoter on 10%Ni/SBA-15 catalysts for CSCRM reaction. The effect of boron loading, reaction temperature and feed composition of reactants was also assessed in terms of catalytic activity, product yield and ratio of H<sub>2</sub> to CO of CSCRM reaction for unpromoted and promoted catalysts. Reaction runs were conducted at temperature ranging from 973-1073 K and atmospheric pressure. The gas hourly space velocity (GHSV) of 36 L g<sub>cat</sub><sup>-1</sup> h<sup>-1</sup> and small average particle size ranging of 100-140 μm were employed for all runs to neglect the presence of internal and external transport resistances for obtaining the intrinsic catalytic activity. In addition, the best B-promoted catalyst has been further studied for longevity test to investigate the catalytic stability and degree of catalyst deactivation with various reaction temperature. At the end of this chapter, the post-characterization for representative spent catalysts was also performed to examine the crystalline structure, morphology and carbon content as well as carbonaceous types on catalyst surface after CSCRM reaction.

#### 6.2 Transient Profiles

The blank test was carried out for CSCRM reaction without the presence of catalyst with time-on-stream in order to assess the catalytic performance of catalyst. The transient conversion profiles for CH<sub>4</sub> and CO<sub>2</sub> conversions at reaction temperature of 1073 K and stoichiometric feedstock composition ( $F_{CH_4} : F_{H_2O} : F_{CO_2} = 3:2:1$ ) with or without the presence of catalyst are displayed in Figure 6.1 and Figure 6.2,

correspondingly. As seen in Figure 6.1, the CH<sub>4</sub> and CO<sub>2</sub> conversions had relatively low values of 8.09% and 13.27%, respectively in the absence of catalyst during CSCRM reaction probably due to the CH<sub>4</sub> decomposition (cf. Eq. 2.6). However, as seen in Figure 6.2, the CH<sub>4</sub> and CO<sub>2</sub> conversions were significantly improved up to 75.79% and 64.98%, correspondingly with the presence of 10%Ni/SBA-15 catalyst during CSCRM reaction. This observation corroborates that the crucial role of Ni-based catalyst during CSCRM reaction to obtain high reactant conversions.

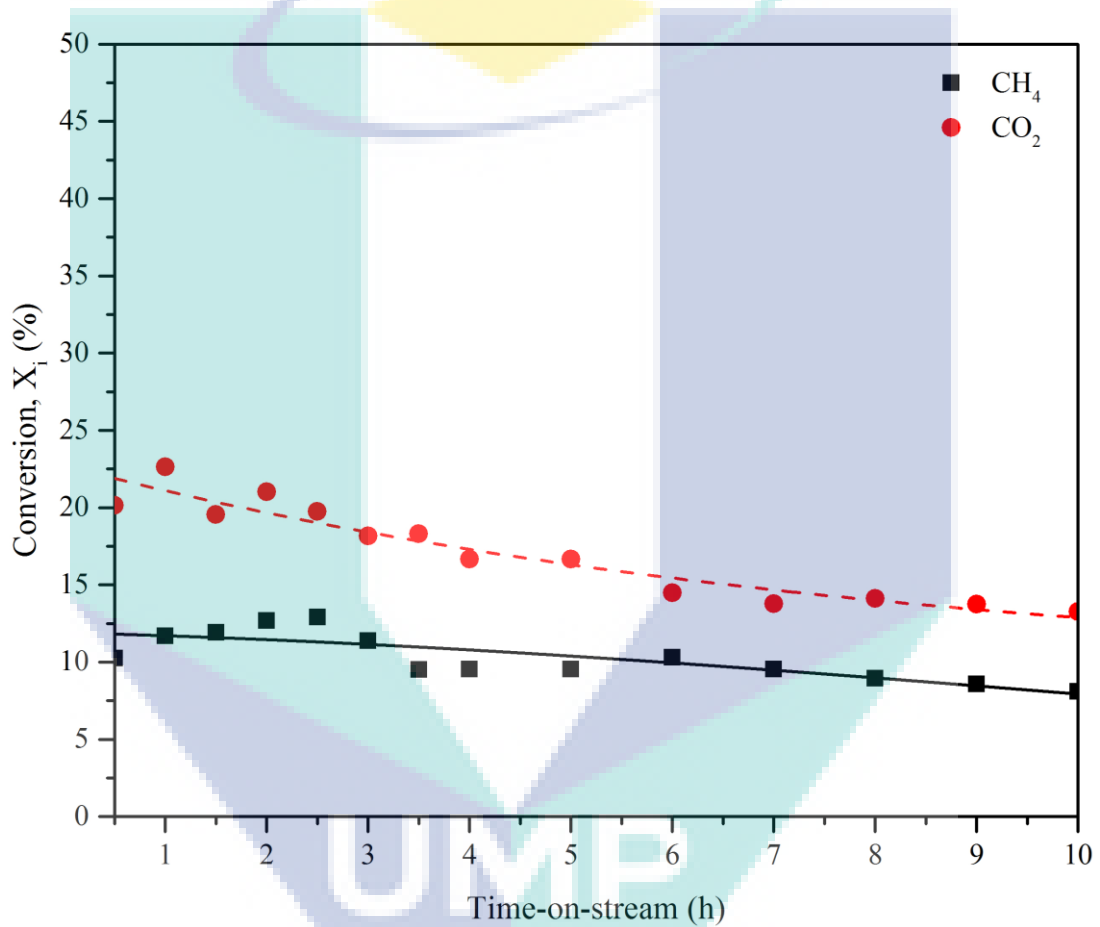


Figure 6.1 The CH<sub>4</sub> and CO<sub>2</sub> conversions for CSCRM reaction without catalyst at reaction temperature of 1073 K and stoichiometric feed composition ( $F_{CH_4} : F_{H_2O} : F_{CO_2} = 3 : 2 : 1$ ).

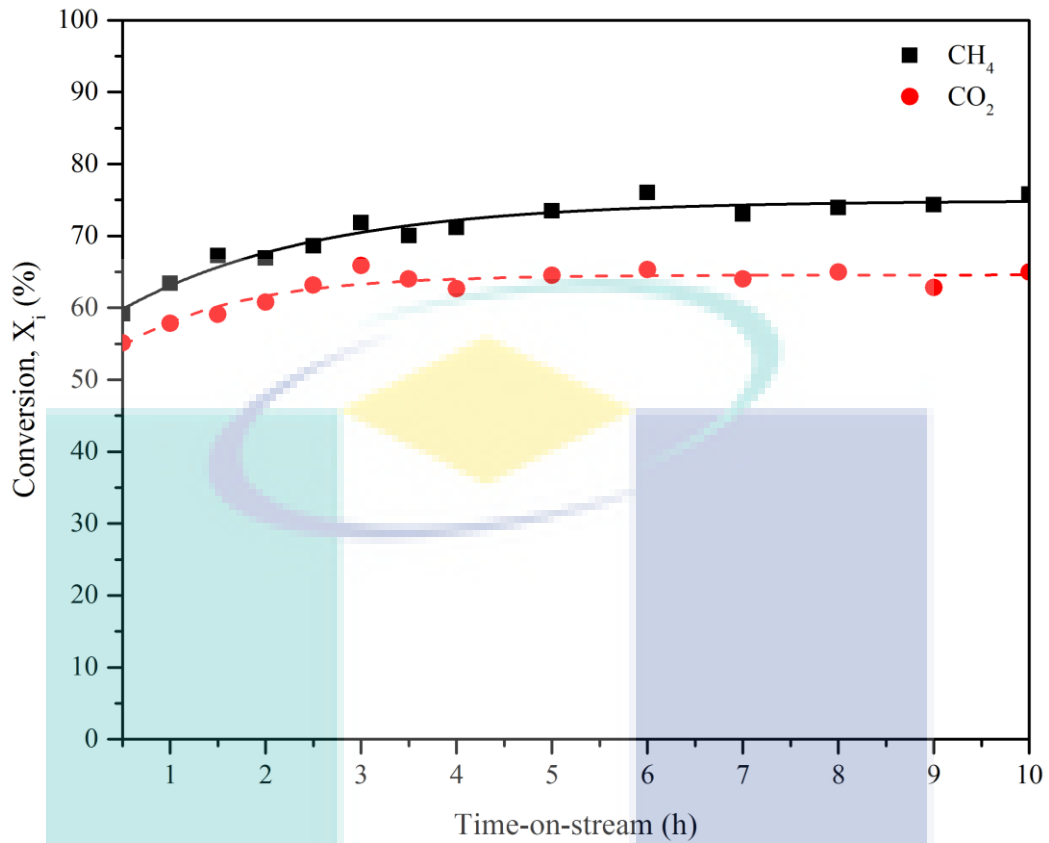


Figure 6.2 The CH<sub>4</sub> and CO<sub>2</sub> conversions for CSCRM reaction with 10%Ni/SBA-15 catalyst at reaction temperature of 1073 K and stoichiometric feed composition ( $F_{CH_4} : F_{H_2O} : F_{CO_2} = 3 : 2 : 1$ ).

### 6.3 Effect of Boron Loading with Various Reaction Temperature

The influence of reaction temperature on catalytic performance for CSCRM was investigated at stoichiometric feedstock composition ( $F_{CH_4} : F_{H_2O} : F_{CO_2} = 3 : 2 : 1$ ) and varying temperature from 973 K to 1073 K for 10 h on-stream. As seen in Figure 6.3, regardless of boron loading, both CH<sub>4</sub> and CO<sub>2</sub> conversions improved with an increase in reaction temperature from 973 K to 1073 K due to the endothermic nature of CSCRM (Özkara-Aydınoğlu, 2010). In addition, 3%B loading appeared to be the best promoter content in terms of reactant conversions irrespective of reaction temperature. For 3%B-10%Ni/SBA-15 catalyst, CH<sub>4</sub> and CO<sub>2</sub> conversions were enhanced significantly about 23.2% and 32.4%, correspondingly with the increment of reaction temperature from 973 to 1073 K. The enhancement of both CH<sub>4</sub> and CO<sub>2</sub> conversions with rising B loading from 1 to 3% was probably owing to the suppression of deposited carbon on catalyst surface in agreement with other studies (Fouskas et al., 2014). In the density functional

theory study of carbon chemisorption on boron-promoted Ni (1 1 1) surface, Xu and Saeys (2007) reported that boron atoms could occupy the octahedral sites of the first subsurface layer of active Ni atoms and hence hinder the diffusion of adsorbed surface carbon ( $C_xH_{1-x}$  with  $x \leq 1$  formed from dissociative  $CH_4$  adsorption (Omeregbe et al., 2017; Foo et al., 2010) into Ni lattice. As a result, it not only prevents the formation of bulk carbon and graphene islands but also retains the on-surface carbon for subsequent gasification by  $CO_2$  and  $H_2O$  oxidizing agents. In addition, Chen et al. (2004) also found that electron density on the surface of active Ni metal was increased due to electron donation from boron dopant. Therefore, the enhancement of electron density on catalyst surface could facilitate  $CO_2$  adsorption and hence increasing catalytic activity.

However, at greater B loading beyond 3%, a substantial drop in reactant conversions was observed for all reaction temperature employed as seen in Figure 6.3. This could be due to the tremendous decline in BET surface area at high B loading (see Table 5.1). Additionally, the excess loading of B dopant could agglomerate on catalyst surface and isolate the active Ni metal from the access of gaseous reactants, resulting in the reduction in catalytic activity. In fact, the degree of interaction between NiO particle and  $B_2O_3$  dopant was highest at 5%B loading as observed from  $H_2$ -TPR measurements (cf. Figure 5.3). The drop in reactant conversions at surplus B loading could be also ascribed to the difference of electronic environment possessed by Ni species depending on the amount of boron loading (Fouskas et al., 2014). Xu and Saeys (2007) revealed that the activation energy for  $CH_4$  dissociation over the B-promoted Ni (111) surface was slightly raised by  $12 \text{ kJ mol}^{-1}$  compared to that of unpromoted Ni (111) surface. They also found that the centre of the 3d states of the Ni (111) surface for B-promoted catalysts was reduced by 0.26 eV and hence weakening the interaction of the antibonding C-H orbital of  $CH_4$  molecule with the Ni 3d electrons. This behaviour could result in a greater activation barrier for C-H bond cleavage.

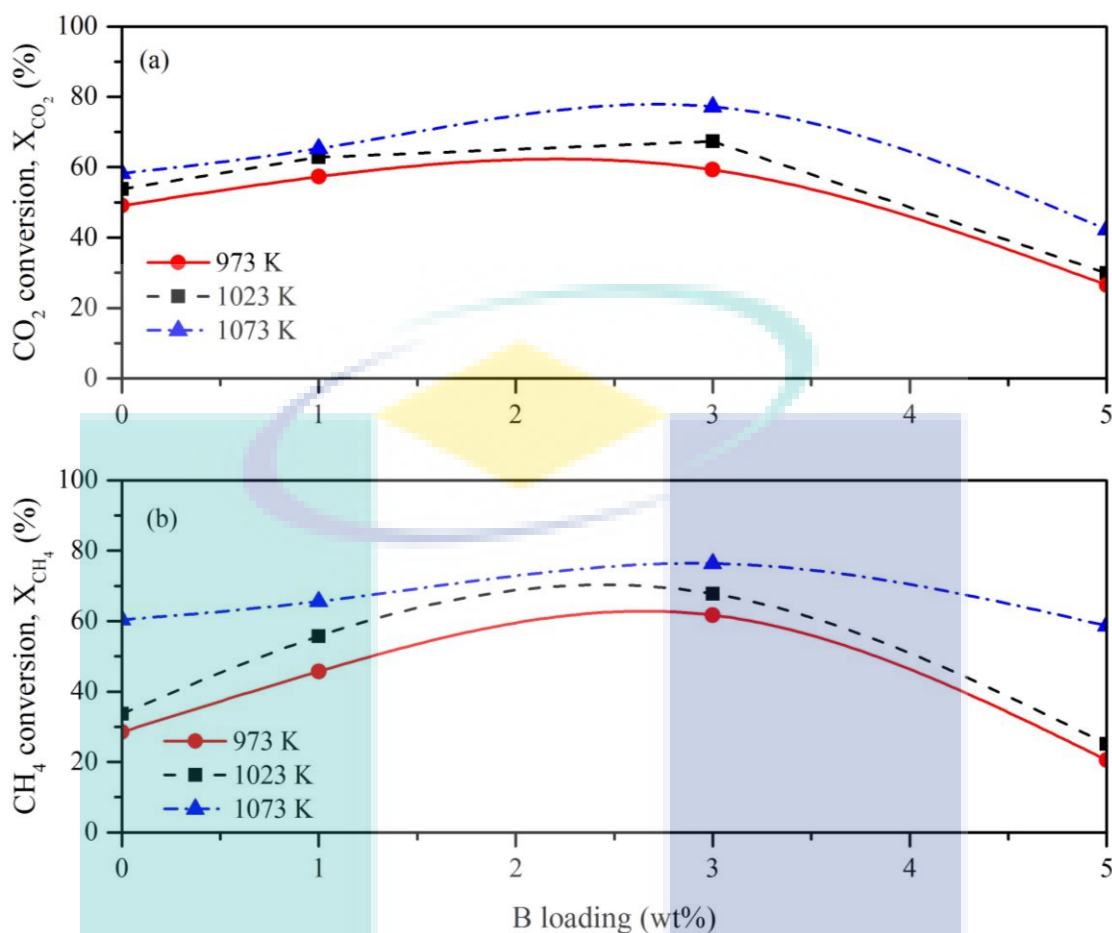


Figure 6.3 Effect of reaction temperature and B loading on (a) CO<sub>2</sub> conversion and (b) CH<sub>4</sub> conversion of unpromoted and promoted 10%Ni/SBA-15 catalysts at stoichiometric feed composition ( $F_{CH_4} : F_{H_2O} : F_{CO_2} = 3 : 2 : 1$ ).

The effect of reaction temperature and boron loading on H<sub>2</sub> and CO yields for X%B-10%Ni/SBA-15 catalysts is shown in Figure 6.4. The yield of H<sub>2</sub> and CO products improved with rising reaction temperature from 973 to 1073 K for all boron loadings. The enhancement in product yields with temperature could be attributed to the endothermic nature of CSCRW leading to growing H<sub>2</sub> and CO formation rates. Additionally, the best product yields were obtained at boron loading of about 1-3%B. In addition, the highest CO and H<sub>2</sub> yields were around 57.8% and 69.4% at 1073 K, respectively comparable with other studies using noble catalysts (Soria et al., 2011).

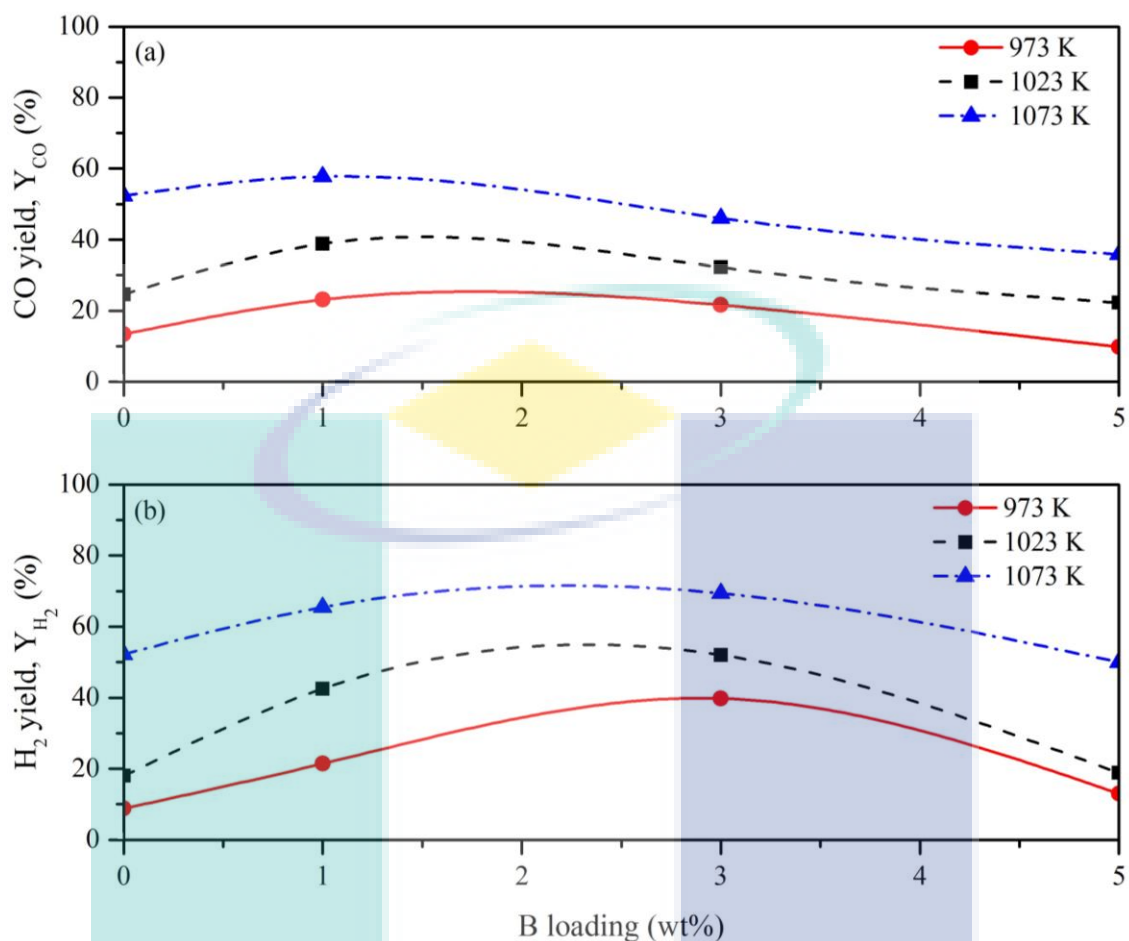


Figure 6.4 Effect of reaction temperature and B loading on (a) CO yield and (b) H<sub>2</sub> yield of unpromoted and promoted 10%Ni/SBA-15 catalysts at stoichiometric feed composition ( $F_{CH_4} : F_{H_2O} : F_{CO_2} = 3:2:1$ ).

Figure 6.5 shows the influence of reaction temperature and B loading on ratio of H<sub>2</sub> to CO for both promoted and unpromoted catalysts. H<sub>2</sub>/CO ratio varied within 1.26 to 2.71 for all catalysts. Irrespective of catalysts used, the increment of H<sub>2</sub>/CO ratio with rising reaction temperature from 973 to 1073 K was observed. This observation could be due to the enhancement of endothermic methane steam reforming reaction reportedly favored for generating H<sub>2</sub>-rich syngas ( $H_2/CO \geq 3$ ) (Özkara-Aydinoğlu, 2010). In addition, H<sub>2</sub>/CO ratio was increased with the addition of B promoter regardless of reaction temperature.

As seen in Figure 6.5, the ratio of H<sub>2</sub> to CO could be easily manipulated within the range of 1.26 to 2.71 by changing reaction temperature and B content. Remarkably, the ideal H<sub>2</sub>/CO ratio of about 2 could be achieved over 3%B-10%Ni/SBA-15 catalyst at 973 K. This desirable H<sub>2</sub>/CO ratio was appropriate for downstream Fischer-Tropsch synthesis to generate long-chain hydrocarbons without the requirement of modification of feed composition (Jang et al., 2016).

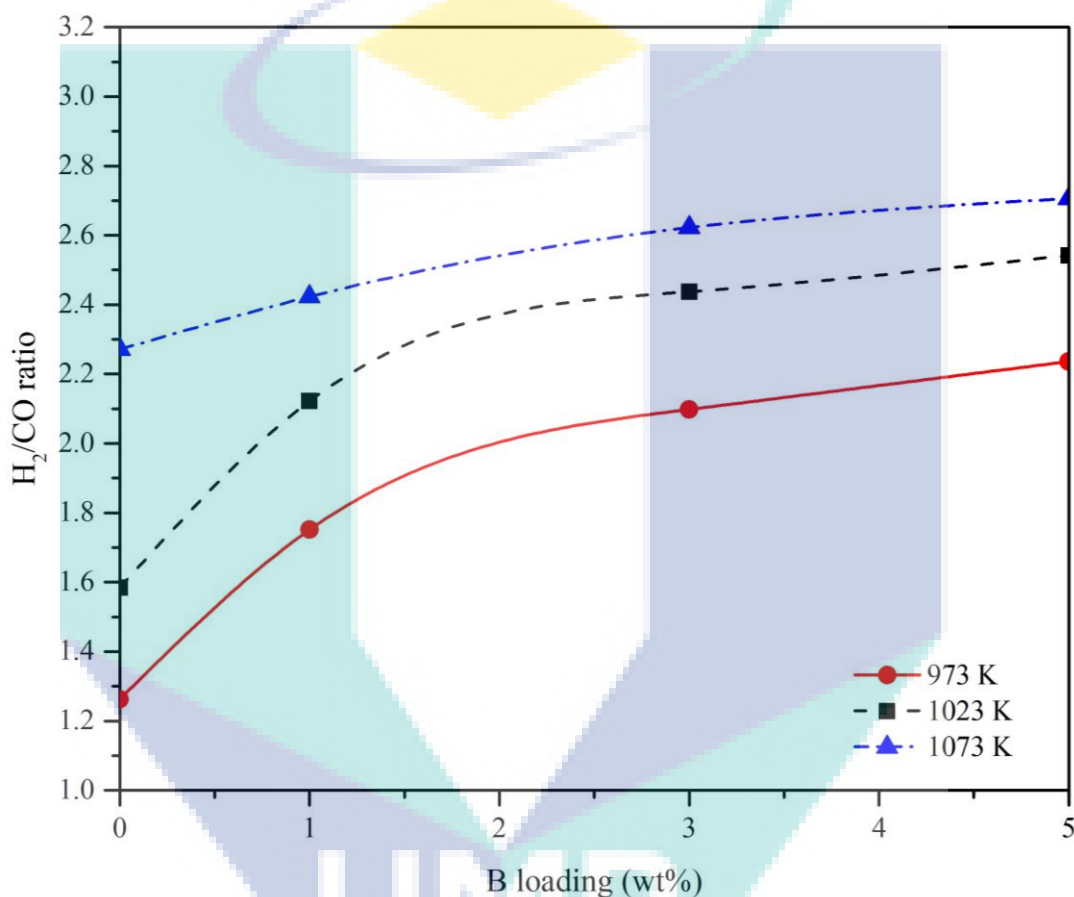


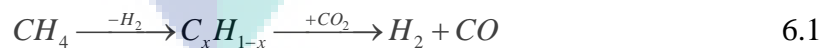
Figure 6.5 Effect of reaction temperature and B loading on H<sub>2</sub>/CO ratio of unpromoted and promoted 10%Ni/SBA-15 catalysts at stoichiometric feed composition ( $F_{CH_4} : F_{H_2O} : F_{CO_2} = 3 : 2 : 1$ ).

## 6.4 Effect of Reactant Partial Pressure

The 3%B loading at reaction temperature of 1073 K appeared to be the best promoter loading for 10%Ni/SBA-15 catalyst in terms of reactant conversions, gaseous product yield and H<sub>2</sub>/CO ratio for CSCRM reaction. Thus, the further evaluation of different reactant partial pressure on CSCRM reaction was performed over the best 3%B-10%Ni/SBA-15 catalyst at reaction temperature of 1073 K and different reactant partial pressure ranging from 10 to 50 kPa in order to evaluate the catalytic performance.

### 6.4.1 Effect of CO<sub>2</sub> Partial Pressure

The influence of CO<sub>2</sub> partial pressure on CSCRM performance was evaluated by varying  $P_{CO_2}$  from 10 to 25 kPa at 1073 K while  $P_{CH_4}$  and  $P_{H_2O}$  were kept constant at 45 kPa and 30 kPa, respectively. As seen in Figure 6.6, a significant increase in both CH<sub>4</sub> and CO<sub>2</sub> conversions was observed with rising  $P_{CO_2}$  from 10 to 15 kPa. Particularly, CH<sub>4</sub> and CO<sub>2</sub> conversions reached to the highest values of 74.6% and 53.9% in that order at  $P_{CO_2}$  of 15 kPa. The improvement of reactant conversions with increasing  $P_{CO_2}$  from 10 to 15 kPa could be assigned to the enhancement of simultaneous CO<sub>2</sub> reforming of CH<sub>4</sub> reaction (cf. Eq. 2.4) in agreement with other studies (Jang et al., 2016; Omoregbe et al., 2017). In addition, the enhancement of CO<sub>2</sub> gasification of deposited carbon (cf. Eq. 2.7) originated from CH<sub>4</sub> decomposition (see Eq. 2.6) could contribute to the increase in CO<sub>2</sub> conversion. In fact, in the study of methane dry reforming reaction, Foo et al. (2011) found that the mechanistic pathway for methane dry reforming reaction was generally a 2-step process in which deposited carbonaceous species ( $C_xH_{1-x}$  with  $x \leq 1$ ) were generated from CH<sub>4</sub> cracking and CO<sub>2</sub> reactant was responsible for the elimination of carbon deposition as given in Eq. 6.1.



Thus, the lowest reactant conversions ( $X_{CH_4} = 18.5\%$  and  $X_{CO_2} = 17.5\%$ ) obtained at  $P_{CO_2} = 10$  kPa could be attributed to the low reverse Boudouard reaction rate (cf. Eq. 2.7) for gasifying carbonaceous species in CO<sub>2</sub>-deficient feedstock. However, a significant decline in both CH<sub>4</sub> and CO<sub>2</sub> conversions at  $P_{CO_2}$  beyond 15 kPa

(stoichiometric conditions) was apparently observed as seen in Figure 6.6. This behavior could suggest the hindrance of CH<sub>4</sub> adsorption on catalyst surface due to the competing adsorption between reactants in the excess presence of CO<sub>2</sub> reactant and extra intermediate H<sub>2</sub>O produced from RWGS (see Eq. 2.5). Thus, the deficiency of adsorbed CH<sub>4</sub> molecules on metallic Ni active sites could lead to a drop in catalytic activity in CO<sub>2</sub>-rich reactant mixture. In fact, as seen in Figure 6.7, both H<sub>2</sub> and CO yields also experienced a significant decline at excessive CO<sub>2</sub> partial pressure beyond the stoichiometric feed composition further confirming the decrease in reforming activity.

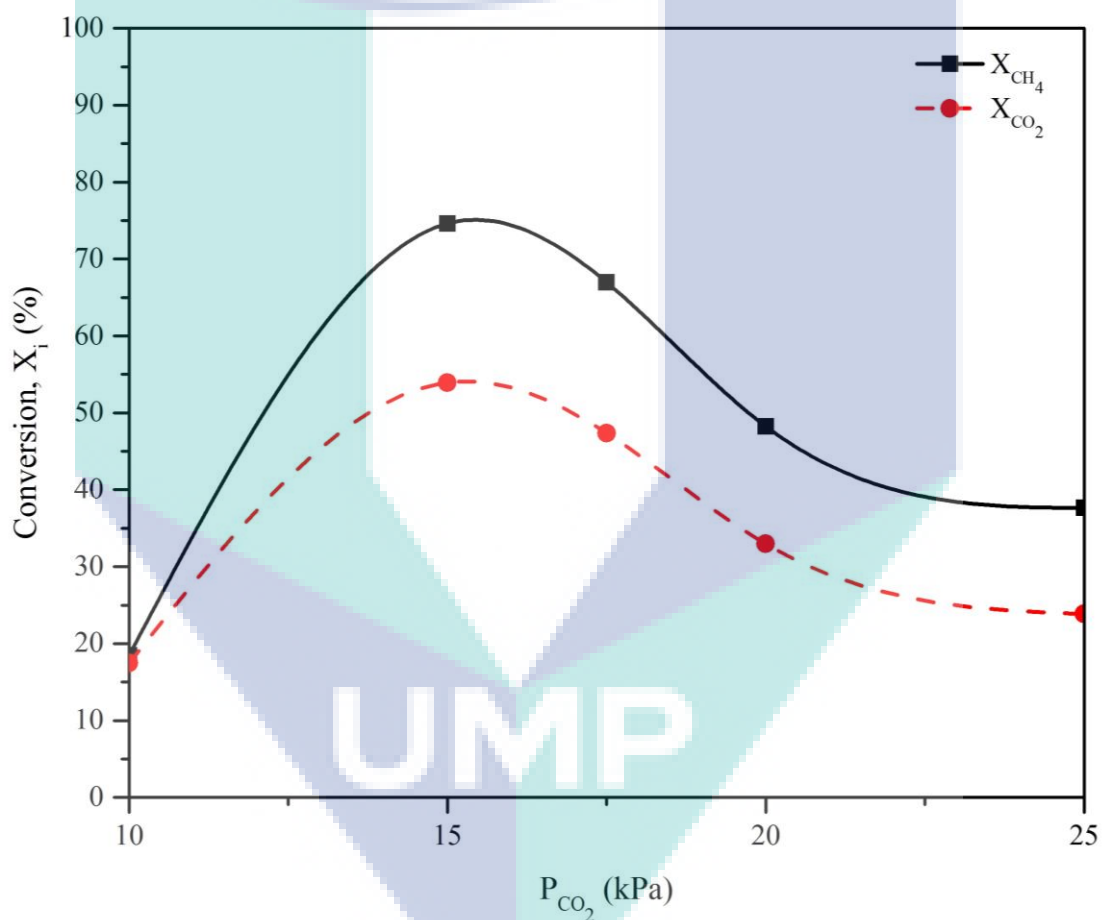


Figure 6.6 Effect of CO<sub>2</sub> partial pressure on CH<sub>4</sub> and CO<sub>2</sub> conversions over 3%B-10%Ni/SBA-15 catalyst at  $P_{CH_4} = 45$  kPa,  $P_{H_2O} = 30$  kPa and 1073 K.

As seen in Figure 6.7, H<sub>2</sub>/CO ratio varied from 1.1 to 2.6 and declined with rising  $P_{CO_2}$  from 15 to 25 kPa reasonably due to the parallel occurrence of RWGS (Jang et al., 2016) and reverse Boudouard reactions generating additional CO gaseous product

with growing  $P_{CO_2}$ . In fact, in the research of CSCRM using catalytic Ni membrane, Ryi et al. (2014) reported the same behavior of  $H_2/CO$  ratio with an increase in  $CO_2/H_2O$  ratio for CSCRM reaction at 1023 K. As shown in Figure 6.7, at the stoichiometric feed composition ( $P_{CH_4} = 45$  kPa,  $P_{H_2O} = 30$  kPa and  $P_{CO_2} = 15$  kPa), the ratio of  $H_2$  to  $CO$  was about 2.6 greater than the theoretical value of 2 for CSCRM. This observation is indicative of the predominance of SRM in comparison with DRM reaction.

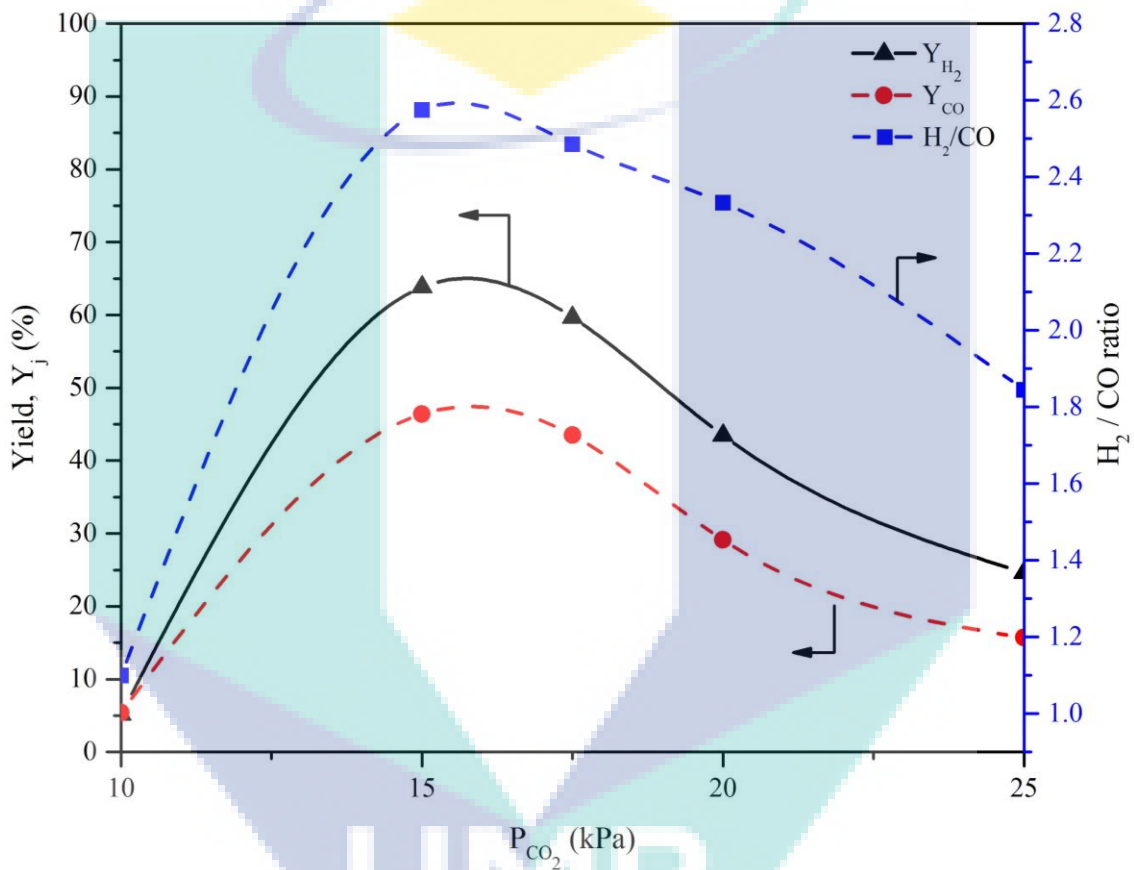


Figure 6.7 Effect of  $CO_2$  partial pressure on  $H_2/CO$  ratio,  $H_2$  and  $CO$  yields over 3%B-10%Ni/SBA-15 catalyst at  $P_{CH_4} = 45$  kPa,  $P_{H_2O} = 30$  kPa and 1073 K.

#### 6.4.2 Effect of $H_2O$ Partial Pressure

Apart from  $CO_2$  reactant,  $H_2O$  is another oxidizing agent playing an important role in CSCRM reaction. Thus, it is crucial to examine the influence of  $H_2O$  partial pressure on CSCRM performance in terms of reactant conversion, product yield and  $H_2/CO$  ratio. Indeed, the role of  $H_2O$  partial pressure in CSCRM reaction was investigated at fixed  $P_{CH_4} = 45$  kPa and  $P_{CO_2} = 15$  kPa while  $P_{H_2O}$  was varied from 10 to

30 kPa as seen in Figure 6.8. The conversion of  $\text{CH}_4$  increased substantially with rising  $P_{\text{H}_2\text{O}}$  from 10 (H<sub>2</sub>O-deficient feedstock) to 30 kPa (stoichiometric feed composition) whilst a highest CO<sub>2</sub> conversion of 67.3% was observed at 20 kPa (see Figure 6.8). The enhancement of  $X_{\text{CH}_4}$  with growing  $P_{\text{H}_2\text{O}}$  was reasonably due to the improvement of steam gasification of deposited carbon (see Eq. 2.8) produced from CH<sub>4</sub> decomposition. In the thermodynamic study of CSCRM using Gibbs free energy minimization approach, Özkara-Aydinoğlu (2010) also found that regardless of reaction temperature, CH<sub>4</sub> conversion increased noticeably with a growth in H<sub>2</sub>O/CH<sub>4</sub> ratio from 0:1 to 3:1. The decline in CO<sub>2</sub> conversion and the increase in CH<sub>4</sub> conversion at  $P_{\text{H}_2\text{O}}$  greater than 20 kPa could suggest that SRM was more preferable than DRM reaction at high  $P_{\text{H}_2\text{O}}$ . Although both CO<sub>2</sub> and H<sub>2</sub>O possess oxidizing property, CH<sub>4</sub> would favorably react with H<sub>2</sub>O instead of CO<sub>2</sub> owing to the greater stability nature of CO<sub>2</sub> molecule in comparison with H<sub>2</sub>O species (Özkara-Aydinoğlu, 2010).

Additionally, in the H<sub>2</sub>O-deficient region ranging from 10 to 25 kPa, CO<sub>2</sub> conversion was always higher than that of CH<sub>4</sub> (cf. Figure 6.8). This could suggest that CO<sub>2</sub> gasification rate was superior to the rate of steam gasification in the deficiency of H<sub>2</sub>O. Thus, DRM reaction could appear to be the dominant reaction in CSCRM at H<sub>2</sub>O-insufficient environment. In fact, as seen in Figure 6.9, the ratio of H<sub>2</sub> to CO was also less than 2 at  $P_{\text{H}_2\text{O}}$  of 10 to 25 further confirming the predominance of DRM reaction.

UMP

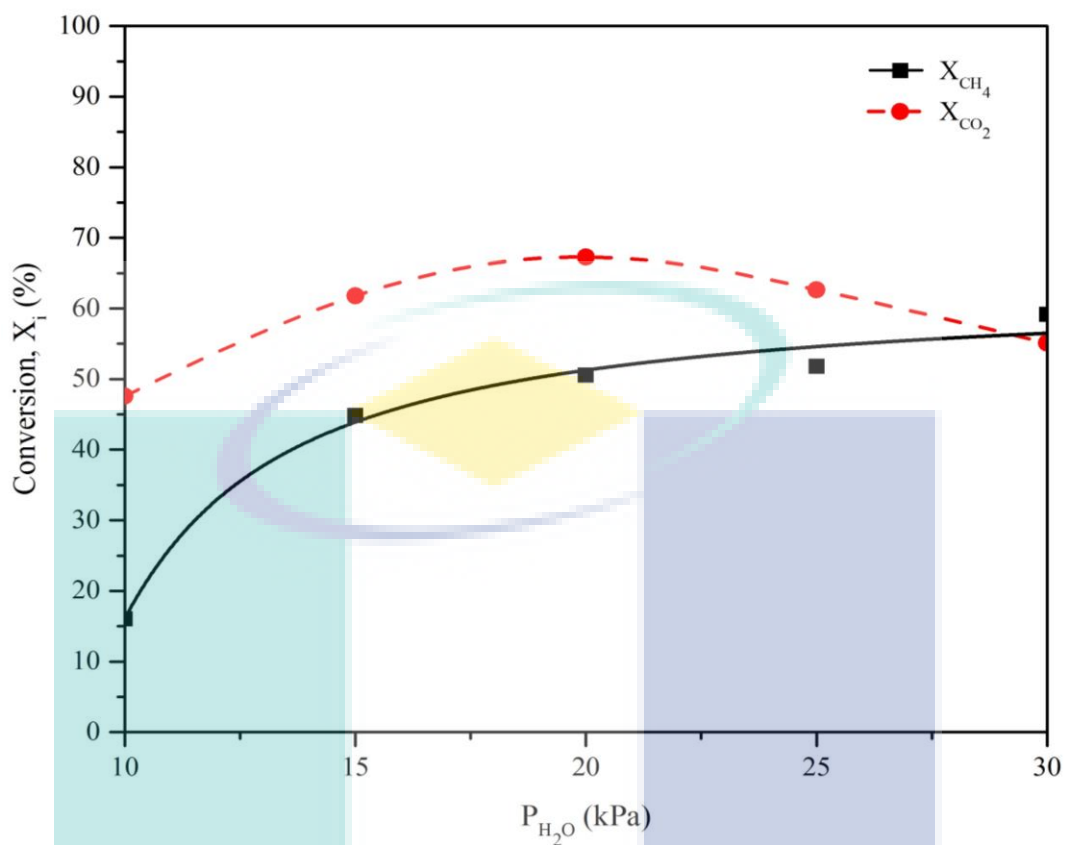


Figure 6.8 Effect of  $H_2O$  partial pressure on  $CH_4$  and  $CO_2$  conversions over 3%B-10%Ni/SBA-15 catalyst at  $P_{CH_4} = 45$  kPa,  $P_{CO_2} = 15$  kPa and 1073 K.

The effect of  $P_{H_2O}$  on CO and  $H_2$  yields for CSCRM reaction is shown in Figure 6.9. The yield of  $H_2$  increased from 33.8% to 47.7% whilst CO yield enhanced from 35.4% to 46.4% with rising  $P_{H_2O}$  from 10 to 30 kPa. The enhancement of product yield with rising  $H_2O$  partial pressure further confirms the growth of catalytic activity.

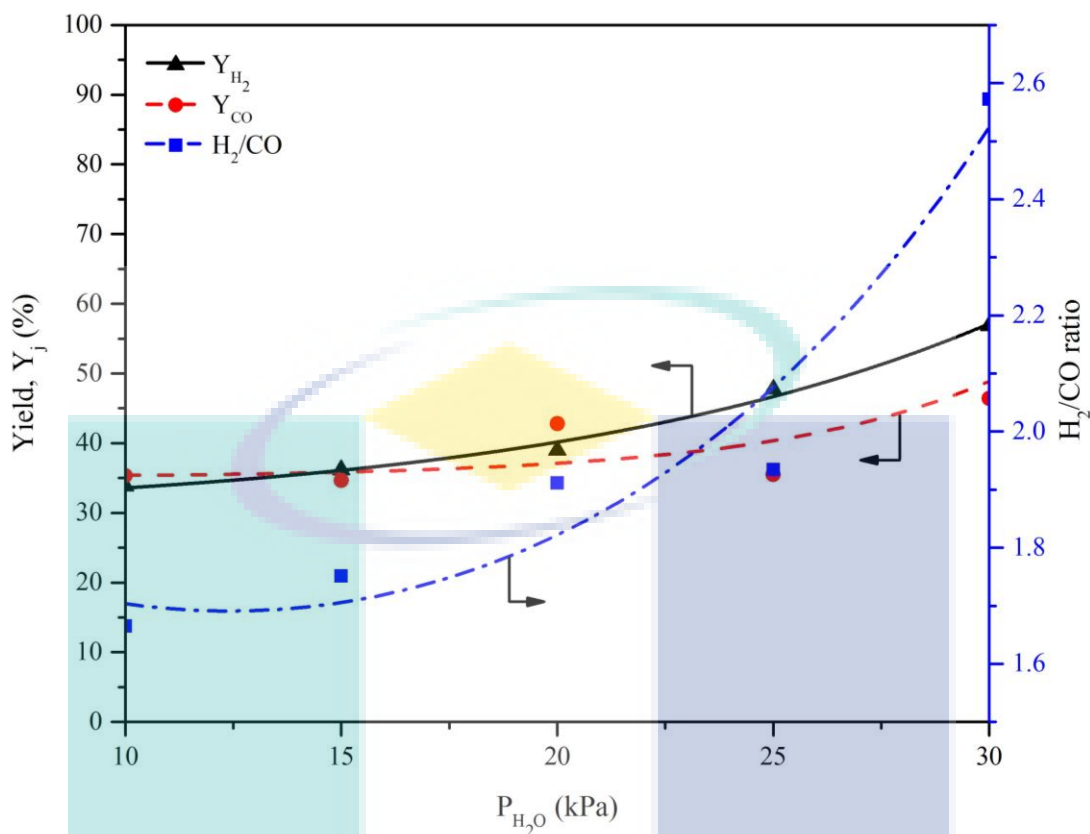


Figure 6.9 Effect of  $H_2O$  partial pressure on  $H_2/CO$  ratio,  $H_2$  and  $CO$  yields over 3%B-10%Ni/SBA-15 catalyst at  $P_{CH_4} = 45$  kPa,  $P_{CO_2} = 15$  kPa and 1073 K.

### 6.4.3 Effect of $CH_4$ Partial Pressure

The influence of  $P_{CH_4}$  on catalytic performance was studied at fixed  $P_{H_2O} = 30$  kPa,  $P_{CO_2} = 15$  kPa and 1073 K with varying  $P_{CH_4}$  of 35-50 kPa. As seen in Figure 6.10 and Figure 6.11, the reactant conversions,  $H_2$  and  $CO$  yields as well as  $H_2/CO$  ratio improved with rising  $P_{CH_4}$  from 35 to 45 kPa and achieved the highest value at  $P_{CH_4}$  of 45 kPa for 3%B-10%Ni/SBA-15 catalyst. However, a significant drop in reactant conversions and product yield as well as  $H_2/CO$  ratio was observed at  $P_{CH_4}$  beyond 45 kPa (see Figure 6.10 and Figure 6.11). The decline in catalytic performance in  $CH_4$ -rich environment could be due to the growing rate of  $CH_4$  decomposition to carbonaceous species encapsulating the active Ni metallic sites (Kumar et al., 2015). In addition, the reducing reactant conversions with rising  $P_{CH_4}$  could suggest that the rate of carbon formation via  $CH_4$  deposition (cf. Eq. 6.2) was superior to that of carbon gasification by

CO<sub>2</sub> (cf. Eq. 6.3) and H<sub>2</sub>O (cf. Eq. 6.4) oxidizing agents in CH<sub>4</sub>-rich feedstock. As a result, the accumulation of unreacted carbonaceous species on catalyst surface could lessen the catalytic activity.

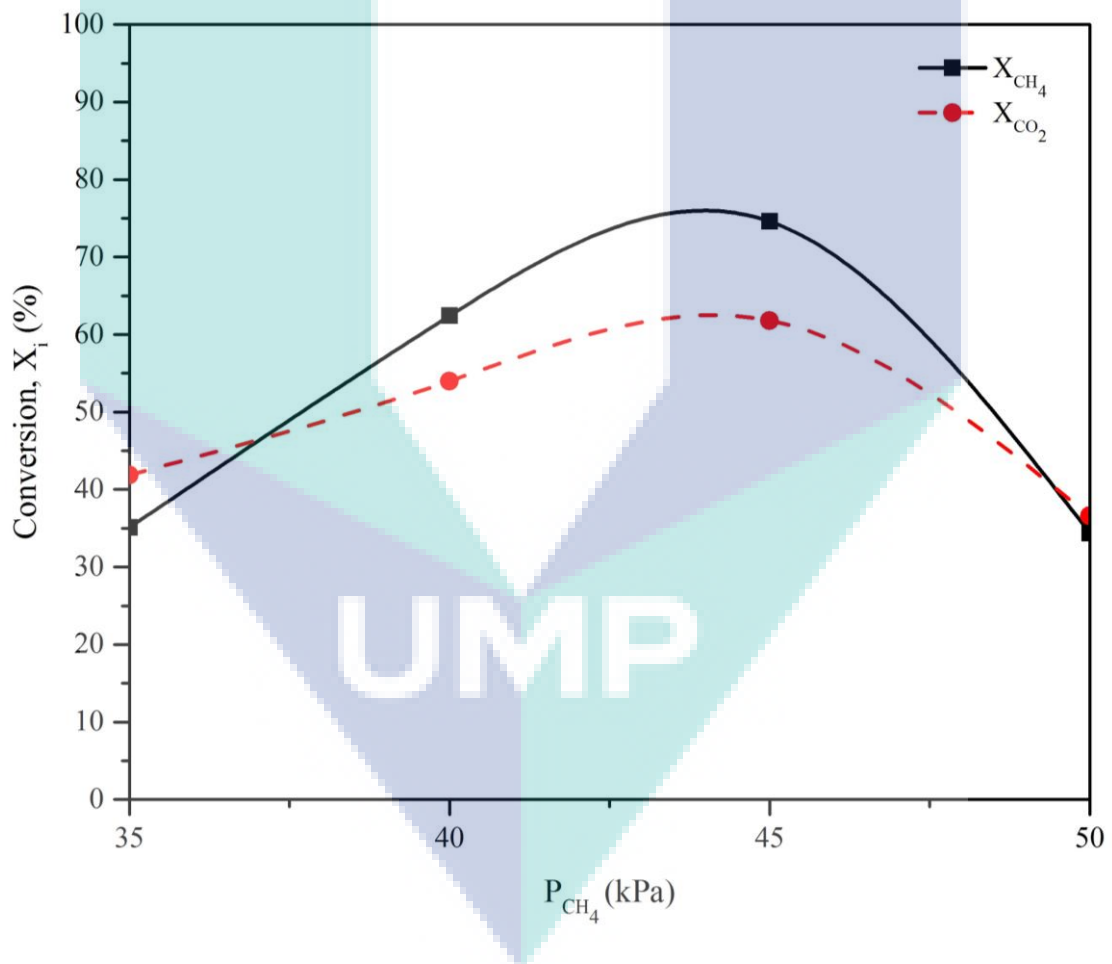
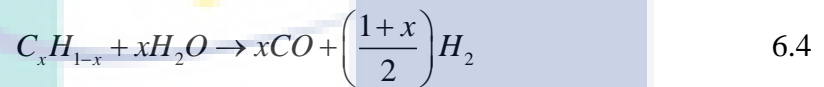
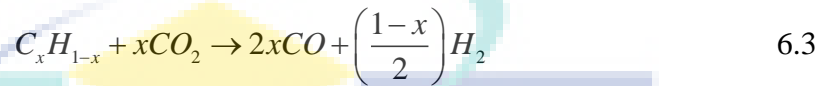
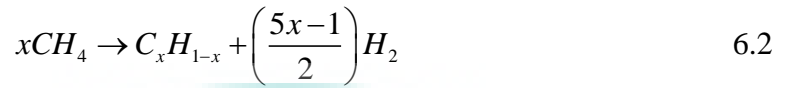


Figure 6.10 Effect of CH<sub>4</sub> partial pressure on CH<sub>4</sub> and CO<sub>2</sub> conversions over 3%B-10%Ni/SBA-15 catalyst at  $P_{H_2O} = 30$  kPa,  $P_{CO_2} = 15$  kPa and 1073 K.

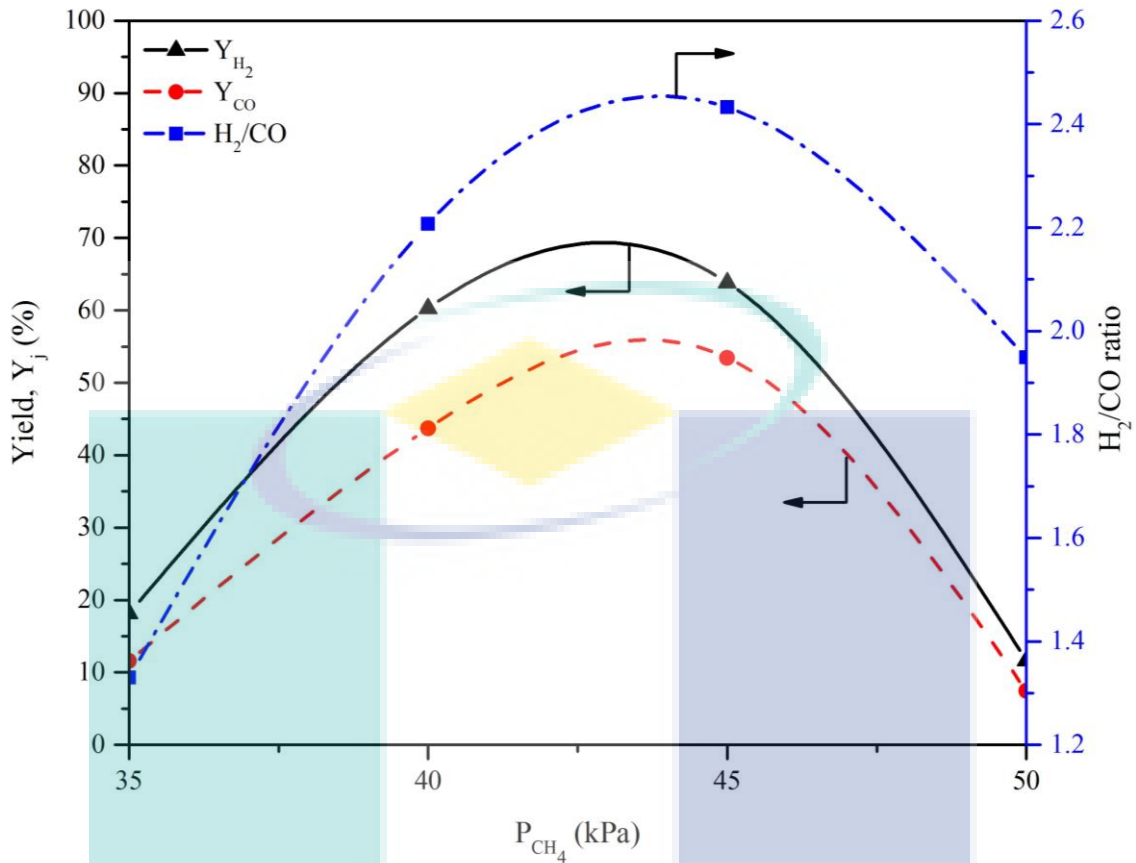


Figure 6.11 Effect of  $CH_4$  partial pressure on  $CH_4$  and  $CO_2$  conversions over 3%B-10%Ni/SBA-15 catalyst at  $P_{H_2O} = 30$  kPa,  $P_{CO_2} = 15$  kPa and 1073 K.

#### 6.4.4 Summary

As discussed at this chapter, the evaluation of different reactant partial pressure on CSCR reaction was performed over the 3%B-10%Ni/SBA-15 catalyst at reaction temperature of 1073 K. At high  $P_{CO_2}$  beyond 15 kPa, the drop in the catalytic performance was visibly observed due to the hindrance of  $CH_4$  adsorption on catalyst surface. In addition, the SRM was predominant with increasing  $P_{H_2O}$  resulted in the rise in  $CH_4$  conversion and a decline in  $CO_2$  conversion. A noticeable drop in reactant conversions was observed at  $P_{CH_4}$  beyond 45 kPa could be due to the increasing rate of  $CH_4$  decomposition encapsulating the active Ni metallic sites. In summary, the  $P_{CO_2}$  of 15 kPa,  $P_{H_2O}$  of 20 kPa and  $P_{CH_4}$  of 45 kPa appeared to be the best feed composition for the CSCR reaction in terms of reactant conversions and product yields.

## 6.5 Longevity Test

The 3%B loading appeared to be the best promoter loading for 10%Ni/SBA-15 catalyst in terms of reactant conversions, gaseous product yield and H<sub>2</sub>/CO ratio for CSCRM reaction. Hence, the longevity tests of CSCRM reaction were conducted over this best 3%B-10%Ni/SBA-15 catalyst for 24 h at stoichiometric feedstock and different reaction temperature ranging from 973 to 1073 K in order to assess the catalytic stability and degree of catalyst deactivation with time-on-stream at various reaction temperatures.

Figure 6.12 shows the 24 h on-stream profiles for CH<sub>4</sub> and CO<sub>2</sub> conversions of CSCRM over 3%B-10%Ni/SBA-15 catalyst at varying reaction temperatures from 973 to 1073 K. Generally, the reactant conversions appeared to be stable with time-on-stream over the period of 24 h irrespective of reaction temperature. In addition, regardless of time-on-stream, the 3%B-10%Ni/SBA-15 catalyst exhibited the highest CH<sub>4</sub> and CO<sub>2</sub> conversions at 1073 K followed by 1023 K and 973 K. A significant increment of about 67.3% and 24.7% for the corresponding CH<sub>4</sub> and CO<sub>2</sub> conversions was observed with rising temperature from 973 to 1073 K reasonably due to the endothermic nature of CSCRM reaction in agreement with the thermodynamic calculations of the Gibbs free energy changes performed by Jabbour et al. (2017). In the paper, they also reported that CH<sub>4</sub> and CO<sub>2</sub> conversions for CSCRM reaction decreased with reducing reaction temperature, especially at temperature below 973 K.

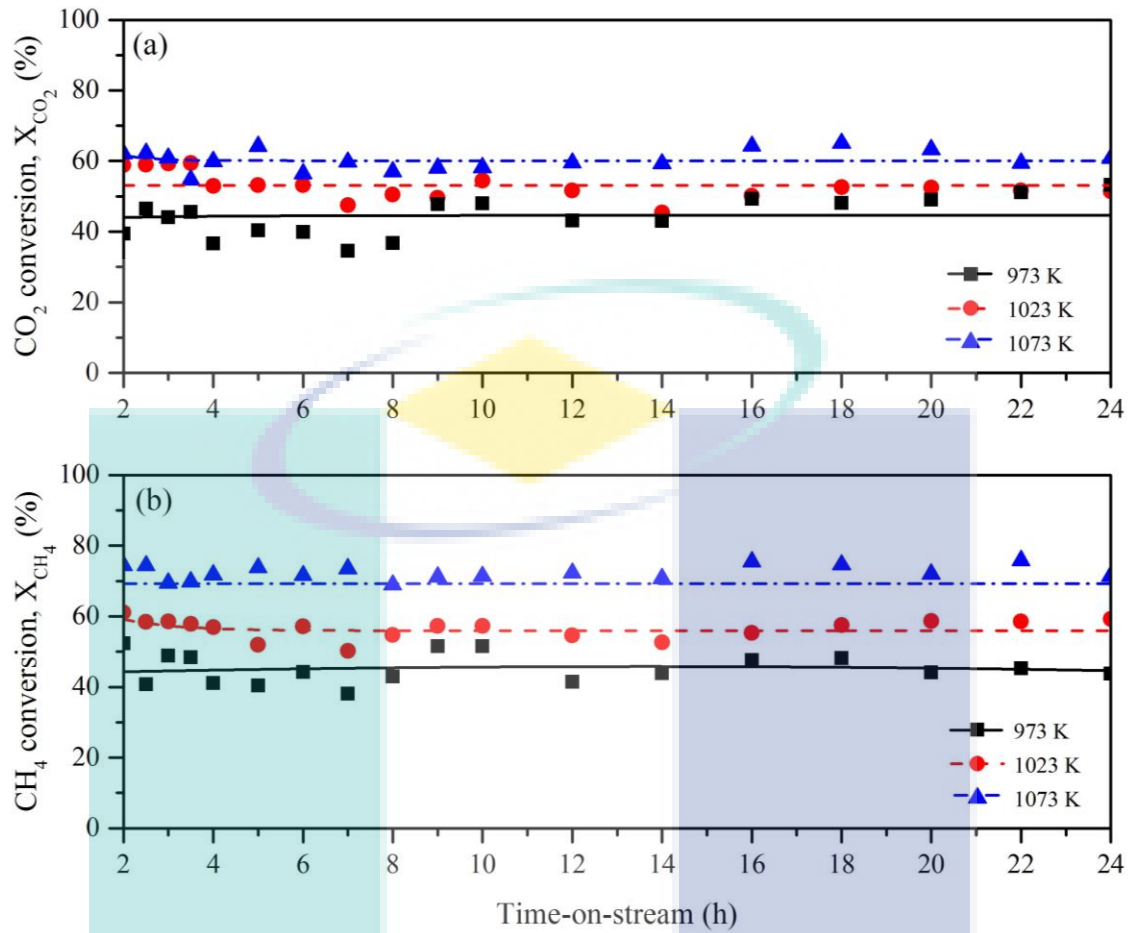


Figure 6.12 Time-on-stream profile for (a) CO<sub>2</sub> and (b) CH<sub>4</sub> conversions over 3%B-10%Ni/SBA-15 catalyst at  $P_{CH_4} = 45$  kPa,  $P_{H_2O} = 30$  kPa,  $P_{CO_2} = 15$  kPa and temperature of 973 to 1073 K.

The time-on-stream profiles for H<sub>2</sub> and CO yields over 3%B-10%Ni/SBA-15 catalyst are also shown in Figure 6.13. The H<sub>2</sub> yield was always greater than CO yield for all reaction temperature. Additionally, the difference between H<sub>2</sub> and CO yields rose from 11.4% (at 973 K) to 17.3% (at 1073 K) could suggest the enhancement of SRM which was dominant at high reaction temperature. Both H<sub>2</sub> and CO yields also experienced a significant improvement with rising reaction temperature from 973 to 1073 K. In the study of thermodynamic equilibrium for CSCRM, Özkara-Aydinoğlu (2010) also found that regardless of feedstock composition, rising reaction temperature led to an increase in both H<sub>2</sub> and CO yields. Additionally, the highest value of H<sub>2</sub> yield was attained at temperature of around 1073 K.

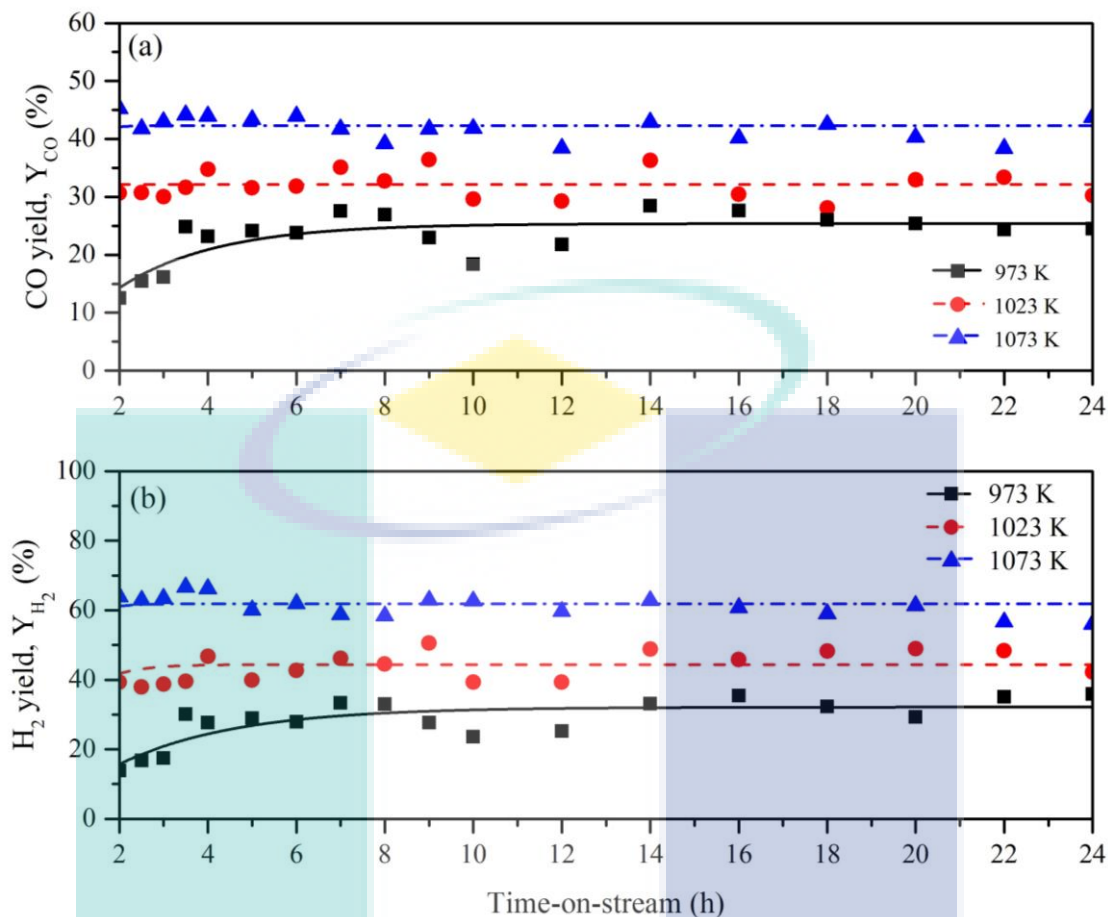


Figure 6.13 Time-on-stream profile for (a) CO and (b)  $H_2$  yields over 3%B-10%Ni/SBA-15 catalyst at  $P_{CH_4} = 45$  kPa,  $P_{H_2O} = 30$  kPa,  $P_{CO_2} = 15$  kPa and temperature of 973 to 1073 K.

As seen in Figure 6.14, the ratio of  $H_2$  to CO was achieved at about 1.2-2.7 suitable for downstream FTS synthesis of synthetic liquid hydrocarbons. An increase in  $H_2/CO$  ratio with rising reaction temperature from 973 to 1073 K was observed with time-on-stream indicating the coexistence of endothermic side reactions (i.e. SRM (cf. Eq. 2.2) and DRM (cf. Eq. 2.4) (Özkara-Aydınoglu, 2010). In fact, in the study of  $(CO_2 + H_2O)/CH_4$  effect on  $H_2/CO$  ratio in CSCRM, Jang et al. (2016) also found that a  $H_2/CO$  ratio of more than 2 was obtained at reaction temperature ranging from 1023 to 1073 K with  $(CO_2 + H_2O)/CH_4$  ratios of 2.0 and 2.9.

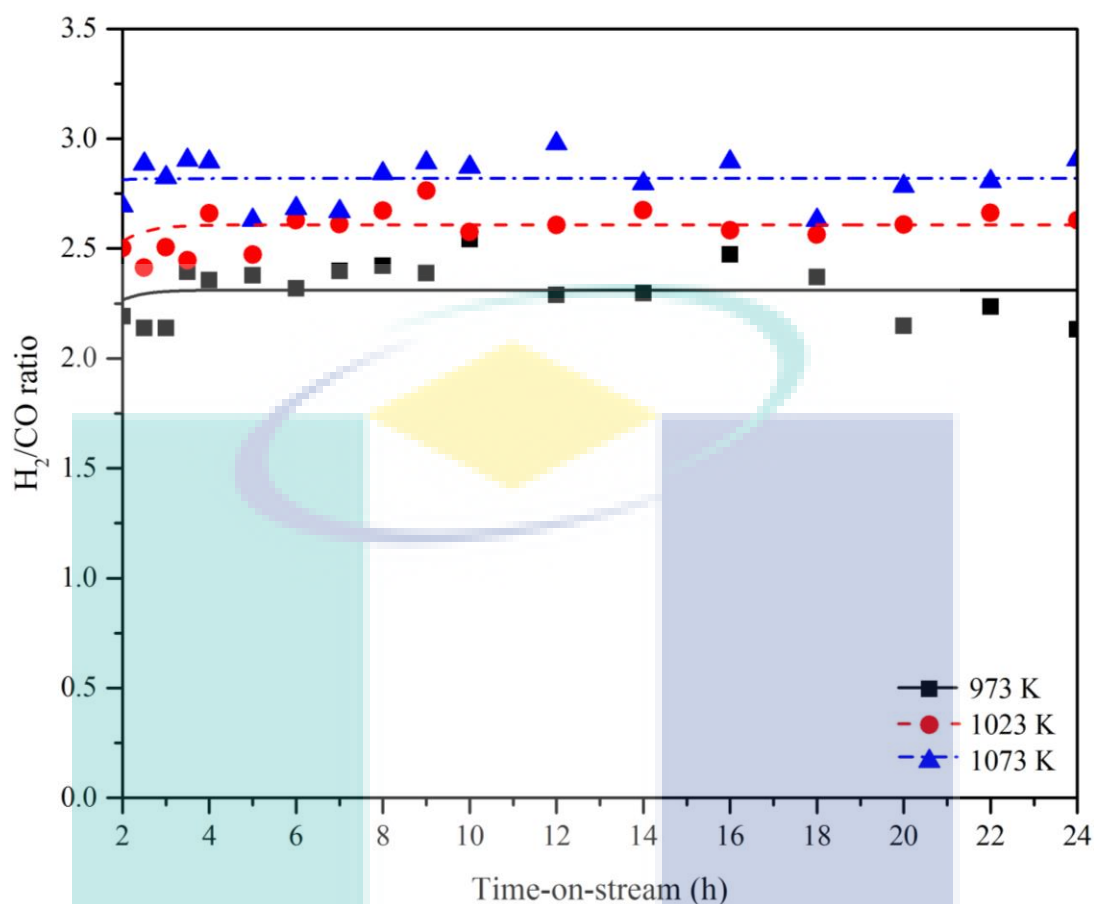


Figure 6.14 Time-on-stream profile for H<sub>2</sub>/CO ratio over 3%B-10%Ni/SBA-15 catalyst at  $P_{CH_4} = 45$  kPa,  $P_{H_2O} = 30$  kPa,  $P_{CO_2} = 15$  kPa and temperature of 973 to 1073 K.

In order to justify the catalytic stability of 3%B-10%Ni/SBA-15 catalyst for CSCR reaction, the degree of catalyst deactivation for each reaction temperature was calculated and compared with previous results of common catalysts reported in recent literature as summarized in Table 6.1. An appreciable decline in degree of catalyst deactivation from 16.4% to 4.0% over 3%B-10%Ni/SBA-15 catalyst was observed with a rise in reaction temperature from 973 to 1073 K during CSCR reaction. The better catalytic stability at reaction temperature of 1073 K was due to the improvement of carbon gasification by CO<sub>2</sub> and H<sub>2</sub>O oxidizing agents thermodynamically favored at high reaction temperature (Kumar et al., 2015).

Amongst the Ni-based catalysts in Table 6.1, the 3%B-10%Ni/SBA-15 catalyst in this study possessed the lowest degree of catalyst deactivation of about 4.0% to 16.4% depending on reaction temperature even though this catalyst was employed for CSCRM reaction over a longer period of time-on-stream at similar reaction conditions. Additionally, 3%B-10%Ni/SBA-15 catalyst exhibited a comparable CH<sub>4</sub> conversion to those of Ce-promoted and Mg-promoted catalysts after 24 h on-stream reaction runs (Koo et al., 2012; Park et al., 2015). From the above observation, 3%B-10%Ni/SBA-15 catalyst seems to be a promising catalyst with high catalytic activity and stability for industrial application of CSCRM. The outstanding performance of 3%B-10%Ni/SBA-15 catalyst in comparison with other promoted and unpromoted Ni-based catalysts (see Table 6.1) could be assigned to the promotional effect of boron addition. According to the DFT calculations performed by Xu and Saeys (2006), boron atoms reportedly suppress the nucleation of graphene islands and carbon diffusion into the Ni lattice by preoccupying the step sites. The addition of boron not only effectively hindered the graphitic carbon formation but also retained the reactivity of filamentous carbon and hence facilitating the steam and CO<sub>2</sub> gasification of deposited carbon on catalyst surface. Thus, boron promotion could restore the active sites of metallic Ni<sup>0</sup> phase and maintain the high catalytic activity with time-on-stream.

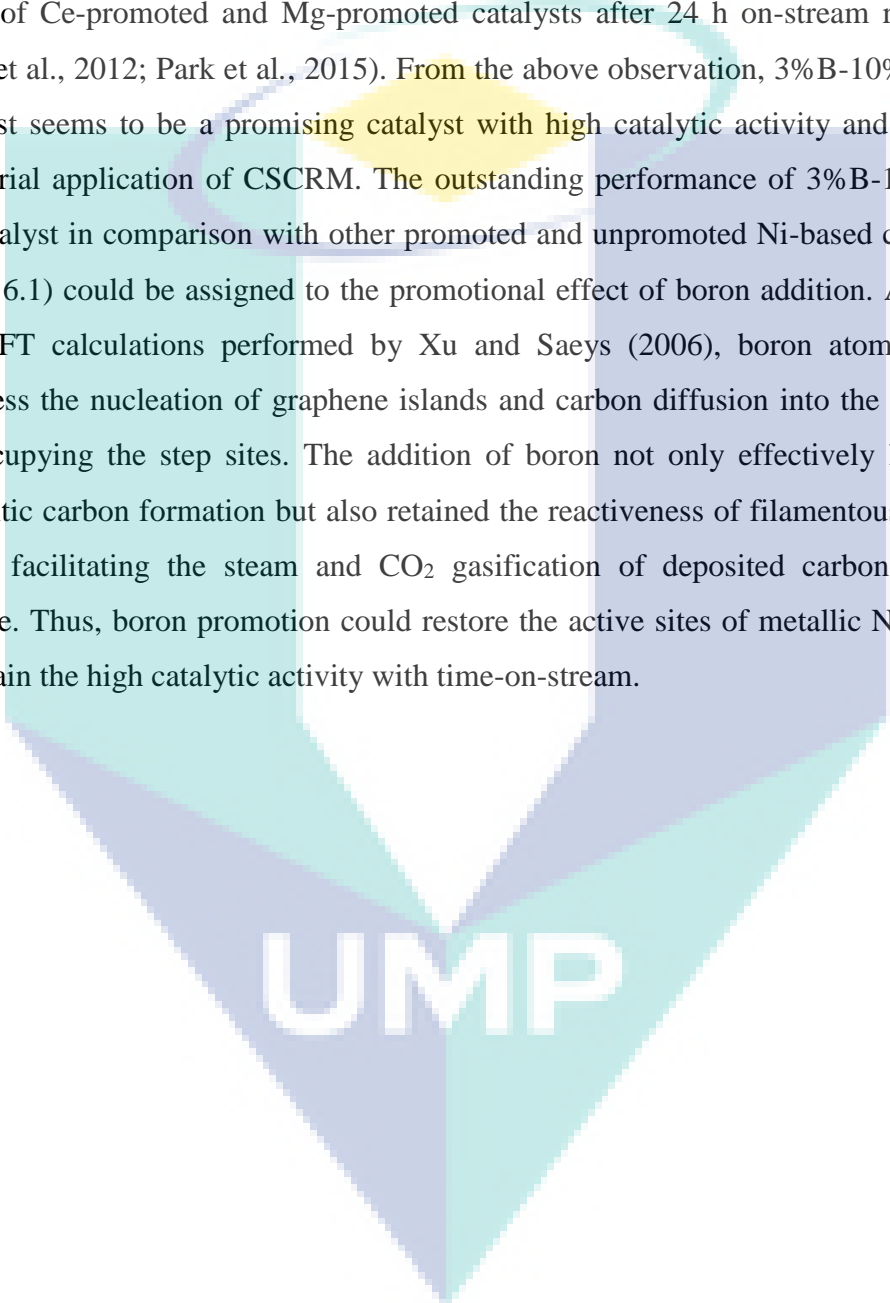
The logo for UIMP (Universiti Malaysia Perlis) is a large, stylized letter 'V' shape. The left side of the 'V' is light blue, the right side is light green, and the bottom point is a darker blue. The letters 'UIMP' are written in white, bold, sans-serif font across the center of the 'V'.

Table 6.1 Summary of degree of catalyst deactivation for CSCRM reaction over various Ni-based catalysts recently reported in literature

Catalysts	Operating conditions			$X_{CH_4_0}$ <sup>b</sup> (%)	$X_{CH_4_f}$ <sup>c</sup> (%)	D <sup>d</sup> (%)	Ref.
	T (K)	CH <sub>4</sub> :H <sub>2</sub> O: CO <sub>2</sub> ratio	TOS <sup>a</sup> (h)				
12%Ni/Al <sub>2</sub> O <sub>3</sub>	923	1:0.8:0.4	20	63.1	18.1	71.3	(Koo et al., 2012)
10%Ni/Al <sub>2</sub> O <sub>3</sub>	1023	1:0.16:0.1	5	72.0	35.0	51.4	(Roh et al., 2007)
6%Ce- 12%Ni/Al <sub>2</sub> O <sub>3</sub>	923	1:0.8:0.4	20	68.6	36.9	46.2	(Koo et al., 2012)
10%Ni/MgAl <sub>2</sub> O <sub>4</sub>	1023	1:1.2:0.4	5	83.1	55.3	33.5	(Park et al., 2015)
10%Ni- 1%La/MgAl <sub>2</sub> O <sub>4</sub>	1173	1:1.2:0.4	5	83.9	62.6	25.4	(Park et al., 2015)
3%B- 10%Ni/SBA-15	973	3:2:1	24	52.4	43.8	16.4	This study
	1023	3:2:1	24	58.9	51.4	12.7	This study
	1073	3:2:1	24	74.4	71.4	4.0	This study

<sup>a</sup>TOS: Time-on-stream.

<sup>b</sup>Initial methane conversion,  $X_{CH_4_0}$  for CSCRM reaction.

<sup>c</sup>Final methane conversion,  $X_{CH_4_f}$  for CSCRM reaction.

<sup>d</sup>Degree of catalyst deactivation for CSCRM reaction,  $D (\%) = \left( 1 - \frac{X_{CH_4_f}}{X_{CH_4_0}} \right) \times 100\%$ .

## 6.6 Post-Reaction Characterization

The characterization of spent catalysts was carried out to examine the crystalline structure, morphology and carbon content as well as carbonaceous types on catalyst surface after CSCRM. Since 3%B-10%Ni/SBA-15 catalyst appeared to be the best catalyst in terms of reactant conversions and H<sub>2</sub> yield at 1073 K, this used catalyst was further selected for post-reaction characterization and the resulting physicochemical attributes of it were compared with those of spent unpromoted catalyst in this section.

### 6.6.1 Raman Spectroscopy Measurements

As seen in Raman spectra of spent catalysts (cf. Figure 6.15 (b)-(c)), both peaks P1 and P2 representative for SBA-15 phase were also detected but the intensity of the first peak P1 was significantly lower compared with that of fresh catalyst (see Figure 6.15 (a)). As aforementioned, the characteristic peaks of NiO phase and SBA-15 support were overlapped at Raman band of peak P1. Thus, a drop in the intensity of peak P1 in comparison with fresh catalyst could be ascribed to the absence of NiO phase, which was reduced to metallic Ni<sup>0</sup> form during H<sub>2</sub> pretreatment prior to CSCRM.

In addition, two major absorption peaks were only observed for spent 10%Ni/SBA-15 catalyst (see Figure 6.15 (b)) at bands of 1340 cm<sup>-1</sup> (D band) and 1572 cm<sup>-1</sup> (G band) indicating the presence of heterogeneity of carbon deposits on catalyst surface. In fact, the D band is widely attributed to the defective sp<sup>3</sup>-bonded carbon atoms in amorphous carbon or carbon nanofilament (CNF) while the G band corresponds to the existence of an ordered carbon structure, *viz.*, graphitic carbon due to the carbon-carbon stretching vibrations of sp<sup>2</sup> carbon (C=C) bonds (Liu et al., 2009; Zawadzki et al., 2014).

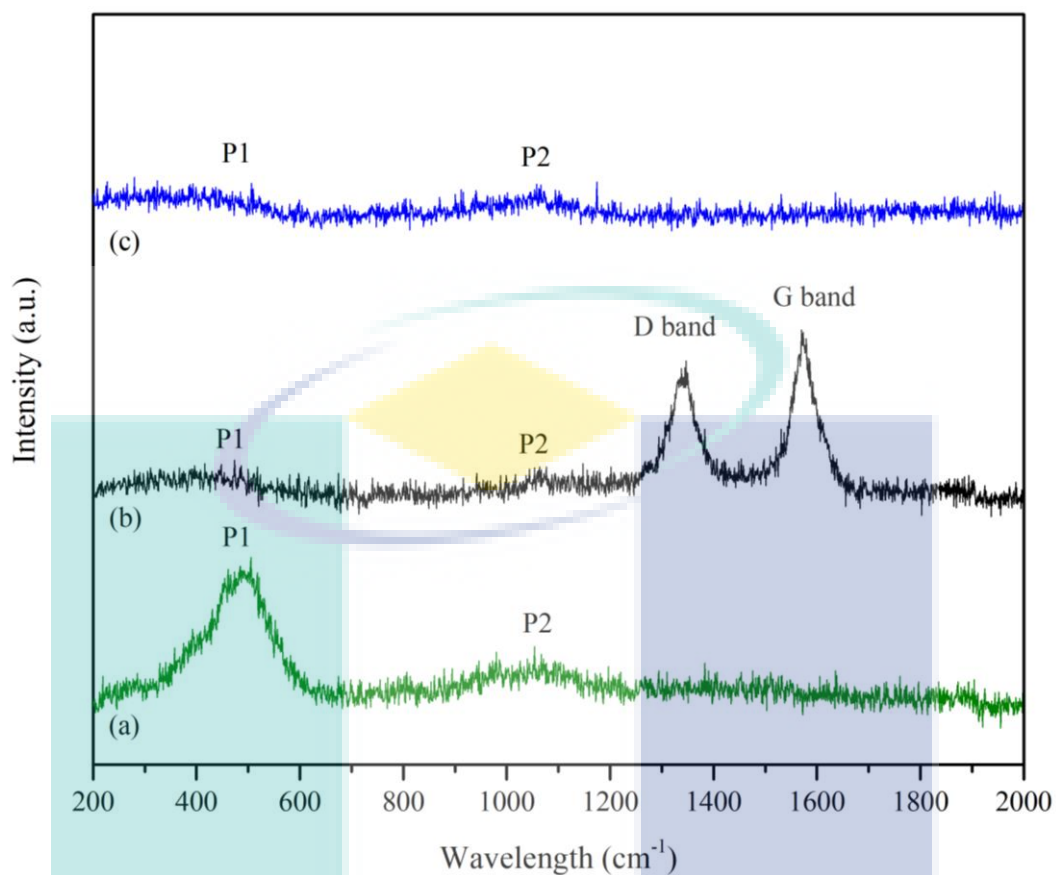


Figure 6.15 Raman spectra of (a) fresh 10%Ni/SBA-15, (b) spent 10%Ni/SBA-15 and (c) spent 3%B-10%Ni/SBA-15 catalysts after CSCRM at stoichiometric feed composition ( $F_{CH_4} : F_{H_2O} : F_{CO_2} = 3 : 2 : 1$ ) and 1073 K.

### 6.6.2 X-ray Diffraction (XRD) Measurements

The XRD analysis was also carried out for examining the crystalline phases of both spent unpromoted and 3%B-promoted catalysts after CSCRM reaction for 10 h on-stream at stoichiometric feed composition and 1073 K. As seen in Figure 6.16 (a)-(d), the apparently observed broad peak ranging from  $15^\circ$  to  $30^\circ$  assigned to the amorphous  $SiO_2$  ( $2\theta = 22.16^\circ$ ) could suggest that the typical siliceous framework of mesoporous SBA-15 support was largely retained with B-addition during CSCRM reaction in agreement with TEM images (see Figure 6.18 discussed later in section 6.5.4). Particularly, the XRD pattern of spent 10%Ni/SBA-15 catalyst (cf. Figure 6.16 (c)) shows a small intense peak (located at  $2\theta = 26.63^\circ$ ) on the shoulder of broad peak ranging from  $15^\circ$  to  $30^\circ$  could be ascribed to the graphite (JCPDS card No. 75-1621) (Zhang et al., 2013).

As seen in Figure 6.16 (d), no characteristic peak corresponding to graphitic carbon detected at the same position for the spent 3%B-10%Ni/SBA-15 catalyst indicated that the surface of B-promoted catalyst was free from graphite. The absence of graphitic carbon on B-promoted catalyst could be a result of strong B adsorption in the octahedral sites of subsurface layer of active Ni metal and hence inhibiting the diffusion of reactive surface carbon into the bulk of Ni to form graphene islands (Fouskas et al., 2014). This result is in line with the observation from Raman spectroscopy measurements (see Figure 6.15).

Additionally, the characteristic peaks at  $2\theta = 44.58^\circ$ ,  $51.86^\circ$  and  $76.38^\circ$  for both spent unpromoted and promoted 10%Ni/SBA-15 catalysts (see Figure 6.16 (c) and (d)) were ascribed to the corresponding (1 1 1), (2 0 0) and (2 2 0) crystal planes of metallic Ni<sup>0</sup> phase (JCPDS card No. 04-0850) (Huang et al., 2006). The typical peaks for NiO phase were also not observed in XRD patterns of both used 10%Ni/SBA-15 and 3%B-10%Ni/SBA-15 catalysts in agreement with Raman analysis of spent catalysts (see Figure 6.15). This behaviour could suggest that the active Ni<sup>0</sup> particles were largely preserved on catalyst surface during CSCRM reaction and resisted to re-oxidation for forming NiO particles possibly owing to the presence of reducing gaseous products (*viz.*, H<sub>2</sub> and CO) and the strong metal-support interaction. The re-oxidation of metallic Ni<sup>0</sup> phase to NiO form during CSCRM reaction has been widely reported in literature (Roh et al., 2009) and is considered as one of the main factors inducing severe catalytic deactivation (Bartholomew, 2001). Thus, the resistance to re-oxidation is most likely an outstanding attribute of the as-synthesized Ni/SBA-15 catalysts in this study.

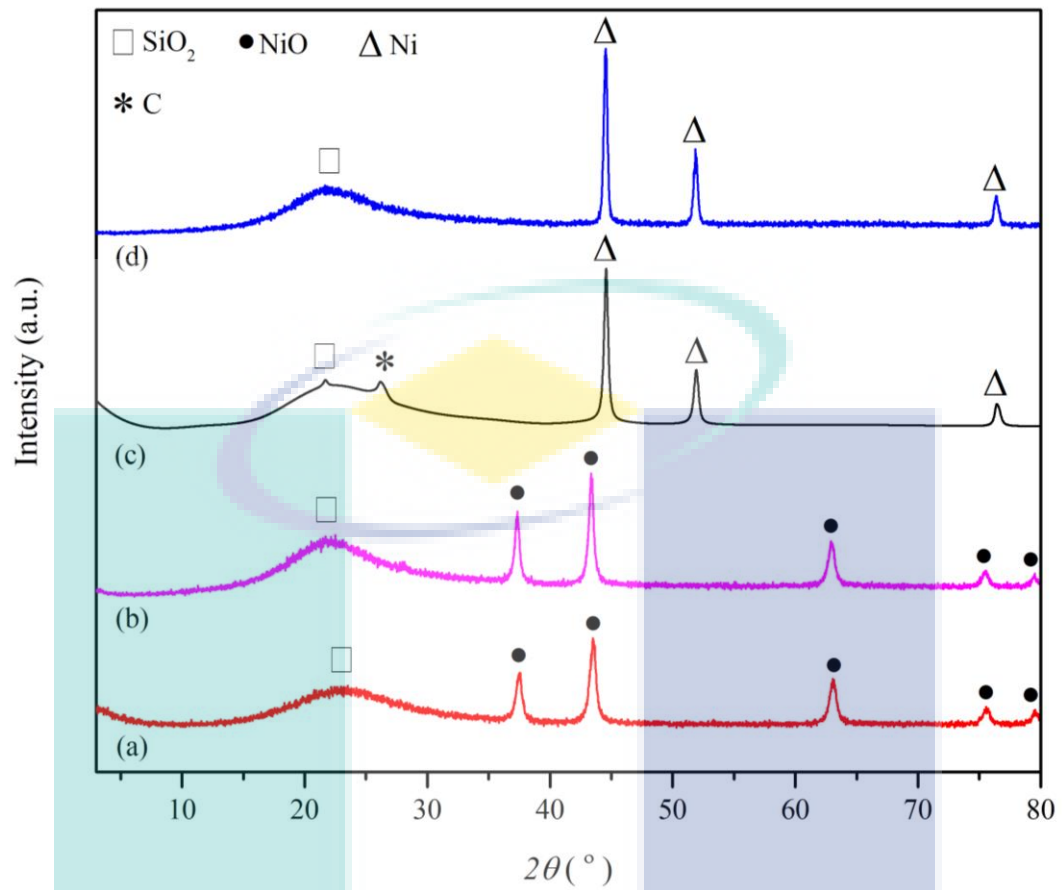


Figure 6.16 XRD patterns of (a) fresh 10%Ni/SBA-15, (b) fresh 3%B-10%Ni/SBA-15, (c) spent 10%Ni/SBA-15 and (d) spent 3%B-10%Ni/SBA-15 catalysts after CSCRM at stoichiometric feed composition ( $F_{\text{CH}_4} : F_{\text{H}_2\text{O}} : F_{\text{CO}_2} = 3 : 2 : 1$ ) and 1073 K.

UMP

### 6.6.3 Scanning Electron Microscopy (SEM) Measurements

The SEM micrographs of both spent 10%Ni/SBA-15 and 3%B-10%Ni/SBA-15 catalysts after CSCRM at 1073 K are shown in Figure 6.17. The wheat-like macroscopic structure of spent catalysts visibly seemed to be mainly preserved. For spent unpromoted 10%Ni/SBA-15 catalyst, the carbon nanofilament was apparently observed and surrounded on the surface of used catalyst after CSCRM reaction (see green circles in Figure 6.17 (b)). Indeed, CNF formation during CSCRM was also reported in other studies (Jabbour et al., 2017; Koo et al., 2012).

However, as seen in Figure 6.17 (d), the catalyst surface of used 3%B-10%Ni/SBA-15 catalyst appeared to be free from filamentous carbon. This could indicate that there was no formation of CNF species or CNF could be present on catalyst surface with a significantly low amount inferior to the detection limit of SEM measurement. The carbon resistance of B-promoted catalyst was possibly due to the preferential occupation of boron on the subsurface octahedral sites of Ni atoms and hence blocking carbon diffusion for forming graphene islands (Xu and Saeys, 2006).

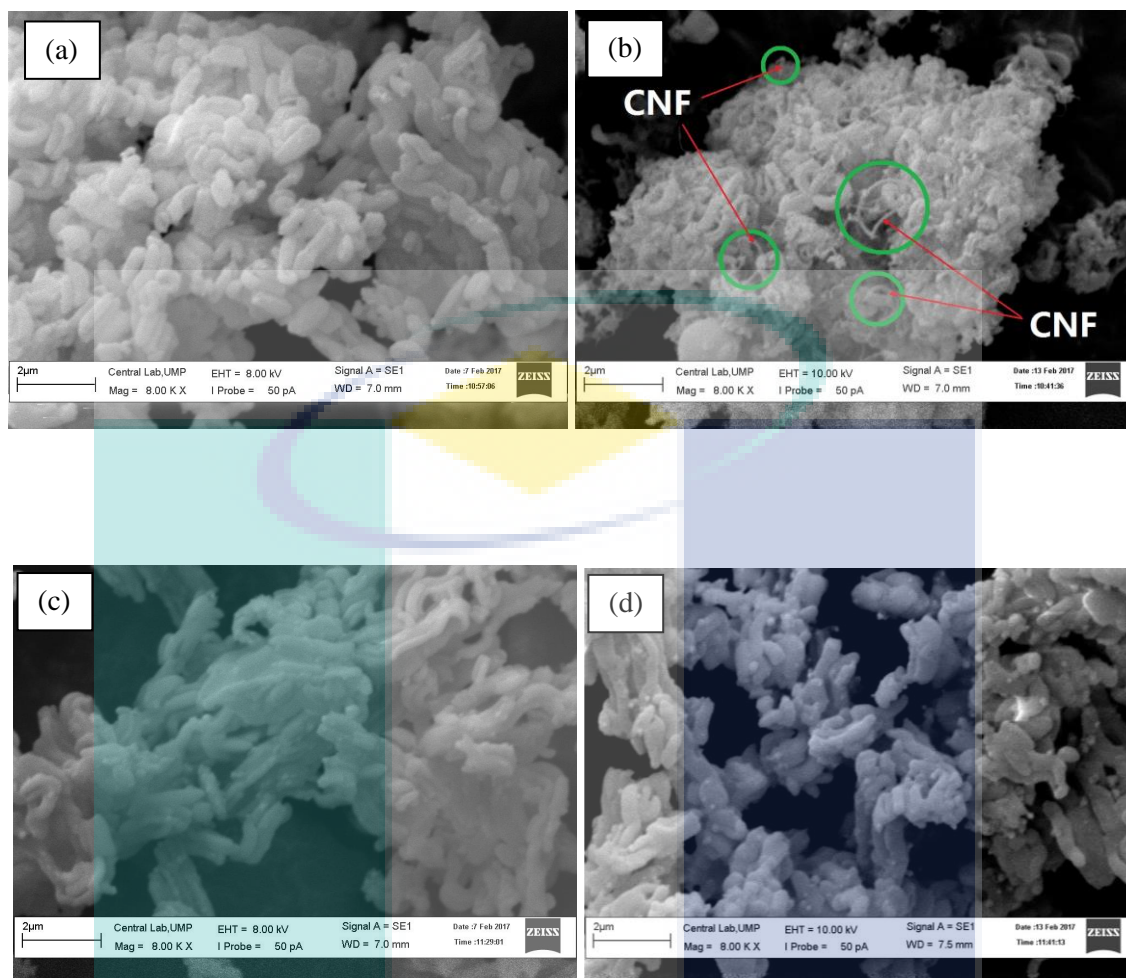


Figure 6.17 SEM images of (a) fresh 10%Ni/SBA-15, (b) spent 10%Ni/SBA-15 fresh, (c) fresh 3%B-10%Ni/SBA-15 and (d) spent 3%B-10%Ni/SBA-15 catalysts after CSCRM at stoichiometric feed composition ( $F_{CH_4} : F_{H_2O} : F_{CO_2} = 3 : 2 : 1$ ) and 1073 K.

#### 6.6.4 Transmission Electron Microscopy (TEM) Measurements

Figure 6.18 displays the TEM images of spent 10%Ni/SBA-15 and 3%B-10%Ni/SBA-15 catalysts. In comparison between fresh and spent catalysts, the ordered hexagonal structure and cylindrical pores belonging to the intrinsic nature of SBA-15 support were largely retained with B-addition during CSCRM reaction. Unlike SEM images (cf. Figure 6.17), CNF species were observed on the surface of spent promoted and unpromoted catalysts. However, as seen in Figure 6.18 (b), graphitic carbon encapsulating Ni particles was visibly observed for spent unpromoted catalyst (referring to green circle). This observation could explain the lowest catalytic activity of unpromoted catalyst for CSCRM reaction. In addition, as previously mentioned, the

absence of graphitic carbon on 3%B-10%Ni/SBA-15 catalyst (see Figure 6.18 (d)) was assigned to the suppression of graphene islands formation reportedly prone to the production of unreactive and undesirable graphite (Xu and Saeys, 2006; Xu and Saeys, 2007). The nonexistence of graphite on the surface of 3%B-10%Ni/SBA-15 catalyst observed by TEM image is also corroborated with results from Raman (see Figure 6.15) and XRD (cf. Figure 6.16) measurements of spent promoted catalysts. Abatzoglou and Fauteux-Lefebvre (2016) previously found that CNF would not result in significant catalytic deterioration due to its reactivity with oxidizing reactants (i.e., CO<sub>2</sub> and H<sub>2</sub>O) to be removed from catalyst surface whereas graphitic carbon arising from methane cracking (cf. Eq. 2.6) could encapsulate active Ni<sup>0</sup> particles and subsequently prevent them from the adsorption of gaseous reactants (Abatzoglou et al., 2016).

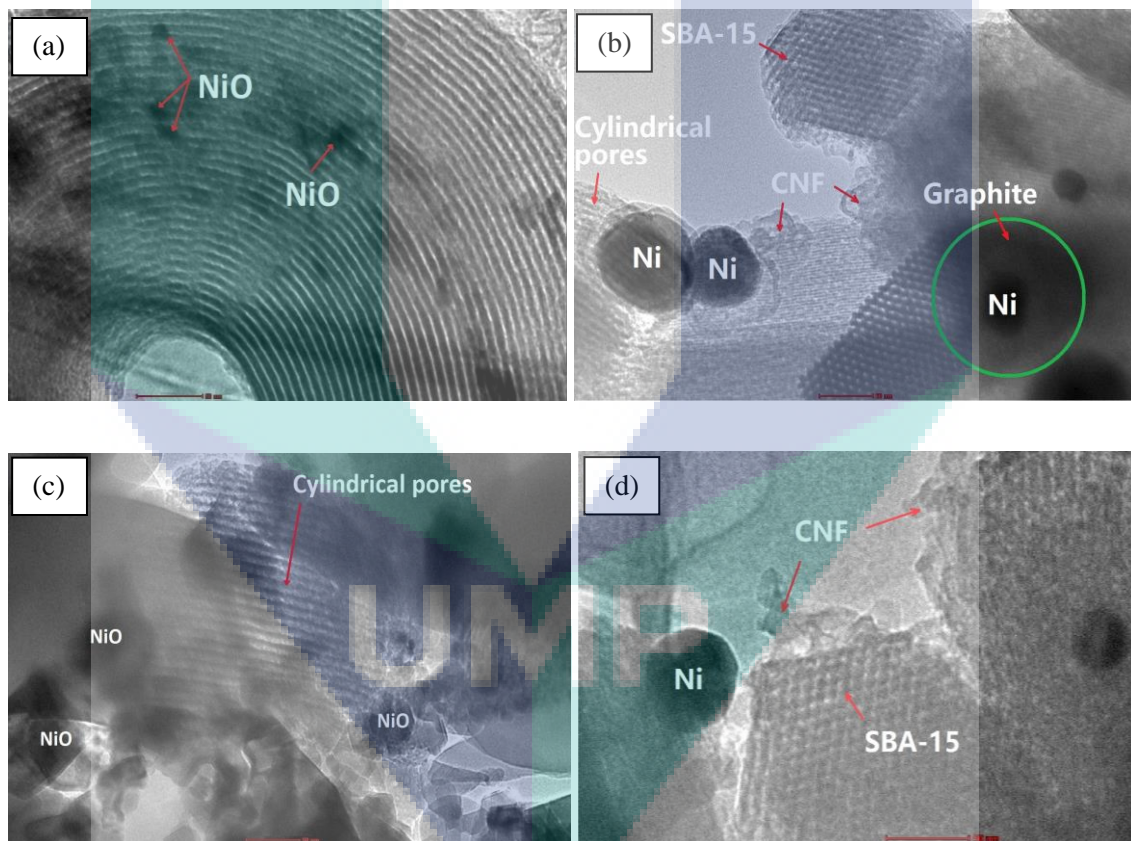


Figure 6.18 TEM images of (a) fresh 10%Ni/SBA-15, (b) spent 10%Ni/SBA-15, (c) fresh 3%B-10%Ni/SBA-15 and (d) spent 3%B-10%Ni/SBA-15 catalysts after CSCRM at stoichiometric feed composition ( $F_{CH_4} : F_{H_2O} : F_{CO_2} = 3 : 2 : 1$ ) and 1073 K.

### 6.6.5 Temperature-programmed Oxidation (TPO) Measurements

Although CNF and graphite on the surface of spent catalysts were qualitatively detected by Raman, SEM and TEM analyses, temperature-programmed oxidation measurements were further performed on spent 10%Ni/SBA-15 and 3%B-promoted catalysts to quantify the amount of total carbon deposition. As seen in TPO profile of spent 10%Ni/SBA-15 catalyst (see Figure 6.19 (a)), two intense peaks P1 and P2 were detected at 613 K and 760 K, respectively. The first oxidation peak P1 at low temperature was ascribed to the oxidation of carbon nanofilament while the second peak P2 located at higher temperature could belong to the gasification of graphite (González et al., 2007; Chen et al., 2013; Selvarajah et al., 2016). However, as seen in Figure 6.19 (b), only low temperature peak P1 was observed and it was shifted to lower temperature of 455 K for 3%B-10%Ni/SBA-15 catalyst. This observation could indicate that the addition of boron promoter not only hindered graphitic carbon formation but also increased the reactivity of CNF species.

Additionally, as seen in Table 6.2, the weight loss measured from TPO analysis for unpromoted and 3%B-promoted catalysts was about 6.4% and 1.5% in this order. Thus, 3%B-10%Ni/SBA-15 catalyst apparently exhibited a stronger inhibiting effect on carbon deposition since the carbon content measured for promoted catalyst was about 4-fold lesser than that of unpromoted catalyst. The lower carbon deposition for promoted catalyst was most likely due to the adsorption competition of boron atoms and carbonaceous species on the octahedral sites of Ni atoms (Xu and Saeys, 2007; Xu et al., 2009). Moreover, CO<sub>2</sub> adsorption on catalyst surface for coke gasification could also be enhanced reasonably due to increasing electron density on active Ni metal surface donated by boron promoter (Xu and Saeys, 2006; Chen et al., 2004). The inhibition of deposited carbon could also contribute to address the superior catalytic activity of B-promoted catalyst to that of unpromoted catalyst.

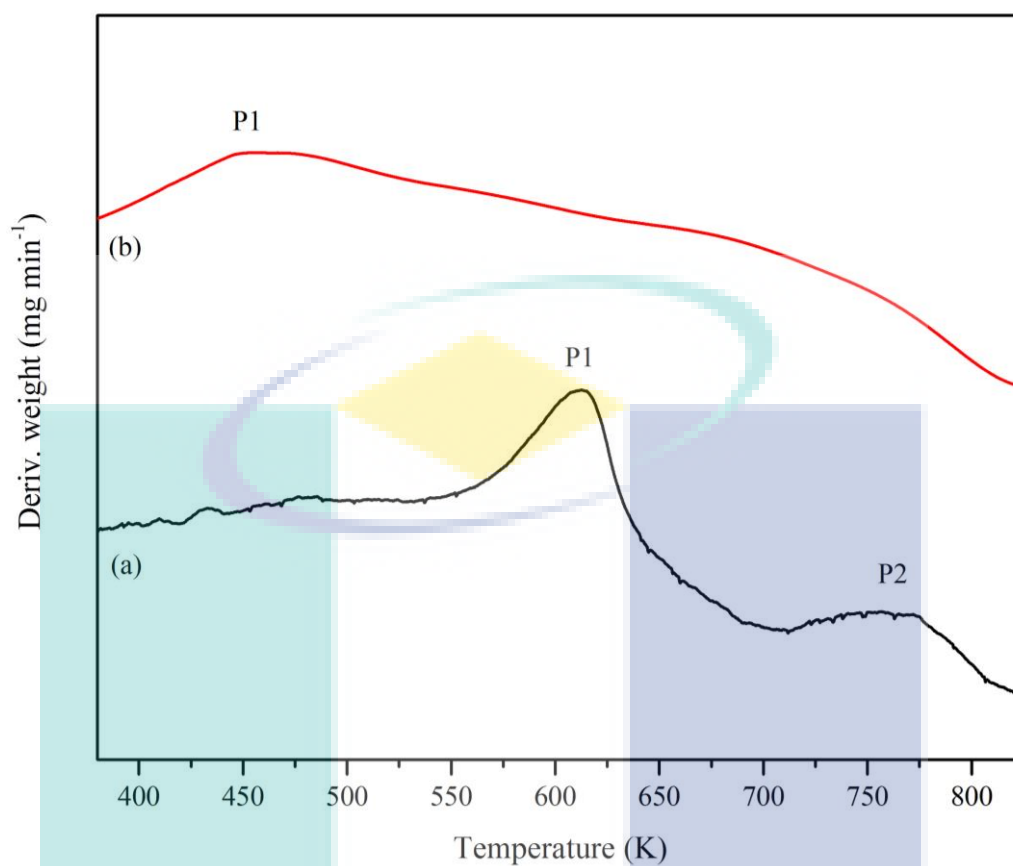


Figure 6.19 TPO profiles of spent (a) 10%Ni/SBA-15 and (b) 3%B-10%Ni/SBA-15 catalysts after CSCRM at stoichiometric feed composition ( $F_{CH_4} : F_{H_2O} : F_{CO_2} = 3:2:1$ ) and 1073 K.

Table 6.2 The weight loss of the spent promoted and unpromoted Ni-based catalysts during TPO measurements

Spent catalysts	Weight loss (%)
10%Ni/SBA-15	6.40
3%B-10%Ni/SBA-15	1.50

## 6.7 Concluding Remarks

The influence of boron dopant on 10%Ni/SBA-15 catalysts has been studied for CSCRM reaction in this chapter. The CH<sub>4</sub> and CO<sub>2</sub> conversions for promoted catalysts were significantly improved with the addition of boron from 1 to 3% by increment about 23.2% and 32.4%, correspondingly with the reaction temperature ranging from 973 to 1073 K. The 3%B appeared to be the best loading for the 10%Ni/SBA-15 catalyst in terms of reactant conversions and H<sub>2</sub> yield respective of the reaction temperature. In terms of reactant partial pressure, the reactant conversions experienced an increase and a drop at  $P_{CO_2}$  beyond 15 kPa could suggest the hindrance of CH<sub>4</sub> adsorption on catalyst surface with rising  $P_{CO_2}$  reactant. Additionally, the CH<sub>4</sub> conversion increased with growing  $P_{H_2O}$  was reasonably due to the improvement of steam gasification of deposited carbon whilst the predominance of SRM resulted in a decline in CO<sub>2</sub> conversion with increasing  $P_{H_2O}$  was observed at high  $P_{H_2O}$  environment. The growing  $P_{CH_4}$  from 35 to 45 kPa resulted in a rise in reactant conversions followed by a significant drop in reactant conversions was observed at  $P_{CH_4}$  beyond 45 kPa. This behavior could be due to the rate of CH<sub>4</sub> decomposition to carbonaceous species was superior and hence, encapsulating the active Ni metallic sites. The  $P_{CO_2}$  of 15 kPa,  $P_{H_2O}$  of 20 kPa and  $P_{CH_4}$  of 45 kPa appeared to be the best feed composition for the CSCRM reaction in terms of reactant conversions and product yields. The longevity test revealed that the 3%B-10%Ni/SBA-15 catalyst exhibited an outstanding catalytic performance by obtaining the lowest degree of catalyst deactivation. In addition, the post-characterization shows that B-promoted catalyst possessed greater carbon-resistance in suppressing the carbon formation, particularly to the graphite formation. This observation further corroborated the enhancement of CSCRM activity over B-promoted catalyst.

## CHAPTER 7

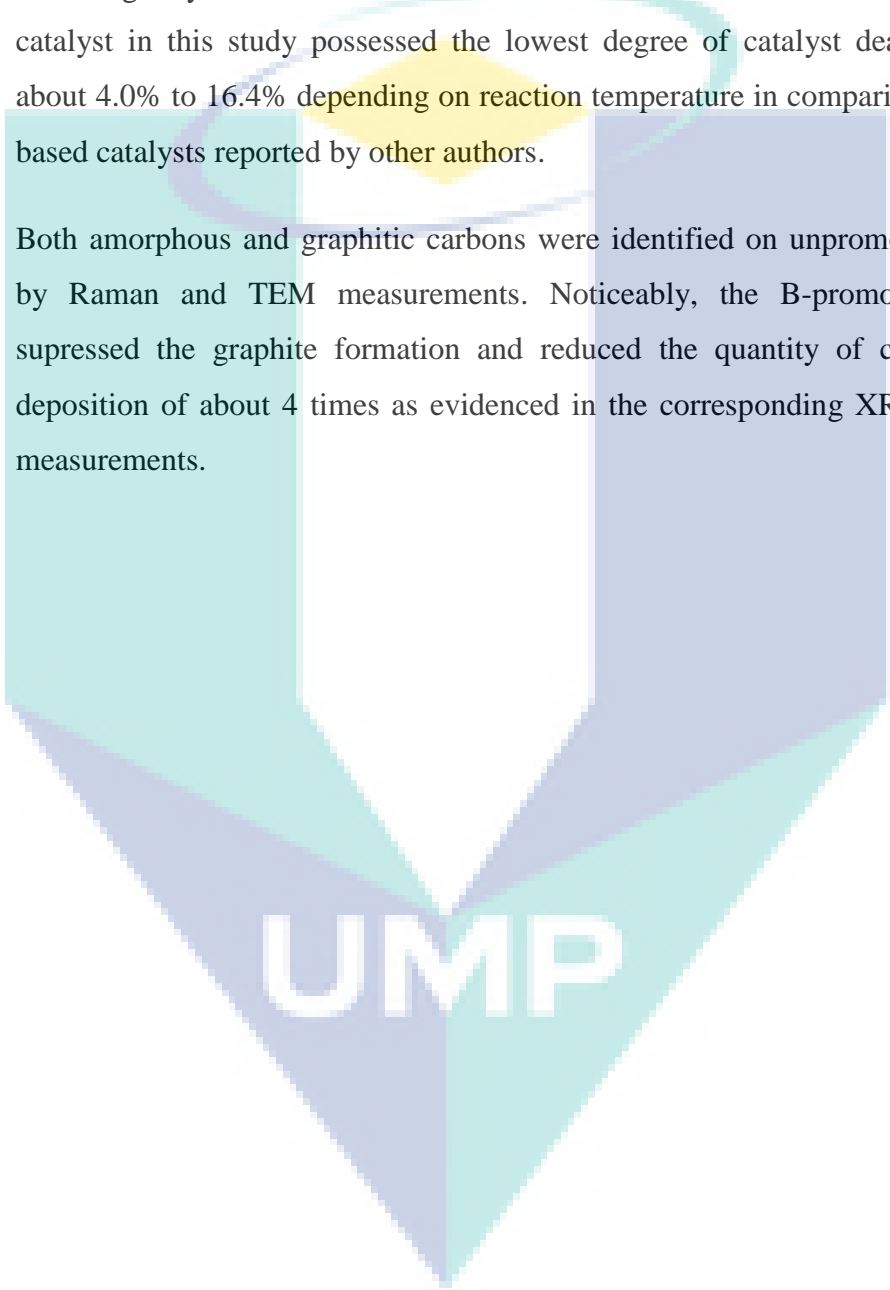
### CONCLUSIONS & RECOMMENDATIONS

#### 7.1 Conclusions

CSCRM reaction is reportedly a prospective substitution of other common reforming processes owing to its high catalytic stability in the coexistence of CO<sub>2</sub> and H<sub>2</sub>O oxidizing reactants and flexible adjustment of H<sub>2</sub>/CO ratios for downstream production (i.e. Fisher-Tropsch and methanol synthesis) by the manipulation of feedstock composition. The objectives of this study have been attained to a large extent and the findings for CSCRM assessment over unpromoted and promoted Ni-based catalysts are summarized as follow:

- i. An inevitable decrease in BET surface area and average NiO crystallite size with boron promotion from 1% to 5%B loading could be due to the agglomeration of metal particles and hence, blocking mesopores of SBA-15 support. H<sub>2</sub>-TPR profiles revealed that the high reduction temperature of 1073 K and long holding time of 2 h employed in this study were sufficient for activating all catalysts during H<sub>2</sub> reduction.
- ii. Regardless of boron loadings, the catalytic activity was improved with an increase in reaction temperature from 973 K to 1073 K due to the endothermic nature of CSCRM. The best promoter loading was about 3%B in terms of CH<sub>4</sub> and CO<sub>2</sub> conversions irrespective of reaction temperatures. The H<sub>2</sub>/CO ratio could be easily manipulated within the range of 1.26-2.71 appropriate for high molecular weight hydrocarbon production from downstream Fischer-Tropsch synthesis.

- iii. In the evaluation of effect of various feed composition on CSCRM reaction, the  $P_{CO_2}$  of 15 kPa,  $P_{H_2O}$  of 20 kPa and  $P_{CH_4}$  of 45 kPa appeared to be the best feed composition for the CSCRM reaction in terms of reactant conversions and product yields.
- iv. The longevity test results for CSCRM shows that the 3%B-10%Ni/SBA-15 catalyst in this study possessed the lowest degree of catalyst deactivation of about 4.0% to 16.4% depending on reaction temperature in comparison with Ni-based catalysts reported by other authors.
- v. Both amorphous and graphitic carbons were identified on unpromoted catalyst by Raman and TEM measurements. Noticeably, the B-promoted catalyst suppressed the graphite formation and reduced the quantity of carbonaceous deposition of about 4 times as evidenced in the corresponding XRD and TPO measurements.

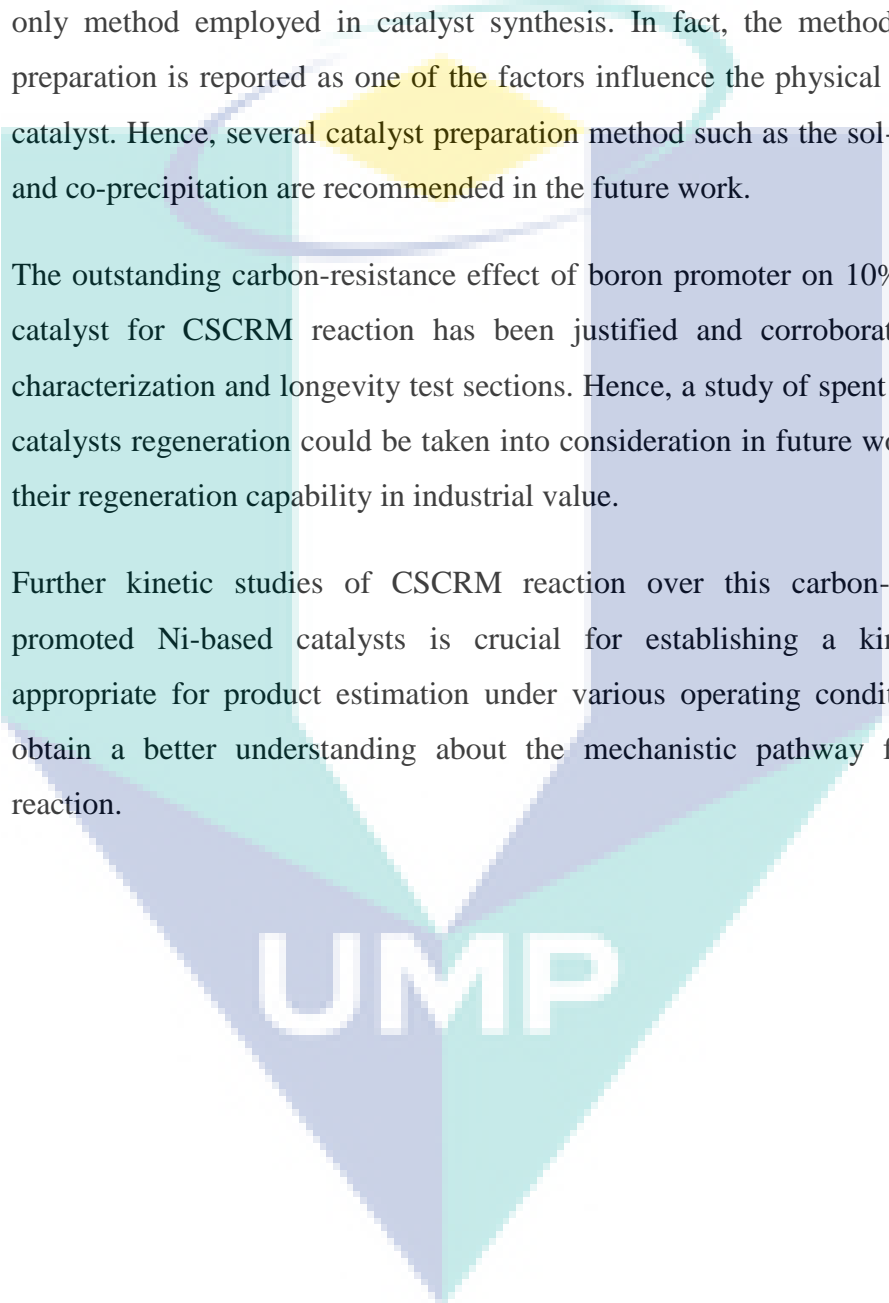
The logo for UIMP (Universiti Malaysia Perlis) is a large, downward-pointing arrow shape. It is composed of four triangular sections meeting at a central point. The top-left and bottom-right sections are light blue, while the top-right and bottom-left sections are a slightly darker shade of blue. The letters 'UIMP' are printed in white, bold, sans-serif font across the center of the arrow.

UIMP

## 7.2 Recommendations

According to the findings obtained from this CSCRM reaction research, recommendations for the future advanced research are suggested as follow:

- i. In this study, the sequential incipient wetness impregnation technique was the only method employed in catalyst synthesis. In fact, the method of catalyst preparation is reported as one of the factors influence the physical attributes of catalyst. Hence, several catalyst preparation method such as the sol-gel, one-pot and co-precipitation are recommended in the future work.
- ii. The outstanding carbon-resistance effect of boron promoter on 10%Ni/SBA-15 catalyst for CSCRM reaction has been justified and corroborated in post-characterization and longevity test sections. Hence, a study of spent B-promoted catalysts regeneration could be taken into consideration in future work to assess their regeneration capability in industrial value.
- iii. Further kinetic studies of CSCRM reaction over this carbon-resistant B-promoted Ni-based catalysts is crucial for establishing a kinetic model appropriate for product estimation under various operating conditions and to obtain a better understanding about the mechanistic pathway for CSCRM reaction.

The logo for UIMP (Universiti Malaysia Perlis) is a large, stylized letter 'V' shape. The left side of the 'V' is light blue, the right side is teal, and the bottom point is a darker blue. The letters 'UIMP' are written in white, bold, sans-serif font across the center of the 'V'.

## REFERENCES

- Abatzoglou, N. and Fauteux-Lefebvre, C. (2016). Review of catalytic syngas production through steam or dry reforming and partial oxidation of studied liquid compounds. *Wiley Interdisciplinary Reviews: Energy and Environment*, 5, 169-187.
- Abdullah, B., Ghani, N.A.A. and Vo, D.V.N. (2017). Recent advances in dry reforming of methane over Ni-based catalysts. *Journal of Cleaner Production*, 162, 170-185.
- Abild-Pedersen, F., Nørskov, J.K., Rostrup-Nielsen, J.R., Sehested, J. and Helveg, S. (2006). Mechanisms for catalytic carbon nanofiber growth studied by Ab initio density functional theory calculations. *Physical Review B*, 73, 115419.
- Adhikari, S., Fernando, S. and Haryanto, A. (2007). Production of hydrogen by steam reforming of glycerin over alumina-supported metal catalysts. *Catalysis Today*, 129, 355-364.
- Anderson, J.B. (1963). A criterion for isothermal behaviour of a catalyst pellet. *Chemical Engineering Science*, 18, 147-148.
- Arcotumapathy, V., Alenazey, F.S., Al-Otaibi, R.L., Vo, D.V.N., Alotaibi, F.M. and Adesina, A.A. (2015). Mechanistic investigation of methane steam reforming over Ce-promoted Ni/SBA-15 catalyst. *Applied Petrochemical Research*, 5, 393-404.
- Argyle, M.D. and Bartholomew, C.H. (2015). Heterogeneous catalyst deactivation and regeneration: a review. *Catalysts*, 5, 145-269.
- Ausubel, J.H. and Marchetti, C. (2001). The evolution of transport. *The Industrial Physicist*, 7, 20-24.
- Azizi, S.N., Ghasemi, S. and Chiani, E. (2013). Nickel/mesoporous silica (SBA-15) modified electrode: An effective porous material for electrooxidation of methanol. *Electrochimica Acta*, 88, 463-472.
- Bae, J.W., Kim, A.R., Baek, S.C. and Jun, K.W. (2011). The role of CeO<sub>2</sub>-ZrO<sub>2</sub> distribution on the Ni/MgAl<sub>2</sub>O<sub>4</sub> catalyst during the combined steam and CO<sub>2</sub> reforming of methane. *Reaction Kinetics, Mechanisms and Catalysis*, 104, 377-388.
- Bahari, M.B., Phuc, N.H.H., Abdullah, B., Alenazey, F. and Vo, D.V.N. (2016). Ethanol dry reforming for syngas production over Ce-promoted Ni/Al<sub>2</sub>O<sub>3</sub> catalyst. *Journal of Environmental Chemical Engineering*, 4, 4830-4838.
- Bakkenne, A., Nuttall, W. and Kazantzis, N. (2016). Sankey-Diagram-based insights into the hydrogen economy of today. *International Journal of Hydrogen Energy*, 41, 7744-7753.

- Bartholomew, C.H. (2001). Mechanisms of catalyst deactivation. *Applied Catalysis A: General*, 212, 17-60.
- Baum, E.J. Chemical Property Estimation: Theory and Application. Lewis Publishers, Boca Raton, 1998.
- Bradford, M.C.J. and Vannice, M.A. (1999). CO<sub>2</sub> reforming of CH<sub>4</sub>. *Catalysis Reviews*, 41, 1-42.
- Brahmkhatri, V. and Patel, A. (2011). 12-Tungstophosphoric acid anchored to SBA-15: An efficient, environmentally benign reusable catalysts for biodiesel production by esterification of free fatty acids. *Applied Catalysis A: General*, 403, 161-172.
- Brik, Y., Kacimi, M., Bozon-Verduraz, F. and Ziyad, M. (2002). Characterization and comparison of the activity of boron-modified Co/TiO<sub>2</sub> catalysts in butan-2-ol conversion and oxidative dehydrogenation of ethane. *Journal of Catalysis*, 211, 470-481.
- Castro Luna, A. and Iriarte, M. (2008). Carbon dioxide reforming of methane over a metal modified Ni-Al<sub>2</sub>O<sub>3</sub> catalyst. *Applied Catalysis A: General*, 343, 10-15.
- Chen, H., Tan, J., Cui, J., Yang, X., Zheng, H., Zhu, Y. and Li, Y. (2017). Promoting effect of boron oxide on Ag/SiO<sub>2</sub> catalyst for the hydrogenation of dimethyl oxalate to methyl glycolate. *Molecular Catalysis*, 433, 346-353.
- Chen, J., Wu, Q., Zhang, J. and Zhang, J. (2008). Effect of preparation methods on structure and performance of Ni/Ce<sub>0.75</sub>Zr<sub>0.25</sub>O<sub>2</sub> catalysts for CH<sub>4</sub>-CO<sub>2</sub> reforming. *Fuel*, 87, 2901-2907.
- Chen, X., Wang, S., Zhuang, J., Qiao, M., Fan, K. and He, H. (2004) Mesoporous silica-supported Ni-B amorphous alloy catalysts for selective hydrogenation of 2-ethylanthraquinone. *Journal of Catalysis*, 227, 419-427.
- Cheng, Z.X., Zhao, X.G., Li, J.L. and Zhu, Q.M. (2001). Role of support in CO<sub>2</sub> reforming of CH<sub>4</sub> over a Ni/γ-Al<sub>2</sub>O<sub>3</sub> catalyst. *Applied Catalysis A: General*, 205, 31-36.
- Choudhary, V.R. and Rajput, A.M. (1996). Simultaneous carbon dioxide and steam reforming of methane to syngas over NiO-CaO catalyst. *Industrial & Engineering Chemistry Research*, 35, 3934-3939.
- Cooper, C.G., Nguyen, T.H., Lee, Y.J., Hardiman, K.M., Safinski, T., Lucien, F.P. and Adesina, A.A. (2008). Alumina-supported cobalt-molybdenum catalyst for slurry phase Fischer-Tropsch synthesis. *Catalysis Today*, 131(1-4), 255-261.
- Das, D. (2001). Hydrogen production by biological processes: A survey of literature. *International Journal of Hydrogen Energy*, 26, 13-28.

- da Silva Veras, T., Mozer, T.S. and da Silva César, A. (2017). Hydrogen: trends, production and characterization of the main process worldwide. *International Journal of Hydrogen Energy*, 42, 2018-2033.
- de Sousa, F.F., de Sousa, H.S., Oliveira, A.C., Junior, M.C., Ayala, A.P., Barros, E.B., Viana, B.C., Josue Filho, M. and Oliveira, A.C. (2012). Nanostructured Ni-containing spinel oxides for the dry reforming of methane: Effect of the presence of cobalt and nickel on the deactivation behaviour of catalysts. *International Journal of Hydrogen Energy*, 37, 3201-3212.
- Di Marcoberardino, G., Sosio, F., Manzolini, G. and Campanari, S. (2015). Fixed bed membrane reactor for hydrogen production from steam methane reforming: Experimental and modeling approach. *International Journal of Hydrogen Energy*, 40, 7559-7567.
- Dixon, A.G. (1997). Heat transfer in fixed beds at very low (<4) tube-to-particle diameter ratio. *Industrial & Engineering Chemistry Research*, 36, 3053-3064.
- Dunn, S. (2002). Hydrogen futures: Toward a sustainable energy system. *International Journal of Hydrogen Energy*, 27, 235-264.
- Dwivedi, P.N. and Upadhyay, S.N. (1977). Particle-fluid mass transfer in fixed and fluidized beds. *Industrial & Engineering Chemistry Process Design & Development*, 16, 157-165.
- Eia, gov. (2016). *International Energy Outlook 2016 - Energy Information Administration*.
- Eswaramoorthi, I. and Dalai, A.K. (2006). Synthesis, characterisation and catalytic performance of boron substituted SBA-15 molecular sieves. *Microporous and Mesoporous Materials*, 93, 1-11.
- Fogler, H.S. (2006). *Elements of Chemical Reaction Engineering*. 4th ed. Upper Saddle River, NJ, USA: Pearson Education, Inc.
- Foo, S.Y., Cheng, C.K., Nguyen, T.H. and Adesina, A.A. (2010). Oxidative CO<sub>2</sub> reforming of methane on alumina-supported Co-Ni catalyst. *Industrial & Engineering Chemistry Research*, 49, 10450-10458.
- Fouskas, A., Kollia, M., Kambolis, A., Papadopoulou, C. and Matralis, H. (2014). Boron-modified Ni/Al<sub>2</sub>O<sub>3</sub> catalysts for reduced carbon deposition during dry reforming of methane. *Applied Catalysis A: General*, 474, 125-134.
- Furimsky, E. and Massoth, F.E. (1999). Deactivation of hydroprocessing catalysts. *Catalysis Today*, 52, 381-495.

- Gálvez, M.E., Albarazi, A. and Da Costa, P. (2015). Enhanced catalytic stability through non-conventional synthesis of Ni/SBA-15 for methane dry reforming at low temperatures. *Applied Catalysis A: General*, 504, 143-150.
- García-Diéguez, M., Pieta, I., Herrera, M., Larrubia, M. and Alemany, L. (2010). Nanostructured Pt- and Ni-based catalysts for CO<sub>2</sub>-reforming of methane. *Journal of Catalysis*, 270, 136-145.
- Gómez, G., Botas, J.Á., Serrano, D.P. and Pizarro, P. (2016). Hydrogen production by methane decomposition over pure silica SBA-15 materials. *Catalysis Today*, 277, 152-160.
- Green, D.W. and Perry, R.H. (2008). *Perry's Chemical Engineers' Handbook*. 8<sup>th</sup> ed. New York, USA: The McGraw-Hill Companies, Inc.
- Gregg, S.J. and Sing, K.S.W. (1982). *Adsorption, surface area and porosity*. 2<sup>nd</sup> ed. New York, USA: Academic Press, Inc.
- He, S., Mei, Z., Liu, N., Zhang, L., Lu, J., Li, X., Wang, J., He, D. and Luo, Y. (2017). Ni/SBA-15 catalysts for hydrogen production by ethanol steam reforming: Effect of nickel precursor. *International Journal of Hydrogen Energy*, 42, 14429-14438.
- Holladay, J.D., Hu, J., King, D.L. and Wang, Y. (2009). An overview of hydrogen production technologies. *Catalysis Today*, 139, 244-260.
- Hou, Z., Chen, P., Fang, H., Zheng, X. and Yashima, T. (2006). Production of synthesis gas via methane reforming with CO<sub>2</sub> on noble metals and small amount of noble-(Rh-) promoted Ni catalysts. *International Journal of Hydrogen Energy*, 31, 555-561.
- Hu, Y.H. and Ruckenstein, E. (2004). Catalytic conversion of methane to synthesis gas by partial oxidation and CO<sub>2</sub> reforming. *Advances in Catalysis*, 48, 297-345.
- Huang, T., Huang, W., Huang, J. and Ji, P. (2011). Methane reforming reaction with carbon dioxide over SBA-15 supported Ni–Mo bimetallic catalysts. *Fuel Processing Technology*, 92, 1868-1875.
- Huang, B., Li, X., Ji, S., Lang, B., Habimana, F. and Li, C. (2008). Effect of MgO promoter on Ni-based SBA-15 catalysts for combined steam and carbon dioxide reforming of methane. *Journal of Natural Gas Chemistry*, 17, 225-231.
- Huang, X.H., Tu, J.P., Zhang, B., Zhang, C.Q., Li, Y., Yuan, Y.F. and Wu, H.M. (2006). Electrochemical properties of NiO–Ni nanocomposite as anode material for lithium ion batteries. *Journal of Power Sources*, 161, 541-544.

- Inderwildi, O.R., Jenkins, S.J. and King, D.A. (2008). Mechanistic studies of hydrocarbon combustion and synthesis on noble metals. *Angewandte Chemie International Edition*, 47, 5253-5255.
- Jabbour, K., Massiani, P., Davidson, A., Casale, S. and El Hassan, N. (2017). Ordered mesoporous “one-pot” synthesized Ni-Mg(Ca)-Al<sub>2</sub>O<sub>3</sub> as effective and remarkably stable catalysts for combined steam and dry reforming of methane (CSDRM). *Applied Catalysis B: Environmental*, 201, 527-542.
- Jang, W.J., Jeong, D.W., Shim, J.O., Kim, H.M., Roh, H.S., Son, I.H. and Lee, S.J. (2016). Combined steam and carbon dioxide reforming of methane and side reactions: Thermodynamic equilibrium analysis and experimental application. *Applied Energy*, 173, 80-91.
- JCPDS powder diffraction file. International centre for diffraction data. PA: Swarthmore, 2000.
- Jensen, M.W. and Ross, M. (2000). The ultimate challenge: developing an infrastructure for fuel cell vehicles. *Environment: Science and Policy for Sustainable Development*, 42, 10-22.
- Jun, K., Roh, H. and Chary, K. (2007). Structure and catalytic properties of ceria-based nickel catalysts for CO<sub>2</sub> reforming of methane. *Catalysis Surveys from Asia*, 11, 97-113.
- Kaczmarczyk, R. and Gurgul, S. (2014). Model approach of carbon deposition phenomenon in steam and dry methane reforming process. *Archives of Metallurgy and Materials*, 59, 145-148.
- Kapokova, L., Pavlova, S., Bunina, R., Alikina, G., Krieger, T., Ishchenko, A., Rogov, V. and Sadykov, V. (2011). Dry reforming of methane over LnFe<sub>0.7</sub>Ni<sub>0.3</sub>O<sub>3-δ</sub> perovskites: Influence of Ln nature. *Catalysis Today*, 164, 227-233.
- Kharat, A.N., Moosavikia, S., Jahromi, B.T. and Badiei, A. (2011). Liquid phase hydroxylation of benzene to phenol over vanadium substituted Keggin anion supported on amine functionalized SBA-15. *Journal of Molecular Catalysis A: Chemical*, 348, 14-19.
- Kim, D., Kwak, B.S., Min, B.K. and Kang, M. (2015). Characterization of Ni and W co-loaded SBA-15 catalyst and its hydrogen production catalytic ability on ethanol steam reforming reaction. *Applied Surface Science*, 332, 736-746.
- Klaewkla, R., Arend, M. and Hoelderich, W.F. (2011). *A review of mass transfer controlling the reaction rate in heterogeneous catalytic systems* (Vol. 5). INTECH Open Access Publisher.

- Koo, K.Y., Roh, H.S., Jung, U.H. and Yoon, W.L. (2012). Combined H<sub>2</sub>O and CO<sub>2</sub> reforming of CH<sub>4</sub> over Ce-promoted Ni/Al<sub>2</sub>O<sub>3</sub> catalyst for gas to liquid (GTL) process: Enhancement of Ni-CeO<sub>2</sub> interaction. *Catalysis Today*, 185, 126-130.
- Koo, K.Y., Lee, S.H., Jung, U.H., Roh, H.S. and Yoon, W.L. (2014). Syngas production via combined steam and carbon dioxide reforming of methane over Ni–Ce/MgAl<sub>2</sub>O<sub>4</sub> catalysts with enhanced coke resistance. *Fuel Processing Technology*, 119, 151-157.
- Kroll, V., Swaan, H., Lacombe, S. and Mirodatos, C. (1996). Methane reforming reaction with carbon dioxide over Ni/SiO<sub>2</sub> Catalyst II. A mechanistic study. *Journal of Catalysis*, 164, 387-398.
- Kumar, N., Shojaee, M. and Spivey, J.J. (2015). Catalytic bi-reforming of methane: from greenhouse gases to syngas. *Current Opinion in Chemical Engineering*, 9, 8-15.
- Landau, M.V., Vradman, L., Wang, X. and Titelman, L. (2005). High loading TiO<sub>2</sub> and ZrO<sub>2</sub> nanocrystals ensembles inside the mesopores of SBA-15: Preparation, texture and stability. *Microporous and Mesoporous Materials*, 78, 117-129.
- Laosiripojana, N., Sutthisripok, W. and Assabumrungrat, S. (2005). Synthesis gas production from dry reforming of methane over CeO<sub>2</sub> doped Ni/Al<sub>2</sub>O<sub>3</sub>: Influence of the doping ceria on the resistance toward carbon formation. *Chemical Engineering Journal*, 112, 13-22.
- Li, D., Zeng, L., Li, X., Wang, X., Ma, H., Assabumrungrat, S. and Gong, J. (2015). Ceria-promoted Ni/SBA-15 catalysts for ethanol steam reforming with enhanced activity and resistance to deactivation. *Applied Catalysis B: Environmental*, 176, 532-541.
- Li, Z., Mo, L., Kathiraser, Y. and Kawi, S. (2014). Yolk–satellite–shell structured Ni–yolk@Ni@SiO<sub>2</sub> nanocomposite: superb catalyst toward methane CO<sub>2</sub> reforming reaction. *ACS Catalysis*, 4, 1526-1536.
- Lin, C., Tao, K., Yu, H., Hua, D. and Zhou, S. (2014). Enhanced catalytic performance of molybdenum-doped mesoporous SBA-15 for metathesis of 1-butene and ethene to propene. *Catalysis Science & Technology*, 4, 4010-4019.
- Liu, D., Quek, X.Y., Wah, H.H.A., Zeng, G., Li, Y. and Yang, Y. (2009). Carbon dioxide reforming of methane over nickel-grafted SBA-15 and MCM-41 catalysts. *Catalysis Today*, 148, 243-250.
- Maier, L., Schädel, B., Delgado, K.H., Tischer, S. and Deutschmann, O. (2011). Steam reforming of methane over nickel: Development of a multi-step surface reaction mechanism. *Topics in Catalysis*, 54, 845-858.

- Marbán, G. and Valdés-Solís, T. (2007). Towards the hydrogen economy. *International Journal of Hydrogen Energy*, 32, 1625-1637.
- Mears, D.E. (1971). Tests for Transport Limitations in Experimental Catalytic Reactors. *Industrial & Engineering Chemistry Process Design and Development*, 10, 541-547.
- Mironova-Ulmane, N., Kuzmin, A., Grabis, J., Sildos, I., Voronin, V.I., Berger, I.F. and Kazantsev, V.A. (2011). Structural and magnetic properties of nickel oxide nanopowders. *In Solid State Phenomena*, 168, 341-344.
- Neumair, S.C., Kaindl, R., Hoffmann, R.D., Huppertz, H. (2012). The new high-pressure borate hydrate  $\text{Cu}_3\text{B}_6\text{O}_{12} \cdot \text{H}_2\text{O}$ . *Solid State Sciences*, 12, 229-235.
- Oemar, U., Kathiraser, Y., Mo, L., Ho, X.K. and Kawi, S. (2016).  $\text{CO}_2$  reforming of methane over highly active La-promoted Ni supported on SBA-15 catalysts: Mechanism and kinetic modelling. *Catalysis Science & Technology*, 6, 1173-1186.
- Olah, G.A., Goepfert, A., Czaun, M., Mathew, T., May, R.B. and Prakash, G.S. (2015). Single step bi-reforming and oxidative bi-reforming of methane (natural gas) with steam and carbon dioxide to metgas ( $\text{CO}-2\text{H}_2$ ) for methanol synthesis: Self-sufficient effective and exclusive oxygenation of methane to methanol with oxygen. *Journal of the American Chemical Society*, 137, 8720-8729.
- Olah, G.A., Goepfert, A., Czaun, M. and Prakash, G.S. (2012). Bi-reforming of methane from any source with steam and carbon dioxide exclusively to metgas ( $\text{CO}-2\text{H}_2$ ) for methanol and hydrocarbon synthesis. *Journal of the American Chemical Society*, 135, 648-650.
- Omae, I. (2006). Aspects of carbon dioxide utilization. *Catalysis Today*, 115, 33-52.
- Omogbe, O., Danh, H.T., Nguyen-Huy, C., Setiabudi, H.D., Abidin, S.Z., Truong, Q.D. and Vo, D.V.N. (2017). Syngas production from methane dry reforming over Ni/SBA-15 catalyst: Effect of operating parameters. *International Journal of Hydrogen Energy*, 42, 11283-11294.
- Özkara-Aydinoğlu, Ş., Özensoy, E. and Aksoylu, A.E. (2009). The effect of impregnation strategy on methane dry reforming activity of Ce promoted Pt/ZrO<sub>2</sub>. *International Journal of Hydrogen Energy*, 34, 9711-9722.
- Özkara-Aydinoğlu, Ş. (2010). Thermodynamic equilibrium analysis of combined carbon dioxide reforming with steam reforming of methane to synthesis gas. *International Journal of Hydrogen Energy*, 35, 12821-12828.

- Park, J.E., Koo, K.Y., Jung, U.H., Lee, J.H., Roh, H.S. and Yoon, W.L. (2015). Syngas production by combined steam and CO<sub>2</sub> reforming of coke oven gas over highly sinter-stable La-promoted Ni/MgAl<sub>2</sub>O<sub>4</sub> catalyst. *International Journal of Hydrogen Energy*, 40, 13909-13917.
- Park, M.H., Choi, B.K., Park, Y.H., Moon, D.J., Park, N.C. and Kim, Y.C. (2015). Kinetics for steam and CO<sub>2</sub> reforming of methane over Ni/La/Al<sub>2</sub>O<sub>3</sub> catalyst. *Journal of Nanoscience and Nanotechnology*, 15, 5255-5258.
- Patterson, A.L. (1939). The Scherrer Formula for X-ray Particle Size Determination. *Physical Review*, 56, 978-982.
- Pudukudy, M., Yaakob, Z. and Akmal, Z.S. (2015). Direct decomposition of methane over SBA-15 supported Ni, Co and Fe based bimetallic catalysts. *Applied Surface Science*, 330, 418-430.
- Rada, S., Culea, M., Culea, E. (2008). Structure of TeO<sub>2</sub>· B<sub>2</sub>O<sub>3</sub> glasses inferred from infrared spectroscopy and DFT calculations. *Journal of Non-Crystalline Solids*, 354, 5491-5495.
- Rath, D. and Parida, K.M. (2011). Copper and nickel modified MCM-41 an efficient catalyst for hydrodehalogenation of chlorobenzene at room temperature. *Industrial & Engineering Chemistry Research*, 50, 2839-2849.
- Roh, H.S., Koo, K.Y., Jeong, J.H., Seo, Y.T., Seo, D.J., Seo, Y.S., Yoon, W.L. and Park, S.B. (2007). Combined reforming of methane over supported Ni catalysts. *Catalysis Letters*, 117, 85-90.
- Roh, H., Potdar, H. and Jun, K. (2004). Carbon dioxide reforming of methane over co-precipitated Ni–CeO<sub>2</sub>, Ni–ZrO<sub>2</sub> and Ni–Ce–ZrO<sub>2</sub> catalysts. *Catalysis Today*, 93, 39-44.
- Roh, H.S., Koo, K.Y. and Yoon, W.L. (2009). Combined reforming of methane over co-precipitated Ni–CeO<sub>2</sub>, Ni–ZrO<sub>2</sub> and Ni–Ce<sub>0.8</sub>Zr<sub>0.2</sub>O<sub>2</sub> catalysts to produce synthesis gas for gas to liquid (GTL) process. *Catalysis Today*, 146, 71-75.
- Ross, J. (2005). Natural gas reforming and CO<sub>2</sub> mitigation. *Catalysis Today*, 100, 151-158.
- Rostrup-Nielsen, J. (2002). Syngas in perspective. *Catalysis Today*, 71, 243-247.
- Ruckenstein, E. and Hu, Y.H. (1998). Combination of CO<sub>2</sub> reforming and partial oxidation of methane over NiO/MgO solid solution catalysts. *Industrial & Engineering Chemistry Research*, 37, 1744-1747.

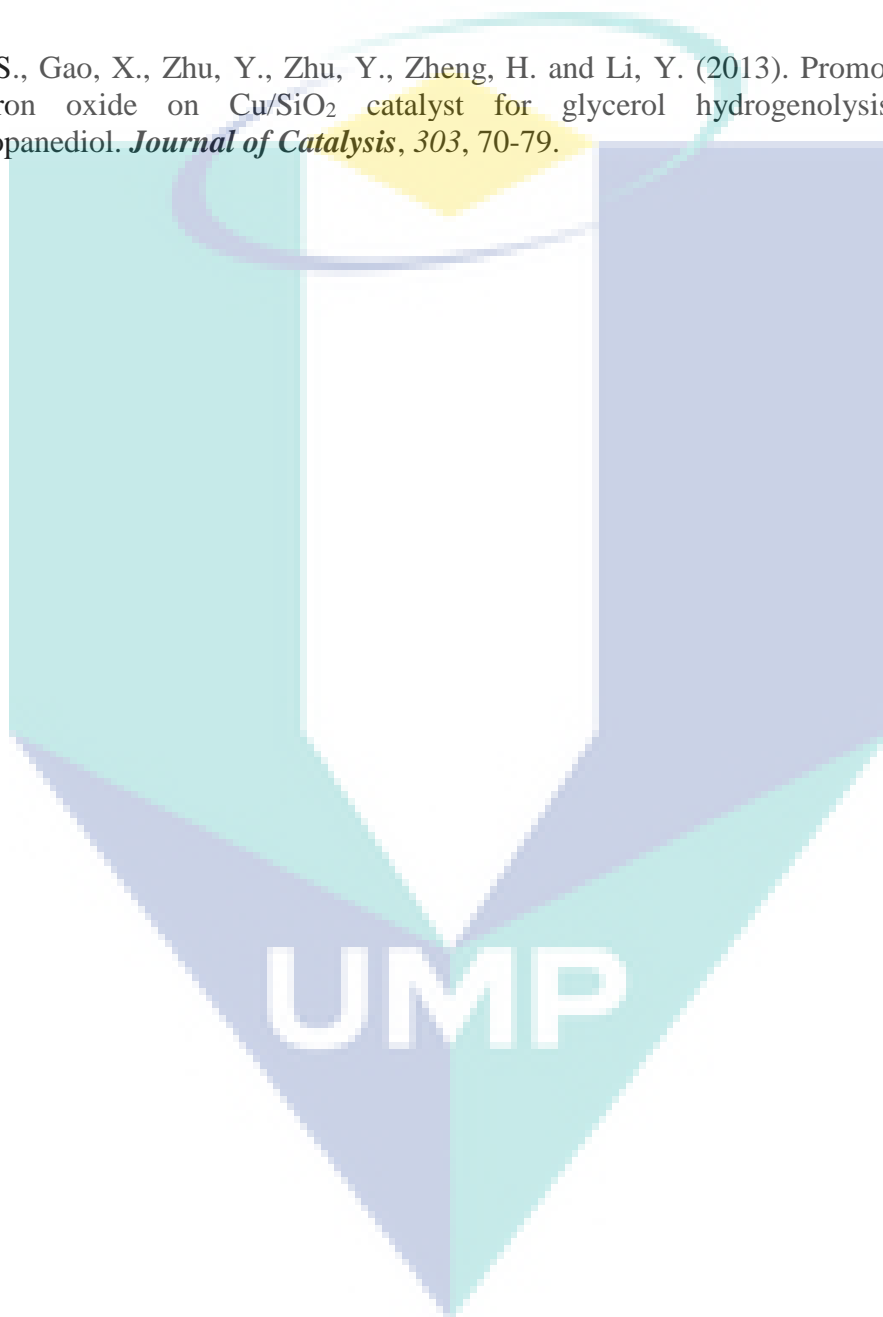
- Ryi, S.K., Lee, S.W., Park, J.W., Oh, D.K., Park, J.S. and Kim, S.S. (2014). Combined steam and CO<sub>2</sub> reforming of methane using catalytic nickel membrane for gas to liquid (GTL) process. *Catalysis Today*, 236, 49-56.
- Sahoo, S., Ray, S. and Singh, I. (2004). Structural characterization of coke on spent hydroprocessing catalysts used for processing of vacuum gas oils. *Applied Catalysis A: General*, 278, 83-91.
- Singh, P.S. (2008). High surface area nanoporous amorphous silica prepared by dodecanol assisted silica formate sol-gel approach. *Journal of Colloid and Interface Science*, 325(1), 207-214.
- Song, S.W., Hidajat, K. and Kawi, S. (2005). Functionalized SBA-15 materials as carriers for controlled drug delivery: Influence of surface properties on matrix-drug interactions. *Langmuir*, 21, 9568-9575.
- Soria, M.A., Mateos-Pedrero, C., Guerrero-Ruiz, A. and Rodríguez-Ramos, I. (2011). Thermodynamic and experimental study of combined dry and steam reforming of methane on Ru/ZrO<sub>2</sub>-La<sub>2</sub>O<sub>3</sub> catalyst at low temperature. *International Journal of Hydrogen Energy*, 36, 15212-15220.
- Stevens, R.W. and Chuang, S.S. (2004). In situ IR study of transient CO<sub>2</sub> reforming of CH<sub>4</sub> over Rh/Al<sub>2</sub>O<sub>3</sub>. *The Journal of Physical Chemistry B*, 108, 696-703.
- Thielemann, J.P., Ressler, T., Walter, A., Tzolova-Müller, G. and Hess, C. (2011). Structure of molybdenum oxide supported on silica SBA-15 studied by Raman, UV-Vis and X-ray absorption spectroscopy. *Applied Catalysis A: General*, 399, 28-34.
- Tsipouriari, V., Efstathiou, A., Zhang, Z. and Verykios, X. (1994). Reforming of methane with carbon dioxide to synthesis gas over supported Rh catalysts. *Catalysis Today*, 21, 579-587.
- Usman, M., Daud, W.W. and Abbas, H.F. (2015). Dry reforming of methane: Influence of process parameters-A review. *Renewable and Sustainable Energy Reviews*, 45, 710-744.
- Verykios, X.E. (2003). Catalytic dry reforming of natural gas for the production of chemicals and hydrogen. *International Journal of Hydrogen Energy*, 28, 1045-1063.
- Wan, H., Li, X., Ji, S., Huang, B., Wang, K. and Li, C. (2007). Effect of Ni loading and Ce<sub>x</sub>Zr<sub>1-x</sub>O<sub>2</sub> promoter on Ni-based SBA-15 catalysts for steam reforming of methane. *Journal of Natural Gas Chemistry*, 16, 139-147.
- Wang, W., Wang, S., Ma, X. and Gong, J. (2011). Recent advances in catalytic hydrogenation of carbon dioxide. *Chemical Society Reviews*, 40, 3703-3727.

- Wang, S. (1999). A comprehensive study on carbon dioxide reforming of methane over Ni/ $\gamma$ -Al<sub>2</sub>O<sub>3</sub>. Catalysts. *Industrial & Engineering Chemistry Research*, 38, 2615-2625.
- Wang, J., Zou, B. and El-Sayed, M.A. (1999). Comparison between the polarized Fourier-transform infrared spectra of aged porous silicon and amorphous silicon dioxide films on Si (100) surface. *Journal of Molecular Structure*, 508, 87-96.
- Wei, J. and Iglesia, E. (2004). Isotopic and kinetic assessment of the mechanism of reactions of CH<sub>4</sub> with CO<sub>2</sub> or H<sub>2</sub>O to form synthesis gas and carbon on nickel catalysts. *Journal of Catalysis*, 224, 370-383.
- Wilhelm, D.J., Simbeck, D.R., Karp, A.D. and Dickenson, R.L. (2001). Syngas production for gas-to-liquids applications: technologies, issues and outlook. *Fuel Processing Technology*, 71, 139-148.
- Xu, J. and Saeys, M. (2006). Improving the coking resistance of Ni-based catalysts by promotion with subsurface boron. *Journal of Catalysis*, 242, 217-226.
- Xu, J. and Saeys, M. (2007). First principles study of the coking resistance and the activity of a boron promoted Ni catalyst. *Chemical Engineering Science*, 62, 5039-5041.
- Xu, J., Chen, L., Tan, K.F., Borgna, A. and Saeys, M. (2009). Effect of boron on the stability of Ni catalysts during steam methane reforming. *Journal of Catalysis*, 261, 158-165.
- Yang, C.M., Liu, P.H., Ho, Y.F., Chiu, C.Y. and Chao, K.J. (2003). Highly dispersed metal nanoparticles in functionalized SBA-15. *Chemistry of Materials*, 15, 275-280.
- Yi, N., Cao, Y., Su, Y., Dai, W.L., He, H.Y. and Fan, K.N. (2005). Nanocrystalline LaCoO<sub>3</sub> perovskite particles confined in SBA-15 silica as a new efficient catalyst for hydrocarbon oxidation. *Journal of Catalysis*, 230, 249-253.
- York, A.P., Xiao, T. and Green, M.L. (2003). Brief overview of the partial oxidation of methane to synthesis gas. *Topics in Catalysis*, 22, 345-358.
- Zangouei, M., Zarringhalam Moghaddam, A., Rzeghi, A. and Omidkhah, M. (2010). Production of syngas by combination of CO<sub>2</sub> reforming and partial oxidation of CH<sub>4</sub> over Ni/Al<sub>2</sub>O<sub>3</sub> catalysts in fixed-bed reactor. *International Journal of Chemical Reactor Engineering*, 8, 1-17.
- Zawadzki, A., Bellido, J.D.A., Lucrédio, A.F. and Assaf, E.M. (2014). Dry reforming of ethanol over supported Ni catalysts prepared by impregnation with methanolic solution. *Fuel Processing Technology*, 128, 432-440.

Zhang, J., Wang, H. and Dalai, A. (2009). Kinetic studies of carbon dioxide reforming of methane over Ni-Co/Al-Mg-O bimetallic catalyst. *Industrial & Engineering Chemistry Research*, 48, 677-684.

Zheng, J., Xia, Z., Li, J., Lai, W., Yi, X., Chen, B., Fang, W. and Wan, H. (2012). Promoting effect of boron with high loading on Ni-based catalyst for hydrogenation of thiophene-containing ethylbenzene. *Catalysis Communications*, 21, 18-21.

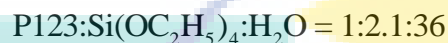
Zhu, S., Gao, X., Zhu, Y., Zhu, Y., Zheng, H. and Li, Y. (2013). Promoting effect of boron oxide on Cu/SiO<sub>2</sub> catalyst for glycerol hydrogenolysis to 1, 2-propanediol. *Journal of Catalysis*, 303, 70-79.



## APPENDIX A CATALYST PREPARATION CALCULATIONS

### A.1 Preparation of SBA-15 support

In order to synthesize a 5 g of SBA-15 support, the mass components were calculated according to desired weight percentage ratio:



Given that 1 mol of  $\text{SiO}_2$  was presented in every 1 mol of  $\text{Si}(\text{OC}_2\text{H}_5)_4$  used in the study, the amount of  $\text{SiO}_2$  needed could be determined by using calculation below.

Since  $208.33 \text{ g mol}^{-1}$  of  $\text{Si}(\text{OC}_2\text{H}_5)_4$  contains  $60.08 \text{ g mol}^{-1}$  of  $\text{SiO}_2$ ,

$$\begin{aligned} \text{Amount of } \text{Si}(\text{OC}_2\text{H}_5)_4 \text{ needed} &= \frac{\text{MW}_{\text{Si}(\text{OC}_2\text{H}_5)_4} \times 5 \text{ g}}{\text{MW}_{\text{SiO}_2}} \\ &= \frac{208.33 \text{ g mol}^{-1} \times 5 \text{ g}}{60.08 \text{ g mol}^{-1}} \\ &= 17.338 \text{ g} \end{aligned}$$

Therefore, the amount of P123 and  $\text{H}_2\text{O}$  needed in gram could be determined based on the weight ratio above.



## A.2 Preparation of Catalyst

The list of catalysts of combined steam and CO<sub>2</sub> reforming of methane is given below:

- i) 10%Ni/SBA-15
- ii) 1%B-10%Ni/SBA-15
- iii) 3%B-10%Ni/SBA-15
- iv) 5%B-10%Ni/SBA-15

In order to prepare 5 g of 10%Ni/SBA-15 catalyst, the mass component was calculated according to desired weight percentage.

$$\begin{aligned}\text{Mass of Ni required} &= 0.10 \times 5 \text{ g} \\ &= 0.50 \text{ g}\end{aligned}$$

$$\begin{aligned}\text{Mass of SBA-15 required} &= 0.90 \times 5 \text{ g} \\ &= 4.50 \text{ g}\end{aligned}$$

Given that 1 mol of Ni was presented in every 1 mol of Ni(NO<sub>3</sub>)<sub>2</sub>·6H<sub>2</sub>O used in the study, the amount of Ni needed could be determined by using calculation below.

Since 290.790 g mol<sup>-1</sup> of Ni(NO<sub>3</sub>)<sub>2</sub>·6H<sub>2</sub>O contains 58.690 g mol<sup>-1</sup> of Ni,

$$\begin{aligned}\text{Amount of Ni(NO}_3)_2 \cdot 6\text{H}_2\text{O needed} &= \frac{\text{MW}_{\text{Ni(NO}_3)_2 \cdot 6\text{H}_2\text{O}} \times 0.50 \text{ g}}{\text{MW}_{\text{Ni}}} \\ &= \frac{290.790 \text{ g mol}^{-1} \times 0.50 \text{ g}}{58.690 \text{ g mol}^{-1}} \\ &= 2.477 \text{ g}\end{aligned}$$

In order to prepare 5 g of 1%B-10%Ni/SBA-15 catalyst, the mass component was calculated according to desired weight percentage.

$$\text{Mass of B required} = 0.01 \times 5 \text{ g}$$

$$= 0.05 \text{ g}$$

$$\text{Mass of Ni required} = 0.10 \times 5 \text{ g}$$

$$= 0.50 \text{ g}$$

$$\text{Mass of SBA-15 required} = 0.89 \times 5 \text{ g}$$

$$= 4.45 \text{ g}$$

Given that 1 mol of B was presented in every 1 mol of  $\text{H}_3\text{BO}_3$  used in the study, the amount of B needed could be determined by using calculation below.

Since  $61.830 \text{ g mol}^{-1}$  of  $\text{H}_3\text{BO}_3$  contains  $10.811 \text{ g mol}^{-1}$  of Bi,

$$\begin{aligned} \text{Amount of } \text{H}_3\text{BO}_3 \text{ needed} &= \frac{\text{MW}_{\text{H}_3\text{BO}_3} \times 0.05 \text{ g}}{\text{MW}_\text{B}} \\ &= \frac{61.830 \text{ g mol}^{-1} \times 0.05 \text{ g}}{10.811 \text{ g mol}^{-1}} = 0.286 \text{ g} \end{aligned}$$

Given that 1 mol of Ni was presented in every 1 mol of  $\text{Ni}(\text{NO}_3)_2 \cdot 6\text{H}_2\text{O}$  used in the study, the amount of Ni needed could be determined by using calculation below.

Since  $290.790 \text{ g mol}^{-1}$  of  $\text{Ni}(\text{NO}_3)_2 \cdot 6\text{H}_2\text{O}$  contains  $58.690 \text{ g mol}^{-1}$  of Ni,

$$\begin{aligned} \text{Amount of } \text{Ni}(\text{NO}_3)_2 \cdot 6\text{H}_2\text{O} \text{ needed} &= \frac{\text{MW}_{\text{Ni}(\text{NO}_3)_2 \cdot 6\text{H}_2\text{O}} \times 0.50 \text{ g}}{\text{MW}_\text{Ni}} \\ &= \frac{290.790 \text{ g mol}^{-1} \times 0.50 \text{ g}}{58.690 \text{ g mol}^{-1}} \\ &= 2.477 \text{ g} \end{aligned}$$

In order to prepare 5 g of 3%B-10%Ni/SBA-15 catalyst, the mass component was calculated according to desired weight percentage.

$$\text{Mass of B required} = 0.03 \times 5 \text{ g}$$

$$= 0.15 \text{ g}$$

$$\text{Mass of Ni required} = 0.10 \times 5 \text{ g}$$

$$= 0.50 \text{ g}$$

$$\text{Mass of SBA-15 required} = 0.87 \times 5 \text{ g}$$

$$= 4.35 \text{ g}$$

Given that 1 mol of B was presented in every 1 mol of  $\text{H}_3\text{BO}_3$  used in the study, the amount of B needed could be determined by using calculation below.

Since  $61.830 \text{ g mol}^{-1}$  of  $\text{H}_3\text{BO}_3$  contains  $10.811 \text{ g mol}^{-1}$  of Bi,

$$\begin{aligned} \text{Amount of } \text{H}_3\text{BO}_3 \text{ needed} &= \frac{\text{MW}_{\text{H}_3\text{BO}_3} \times 0.15 \text{ g}}{\text{MW}_\text{B}} \\ &= \frac{61.830 \text{ g mol}^{-1} \times 0.15 \text{ g}}{10.811 \text{ g mol}^{-1}} \\ &= 0.858 \text{ g} \end{aligned}$$

Given that 1 mol of Ni was presented in every 1 mol of  $\text{Ni}(\text{NO}_3)_2 \cdot 6\text{H}_2\text{O}$  used in the study, the amount of Ni needed could be determined by using calculation below.

Since  $290.790 \text{ g mol}^{-1}$  of  $\text{Ni}(\text{NO}_3)_2 \cdot 6\text{H}_2\text{O}$  contains  $58.690 \text{ g mol}^{-1}$  of Ni,

$$\begin{aligned} \text{Amount of } \text{Ni}(\text{NO}_3)_2 \cdot 6\text{H}_2\text{O} \text{ needed} &= \frac{\text{MW}_{\text{Ni}(\text{NO}_3)_2 \cdot 6\text{H}_2\text{O}} \times 0.50 \text{ g}}{\text{MW}_\text{Ni}} \\ &= \frac{290.790 \text{ g mol}^{-1} \times 0.50 \text{ g}}{58.690 \text{ g mol}^{-1}} \\ &= 2.477 \text{ g} \end{aligned}$$

In order to prepare 5 g of 5%B-10%Ni/SBA-15 catalyst, the mass component was calculated according to desired weight percentage.

$$\text{Mass of B required} = 0.05 \times 5 \text{ g}$$

$$= 0.25 \text{ g}$$

$$\text{Mass of Ni required} = 0.10 \times 5 \text{ g}$$

$$= 0.50 \text{ g}$$

$$\text{Mass of SBA-15 required} = 0.85 \times 5 \text{ g}$$

$$= 4.25 \text{ g}$$

Given that 1 mol of B was presented in every 1 mol of  $\text{H}_3\text{BO}_3$  used in the study, the amount of B needed could be determined by using calculation below.

Since  $61.830 \text{ g mol}^{-1}$  of  $\text{H}_3\text{BO}_3$  contains  $10.811 \text{ g mol}^{-1}$  of B,

$$\begin{aligned} \text{Amount of } \text{H}_3\text{BO}_3 \text{ needed} &= \frac{\text{MW}_{\text{H}_3\text{BO}_3} \times 0.25 \text{ g}}{\text{MW}_B} \\ &= \frac{61.830 \text{ g mol}^{-1} \times 0.25 \text{ g}}{10.811 \text{ g mol}^{-1}} \\ &= 1.430 \text{ g} \end{aligned}$$

Given that 1 mol of Ni was presented in every 1 mol of  $\text{Ni}(\text{NO}_3)_2 \cdot 6\text{H}_2\text{O}$  used in the study, the amount of Ni needed could be determined by using calculation below.

Since  $290.790 \text{ g mol}^{-1}$  of  $\text{Ni}(\text{NO}_3)_2 \cdot 6\text{H}_2\text{O}$  contains  $58.690 \text{ g mol}^{-1}$  of Ni,

$$\begin{aligned} \text{Amount of } \text{Ni}(\text{NO}_3)_2 \cdot 6\text{H}_2\text{O} \text{ needed} &= \frac{\text{MW}_{\text{Ni}(\text{NO}_3)_2 \cdot 6\text{H}_2\text{O}} \times 0.50 \text{ g}}{\text{MW}_{\text{Ni}}} \\ &= \frac{290.790 \text{ g mol}^{-1} \times 0.50 \text{ g}}{58.690 \text{ g mol}^{-1}} \\ &= 2.477 \text{ g} \end{aligned}$$

**APPENDIX B**  
**COMBINED STEAM AND CO<sub>2</sub> REFORMING OF METHANE REACTION**  
**CALCULATION**

**B.1 Calculation of Catalytic Performance**

An example for estimating catalytic activity during CSCRM reaction is given in this section. Table B.1 shows the outlet flow rate from CSCRM reaction over 10%Ni/SBA-15 catalyst at 1073 K,  $P_{CH_4} = 45$  kPa,  $P_{H_2O} = 30$  kPa and  $P_{CO_2} = 15$  kPa .

Table B.1 Outlet flow rate (ml min<sup>-1</sup>) obtained from CSCRM reaction over 10%Ni/SBA-15 catalyst at 1073 K,  $P_{CH_4} = 45$  kPa,  $P_{H_2O} = 30$  kPa and  $P_{CO_2} = 15$  kPa

Species	Outlet flow rate (ml min <sup>-1</sup> )						
	1 h	2 h	3 h	4 h	5 h	6 h	7 h
CH <sub>4</sub>	9.28	7.56	7.82	7.92	8.48	9.11	8.52
CO <sub>2</sub>	2.28	3.15	2.68	3.16	3.20	3.27	3.17
N <sub>2</sub>	16.30	17.05	20.81	15.55	13.25	11.17	12.41
H <sub>2</sub>	39.88	47.84	41.75	51.63	49.25	47.47	45.15
CO	17.87	19.45	19.38	20.87	20.28	19.92	18.82

The inlet flow rates of CH<sub>4</sub>, H<sub>2</sub>O, CO<sub>2</sub> and N<sub>2</sub> are given as 26.31 ml min<sup>-1</sup>, 17.76 ml min<sup>-1</sup>, 7.83 ml min<sup>-1</sup> and 6.38 ml min<sup>-1</sup>, respectively.

The conversion for CH<sub>4</sub> and CO<sub>2</sub> at 1 h are calculated as:

$$X_{CH_4} (\%) = \frac{F_{CH_4}^{In} - F_{CH_4}^{Out}}{F_{CH_4}^{In}} \times 100\% \quad \text{B.1}$$

$$X_{CH_4} (\%) = \frac{26.31 - 9.28}{26.31} \times 100\% = 64.71\%$$

$$X_{CO_2} (\%) = \frac{F_{CO_2}^{In} - F_{CO_2}^{Out}}{F_{CO_2}^{In}} \times 100\% \quad \text{B.2}$$

$$X_{CO_2} (\%) = \frac{7.83 - 2.28}{7.83} \times 100\% = 70.82\%$$

The H<sub>2</sub> and CO yield,  $Y_{H_2}$  and  $Y_{CO}$  are calculated as:

$$Y_{H_2} (\%) = \frac{2F_{H_2}^{Out}}{4F_{CH_4}^{In} + 2F_{H_2O}^{In}} \times 100\% \quad \text{B.3}$$

$$Y_{H_2} (\%) = \frac{2(39.88)}{4(26.31) + 2(17.76)} \times 100\% = 56.67\%$$

$$Y_{CO} (\%) = \frac{F_{CO}^{Out}}{F_{CH_4}^{In} + F_{CO_2}^{In}} \times 100\% \quad \text{B.4}$$

$$Y_{CO} (\%) = \frac{(17.87)}{(26.31) + (7.83)} \times 100\% = 52.34\%$$

The H<sub>2</sub>/CO product ratio can be computed from:

$$\frac{H_2}{CO} = \frac{r_{H_2}}{r_{CO}} \quad \text{B.5}$$

$$\frac{H_2}{CO} = \frac{2.73 \times 10^{-4}}{1.21 \times 10^{-4}} = 2.23$$

UMP

## APPENDIX C CALIBRATION CURVES

### C.1 Calibration Curve for Syringe Pump

Equipment: syringe pump with a 30 ml syringe, 10 ml pipette, tube, retort stand and stopwatch

Chemical: distilled water

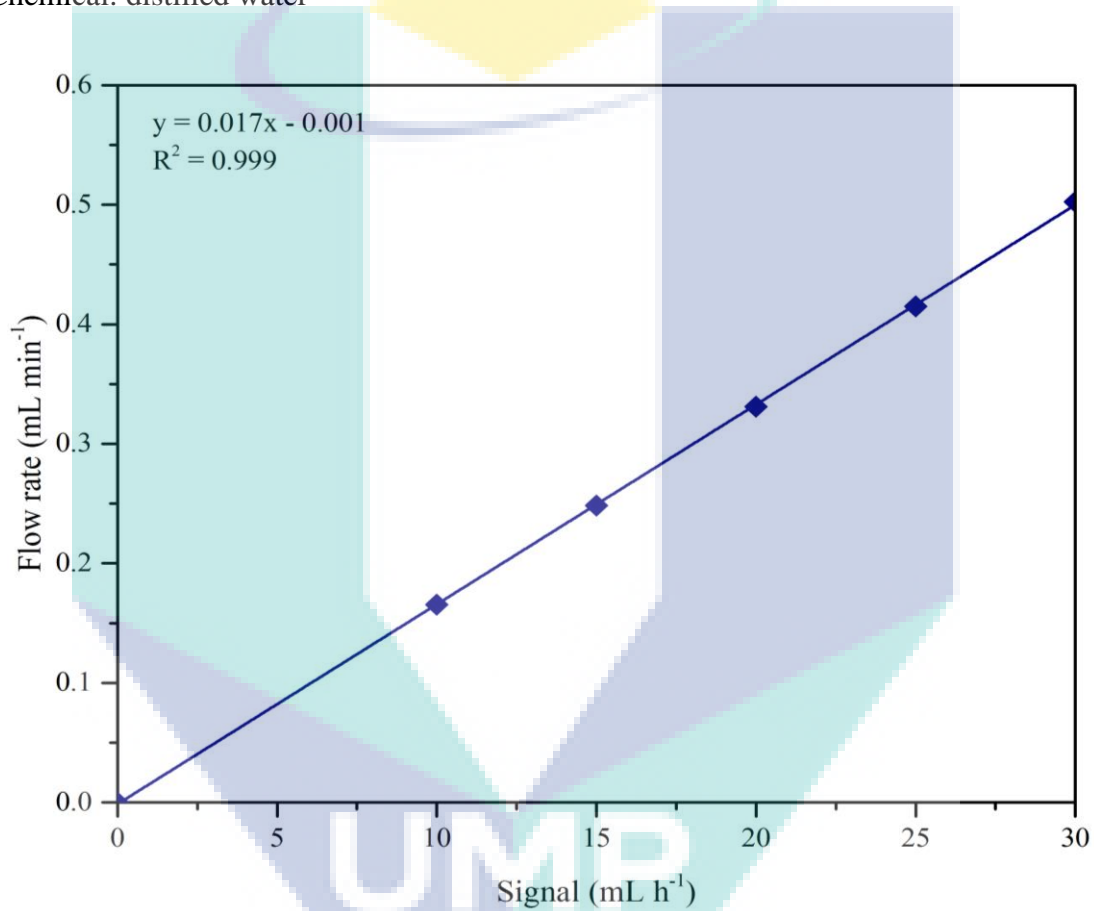


Figure C.1 The calibration curve of syringe pump using distilled water.

## C.2 Calibration Curve for Mass Flow Controller (MFC)

Equipment: mass flow controller (MFC), bubble flowmeter, stopwatch

Gases: CH<sub>4</sub>, N<sub>2</sub>, H<sub>2</sub> and CO<sub>2</sub>

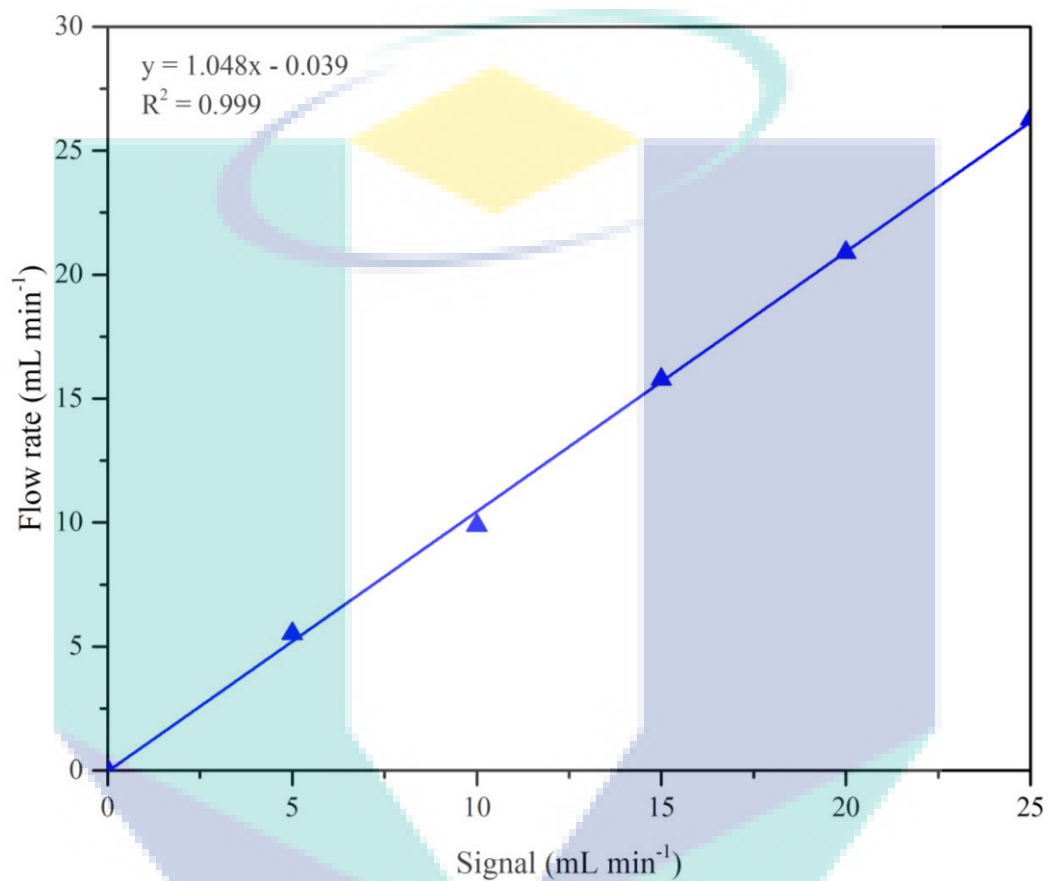


Figure C.2 The calibration curve of MFC using CH<sub>4</sub> gas.

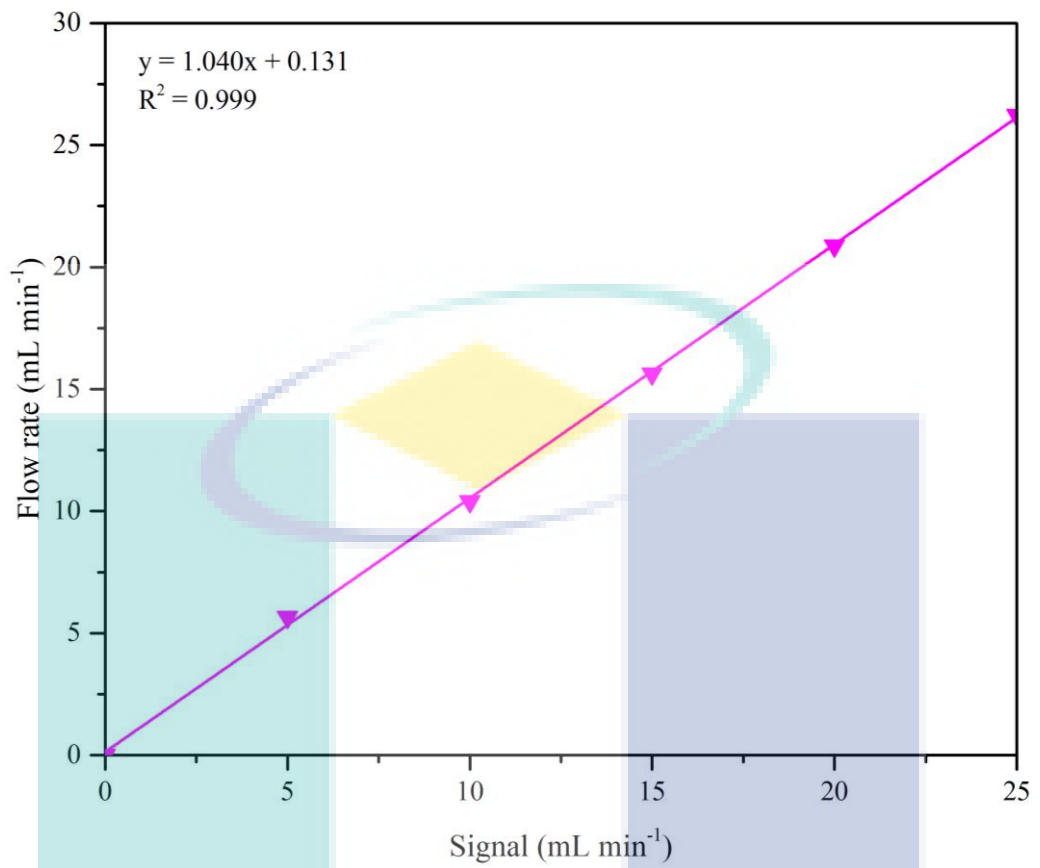


Figure C.3 The calibration curve of MFC using N<sub>2</sub> gas.

UMP

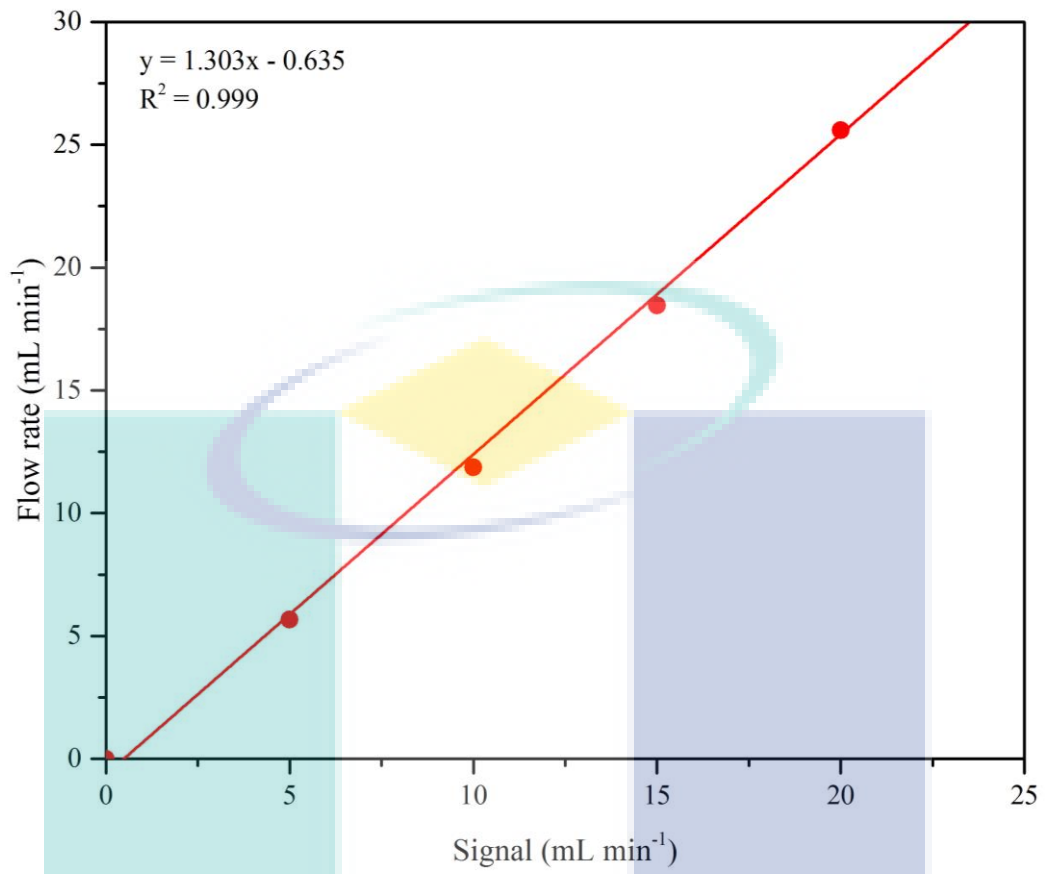


Figure C.4 The calibration curve of MFC using H<sub>2</sub> gas.

UMP

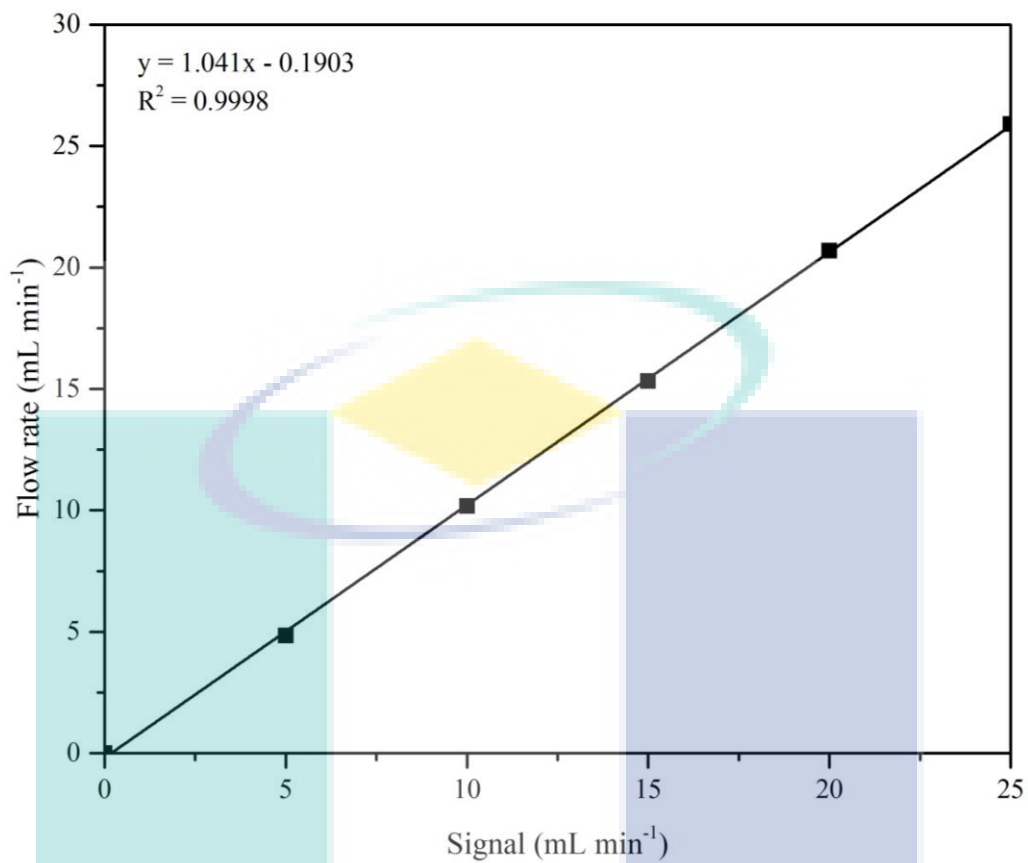


Figure C.5 The calibration curve of MFC using CO<sub>2</sub> gas.

UMP

## APPENDIX D TRANSPORT RESISTANCE CALCULATIONS

### D.1 External Mass Transfer Resistance

The external mass transfer resistances could be neglected when the calculated value for the formula below less than 0.15 (Mears, 1971).

$$\frac{(-r_{\text{exp}})\rho_b R_p n}{k_c C_{Ab}} < 0.15 \quad \text{D.1}$$

where  $(-r_{\text{exp}}) = 6.32 \times 10^{-5} \text{ mol g}_{\text{cat}}^{-1} \text{ s}^{-1}$

$$\rho_b = 0.67 \text{ g cm}^{-3}$$

$$R_p = 9.75 \times 10^{-5} \text{ m}$$

$$n = 1.4$$

$$C_{Ab} = 4.09 \times 10^{-5} \text{ mol cm}^{-3}$$

The mass transfer coefficient,  $k_c$  could be determined as follow.

#### Calculation of mass transfer coefficient, $k_c$

Density of the gas mixture,  $\rho_g$  is calculated:

$$\rho_g = \frac{W_g P}{RT} \quad \text{D.2}$$

where P = standard pressure (101325 Pa)

R = ideal gas constant ( $8.314 \text{ m}^3 \text{ Pa K}^{-1} \text{ mol}^{-1}$ )

T = reaction temperature (1073 K)

Molar mass of gas mixture,  $W_g = \sum_i M_i y_i$  (where  $i$ :  $\text{N}_2$ ,  $\text{CO}_2$ ,  $\text{CH}_4$  and  $\text{H}_2\text{O}$ ) =  $0.022 \text{ kg mol}^{-1}$

$$\rho_g = \frac{0.022 \frac{\text{kg}}{\text{mol}} \times 101325 \text{ Pa}}{8.314 \frac{\text{m}^3 \cdot \text{Pa}}{\text{K} \cdot \text{mol}} \times 1073 \text{ K}} = 0.251 \text{ kg m}^{-3}$$

The superficial gas velocity,  $U$  was determined by using equation below while the volumetric gas flow rate,  $V = 60 \text{ mL min}^{-1}$  at 298 K:

$$U = \frac{V}{A} = \frac{60 \frac{\text{mL}}{\text{min}} \times 1 \text{ m}^3 \times 1 \text{ min} \times 1073 \text{ K}}{4.90 \times 10^{-5} \text{ m}^2 \times 10^6 \text{ mL} \times 60 \text{ s} \times 298 \text{ K}} = 7.35 \times 10^{-2} \text{ m s}^{-3} \quad \text{D.3}$$

Viscosity of the gas mixture was calculated by applying Eqs. D.4 to D.6:

$$\mu_g = \sum_i \frac{y_i \mu_i}{\sum_{j \neq i} y_j \phi_{ij}} \quad \text{D.4}$$

$$\phi_{ji} = \left( \frac{\mu_j}{\mu_i} \right) \left( \frac{M_i}{M_j} \right) \phi_{ij} \quad \text{D.5}$$

$$\phi_{ij} = \frac{\left[ 1 + \left( \frac{\mu_i}{\mu_j} \right)^{\frac{1}{2}} \left( \frac{M_j}{M_i} \right)^{\frac{1}{4}} \right]^2}{\left[ 8 \left( 1 + \left( \frac{M_i}{M_j} \right) \right) \right]^{\frac{1}{2}}} \quad \text{D.6}$$

where  $i, j = \text{N}_2, \text{CH}_4, \text{H}_2\text{O}$  and  $\text{CO}_2$

$y$  = mole fraction of component gases

( $\text{CH}_4 = 0.444, \text{H}_2\text{O} = 0.296, \text{CO}_2 = 0.148$  and  $\text{N}_2 = 0.112$ )

$M$  = molecular weight of component gases

( $\text{CH}_4 = 16.04 \text{ g mol}^{-1}, \text{H}_2\text{O} = 18.02 \text{ g mol}^{-1},$

$\text{CO}_2 = 44.01 \text{ g mol}^{-1}$  and  $\text{N}_2 = 28.01 \text{ g mol}^{-1}$ )

$\mu$  = viscosity of component gases

( $\text{CH}_4 = 2.94 \times 10^{-5} \text{ kg m}^{-1} \text{ s}^{-1}, \text{H}_2\text{O} = 4.08 \times 10^{-5} \text{ kg m}^{-1} \text{ s}^{-1},$

$\text{CO}_2 = 4.19 \times 10^{-5} \text{ kg m}^{-1} \text{ s}^{-1}, \text{N}_2 = 4.35 \times 10^{-5} \text{ kg m}^{-1} \text{ s}^{-1}$  )

Therefore, the value of  $\phi$  can be determined by substituting the values of  $M$  and  $\mu$  in Eqs, D.5 and D.6 and subsequent values of  $\phi$  and  $y$  are substituted in Eq. D.4 to obtain  $\mu_g = 1.84 \times 10^{-5} \text{ kg m}^{-1} \text{ s}^{-1}$ .

Therefore, Reynolds number (Re) can be estimated by using Eq. D.7:

$$\text{Re} = \frac{\rho_g U d_p}{\mu_g} \quad \text{D.7}$$

$$\text{Re} = \frac{\left(0.251 \frac{\text{kg}}{\text{m}^3}\right) \left(7.35 \times 10^{-2} \frac{\text{m}}{\text{s}^3}\right) \left(1.95 \times 10^{-4} \text{ m}\right)}{1.84 \times 10^{-5} \text{ kg m}^{-1} \text{ s}^{-1}} = 0.196$$

The diffusivity of  $\text{CH}_4$  into a mixture of  $\text{H}_2\text{O}$ ,  $\text{CO}_2$  and  $\text{N}_2$  is given by:

$$D_g = \frac{1 - y_i}{\sum_j \frac{y_j}{D_{ij}}} \quad \text{D.8}$$

$$D_{ij} = \frac{1 \times 10^{-3} T^{1.75} \sqrt{\frac{(M_i + M_j)}{M_i M_j}}}{P \left[ \left( \sum v_i \right)^{\frac{1}{3}} + \left( \sum v_j \right)^{\frac{1}{3}} \right]^2} \quad \text{D.9}$$

where  $i = \text{CH}_4$

$j = \text{H}_2\text{O}, \text{CO}_2, \text{N}_2$

$y$  = mole fraction of component gases ( $\text{CH}_4 = 0.444$ ,  $\text{H}_2\text{O} = 0.296$ ,  $\text{CO}_2 = 0.148$ ,  $\text{N}_2 = 0.112$ )

$M$  = molecular weight of component gases

( $\text{CH}_4 = 16.04 \text{ g mol}^{-1}$ ,  $\text{H}_2\text{O} = 18.02 \text{ g mol}^{-1}$ ,  $\text{CO}_2 = 44.01 \text{ g mol}^{-1}$ ,  $\text{N}_2 = 28.013 \text{ g mol}^{-1}$ )

$P$  = standard pressure (1 atm)

$T$  = reaction temperature (1073 K)

$v$  = atomic diffusion volumes

( $\text{CH}_4 = 24.42 \text{ cm}^3 \text{ mol}^{-1}$ ,  $\text{H}_2\text{O} = 9.44 \text{ cm}^3 \text{ mol}^{-1}$ ,  $\text{CO}_2 = 26.9 \text{ cm}^3 \text{ mol}^{-1}$ ,  $\text{N}_2 = 17.9 \text{ cm}^3 \text{ mol}^{-1}$ )

$$D_g = \frac{1 - 0.444}{\sum \left( \frac{0.296}{2.75 \times 10^{-4} \frac{\text{m}^2}{\text{s}}} + \frac{0.148}{1.69 \times 10^{-4} \frac{\text{m}^2}{\text{s}}} + \frac{0.112}{2.07 \times 10^{-4} \frac{\text{m}^2}{\text{s}}} \right)} = 2.23 \times 10^{-4} \text{ m}^2 \text{ s}^{-1}$$

The Schmidt number,  $Sc$  can be estimated as follow:

$$Sc = \frac{\mu_g}{\rho_g D_g} \quad \text{D.10}$$

$$Sc = \frac{1.84 \times 10^{-5} \frac{\text{kg}}{\text{m.s}}}{\left( 0.251 \frac{\text{kg}}{\text{m}^3} \right) \left( 2.23 \times 10^{-4} \frac{\text{m}^2}{\text{s}} \right)} = 0.328$$

Since the Reynolds number,  $Re < 350$ , the estimation for Colburn's mass transfer factor can be performed by using Eq. D.11.

$$j_D = \frac{1}{\varepsilon} \left[ \left( \frac{0.765}{Re^{0.82}} \right) + \left( \frac{0.365}{Re^{0.386}} \right) \right] \quad \text{D.11}$$

where  $\varepsilon =$  void fraction (0.8),

$$j_D = \frac{1}{0.8} \left[ \left( \frac{0.765}{0.196^{0.82}} \right) + \left( \frac{0.365}{0.196^{0.386}} \right) \right] = 4.494$$

Therefore,  $k_c$  can be determined by using Eq. (D.12),

$$k_c = \frac{j_D U}{Sc^{\frac{2}{3}}} \quad \text{D.12}$$

$$k_c = \frac{(4.494) \left( 7.35 \times 10^{-2} \frac{\text{m}}{\text{s}} \right)}{0.328^{\frac{2}{3}}} = 69.403 \text{ cm s}^{-1}$$

Thus, the value of Mears criterion is:

$$\frac{(-r_{\text{exp}}) \rho_b R_p n}{k_c C_{Ab}} = \frac{\left( 6.32 \times 10^{-5} \frac{\text{mol}}{\text{g}_{\text{cat}} \cdot \text{s}} \right) \left( 0.67 \frac{\text{g}}{\text{cm}^3} \right) \left( 9.75 \times 10^{-3} \text{ cm} \right) (1.4)}{\left( 69.403 \frac{\text{cm}}{\text{s}} \right) \left( 4.09 \times 10^{-5} \frac{\text{mol}}{\text{cm}^3} \right)} = 2.04 \times 10^{-4} < 0.15$$

## D.2 Internal (Intraparticle) Mass Transfer Resistance

Weisz-Prater criterion is expressed in Eq. D.13 to assure the effect of pore diffusion resistance is negligible.

$$\frac{(-r_{\text{exp}})\rho_c R_p^2}{D_{\text{eff}} C_{Ab}} < 1 \quad \text{D.13}$$

where  $(-r_{\text{exp}}) = 6.32 \times 10^{-5} \text{ mol g}_{\text{cat}}^{-1} \text{ s}^{-1}$

$$\rho_c = 3.35 \text{ g cm}^{-3}$$

$$R_p = 9.75 \times 10^{-5} \text{ m}$$

$$C_{Ab} = 4.09 \times 10^{-5} \text{ mol cm}^{-3}$$

( $C_{Ab} = C_{As}$  since external mass transfer effects is negligible)

$D_{\text{eff}}$  = effective diffusivity of  $\text{CH}_4$  into a mixture of  $\text{H}_2\text{O}$ ,  $\text{CO}_2$  and  $\text{N}_2$  ( $\text{m}^2 \text{ s}^{-1}$ )

### Determination of effective diffusivity, $D_{\text{eff}}$

The effective diffusivity was estimated by using Eq. D.14,

$$D_{\text{eff}} = \frac{D_g \omega_p \sigma_c}{\tilde{\tau}} \quad \text{D.14}$$

where  $D_g$  = diffusivity of  $\text{CH}_4$  into a mixture of  $\text{H}_2\text{O}$ ,  $\text{CO}_2$  and  $\text{N}_2$  ( $2.23 \times 10^{-4} \text{ m}^2 \text{ s}^{-1}$ )

$\omega_p$  = catalyst pellet porosity (0.4)

$\sigma_c$  = construction factor (0.8)

$\tilde{\tau}$  = tortuosity (3)

$$D_{\text{eff}} = \frac{\left(2.23 \times 10^{-4} \frac{\text{m}^2}{\text{s}}\right)(0.4)(0.8)}{3} = 2.376 \times 10^{-5} \text{ m}^2 \text{ s}^{-1}$$

Therefore, the value of Weisz-Prater criterion can be evaluated as:

$$\frac{(-r_{\text{exp}})\rho_c R_p^2}{D_{\text{eff}} C_{Ab}} = \frac{\left(6.32 \times 10^{-5} \frac{\text{mol}}{\text{g}_{\text{cat}} \cdot \text{s}}\right) \left(3.35 \frac{\text{g}}{\text{cm}^3}\right) \left(9.75 \times 10^{-5} \text{ m}\right)^2}{\left(2.376 \times 10^{-5} \frac{\text{m}^2}{\text{s}^{-1}}\right) \left(4.09 \times 10^{-5} \frac{\text{mol}}{\text{cm}^3}\right)} = 2.07 \times 10^{-3} < 1$$

### D.3 External Heat Transfer Resistance

The Mears criterion for negligible external heat transfer resistances is expressed in Eq. D.15 (Fogler, 2006).

$$\frac{|(-\Delta H_r)|(-r_{\text{exp}})\rho_b R_p E_A}{hRT_b^2} < 0.15 \quad \text{D.15}$$

where  $(-r_{\text{exp}}) = 6.32 \times 10^{-5} \text{ mol g}_{\text{cat}}^{-1} \text{ s}^{-1}$

$$\rho_b = 670 \text{ kg m}^{-3}$$

$$R_p = 9.75 \times 10^{-5} \text{ m}$$

$$-\Delta H_r = 245.45 \times 10^3 \text{ J mol}^{-1}$$

$$E_A = 87.37 \times 10^3 \text{ J mol}^{-1}$$

$h$  = heat transfer coefficient between gas mixture and catalyst ( $\text{J m}^{-2} \text{ s}^{-1} \text{ K}^{-1}$ )

$R$  = ideal gas constant ( $8.314 \text{ J mol}^{-1} \text{ K}^{-1}$ )

$T_b$  = reactant gas bulk temperature (1073 K)

### Heat transfer coefficient ( $h$ ) calculation

The Eq. D.16 shows the relation between heat transfer coefficient,  $j$  factor of heat and mass transfer, developed by Colburn-Chilton analogy. By rearranging the equation, the value of  $h$  can be computed.

$$j_D = j_H = \frac{h \text{Pr}^{\frac{2}{3}}}{C_{pg} \rho_g U} \quad \text{D.16}$$

where  $j_H = j$ -factor for heat transfer ( $j_H = j_D$ )

$C_{pg}$  = specific heat capacity of feed gas mixture at constant pressure ( $\text{J kg}^{-1} \text{K}^{-1}$ )

$\text{Pr}$  = Prandtl number

$\rho_g$  = density of the gas mixture ( $0.251 \text{ kg m}^{-3}$ )

$U$  = superficial gas velocity ( $7.35 \times 10^{-2} \text{ m s}^{-1}$ )

The specific heat capacity of the gas mixture ( $C_{pg}$ ) at constant pressure can be determined by using Eq. D.17.

$$C_{pg} = \sum_i y_i C_p^i = 3.11 \times 10^3 \text{ J kg}^{-1} \text{K}^{-1} \quad \text{D.17}$$

where  $i = \text{CH}_4, \text{H}_2\text{O}, \text{CO}_2$  and  $\text{N}_2$

$y$  = mole fraction of component gases

( $\text{CH}_4 = 0.444, \text{H}_2\text{O} = 0.296, \text{CO}_2 = 0.148, \text{N}_2 = 0.112$ )

$C_p$  = specific heat capacity of gas components

( $\text{CH}_4 = 4.724 \times 10^3 \text{ J kg}^{-1} \text{K}^{-1}, \text{H}_2\text{O} = 2.340 \times 10^3 \text{ J kg}^{-1} \text{K}^{-1},$

$\text{CO}_2 = 1.251 \times 10^3 \text{ J kg}^{-1} \text{K}^{-1}, \text{N}_2 = 1.181 \times 10^3 \text{ J kg}^{-1} \text{K}^{-1}$ )

The thermal conductivity of gas mixture ( $\lambda_g$ ) was determined from Eqs. D.18, D.19 and D.20.

$$\lambda_g = \sum_i \frac{y_i \lambda_i}{\sum_{j \neq i} y_j \psi_{ij}} \quad \text{D.18}$$

$$\psi_{ij} = \frac{1}{4} \left\{ 1 + \left[ \left( \frac{\mu_i}{\mu_j} \right) \left( \frac{M_j}{M_i} \right)^{\frac{3}{4}} \left( \frac{T + S_i}{T + S_j} \right)^{\frac{1}{2}} \right]^2 \right\} \left( \frac{T + S_{ij}}{T + S_i} \right) \quad \text{D.19}$$

$$S_{ij} = S_{ji} = C (S_i S_j)^{\frac{1}{2}} \quad \text{D.20}$$

where  $i, j = \text{CH}_4, \text{H}_2\text{O}, \text{CO}_2$  and  $\text{N}_2$

$y$  = mole fraction of component gases

( $\text{CH}_4 = 0.444, \text{H}_2\text{O} = 0.296, \text{CO}_2 = 0.148, \text{N}_2 = 0.112$ )

$\lambda$  = thermal conductivity of gas components

( $\text{CH}_4 = 0.186 \text{ J m}^{-1} \text{ s}^{-1} \text{ K}^{-1}, \text{H}_2\text{O} = 0.106 \text{ J m}^{-1} \text{ s}^{-1} \text{ K}^{-1},$   
 $\text{CO}_2 = 0.072 \text{ J m}^{-1} \text{ s}^{-1} \text{ K}^{-1}, \text{N}_2 = 0.071 \text{ J m}^{-1} \text{ s}^{-1} \text{ K}^{-1}$ )

$\mu$  = viscosity of gas components

( $\text{CH}_4 = 2.938 \times 10^{-5} \text{ kg m}^{-1} \text{ s}^{-1}, \text{H}_2\text{O} = 4.081 \times 10^{-5} \text{ kg m}^{-1} \text{ s}^{-1},$   
 $\text{CO}_2 = 4.190 \times 10^{-5} \text{ kg m}^{-1} \text{ s}^{-1}, \text{N}_2 = 4.347 \times 10^{-5} \text{ kg m}^{-1} \text{ s}^{-1}$ )

$M$  = molecular weight of gas components

( $\text{CH}_4 = 16.04 \text{ g mol}^{-1}, \text{H}_2\text{O} = 18.02 \text{ g mol}^{-1},$   
 $\text{CO}_2 = 44.01 \text{ g mol}^{-1}, \text{N}_2 = 28.01 \text{ g mol}^{-1}$ )

$T$  = gas mixture temperature (1073 K)

$C = 1$  for both gases non-polar and  $C = 0.73$  even if one of the gas is polar

$S = 1.5 \times \text{boiling point (K)}$

( $\text{CH}_4 = 111.5 \text{ K}, \text{H}_2\text{O} = 373.0 \text{ K}, \text{CO}_2 = 194.5 \text{ K}, \text{N}_2 = 77.2 \text{ K}$ )

Thus, the value of thermal conductivity of the gas mixture,  $\lambda_g = 7.416 \times 10^2 \text{ J m}^{-1} \text{ s}^{-1} \text{ K}^{-1}$  is obtained after substituting all the values in above equations. After that, the Prandtl number, Pr can be estimated as shown in Eq. D.21 below.

$$\text{Pr} = \frac{C_{pg} \mu_g}{\lambda_g} \quad \text{D.21}$$

$$\text{Pr} = \frac{\left(3.11 \times 10^3 \frac{\text{J}}{\text{kg.K}}\right) \left(1.84 \times 10^{-5} \frac{\text{kg}}{\text{m.s}}\right)}{\left(7.416 \times 10^2 \frac{\text{J}}{\text{m.s.K}}\right)} = 0.769$$

Hence, the heat transfer coefficient ( $h$ ) is

$$h = \frac{j_D C_{pg} \rho_g U}{\text{Pr}^{\frac{2}{3}}}$$

$$h = \frac{(4.494) \left(3.11 \times 10^3 \frac{\text{J}}{\text{kg.K}}\right) \left(0.251 \frac{\text{kg}}{\text{m}^3}\right) \left(7.35 \times 10^{-2} \frac{\text{m}}{\text{s}}\right)}{(0.769)^{\frac{2}{3}}} = 306.985 \text{ J m}^{-2} \text{ s}^{-1} \text{ K}^{-1}$$

The value for external heat transfer resistances is

$$\frac{|(-\Delta H_r)| (-r_{\text{exp}}) \rho_b R_p E_A}{h R T_b^2}$$

$$\frac{\left(245.449 \frac{\text{kJ}}{\text{mol}}\right) \left(6.32 \times 10^{-5} \frac{\text{mol}}{\text{g}_{\text{cat}} \cdot \text{s}}\right) \left(670 \frac{\text{kg}}{\text{m}^3}\right) \left(9.75 \times 10^{-5} \text{m}\right) \left(87.37 \times 10^3 \frac{\text{J}}{\text{mol}}\right)}{\left(306.985 \frac{\text{J}}{\text{m}^2 \cdot \text{s.K}}\right) \left(8.314 \frac{\text{J}}{\text{mol.K}}\right) (1073)^2}$$

$$= 3.013 \times 10^{-5} < 0.15$$

#### D.4 Internal Heat Transfer Resistance

The Anderson criterion for negligible intraparticle heat transfer resistance is expressed in Eq. D.22.

$$\frac{|(-\Delta H_r)|(-r_{\text{exp}})\rho_b R_p^2 E_A}{\lambda_p R T_s^2} < 0.75 \quad \text{D.22}$$

where  $(-r_{\text{exp}}) = 6.32 \times 10^{-5} \text{ mol g}_{\text{cat}}^{-1} \text{ s}^{-1}$

$$\rho_b = 670 \text{ kg m}^{-3}$$

$$R_p = 9.75 \times 10^{-5} \text{ m}$$

$$-\Delta H_r = 245.45 \times 10^3 \text{ J mol}^{-1}$$

$$E_A = 87.37 \times 10^3 \text{ J mol}^{-1}$$

$$\lambda_p = \text{thermal conductivity of catalyst pellet (J m}^{-2} \text{ s}^{-1} \text{ K}^{-1})$$

$$R = \text{ideal gas constant (8.314 J mol}^{-1} \text{ K}^{-1})$$

$$T_b = T_s = \text{reactant gas bulk temperature} \\ (\text{1073 K since external heat transport effect is negligible})$$

The thermal conductivity of catalyst pellet,  $\lambda_p$  can be determined from the Eq. D.23.

$$\log(\lambda_p \times 10^5) = 0.859 + 3.12 \left( \frac{\lambda_m}{\omega_p} \right) \quad \text{D.23}$$

where  $\omega_p = \text{catalyst pellet porosity (0.4)}$

$$\lambda_m = \text{thermal of the catalyst material (Silica = } 2.6 \text{ J m}^{-1} \text{ s}^{-1} \text{ K}^{-1})$$

Thus, the value of  $\lambda_p = 6.42 \times 10^3 \text{ J m}^{-1} \text{ s}^{-1} \text{ K}^{-1}$ .

The value of internal heat transfer resistances is

$$\frac{|(-\Delta H_r)|(-r_{\text{exp}})\rho_b R_p^2 E_A}{\lambda_p R T_s^2} < 0.75$$

$$\frac{\left(245.449 \frac{\text{kJ}}{\text{mol}}\right)\left(6.32 \times 10^{-5} \frac{\text{mol}}{\text{g}_{\text{cat}} \cdot \text{s}}\right)\left(670 \frac{\text{kg}}{\text{m}^3}\right)\left(9.75 \times 10^{-5} \text{m}\right)^2\left(87.37 \times 10^3 \frac{\text{J}}{\text{mol}}\right)}{\left(6.42 \times 10^3 \frac{\text{J}}{\text{m}^2 \cdot \text{s} \cdot \text{K}}\right)\left(8.314 \frac{\text{J}}{\text{mol} \cdot \text{K}}\right)(1073)^2}$$

$$= 1.514 \times 10^{-11} < 0.75$$

### D.5 Wall and Radial Heat Dispersion Effects

If the ratio of diameter in Eq. D.24 is larger than 4, the effects of wall heat transfer can be neglected.

$$\frac{d_t}{d_p} > 4 \quad \text{D.24}$$

where  $d_t$  = diameter of reactor tube ( $7.9 \times 10^{-3}$  m)

$d_p$  = diameter of catalyst particle ( $1.95 \times 10^{-4}$  m)

The ratio of diameter is

$$\frac{7.9 \times 10^{-3} \text{ m}}{1.95 \times 10^{-4} \text{ m}} = 40.5 > 4$$

By using the Mears criterion in Eq. D.25, the radial heat dispersion effect can be estimated.

$$\left(\frac{E_A}{RT_w}\right)\left(\frac{|(-\Delta H_r)|(-r_{\text{exp}})\rho_b R_p^2 [(1-\varepsilon)/(1-b)]}{4\lambda_p T_w}\right)\left(\frac{1}{8} + \frac{B_p}{Bi_w R_t}\right) < 0.05 \quad \text{D.25}$$

where  $T_w = T_b = 1073$  K

$\varepsilon$  = void fraction in the catalyst bed (0.8)

$b$  = inert solids fraction of the catalyst bed (0)

$R_t$  = radius of reactor tube ( $3.95 \times 10^{-3}$  m)

Wall Biot number ( $Bi_w$ ) can be determined by Eq. D.26.

$$Bi_w = \frac{h_w d_p}{\lambda_p} \quad \text{D.26}$$

where  $h_w$  = heat transfer coefficient of reactor tube wall (quartz tube)

$d_p$  = diameter of catalyst particle ( $1.95 \times 10^{-4}$  m)

$\lambda_p$  = thermal conductivity of catalyst pellet ( $6.42 \times 10^3 \text{ J m}^{-2} \text{ s}^{-1} \text{ K}^{-1}$ )

$$Bi_w = \frac{\left(30 \frac{\text{J}}{\text{m}^2 \cdot \text{s} \cdot \text{K}}\right) (1.95 \times 10^{-4} \text{ m})}{\left(6.42 \times 10^3 \frac{\text{J}}{\text{m} \cdot \text{s} \cdot \text{K}}\right)} = 9.11 \times 10^{-7}$$

Therefore, the value of radial heat dispersion can be estimated as shown below.

$$\left( \frac{87.37 \times 10^3 \frac{\text{J}}{\text{mol}}}{\left(8.314 \frac{\text{J}}{\text{mol} \cdot \text{K}}\right) (1073 \text{ K})} \right) \times \left( \frac{\left(245.449 \times 10^3 \frac{\text{J}}{\text{mol}}\right) \left(6.32 \times 10^{-5} \frac{\text{mol}}{\text{g}_{\text{cat}} \cdot \text{s}}\right) \left(670 \frac{\text{kg}}{\text{m}^3}\right) (9.75 \times 10^{-5} \text{ m})^2 [(1-0.4)/(1-0)]}{4 \left(6.42 \times 10^3 \frac{\text{J}}{\text{m} \cdot \text{s} \cdot \text{K}}\right) (1073 \text{ K})} \right) \times$$

$$\left( \frac{1}{8} + \frac{670 \frac{\text{kg}}{\text{m}^3}}{\left(9.11 \times 10^{-7}\right) (3.95 \times 10^{-3} \text{ m})} \right) = 2.05 \times 10^{-9} < 0.05$$

## LIST OF PUBLICATIONS

### Patent

1. A Multi-functional Ni-based Catalyst for Enhanced Syngas Production, Patent No. PI2016400011, May 11, Malaysian Intellectual Property (MYIPO).

Inventor(s): 1. Vo Nguyen Dai Viet 2. **Tan Ji Siang** 3. Sharanjit Singh

2. A Novel Multifunctional Catalytic Reactor System for Sustainable Hydrogen Production, Patent No. PI2015001572, June 16, Malaysian Intellectual Property (MYIPO).

Inventor(s): 1. Vo Nguyen Dai Viet 2. **Tan Ji Siang** 3. Tai Chan Kong

### Patent

This study:

1. **T.J. Siang**, T.L.M. Pham, N.V. Cuong, P.T.T. Phuong, N.H.H. Phuc, Q.D. Truong, D.-V.N. Vo. (2018). Combined steam and CO<sub>2</sub> reforming of methane for syngas production over carbon-resistant boron-promoted Ni/SBA-15 catalysts. *Microporous and Mesoporous Materials*, 262, 122-132.

Other studies:

1. **T.J. Siang**, S. Singh, O. Omoregbe, L.G. Bach, N.H.H. Phuc, D.-V.N. Vo. (2017). Hydrogen production from CH<sub>4</sub> dry reforming over bimetallic Ni-Co/Al<sub>2</sub>O<sub>3</sub> catalyst. *Journal of the Energy Institute* (Article in Press, DOI: 10.1016/j.joei.2017.06.001).
2. **T.J. Siang**, H.T. Danh, S. Singh, Q.D. Truong, H.D. Setiabudi, D.-V.N. Vo. (2017). Syngas production from combined steam and carbon dioxide reforming of methane over Ce-modified silicasupported nickel catalysts. *Chemical Engineering Transactions*, 56, 1129-1134.
3. **T.J. Siang**, H.T. Danh, S. Singh, Q.D. Truong, H.D. Setiabudi, D.-V.N. Vo. (2017). Syngas production from CO<sub>2</sub> reforming and CO<sub>2</sub>-steam reforming of methane over Ni/Ce-SBA-15 catalyst. *IOP Conference Series: Materials Science and Engineering*, 206, 12017.

4. S. Singh, N.T.A. Nga, T.L.M. Pham, **T.J. Siang**, P.T.T. Phuong, M.R. Khan, D.-V.N. Vo. (2017). Metgas production from Bi-reforming of methane over lamodified santa barbara amorphous-15 supported nickel catalyst. *Chemical Engineering Transactions*, 56, 1573-1578.
5. M.B. Bahari, B.C. Goo, **T.J. Siang**, H.T. Danh, T.L.M. Pham, N. Ainirazali, D.-V.N. Vo. (2016). Hydrogen-rich syngas production from ethanol dry reforming on La-doped Ni/Al<sub>2</sub>O<sub>3</sub> catalysts: Effect of promoter loading, *Procedia Engineering*, 148, 654-661.

### Conference

1. **T.J. Siang**, H.T. Danh, S. Singh, Q.D. Truong, H.D. Setiabudi, D.-V.N. Vo. *Syngas production from CO<sub>2</sub> reforming and CO<sub>2</sub>-steam reforming of methane over Ni/SBA-15 catalyst*. 29<sup>th</sup> Symposium of Malaysian Chemical Engineers (SOMChE2016), Dec 1-3, Miri, Malaysia.
2. **T.J. Siang**, H.T. Danh, S. Singh, Q.D. Truong, H.D. Setiabudi, D.-V.N. Vo. *Syngas production from combined steam and CO<sub>2</sub> reforming of methane over Ce-modified silica-supported Ni catalysts*. 9<sup>th</sup> Regional Conference on Chemical Engineering (RCChE-2016), Nov 21-22, Kuala Lumpur, Malaysia.
3. **T.J. Siang**, H.M. Zakaria, K. Selvarajah, B. Abdullah, F. Alenazey, D.-V.N. Vo. *CO<sub>2</sub> (dry) reforming of methane over Ce-promoted Ni/Al<sub>2</sub>O<sub>3</sub> catalyst*. Fluids Engineering: Challenges and Opportunities (FluidsChe 2015). Nov 25-27, Langkawi Island, Malaysia.
4. **T.J. Siang**, F.-L.W. Ming, F. Alenazey, D.-V.N. Vo. *Hydrogen production from CH<sub>4</sub> dry reforming over bimetallic Ni-Co/Al<sub>2</sub>O<sub>3</sub> catalyst*. 5<sup>th</sup> International Conference On Environment 2015 (ICENV 2015), Aug 18-19, Penang, Malaysia.
5. S. Singh, **T.J. Siang**, T.L.M. Pham, P.T.T. Phuong, M.R. Khan, D.-V.N. Vo. *Metgas production from bi-reforming of methane over La-modified SBA-15 supported Ni catalyst*. 9<sup>th</sup> Regional Conference on Chemical Engineering (RCChE-2016), Nov 21-22, Kuala Lumpur, Malaysia.
6. O. Omoregbe, **T.J. Siang**, H.T. Danh, H.D. Setiabudi, S.Z. Abidin, D.-V.N. Vo, *Syngas production from methane dry reforming over Ni/SBA-15 catalyst: Effect of operating parameters*, 251<sup>st</sup> ACS National Meeting & Exposition, Mar 13-17, San Diego, USA.
7. M.B. Bahari, **T.J. Siang**, D.-V.N. Vo. *Ethanol dry reforming over Ce-promoted Ni/Al<sub>2</sub>O<sub>3</sub> catalyst for hydrogen synthesis*. National Conference for Postgraduate Research (NCON-PGR) 2015, Jan 24-25, 2015, Kuantan, Malaysia.

8. S. Singh, H.T. Danh, **T.J. Siang**, P.T.T. Phuong, M.R. Khan, D.-V.N. Vo. *Influence of reaction parameters on La-modified SBA-15 supported Ni catalyst for methane dry reforming*. 29<sup>th</sup> Symposium of Malaysian Chemical Engineers (SOMChE2016), Dec 1-3, Miri, Malaysia.
9. S. Singh, O. Omoregbe, **T.J. Siang**, F. Fayaz, D.-V.N. Vo. *A short review on mesoporous silica-supported catalysts for methane dry reforming*, The Third National Conference for Postgraduate Research 2016 (NCON-PGR2016), Sept 24-25, Pekan, Malaysia.
10. M.B. Bahari, B.C. Goo, **T.J. Siang**, H.T. Danh, T.L.M. Pham, N. Ainirazali, D.-V.N. Vo. *Hydrogen-rich syngas production from ethanol dry reforming on La-doped Ni/Al<sub>2</sub>O<sub>3</sub> catalysts: Effect of promoter loading*. 4<sup>th</sup> International Conference on Process Engineering and Advanced Materials (ICPEAM2016), Aug 15-17, Kuala Lumpur, Malaysia.

### **Exhibitions**

1. **T.J. Siang**, T.K. Wei and D.-V.N. Vo. *Hydrogen production from CH<sub>4</sub> dry reforming over bimetallic Ni-Co/Al<sub>2</sub>O<sub>3</sub> catalyst*. Creation, Innovation, Technology & Research Exposition 2015 (CITREX 2015), Mar 9-10, Universiti Malaysia Pahang, Pahang, Malaysia. [**Bronze medal**]
2. G.B. Chin, **T.J. Siang**, M.B. Bahari. *Hydrogen-rich syngas production from ethanol dry reforming on La-doped Ni/Al<sub>2</sub>O<sub>3</sub> catalysts: Effect of promoter loading*. International Festival Innovation on Green Technology (i-FINOG 2016), Apr 15-17, Universiti Malaysia Pahang, Pahang, Malaysia. [**Gold medal**]
3. D.-V.N. Vo, O. Omoregbe, S. Singh, **T.J. Siang**. *Multi-functional Ni/SBA-15 catalyst for syngas production*. International Trade Fair Ideas Inventions New Products 2016 (IENA 2016), Oct 27-30, Exhibition Center Nuremberg Hall, Nuremberg, Germany. [**Gold medal**]
4. D.-V.N. Vo, O. Omoregbe, S. Singh, **T.J. Siang**, F. Fayaz. *Multi-functional modified Ni/SBA-15 catalyst for syngas production from various H-containing compounds*. International Invention, Innovation & Technology Exhibition 2016 (ITEX 2016), May 12-14, Kuala Lumpur Convention Centre, Kuala Lumpur, Malaysia. [**Gold medal**]
5. D.-V.N. Vo, O. Omoregbe, **T.J. Siang**, S. Singh. *Multi-functional modified Ni/SBA-15 catalysts for syngas production from various H-containing compounds*. Citrex2016, Mar 7-8, UMP, Kuantan, Pahang, Malaysia. [**Gold medal**]

6. D.-V.N. Vo, **T.J. Siang** and T.C. Kong. *A novel multifunctional catalytic reactor system for sustainable hydrogen production*. Malaysia Technology Expo 2016 (MTE 2016), Feb 18-20, Putra World Trade Centre, Kuala Lumpur, Malaysia. [**Silver medal**]
7. D.-V.N. Vo, T.C. Kong, **T.J. Siang**, K.R. Shuan, M.B. Bahari. *A novel multifunctional catalytic reactor system for sustainable hydrogen production*. Creation, Innovation, Technology & Research Exposition 2015 (CITREX 2015), Mar 9-10, Universiti Malaysia Pahang, Pahang, Malaysia. [**Gold medal**]
8. D.-V.N. Vo, M.B. Bahari, **T.J. Siang**, T.K. Wei, N. Ainirazali. *Dry reforming of ethanol for hydrogen generation over La-promoted Ni/Al<sub>2</sub>O<sub>3</sub> catalyst*. Creation, Innovation, Technology & Research Exposition 2015 (CITREX 2015), Mar 9-10, Universiti Malaysia Pahang, Pahang, Malaysia. [**Silver medal**]

